frontiers | Research Topics

Network physiology, insights in systems interactions and organ networks 2021

Edited by
Plamen Ch. Ivanov

Published in
Frontiers in Network Physiology

ISSN 1664-8714
ISBN 978-2-8325-2523-4
DOI 10.3389/978-2-8325-2523-4

About Frontiers

Frontiers is more than just an open access publisher of scholarly articles: it is a pioneering approach to the world of academia, radically improving the way scholarly research is managed. The grand vision of Frontiers is a world where all people have an equal opportunity to seek, share and generate knowledge. Frontiers provides immediate and permanent online open access to all its publications, but this alone is not enough to realize our grand goals.

Frontiers journal series

The Frontiers journal series is a multi-tier and interdisciplinary set of open-access, online journals, promising a paradigm shift from the current review, selection and dissemination processes in academic publishing. All Frontiers journals are driven by researchers for researchers; therefore, they constitute a service to the scholarly community. At the same time, the *Frontiers journal series* operates on a revolutionary invention, the tiered publishing system, initially addressing specific communities of scholars, and gradually climbing up to broader public understanding, thus serving the interests of the lay society, too.

Dedication to quality

Each Frontiers article is a landmark of the highest quality, thanks to genuinely collaborative interactions between authors and review editors, who include some of the world's best academicians. Research must be certified by peers before entering a stream of knowledge that may eventually reach the public - and shape society; therefore, Frontiers only applies the most rigorous and unbiased reviews. Frontiers revolutionizes research publishing by freely delivering the most outstanding research, evaluated with no bias from both the academic and social point of view. By applying the most advanced information technologies, Frontiers is catapulting scholarly publishing into a new generation.

What are Frontiers Research Topics?

Frontiers Research Topics are very popular trademarks of the *Frontiers journals series*: they are collections of at least ten articles, all centered on a particular subject. With their unique mix of varied contributions from Original Research to Review Articles, Frontiers Research Topics unify the most influential researchers, the latest key findings and historical advances in a hot research area.

Find out more on how to host your own Frontiers Research Topic or contribute to one as an author by contacting the Frontiers editorial office: frontiersin.org/about/contact

Network physiology, insights in systems interactions and organ networks: 2021

Topic editor
Plamen Ch. Ivanov — Boston University, United States

Citation
Ivanov, P. C., ed. (2023). *Network physiology, insights in systems interactions and organ networks: 2021*. Lausanne: Frontiers Media SA.
doi: 10.3389/978-2-8325-2523-4

Table of contents

frontiers in Network Physiology

ORIGINAL RESEARCH
published: 28 September 2021
doi: 10.3389/fnetp.2021.746118

Information Optimized Multilayer Network Representation of High Density Electroencephalogram Recordings

Francesc Font-Clos[1], *Benedetta Spelta*[1], *Armando D'Agostino*[2,3], *Francesco Donati*[2,3], *Simone Sarasso*[4], *Maria Paola Canevini*[2,3], *Stefano Zapperi*[1,5] *and Caterina A. M. La Porta*[6,7]*

[1]*Center for Complexity and Biosystems, Department of Physics, University of Milan, Milano, Italy,* [2]*Department of Health Sciences, University of Milan, Milano, Italy,* [3]*Department of Mental Health and Addiction, ASST Santi Paolo e Carlo, Milano, Italy,* [4]*Department of Biomedical and Clinical Sciences 'Luigi Sacco', Milano, Italy,* [5]*CNR-Consiglio Nazionale delle Ricerche, Istituto di Chimica della Materia Condensata e di Tecnologie per l'Energia, Milano, Italy,* [6]*Center for Complexity and Biosystems, Department of Environmental Science and Policy, University of Milan, Milano, Italy,* [7]*CNR-Consiglio Nazionale delle Ricerche, Istituto di Biofisica, Milano, Italy*

High-density electroencephalography (hd-EEG) provides an accessible indirect method to record spatio-temporal brain activity with potential for disease diagnosis and monitoring. Due to their highly multidimensional nature, extracting useful information from hd-EEG recordings is a complex task. Network representations have been shown to provide an intuitive picture of the spatial connectivity underlying an electroencephalogram recording, although some information is lost in the projection. Here, we propose a method to construct multilayer network representations of hd-EEG recordings that maximize their information content and test it on sleep data recorded in individuals with mental health issues. We perform a series of statistical measurements on the multilayer networks obtained from patients and control subjects and detect significant differences between the groups in clustering coefficient, betwenness centrality, average shortest path length and parieto occipital edge presence. In particular, patients with a mood disorder display a increased edge presence in the parieto-occipital region with respect to healthy control subjects, indicating a highly correlated electrical activity in that region of the brain. We also show that multilayer networks at constant edge density perform better, since most network properties are correlated with the edge density itself which can act as a confounding factor. Our results show that it is possible to stratify patients through statistical measurements on a multilayer network representation of hd-EEG recordings. The analysis reveals that individuals with mental health issues display strongly correlated signals in the parieto-occipital region. Our methodology could be useful as a visualization and analysis tool for hd-EEG recordings in a variety of pathological conditions.

Keywords: high density electroencephalogram, multilayer networks, bipolar disorder, maximum information, first episode psychosis

OPEN ACCESS

Edited by:
Plamen Ch. Ivanov,
Boston University, United States

Reviewed by:
Ginestra Bianconi,
Queen Mary University of London, United Kingdom
Sebastiano Stramaglia,
University of Bari Aldo Moro, Italy
Pedro Carpena,
University of Malaga, Spain

***Correspondence:**
Caterina A. M. La Porta
caterina.laporta@unimi.it

Specialty section:
This article was submitted to Systems Interactions and Organ Networks, a section of the journal Frontiers in Network Physiology

Received: *23 July 2021*
Accepted: *13 September 2021*
Published: *28 September 2021*

Citation:
Font-Clos F, Spelta B, D'Agostino A, Donati F, Sarasso S, Canevini MP, Zapperi S and La Porta CAM (2021) Information Optimized Multilayer Network Representation of High Density Electroencephalogram Recordings. Front. Netw. Physiol. 1:746118. doi: 10.3389/fnetp.2021.746118

1 INTRODUCTION

Recent developments in neuroscience are giving rise to an increasing amount of data on the functioning of the brain at different scales, from molecular processes at the level of single neurons to macroscopic signals encompassing the whole brain, as in electroencephalogram (EEG) or functional magnetic resonance imaging (fMRI). Despite the trove of accumulating data, disentangling the complexity of brain function is still a largely open issue. A particularly important goal is to develop tools that are able to extract useful information from brain activity measurements on individual subjects in order to identify potential network dysfunction and support diagnosis (Bassett, 2021).

It is becoming increasingly clear that brain activity is strongly interconnected and hierarchically organized, requiring a sophisticated mathematical description to infer its underlying properties from measurements. The emerging field of *network neuroscience* is advocating the use of networks descriptions for a statistical analysis of brain functions at multiple spatio-temporal scales (Bassett and Sporns, 2017). As in many other applications, a network representation can be derived by suitably thresholding the covariance matrix of the signal recorded at different locations (Masuda et al., 2018) with sophisticated metodologies to chose an optimal threshold (De Vico Fallani et al., 2017) or using singular value decomposition of the multidimensional signal (Worsley et al., 2005). A typical feature of many complex networks that appears promising to describe the hierarchical brain organization is the small-world topology involving at the same time small-scale local clusters and long-range connections between distant areas (Bassett and Bullmore, 2006). Networks provide a visual representation of brain connectivity (Rubinov and Sporns, 2010), but extracting robust statistical information from brain network is a challenging task. Measures at the intersection between neuroscience and complexity theory have emerged such as topological data analysis (Phinyomark et al., 2017) or multivariate auto-regressive models (Astolfi et al., 2007).

EEG recordings have attracted a wide interest for many years in the study of brain function due to the relative simplicity in which spatially localized time dependent data can be acquired through non-invasive instrumentation. EEG data are conventionally analyzed by sampling time depended signals into different frequency bands at different locations on the scalp and then looking for specific signatures in each band. For instance, resting state EEG in patients diagnosed with First Episode Psychosis and Bipolar Disorder revealed a general trend of increased delta (0.5–4 Hz) and theta (4–8 Hz) activity, and a decrease in alpha (8–13 Hz) activity (Clementz et al., 1994). Resting state EEG of bipolar patients has also been studied using complex network analysis in Kim et al. (2013), yielding differences from healthy control subjects across several network measures such as clustering coefficient or characteristic path length. More recently, machine learning combined with complex network analysis was used to classify non-epileptic and epileptic EEG signals (Gao et al., 2020). Network analysis was also performed for EEG signals recorded in Alzheimer Disease patients during cognitive tasks and resting state (Das and Puthankattil, 2020), revealing a higher betweenness centrality in patients compared to controls subjects.

Since EEG signals are highly multidimensional, considering their dependence on time, location and frequency band, a projection into a single network may overshadow some essential feature of the system. To overcome this limitation, multilayer netwroks have been recently proposed as a promising tool to study the dynamics of brain activity, reducing the information loss due to the projection into a single network (Muldoon and Bassett, 2016; De Domenico, 2017). A multilayer network can be seen as an interconnected set single-layer networks where each layer represents a particular dimension of the original signal (Aleta and Moreno, 2019; Bianconi, 2018). In the context of EEG we can assign distinct layers to different time windows and/or different frequency bands and assign each electrode to a node in each single-layer network. For example, a time-based multilayer complex network analysis was perfomed on EEG recordings in patients with epilepsy (Leitgeb et al., 2020). The central issues in multilayer network based methods for EEG signal is to find a representation that minimizes information loss and introduce suitable statistical tools to extract readable information from the networks.

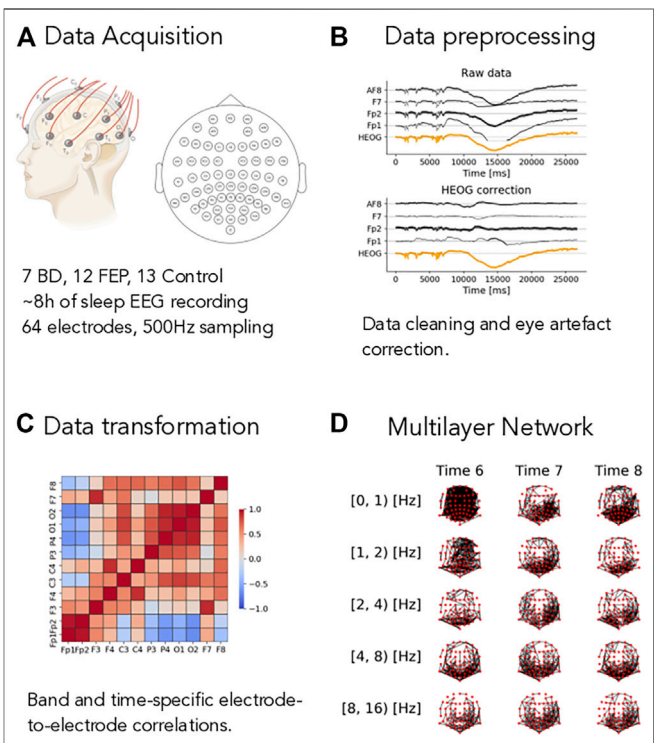

FIGURE 1 | Overview of the method. **(A)** Short description of the dataset, see Methods for complete details. **(B)** Example of the eye-artifact correction method, showing the correlation of the signal from electrodes AF8, F7, Fp1, and Fp2 (black lines) with horizontal eye movements (HEOG, orange line) before (Raw data panel) and after (HEOG correction panel) the eye-artifact correction method. **(C)** Example of a electrode-to-electrode correlation matrix, depicted as a heatmap. Correlation goes from −1 (blue shading) to +1 (red shading). Correlations are both time- and band-specific. **(D)** Example of the resulting band- and time-depended multilayer networks, where nodes represent electrode and edges represent high correlations, see Methods for the details of the different thresholding procedures.

In this paper, we propose a multilayer network representation of EEG signals that maximize the information content and apply it to a set of sleep EEG data from patients diagnosed with First Episode Psychosis (FEP) or Bipolar Disorder (BD) and compared with control subjects. We then use a set of network measures and show that it is easier to reliably stratify patients from control subjects when using network representations with constant edge densities.

2 RESULTS

2.1 Maximization of Total Information Change Over Time

Sleep hd-EEG recordings from 12 FEP, seven BD patients, and 13 control subjects were analyzed, see Methods for details and **Figure 1**. Raw data are extremely fine-grained: the sampling frequency of 500 Hz during an average of 8 h of sleep, multiplied by the 64 electrodes that comprise the EEG headset yields approximately, 1,000,000,000 measurements per patient. Clearly, these measurements are not all independent of each other, but they encode information that spans several sleep phases and brain regions. Therefore, we aim at finding a satisfactory compromise between compression and information.

To do so, we process the raw sleep EEG records through our pipeline as described in Methods in detail and illustrated in **Figure 1**. The first step is to remove artifacts from the data. Eye-movement artifacts are well known to influence raw sleep EEG data. To mitigate their impact on our results, we use a fast linear regression model to correct for eye movements, see Methods for details and **Figure 1B**: in this illustrative figure, the horizontal electro-oculogram potential (HEOG) well correlated with channels AF8, F7, FP2 and FP1 in the top plot. After the correction step (bottom plot in pannel B), this dependence was almost completely eliminated. After splitting the signal into different frequency bands (see Methods for details), we compute time- and band-specific electrode-to-electrode correlations of the form $C^b_{ij}(t)$, represented as a heatmap in **Figure 1C**. Finally, we construct time-varying multilayer networks using an innovative strategy that takes into account the whole dataset (and not each time snapshot individually), maximising the total amount of information contained in the time-varying dataset. **Figure 1D** offers a visual representation of the final output we obtain after processing the raw EEG data: a set of time-varying multilayer networs, where different layers correspond to different frequency bands, network nodes represent electrodes and edges represent high EEG correlations.

Networks offer a simplified and effective representation of interactions between nodes, but deciding the correlation threshold beyond which edges are added to the network is a nontrivial subject. In order to make an informed choice, here we introduce the Integrated Jensen-Shannon Divergence (IJSD),

$$\mathcal{I}(\theta) = \sum_{t=1}^{\theta} D(\rho_{t-1}, \rho_t), \tag{1}$$

a measure of the total information change over time (Grosse et al., 2002), computed as the sum of the Jensen-Shannon divergence of each epoch with respect to the previous one. Here ρ_t are the density matrices associated to each network in the framework of spectral entropies (Domenico and Biamonte, 2016), see Methods for details. The value of $\mathcal{I}$ depends on θ in non-trivial ways, but the limit cases are clear: if θ is too low (high), all edges are present (absent) at all time steps, so there is no information change over time and thus $\mathcal{I} = 0$ for both $\theta = 0$ and $\theta = 1$. It is only for intermediate values of the correlation threshold θ that the sequence of multilayer networks can display richer temporal variations, yielding a higher information change. This can be clearly seen in **Figure 2** panels (A, B, C), which show the value of $\mathcal{I}$ as a function of θ for one BD, one FEP and one control example. As anticipated, $\mathcal{I}(\theta) = 0$ for both $\theta = 0$ and $\theta = 1$, with a clear maximum at around $\theta \sim 0.7$ for most frequency bands.

2.2 Fixed-Threshold and Fixed-Density Networks

We implement two strategies to choose the optimal correlation threshold $\theta^\star$ from the analysis of the information content quantified by IJSD. In the first approach, we set a global absolute value for the correlation threshold, while in the second approach that value is relative to each network and chosen to maintain a constant edge density, keeping only the interactions with highest absolute correlation. In both cases, the adjacency matrices can be build as

$$A^b_{ij}(t) = \begin{cases} 1 & \text{if } |C^b_{ij}(t)| \geq \theta^* \\ 0 & \text{else} \end{cases} \tag{2}$$

that is, we place edges for both large positive and large negative correlations.

The optimal correlation threshold $\theta^\star$ for fixed-threshold networks is computed as the average of the band- and patient-specific optimal values that result from optimizing each case separately,

$$\theta^* = \langle \theta^*_{b,p} \rangle_{b,p} \tag{3}$$

$$\theta^*_{b,p} = \text{argmax}_{\theta \in [0,1]} \mathcal{I}_{b,p}(\theta) \tag{4}$$

where $\mathcal{I}_\theta(b, p)$ denotes the IJSD of patient p at frequency band b. In other words, for each patient p we compute a band-specific optimal threshold $\theta^*_{b,p}$. The group averages and variability of these are shown in **Figure 2**. Taking the average of all $\theta^*_{b,p}$, we reach an overall value of $\theta^\star = 0.72$, shown as a black solid line in **Figure 2**. Overall, the figure shows that a single global threshold can reasonably accommodate for the band- and patient-specific optimal values.

The second approach consists in keeping the same fraction of edges in all networks, yielding what we call *fixed-density* networks. The optimal density value in this case is set so that it coincides with the average density of the fixed-threshold networks. This second approach takes into account that different patients, time point or bands might have different intrinsic correlation levels, and presents additional advantages from the network analysis point of view.

2.3 Network Edge Presence Shows Differences Between Groups

We investigate the group differences between BD and control patients, as well as between FEP and control patients. To do so, we need to condense the information contained in our multilayer and time-varying networks into simpler summary statistics. A

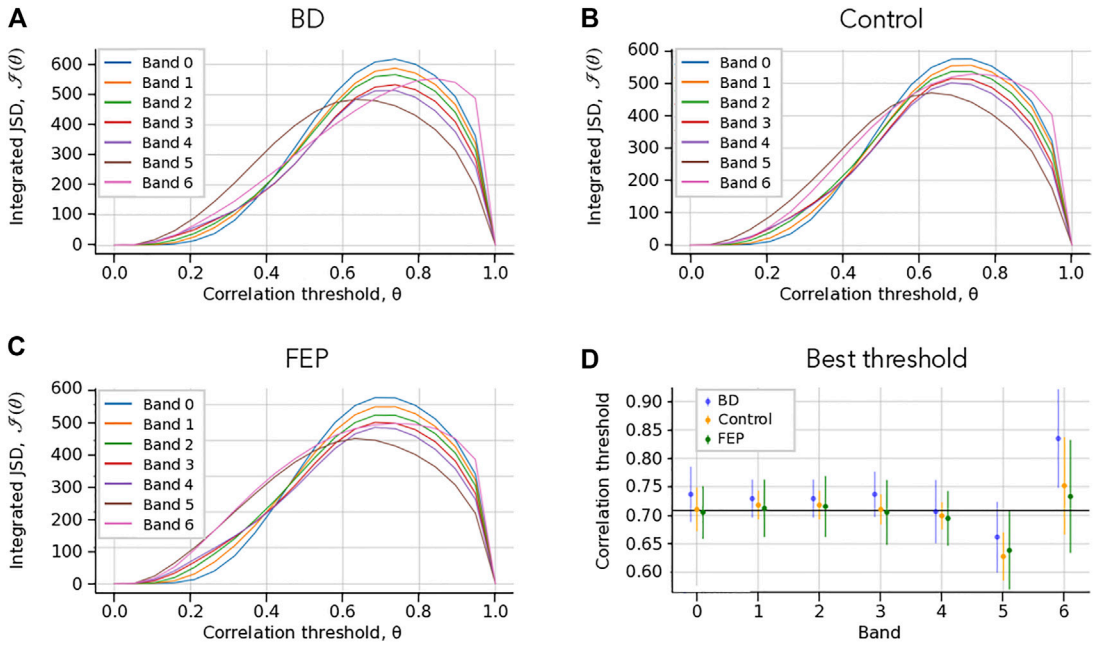

FIGURE 2 | Choice of correlation thresholds. **(A–C)** Check Which Patient. Integrated Jensen-Shannon divergence (JSD) as a function of the correlation threshold θ, for each band (colored lines), for BD **(A)**, Control **(B)** and FEP **(C)** patients. The panel shows a consistent maximum of the integrated JSD at around $\theta = 0.7$. **(B)** Threshold that maximizes the integrated JSD. The errorbars correspond to the average over different patients. The overall chosen best threshold is marked as a solid horizontal black line, see Methods for details. The panel shows that a single correlation threshold value can accommodate all patient groups and frequency bands.

simple yet useful measure in this case is what we coin as *edge presence*, which is the fraction of time an edge is present (that is, $A^b_{ij}(t) = 1$) during one full EEG sleep session. Formally,

$$P^b_{ij} = \langle A^b_{ij}(t) \rangle_t \tag{5}$$

Figure 3 shows the group differences of P^b_{ij} for each edge (i, j) and each band when comparing BD patients with controls (panels A, C), as well as FEP patients with controls (panels B, D). This analysis is shown both for fixed-density networks (A, B) and for fixed-threshold networks (C, D). In both cases we see differences in the parieto-occipital area, but the signal is stronger for fixed-density networks. If we focus on **Figure 3A**, for instance, we see that BD patients tend to have a lower edge presence in the parieto-occipital area (strong blue edges). Notice that we employ a colorbar that goes from red to transparent to blue, so that edges that do not have strong differences are effectively not drawn. Overall, the figure shows important differences in the parieto-occipital area, with a similar but stronger signal for fixed-density networks.

2.4 Parieto-Occipital Correlations and Clustering Measures Differ Between Groups

Motivated by the results shown visually in **Figure 3**, we construct a parieto-occipital (PO) specific measure. Selecting the 18 electrodes of that region (see methods for details), we compute the difference of PO presence between the PO area and the rest.

$$P_{\mathrm{PO}} = \langle P^b_{ij} \rangle_{(ij)\in \mathrm{PO}} - \langle P^b_{ij} \rangle_{(ij)\notin \mathrm{PO}} \tag{6}$$

Additionally, we also consider the average clustering coefficient, the average shortest path length and the betweenness centrality as measures related to clustering and information navigability as candidates to better quantify the differences that we see in **Figure 3**.

Figure 4 shows boxplots of these four measures comparing, BD and FEP patients with control subjects. Statistically significant differences are marked with a star, see Methods for details. Panels (A, B) show that for bands 1 to 4 (that is, between 1 and 16 Hz), FEP patients have a higher clustering coefficient when compared to controls, while panels (C, D) shows some significant results on the same range of frequencies for the average shortest path length, both for BD and for FEP patients. Turning to betweenness centrality, panel E shows that when using fixed-threshold networks, FEP patients significantly differ from controls in bands 2, 3, and 4 (2–16 Hz) Interestingly, when looking at the parieto-occipital relative presence (panels G, H), we observe a different pattern of marked differences between BD and control patients for lower frequency bands, 0.5–4 Hz. This is consistent with the fact that the more standard network measures used in panels A to F treat all nodes under the same footing, independently of the brain region they correspond to, while PO presence is a tailor-made measure, specifically designed to capture the visual results of **Figure 3** taking into account the location of parieto-occipital electrodes.

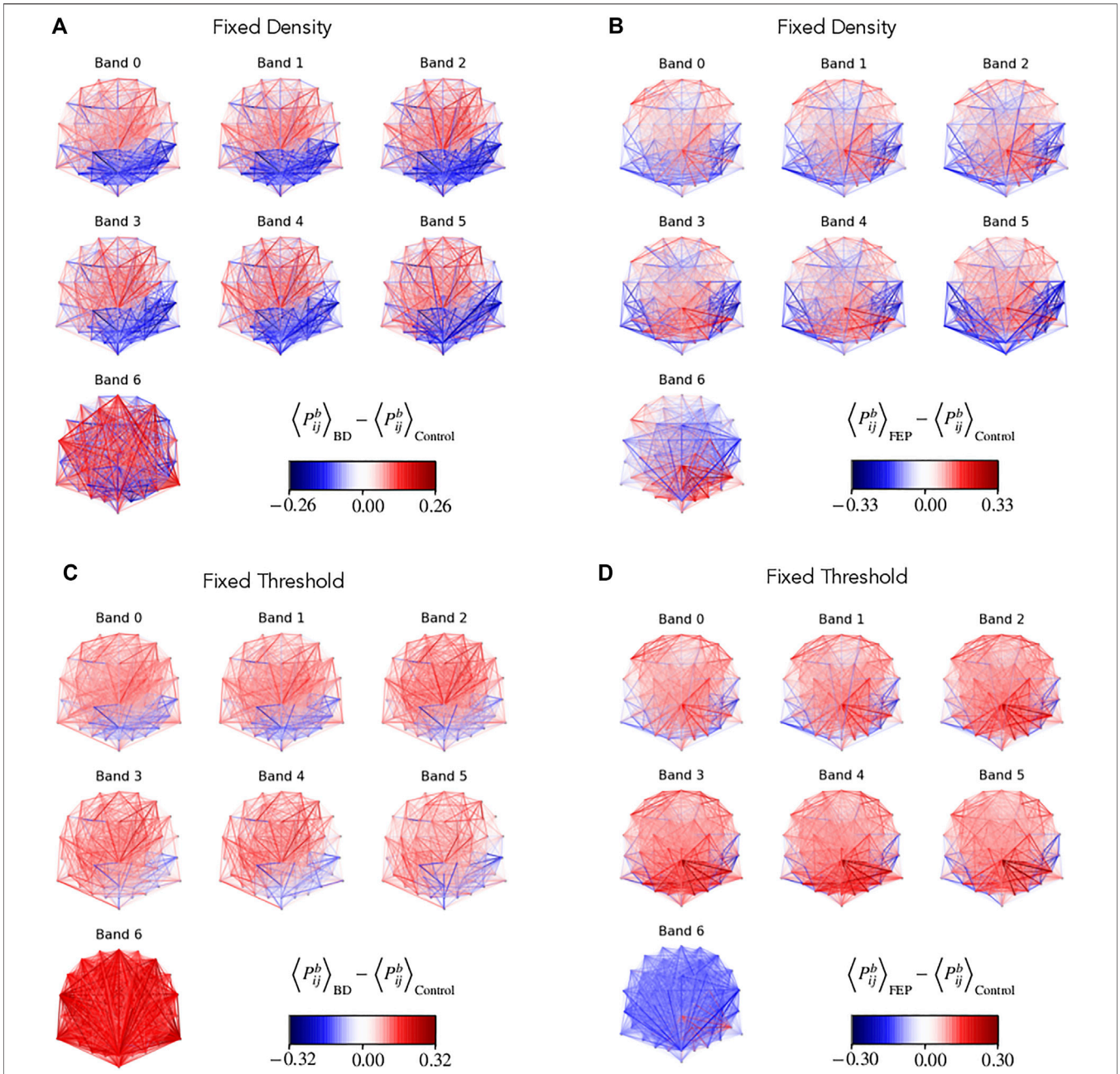

FIGURE 3 | Network edge presence highlights differences between groups. Multilayer EEG fixed-density **(A, B)** or fixed-threshold **(C, D)** networks, with edges colored according to the average BD **(A, D)** or FEP **(C, D)** presence minus the corresponding average value of control patients. Edge presence is a measure of the fraction of time an edge is active, see Methods for details. The four panels use a divergent colormap that is blue for negatives values, red for positive values, and becomes gradually transparent as values approach zero. Overall, the panel visually shows clear differences between BD and control patients, and between FEP and control patients.

2.5 Network Measures Correlate With Edge Density

It is interesting to ask if the network measures shown in **Figure 4** are correlated with network edge density, for the case of fixed-threshold networks. **Figure 5** shows how indeed edge density is a strong driver of average clustering coefficient, average shortest path length and betweenness centrality for all patient groups, but not of parieto-occipital presence. This is consistent with the fact that, by construction, P_{PO} is a relative difference of two averages taken on the same network.

3 DISCUSSION

Hd-EEG represents an attractive method to study brain function by providing non-invasive spatio-temporal measurements of brain activity with possible applications to disease diagnosis

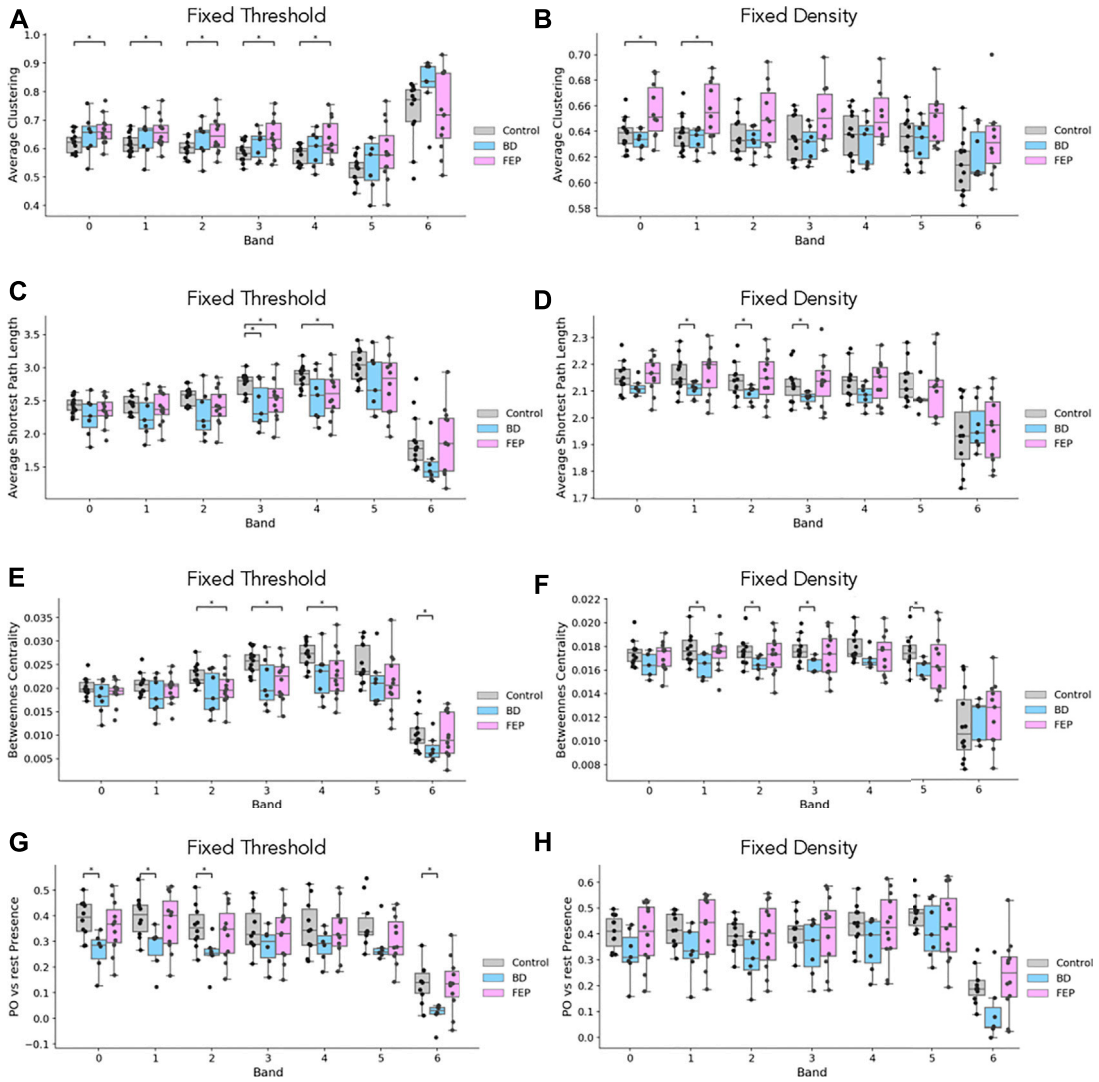

FIGURE 4 | EEG network measures evidence differences between groups. Boxplots of average clustering **(A, B)**, average shortest path length **(C, D)**, betweenness centrality **(E, F)** and parieto-occipital presence **(G, H)** for control (gray), BD (blue) and FEP (pink) patients. Panels in the left column correspond to fixed-threshold networks, while panels in the right column correspond to fixed-denstiy networks.

and monitoring. While it is relatively easy to obtain large amount of data from individual subjects, extracting useful information from hd-EEG recordings is a challenging task. Hd-EEG only provides an indirect far-field measurement of the underlying electrical activity and is intrinsically subject to noise. Furthermore, hd-EEG recordings typically involve noisy signals recorded in parallel through different electrodes for long time periods so that even the mere visualization of the data is complex.

Network representations have been shown in the past to provide a useful tool to highlight the connectivity and spatio-temporal correlation of brain activity as revealed from EEG or other measurments such as fMRI. Due to the complexity of hd-EEG recordings, multilayer networks are more appropriate to represent the data since they provide separate visualization for potentially crucial features of EEG signals such as the frequency band and/or the time dependence. An effective network representation of hd-EEG recordings should be able to extract most of the relevant information from the signal cross-correlation. To address this issue, we use the IJSD to quantify information content in the multilayer network (Domenico and Biamonte, 2016) and adjust correlation threshold parameters to maximize it. In this way, we obtain a multilayer networks that maximizes the information content of the underlying hd-EEG recordings and test it on a set of EEG data obtained from patients with mental health issue, as well as healthy control subjects.

Statistical analysis on the resulting multilayer networks reveals a number of distinguishing topological features between patients and the control group. In particular, observed differences in parieto-occipital edge presence appear to be particularly relevant. These results indicate a stronger correlation of EEG

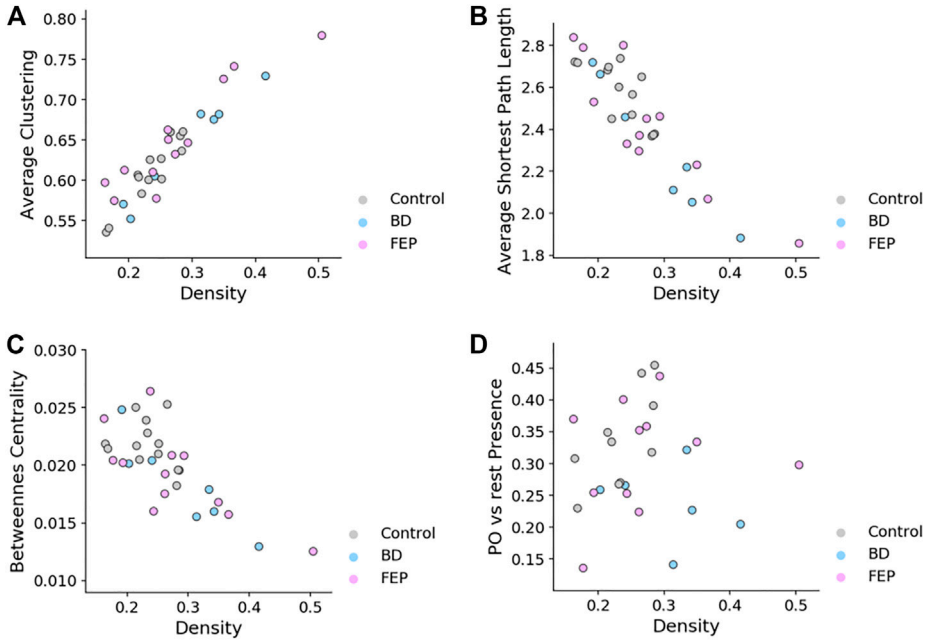

FIGURE 5 | Fixed-threshold networks yield measures that correlate with edge density. Scatter plots of average clustering **(A)**, average shortest path length **(B)**, betweenness centrality **(C)** and parieto-occipital presence **(D)** vs. network density, for fixed-threshold networks. Overall, the panel shows that all measures except parieto-occipital presence correlate with network density.

TABLE 1 | Recording time and sleep time. Sleep time is obtained by visual scoring according to the American Academy of Sleep Medicine (AASM) Manual for the Scoring of Sleep and Associated Events (Berry, R. B., Brooks, R., Gamaldo, C. E. and Susan, M. 2012). All values expressed in minutes.

	FEP	BD	Healthy control
Recording Time (mean ± S.D.)	431.02 ± 136.94	526.06 ± 44.84	489.22 ± 42.44
Total Sleep Time (mean ± S.D.)	300.02 ± 115.75	351.77 ± 102.38	361.47 ± 73.92

signals in that area for BD patients with respect to control subjects, a feature that warrants further study and could potentially be used as a diagnostic tool.

An important issue in our analysis is that most statistical indicators crucially depend on the density of edges present in the network. To discount this effect, we constructed and analyzed constant-density multilayer networks. While our analysis only considers pairwise correlations, future work could also extend our analysis to the study of interactions between groups of nodes (Battiston et al., 2020).

We applied our strategy to a particular set of EEG recordings from patients with mental disorders, but the methodology could readily be generalized and applied to a variety of pathological conditions. It would be interesting for instance to use our multilayer network approach to predict the response of individual patients to specific drugs. Finally, the analysis of EEG signals could be enriched by measuring at the same time other physiological signals, such as heartbeat or respiration adding further layers to the network, in the spirit of the emerging field of network physiology (Bashan et al., 2012; Bartsch et al., 2015; Ivanov et al., 2016).

4 METHODS

4.1 Data

Hd-EEG recordings where obtained from San Paolo Hospital in Milano. In particular, the dataset consists of sleep EEG recordings from 12 FEP patients (Eight males and four females, mean age 21.0 ± 3.77), seven BD patients (Three males and four females, mean age 34.57 ± 7.09), and 13 control subjects (Six males and seven females, mean age 25.61 ± 10.64). All participants underwent an in-laboratory sleep hd-EEG recording with a 64-electrode Easycap net designed to enhance electrode contact with the scalp (BrainAmp, Brain Products GmbH, Gilching, Germany). The night of the recording, all subjects were accommodated in a sleep suite and allowed to sleep within 1 h of their usual bedtime. All subjects were recorded throughout the night and until they woke up naturally the next morning. **Table 1** shows the average length of recording sessions and total sleep time for each participant group. The headset has 64 unipolar electrodes positioned following the standard 10–20 system, and include two channels that record eye movements (one for vertical movements and one for horizontal movements).

All recordings had a sampling frequency of 500 Hz. Data was provided in anonymized form as pairs of *.set* and *.fdt* files.

4.2 Data Preprocessing

Our preprocessing pipeline transforms the raw EEG recordings into correlation tensors of the form $C^b_{ij}(t)$, with (i, j) denoting and edge between electrodes i and j, b a specific frequency band, and t a 30-s epoch. The steps we carry are as follows:

1. Epochs division: divide the raw signal into epochs of approximately 30 s, see below for details, obtaining a signal $S_i(t)$ for electrode i and epoch t.
2. Artifact correction: apply eye-movement correction.
3. Bands division: divide the corrected signal into seven frequency bands. This gives a signal $S^b_i(t)$ with $b \in \{0, \ldots, 6\}$.
4. Correlation analysis: compute electrode-to-electrode Pearson correlations, obtaining a correlation tensor of the form $C^b_{ij}(t)$.

Epochs division: We divide EEG recordings into epochs of around 30 s following Aboalayon et al. (2016). To be precise, each epoch has a length of 2^{14} raw time points which, at a sampling frequency of 500 Hz, corresponds to 32.768 s. This choice is particularly convenient because pure powers of two allow for faster discrete Fourier transform calculations.

Artifact correction: Following Gratton et al. (1983), we correct for eye-movements using a linear regression equation of the form

$$Y = XB \tag{7}$$

where Y corresponds to the EEG data (62 channels in our case), X corresponds to the eye-movement data (Two channels in our case), and B is the regression coefficient matrix to be determined. Solving for B *via* least squares, the corrected signal X^* is computed as

$$X^* = (X - YB)^T \tag{8}$$

Bands division: We use seven frequency bands, numbered from 0 to 6 throughout the manuscript, which logarithmically interpolate the 0.5–64 Hz range typical of brain waves.

- Band 0: (0.5, 1) Hz.
- Band 1: (1, 2) Hz.
- Band 2: (2, 4) Hz.
- Band 3: (4, 8) Hz.
- Band 4: (8, 16) Hz.
- Band 5: (16, 32) Hz.
- Band 6: (32, 64) Hz.

4.3 Correlation Analysis

We use the Pearson correlation coefficient to measure the strength and direction of dependence between the signals x_i, x_j recorded by two electrodes i, j,

$$C_{ij} = \frac{\mathrm{cov}(x_i, x_j)}{\sigma_{x_i}\sigma_{x_j}}. \tag{9}$$

Repeating this measurement for each band b and timepoint t, we get a full correlation tensor $C^b_{ij}(t)$.

4.4 Jensen-Shannon Divergence

We use Jensen-Shannon Divergence (JSD) as a distance measure between networks, in the framework of spectral entropies (Domenico and Biamonte, 2016). For a pair of networks with density matrices ρ and σ, the JSD is defined as

$$J(\rho\|\sigma) = S\left(\frac{\rho+\sigma}{2}\right) - \frac{1}{2}[S(\rho) + S(\sigma)], \tag{10}$$

where $S(\rho)$ is the spectral entropy of the network,

$$S(\rho) = \log_2 Z + \frac{\tau}{\ln 2}\mathrm{Tr}[L\rho], \tag{11}$$

with L denoting the Laplacian, τ diffusion time and the density matrix ρ defined as

$$\rho = \frac{e^{-\tau L}}{Z}, \qquad Z = \mathrm{Tr}(e^{-\tau L}) \tag{12}$$

4.5 Network Measures

Parieto-occipital edge presence: The parieto-occipital area is mapped to the following electrodes: P7, P5, P3, P1, PZ, P2, P4, P6, P8, PO7, PO3, PO4, PO8, O1, OZ, O2, and IZ. From this list, the parieto-occipital presence is computed as explained in the main text, mainly the difference of average presence between nodes in the parieto-occipital area and the rest.

Clustering Coefficient: We use the standard definition of clustering coefficient,

$$c_i = \frac{2 \cdot t_i}{k_i \cdot (k_i - 1)} \tag{13}$$

as implemented in the networkx python library (Hagberg et al., 2008), where t_i is the number of triangles in which node i is involved and k_i is the node degree. Averaging over all nodes, we define the clustering coefficient of the network as

$$c = \frac{1}{N}\sum_{i=1}^{N} c_i \tag{14}$$

Betweenness Centrality: We use the convention of Brandes (2008), which defines a node-dependent quantity as follows:

$$c_B(i) = \frac{2}{(N-1)(N-2)} \sum_{j,k \in V} \frac{\sigma(j, k|i)}{\sigma(j, k)} \tag{15}$$

where $\sigma(j, k|i)$ is the number of shortest path that connect nodes j and k that passes through i and $\sigma(j, k|i) = 0$ if $i = j, k$. $\sigma(j, k)$ is the total number of shortest path connecting j and k and $\sigma(j, k) = 1$ if $j = k$. By convention the fraction $\frac{\sigma(j,k|i)}{\sigma(j,k)}$ is considered zero if both elements are zero. We then average over all nodes to get a single measure for each network:

$$\mathrm{BC} = \frac{1}{N}\sum_{i=1}^{N} c_B(i). \tag{16}$$

Average Shortest Path Length: We start from the standard definition of average shortest path length (ASPL) for a connected graph G

$$a_G = \frac{1}{N \cdot (N-1)} \sum_{i \neq j} d(i,j). \quad (17)$$

where $d(i, j)$ is defined as the length of the shortest path connecting two nodes, j. If i and j belong to two different connected components $d(i, j)$ is said to be infinite, while $d(i, j) = 0$ if $i = j$.

In our setting, networks can have more than one connected component, and we do not want to limit ourselves to the largest connected component as important information could be missed. Hence we employ a weighted version of the ASPL,

$$wa_G = \frac{\sum_{c=1}^{n_c} a_c \cdot w_c}{\sum_{c=1}^{n_c} w_c} \quad (18)$$

where n_c is the number of connected components with more than two nodes and $w_c = N_c \cdot (N_c - 1)$, N_c is the number of nodes of component c. This formulation takes into account the ASPL of all nodes but effectively gives more weight to the larger components.

4.6 Statistical Analysis

Group differences are assessed with a two-sided T-test without assuming equal variances between groups, as implemented in the *ttest_ ind* function from the *scipy* Python scientific library. Cases marked as significant (∗) in **Figure 4** correspond to a p-value below 0.05.

4.7 Ethical Approval

Data from the SPINDLE-1 study, approved by the Milan Area A Interhospital Ethics Committee (Approval n. 22864). All participants signed an informed consent for participation in the SPINDLE-1 study.

DATA AVAILABILITY STATEMENT

The raw data supporting the conclusions of this article will be made available by the authors, without undue reservation.

ETHICS STATEMENT

The studies involving human participants were reviewed and approved by Milan Area A Interhospital Ethics Committee (Approval n. 22864). The patients/participants provided their written informed consent to participate in this study.

AUTHOR CONTRIBUTIONS

FF-C and BS analyzed the data. AD'A, FD, SS, and MC perfomed experimental recording. SZ and CL coordinated the project. FF-C, SZ, and CL wrote the paper.

FUNDING

AD'A was partly supported by the Italian Ministry of Health (GR-2018-12367290).

ACKNOWLEDGMENTS

The authors thank all study participants and Anna Castelnovo, Cecilia Casetta, Renata del Giudice, and Maria Concetta Sapienza, who actively contributed to patient recruitment and hd-EEG recordings.

REFERENCES

Aboalayon, K., Faezipour, M., Almuhammadi, W., and Moslehpour, S. (2016). Sleep Stage Classification Using EEG Signal Analysis: A Comprehensive Survey and New Investigation. *Entropy* 18, 272. doi:10.3390/e18090272

Aleta, A., and Moreno, Y. (2019). Multilayer Networks in a Nutshell. *Annu. Rev. Condens. Matter Phys.* 10, 45–62. doi:10.1146/annurev-conmatphys-031218-013259

Astolfi, L., Cincotti, F., Mattia, D., Marciani, M. G., Baccala, L. A., de Vico Fallani, F., et al. (2007). Comparison of Different Cortical Connectivity Estimators for High-Resolution EEG Recordings. *Hum. Brain Mapp.* 28, 143–157. doi:10.1002/hbm.20263

Bartsch, R. P., Liu, K. K. L., Bashan, A., and Ivanov, P. C. (2015). Network Physiology: How Organ Systems Dynamically Interact. *PloS one* 10, e0142143. doi:10.1371/journal.pone.0142143

Bashan, A., Bartsch, R. P., Kantelhardt, J. W., Havlin, S., and Ivanov, P. Ch. (2012). Network Physiology Reveals Relations between Network Topology and Physiological Function. *Nat. Commun.* 3, 702–709. doi:10.1038/ncomms1705

Bassett, D. (2021). Mechanisms of Brain Network Dysfunction. *Biol. Psychiatry* 89, S2–S3. doi:10.1016/j.biopsych.2021.02.026

Bassett, D. S., and Bullmore, E. (2006). Small-world Brain Networks. *Neuroscientist* 12, 512–523. doi:10.1177/1073858406293182

Bassett, D. S., and Sporns, O. (2017). Network Neuroscience. *Nat. Neurosci.* 20, 353–364. doi:10.1038/nn.4502

Battiston, F., Cencetti, G., Iacopini, I., Latora, V., Lucas, M., Patania, A., et al. (2020). Networks beyond Pairwise Interactions: Structure and Dynamics. *Phys. Rep.* 874, 1–92. doi:10.1016/j.physrep.2020.05.004

Bianconi, G. (2018). *Multilayer Networks: Structure and Function*. Oxford University Press.

Brandes, U. (2008). On Variants of Shortest-Path Betweenness Centrality and Their Generic Computation. *Social Networks* 30, 136–145. doi:10.1016/j.socnet.2007.11.001

Clementz, B. A., Sponheim, S. R., Iacono, W. G., and Beiser, M. (1994). Resting EEG in First-Episode Schizophrenia Patients, Bipolar Psychosis Patients, and Their First-Degree Relatives. *Psychophysiology* 31, 486–494. doi:10.1111/j.1469-8986.1994.tb01052.x

Das, S., and Puthankattil, S. D. (2020). Complex Network Analysis of MCI-AD EEG Signals under Cognitive and Resting State. *Brain Res.* 1735, 146743. doi:10.1016/j.brainres.2020.146743

De Domenico, M. (2017). Multilayer Modeling and Analysis of Human Brain Networks. *Gigascience* 6, 1–8. doi:10.1093/gigascience/gix004

De Vico Fallani, F., Latora, V., and Chavez, M. (2017). A Topological Criterion for Filtering Information in Complex Brain Networks. *Plos Comput. Biol.* 13, e1005305. doi:10.1371/journal.pcbi.1005305

Domenico, M. D., and Biamonte, J. (2016). Spectral Entropies as Information-Theoretic Tools for Complex Network Comparison. *Phys. Rev. X* 6. doi:10.1103/physrevx.6.041062

Gao, Z., Dang, W., Wang, X., Hong, X., Hou, L., Ma, K., et al. (2020). Complex Networks and Deep Learning for EEG Signal Analysis. *Cogn. Neurodyn.* doi:10.1007/s11571-020-09626-1

Gratton, G., Coles, M. G. H., and Donchin, E. (1983). A New Method for Off-Line Removal of Ocular Artifact. *Electroencephalography Clin. Neurophysiol.* 55, 468–484. doi:10.1016/0013-4694(83)90135-9

Grosse, I., Bernaola-Galván, P., Carpena, P., Román-Roldán, R., Oliver, J., and Stanley, H. E. (2002). Analysis of Symbolic Sequences Using the Jensen-Shannon Divergence. *Phys. Rev. E* 65, 041905. doi:10.1103/PhysRevE.65.041905

Hagberg, A. A., Schult, D. A., and Swart, P. J. (2008). "Exploring Network Structure, Dynamics, and Function Using Networkx," in Proceedings of the 7th Python in Science Conference. Editors G. Varoquaux, T. Vaught, and J. Millman (Pasadena, CA USA, 11–15.

Ivanov, P. C., Liu, K. K., and Liu, R. P. (2016). Focus on the Emerging New fields of Network Physiology and Network Medicine. *New J. Phys.* 18, 100201. doi:10.1088/1367-2630/18/10/100201

Kim, D.-J., Bolbecker, A. R., Howell, J., Rass, O., Sporns, O., Hetrick, W. P., et al. (2013). Disturbed Resting State EEG Synchronization in Bipolar Disorder: A Graph-Theoretic Analysis. *NeuroImage: Clin.* 2, 414–423. doi:10.1016/j.nicl.2013.03.007

Leitgeb, E. P., Šterk, M., Petrijan, T., Gradišnik, P., and Gosak, M. (2020). The Brain as a Complex Network: Assessment of EEG-Based Functional Connectivity Patterns in Patients with Childhood Absence Epilepsy. *Epileptic Disord.* 22, 519–530. doi:10.1684/epd.2020.1203

Masuda, N., Kojaku, S., and Sano, Y. (2018). Configuration Model for Correlation Matrices Preserving the Node Strength. *Phys. Rev. E* 98, 012312. doi:10.1103/PhysRevE.98.012312

Muldoon, S. F., and Bassett, D. S. (2016). Network and Multilayer Network Approaches to Understanding Human Brain Dynamics. *Philos. Sci.* 83, 710–720. doi:10.1086/687857

Phinyomark, A., Ibáñez-Marcelo, E., and Petri, G. (2017). Resting-State fMRI Functional Connectivity: Big Data Preprocessing Pipelines and Topological Data Analysis. *IEEE Trans. Big Data* 3, 415–428. doi:10.1109/tbdata.2017.2734883

Rubinov, M., and Sporns, O. (2010). Complex Network Measures of Brain Connectivity: Uses and Interpretations. *Neuroimage* 52, 1059–1069. doi:10.1016/j.neuroimage.2009.10.003

Worsley, K. J., Chen, J.-I., Lerch, J., and Evans, A. C. (2005). Comparing Functional Connectivity *via* Thresholding Correlations and Singular Value Decomposition. *Phil. Trans. R. Soc. B* 360, 913–920. doi:10.1098/rstb.2005.1637

Conflict of Interest: The authors declare that the research was conducted in the absence of any commercial or financial relationships that could be construed as a potential conflict of interest.

Publisher's Note: All claims expressed in this article are solely those of the authors and do not necessarily represent those of their affiliated organizations, or those of the publisher, the editors and the reviewers. Any product that may be evaluated in this article, or claim that may be made by its manufacturer, is not guaranteed or endorsed by the publisher.

frontiers in Network Physiology

ORIGINAL RESEARCH
published: 06 October 2021
doi: 10.3389/fnetp.2021.734344

Treatment Tone Spacing and Acute Effects of Acoustic Coordinated Reset Stimulation in Tinnitus Patients

Tina Munjal[1,2†], Alexander N. Silchenko[3†], Kristina J. Pfeifer[2†], Summer S. Han[2,4], Jessica K. Yankulova[2], Matthew B. Fitzgerald[1], Ilya Adamchic[5] and Peter A. Tass[2]*

[1]Department of Otolaryngology—Head and Neck Surgery, Stanford University, Stanford, CA, United States, [2]Department of Neurosurgery, Stanford University, Stanford, CA, United States, [3]Institute of Neuroscience and Medicine (INM-7: Brain and Behavior), Jülich Research Center, Jülich, Germany, [4]Quantitative Sciences Unit, Stanford University School of Medicine, Stanford, CA, United States, [5]Department of Radiology, Klinikum Friedrichshain, Berlin, Germany

Acoustic coordinated reset (aCR) therapy for tinnitus aims to desynchronize neuronal populations in the auditory cortex that exhibit pathologically increased coincident firing. The original therapeutic paradigm involves fixed spacing of four low-intensity tones centered around the frequency of a tone matching the tinnitus pitch, f_T, but it is unknown whether these tones are optimally spaced for induction of desynchronization. Computational and animal studies suggest that stimulus amplitude, and relatedly, spatial stimulation profiles, of coordinated reset pulses can have a major impact on the degree of desynchronization achievable. In this study, we transform the tone spacing of aCR into a scale that takes into account the frequency selectivity of the auditory system at each therapeutic tone's center frequency via a measure called the gap index. Higher gap indices are indicative of more loosely spaced aCR tones. The gap index was found to be a significant predictor of symptomatic improvement, with larger gap indices, i.e., more loosely spaced aCR tones, resulting in reduction of tinnitus loudness and annoyance scores in the acute stimulation setting. A notable limitation of this study is the intimate relationship of hearing impairment with the gap index. Particularly, the shape of the audiogram in the vicinity of the tinnitus frequency can have a major impact on tone spacing. However, based on our findings we suggest hypotheses-based experimental protocols that may help to disentangle the impact of hearing loss and tone spacing on clinical outcome, to assess the electrophysiologic correlates of clinical improvement, and to elucidate the effects following chronic rather than acute stimulation.

Keywords: coordinated reset, tinnitus, auditory filter, ERB, gap index, sensorineural hearing loss (SNHL), neuromodulation, neuroplasticity

OPEN ACCESS

Edited by:
Plamen Ch. Ivanov, Boston University, United States

Reviewed by:
Jennifer Lentz, Indiana University Bloomington, United States
Neslihan Serap Sengor, Istanbul Technical University, Turkey

***Correspondence:**
Tina Munjal
tina.munjal@stanford.edu

†*These authors share first authorship*

Specialty section:
This article was submitted to Systems Interactions and Organ Networks, a section of the journal Frontiers in Network Physiology

Received: *01 July 2021*
Accepted: *20 September 2021*
Published: *06 October 2021*

Citation:
Munjal T, Silchenko AN, Pfeifer KJ, Han SS, Yankulova JK, Fitzgerald MB, Adamchic I and Tass PA (2021) Treatment Tone Spacing and Acute Effects of Acoustic Coordinated Reset Stimulation in Tinnitus Patients. Front. Netw. Physiol. 1:734344. doi: 10.3389/fnetp.2021.734344

INTRODUCTION

Network dynamics—occurring at multiple levels and spatio-temporal scales—play a crucial role in several physiologic and pathophysiologic domains (Bashan et al., 2012; Ivanov et al., 2016). Chronic tinnitus is such a network phenomenon, across both auditory and non-auditory brain areas (Schlee et al., 2008). An EEG study revealed that acoustic coordinated reset (aCR) induced spread of desynchronization of tinnitus-related abnormal neuronal synchrony from auditory to non-auditory brain areas (Silchenko et al., 2013; Adamchic et al., 2014b). Optimizing the spread of

desynchronization effects, e.g., by selecting optimal parameters of aCR stimulation, may be key to further improving therapeutic outcome. In general, a number of studies have dealt with the spreading dynamics on complex brain dynamics (O'Dea et al., 2013; Misic et al., 2015). Stimuli of different frequency (i.e., pitch) may be fed into the complex tinnitus-related brain network in a multitude of different ways, e.g., with stimulus frequencies being narrowly or widely spaced, confined to only one auditory perceptual channel or widely spread across several channels. We here study a first and fundamental step in manipulating the complex network of auditory and non-auditory brain areas by analyzing the impact of the spacing of aCR stimulation tones on acute therapeutic effects of aCR stimulation.

Tinnitus, or the perception of sound in the absence of any external stimuli (Henry et al., 2005), affects approximately 10% of the adult population (Bhatt et al., 2016). Primary tinnitus is idiopathic and may or may not be associated with sensorineural hearing loss (SNHL). Secondary tinnitus is associated with a specific underlying cause other than SNHL or an identifiable organic condition (Tunkel et al., 2014). There are three proposed mechanisms for the generation of primary tinnitus: increased neural synchrony, reorganization of tonotopic maps, and increased spontaneous firing rates (Eggermont and Tass, 2015). These mechanisms are hypothesized to be an attempt by the central nervous system (CNS) to restore evoked neural activity to pre-hearing loss levels. Nevertheless, only approximately 30% of individuals with hearing loss have tinnitus (Nondahl et al., 2011). Thus, it stands to reason that there are some purely CNS-driven factors that contribute to its generation. However, map reorganization seems not to be strictly required for the generation of tinnitus (Langers et al., 2012), and reorganization of cortical maps takes weeks, whereas abnormal synchrony can be seen rapidly following initial insult (Ortmann et al., 2011). Thus, pathological neuronal synchrony is the mechanism targeted in this study.

Abnormal neuronal synchrony has also been demonstrated to play an important role in a number of other brain disorders, including Parkinson's disease (PD) (Lenz et al., 1994; Nini et al., 1995; Hammond et al., 2007), migraine (Angelini et al., 2004; Bjork and Sand, 2008), and epilepsy (Wong et al., 1986). To specifically counteract abnormal neuronal synchrony, coordinated reset (CR) stimulation was computationally developed based on methods from non-linear dynamics and statistical physics (Tass, 2003). CR stimulation employs sequences of phase resetting stimuli administered to neuronal sub-populations involved in abnormal synchronization processes (Tass, 2003). As shown in computational studies, in the presence of spike-timing-dependent plasticity (STDP) (Gerstner et al., 1996; Markram et al., 1997; Bi and Poo, 1998), CR stimulation may cause long-lasting desynchronization (Tass and Majtanik, 2006; Hauptmann and Tass, 2007; Popovych and Tass, 2012; Kromer and Tass, 2020). CR stimulation may reduce the rate of coincidences, which, mediated by STDP, causes a reduction of synaptic weights, ultimately shifting the network from an attractor with abnormal synaptic connectivity and abnormal neuronal synchrony to an attractor with weak connectivity and synchrony. This long-term desynchronization mechanism was coined anti-kindling (Tass and Majtanik, 2006).

The CR approach was initially developed for the treatment of PD, essential tremor, and epilepsy (Tass, 2003; Tass and Majtanik, 2006). Sustained, long-lasting (i.e., resistant to tolerance) after-effects on motor function lasting for several weeks were demonstrated in parkinsonian nonhuman primates treated with electrical CR stimulation administered to the subthalamic nucleus (STN) for a few hours only (Tass et al., 2012b; Wang et al., 2016). In contrast, effects of standard deep brain stimulation (i.e., periodic stimulation at rates greater than 100 Hz) vanished within 30 min (Tass et al., 2012b; Wang et al., 2016). Analogously, cumulative and lasting after-effects of electrical CR stimulation of the STN on Unified Parkinson's Disease Rating Scale (UPDRS) motor scores and beta band local field power were also demonstrated in PD patients (Adamchic et al., 2014a).

As shown computationally, anti-kindling can robustly be induced in networks with STDP regardless of whether CR stimulation is administered directly to the soma or through synapses (Popovych and Tass, 2012). Subsequently, non-invasive CR was developed to treat tinnitus with acoustic stimuli (Tass et al., 2012a) and PD with vibratory stimuli (Tass, 2017; Syrkin-Nikolau et al., 2018; Pfeifer et al., 2021). Non-invasive aCR makes use of the tonotopic organization of the central auditory system and aims to desynchronize the abnormal tinnitus-related synchronized neural activity by periodically delivering sequences of randomly ordered sinusoidal tones with frequencies adapted to the tinnitus frequency (Tass et al., 2012a; Tass and Popovych, 2012). A randomized, single-blind, placebo-controlled 12-week proof of concept study in 63 patients with chronic subjective tonal tinnitus receiving aCR stimulation for 4–6 hours per day revealed significant therapeutic and electrophysiological effects compared to baseline (Tass et al., 2012a).

By design, effective CR stimulation requires phase resetting stimuli to be delivered to different subpopulations of a synchronized population of neurons (Tass, 2003). Accordingly, careful selection of the stimulation amplitude is key to the effects of CR. For instance, in parkinsonian nonhuman primates treated with CR deep brain stimulation (DBS) delivered to the subthalamic nucleus, it was shown that both acute effects (during five consecutive days with 2 hours of stimulation per day) and long-lasting after-effects (following cessation of stimulation) were weak when using strong stimulation amplitudes as are employed in conventional DBS. However, the effects became pronounced and lasted for a month when the stimulation amplitudes were one-third of those used in conventional DBS (Tass et al., 2012b). For a given spatial stimulation profile, the stimulation amplitude determines the amount of spatial overlap of the separately stimulated neuronal subpopulations (Tass, 2003; Manos et al., 2018). To that end, the present study aims to elucidate the optimal spatial stimulation profiles for aCR tones in order to achieve higher levels of desynchronization in the tinnitus focus of the auditory cortex.

For acoustic stimulation of the inner ear, auditory filters provide an equivalent concept to spatial stimulation profiles

for electrical stimulation of neuronal tissue (Fletcher, 1940). Different auditory frequencies cause mechanical resonances at different points along the basilar membrane in the cochlea of the inner ear. Its spatially dependent mechanical sensitivity gives rise to a tonotopic organization of the basilar membrane to audio frequencies which can be represented as an array of "auditory filters", i.e., overlapping band-pass filters (Fletcher, 1940), which continue to be represented tonotopically throughout the ascending auditory pathway to the level of the cortex. A second tone administered within the frequency range of an auditory filter causes auditory masking, i.e., it affects the perception of a first tone (Fletcher, 1940).

In psychoacoustics, the bandwidth of an auditory filter in human hearing is approximated by the corresponding equivalent rectangular bandwidth (ERB). An ERB describes a rectangular band-pass filter that passes the same amount of energy as its corresponding auditory filter (Moore and Glasberg, 1983; Glasberg and Moore, 1990). In this study, we use a mathematic model for tinnitus frequency and hearing impairment-induced increase of ERB width (Tass et al., 2019). This provides us with the possible range of spatial stimulation profiles achievable by regular aCR stimulation (Tass et al., 2012a). Second, given the validity and limitations of the mathematical ERB model (Tass et al., 2019), we here elucidate which spacing arrangements of CR tone ERBs may be favorable for tinnitus suppression. In particular, we focus on whether CR tones should be densely packed with corresponding ERBs overlapping or more widely spaced with gaps in between their ERBs. The ERB width depends on the ERB's center frequency as well as the hearing impairment at that frequency (Moore and Glasberg, 1983; Glasberg and Moore, 1990; Tass et al., 2019). Hence, ERB widths of the original four CR tones (Tass et al., 2012a), as well as their mutual spatial arrangement, may vary depending on the tinnitus frequency and the hearing impairment.

On the whole, the findings presented herein are a re-analysis of the data acquired from 18 subjects with tinnitus from (Adamchic et al., 2017) who were treated with aCR stimulation. The method of re-analysis is based on the mathematical model of the ERB-scale, with dependencies on tinnitus frequency and hearing loss, described in (Tass et al., 2019). To detect favorable ERB spacing arrangements, we define in this manuscript a quantity called the "gap index" which quantifies the spacing between adjacent auditory filters. As will be described in the manuscript, the gap index serves as a comprehensive index of tone spacing, regardless of whether the ERBs of the CR tones have gaps or overlaps between them. We then assess the relationship of the gap index with the corresponding degree of clinical tinnitus suppression in a study of patients with chronic subjective tinnitus stimulated with two different variants of aCR stimulation which differ with respect to CR tone selection and, importantly, tone spacing (Adamchic et al., 2017). Regular aCR makes use of four tones with fixed spacing that is consistent across cycles. On the contrary, in noisy aCR, the tones are randomized prior to each cycle, resulting in a distinct spacing profile with each cycle (Tass et al., 2012a).

METHODS

Participants

This study was approved by the Ethics Committee of Cologne University's Faculty of Medicine. Written informed consent was obtained from all subjects according to the Declaration of Helsinki and Good Clinical Practice. Participants were 18 individuals with subjective bilateral chronic tonal tinnitus (15 males and 3 females). Individuals with pulsatile, buzzing, roaring, or hissing tinnitus and subjects with a history of auditory hallucinations, Ménière's disease, middle ear disorders, and diagnosed neurological or mental disorders, as well as individuals taking CNS-acting medication or using hearing aids, were excluded. The mean age was 45.89 (±12.97 standard deviation, SD) years, and the mean tinnitus duration was 9.83 (±7.08) years. Otoscopic examination was performed in all participants. Additional details can be found in (Adamchic et al., 2017).

Audiometric Testing

Extended high-frequency air conduction audiometry was performed in all subjects, ranging from 125 Hz to 16 kHz, with thresholds measured in dB HL. While estimates of the frequency distribution of the tinnitus pitch match (f_T) vary across studies (Reed, 1960; Meikle and Taylor-Walsh, 1984; Savastano, 2004), the prevalence of f_T above 4,000 Hz in these studies is consistently sizeable. Thus, in order to comprehensively estimate hearing in the ranges possibly affected by the tinnitus, a five-frequency pure tone average (5-PTA) was calculated for each subject as the average of thresholds at 500, 1,000, 2000, 4,000, and 8,000 Hz.

The tinnitus pitch was determined by means of a pure tone matching procedure (from 0.5 to 13 kHz) (Adamchic et al., 2017). Starting from either well above or well below the subject's tinnitus frequency, subjects had to adjust the frequency of a pure tone to the perceived pitch of their tinnitus. The tinnitus pitch matching procedure required patients to confirm the best matching pitch twice with a maximum modulus of the difference between two matched tones <100 Hz. Tinnitus pitches obtained ranged from 675 to 9,800 Hz. Audiometric data, tinnitus pitch, and tinnitus duration can be found in **Supplementary Table S1**.

Stimulation Protocols and Symptom Scoring

Figure 1A illustrates the stimulation patterns for aCR. The aCR stimulation comprises the four tones whose frequencies are specified as fixed percentages relative to f_T. There are two forms of aCR, referred to as "regular" and "noisy." In *regular aCR*, two tones are placed below f_T and two are placed above f_T ($f_1 = 0.76 \cdot f_T$, $f_2 = 0.9 \cdot f_T$, $f_3 = 1.1 \cdot f_T$, $f_4 = 1.4 \cdot f_T$) (**Figure 1B**). For the *noisy aCR stimulation*, prior to each cycle, four frequencies $f_1, \ldots, f_4$ are randomly chosen out of a set of frequencies c_1 to c_{12} with equal probability (**Figure 1B**) in the following way: f_1 is chosen from the set $S_1 = \{c_1, c_2, c_3\}$, f_2 is

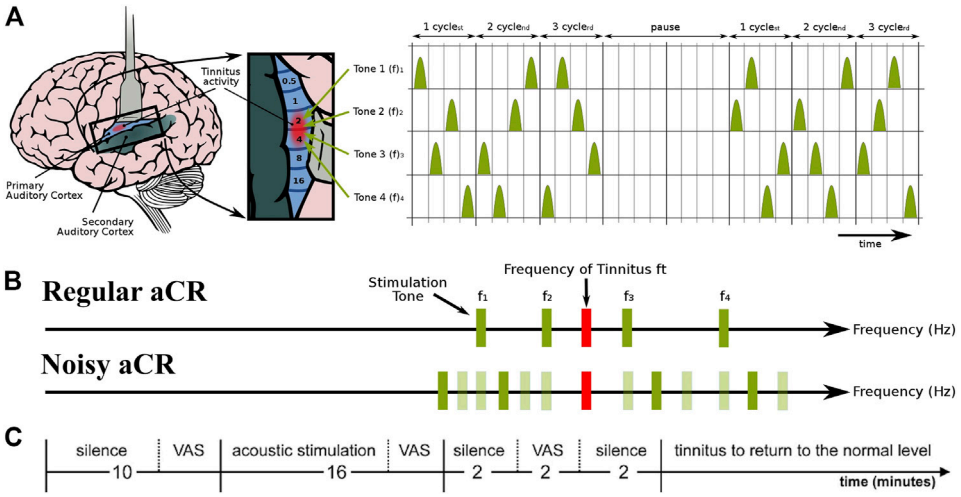

FIGURE 1 | Schematic of the experimental paradigm and the two types of acoustic CR stimulation. **(A)** aCR stimulation pattern. For aCR, we employ the tonotopic organization of the primary auditory cortex (**left panel**, brain adapted from (Chittka and Brockmann, 2005) with kind permission of the authors) and deliver brief sinusoidal tones of different frequencies (pitch) $f_1, \ldots, f_4$ equidistantly in time at a cycle repetition rate of 1.5 Hz (Tass et al., 2012a). Three CR cycles, each comprising a randomized sequence of four tones **(right panel)**, were followed by two silent cycles without stimuli ("pause"). The 3 cycles stim ON-2 cycles stim OFF pattern was repeated periodically (Tass, 2003; Tass and Majtanik, 2006; Lysyansky et al., 2011). Right panel from (Tass et al., 2012a) with kind permission by the authors. Copyright by Forschungszentrum Jülich GmbH. **(B)** Schematic illustration of the stimulus tones and repetition rates of regular aCR and noisy aCR. Panel partly redrawn from (Tass et al., 2012a) with kind permission by the authors. Copyright by Forschungszentrum Jülich GmbH. **(C)** Experimental session. During the first 10 min of silence, the baseline VAS-L and VAS-A scores were obtained. Thereafter, one of the two stimulation paradigms, i.e., regular aCR or noisy aCR, was performed for 16 min. VAS-L and VAS-A were obtained during stimulation and at the end of this stimulation period. After each session, participants received a pause during which tinnitus returned to the normal level. Thereafter the next session was started. Panel partly redrawn from (Adamchic et al., 2017) with kind permission by the authors. Copyright by Forschungszentrum Jülich GmbH.

chosen from the set $S_2 = \{c_4, c_5, c_6\}$, f_3 is chosen from the set $S_3 = \{c_7, c_8, c_9\}$, and f_4 is chosen from the set $S_4 = \{c_{10}, c_{11}, c_{12}\}$, where $c_j = d_j f_T$ and $d_1 = 0.69$, $d_2 = 0.728$, $d_3 = 0.766$, $d_4 = 0.810$, $d_5 = 0.855$, $d_6 = 0.900$, $d_7 = 1.100$, $d_8 = 1.182$, $d_9 = 1.265$, $d_{10} = 1.400$, $d_{11} = 1.505$, $d_{12} = 1.610$. The duration of the acoustic tones is 150 ms for both protocols.

The frequency span for regular aCR stimulation reads $f_4 - f_1 = 0.63 \cdot f_T$. For noisy aCR stimulation, the frequency span ranges from $c_{12} - c_1 = 0.920 \cdot f_T$ to $c_{10} - c_3 = 0.634 \cdot f_T$ with an average (over stimulation cycles) of $\overline{S_4} - \overline{S_1} = 0.777 \cdot f_T$. Thus, the average frequency span of noisy aCR stimulation is approximately 23% greater than that of aCR stimulation, which means an even higher total span for the ERBs centered at the stimulation tone frequencies. In the case of aCR stimulation, the distances between adjacent tones are $f_2 - f_1 = 0.134 \cdot f_T$, $f_3 - f_2 = 0.2 \cdot f_T$, $f_4 - f_3 = 0.3 \cdot f_T$. For the noisy aCR stimulation, the average distance between adjacent sets of tones is given by $\overline{S_2} - \overline{S_1} = 0.127 \cdot f_T, \overline{S_3} - \overline{S_2} = 0.327 \cdot f_T$, $\overline{S_4} - \overline{S_3} = 0.323 \cdot f_T$, where $\overline{S_1}, .., \overline{S_4}$ are the mean frequencies of the corresponding sets defined above. Thus, the distance between the inner sets of tones of the noisy aCR stimulation is on average 64% greater than the distance between the inner CR tones f_2 and f_3. Accordingly, aCR stimulation is more closely spaced around the tinnitus frequency f_T than is noisy aCR. More details about the frequency spacing for both protocols can be found in the article (Adamchic et al., 2017). For both stimulation protocols in this study, stimulation tones were equally loud. The loudness of the stimulation tones was set using the following procedure: First the intensity of the stimulation tone with the lowest frequency was set at threshold +20 dB. Loudness of the other stimulation tones was set so that they were perceived by the participant as equally loud as the first tone. Participants who were not able to hear all stimulation tones were excluded from the study.

The first part of each experimental session consisted of a 10-min period of silence (**Figure 1C**). The participants sat still and listened to their tinnitus. At the end of this baseline period, the participants were asked to indicate the mean tinnitus loudness and annoyance during the baseline resting period on a 100 mm long visual analogue scale (VAS) verbally anchored at the endpoints (Adamchic et al., 2012). VAS for loudness (VAS-L; tinnitus is not audible = 0, tinnitus is extremely loud = 100) and annoyance (VAS-A; tinnitus is not annoying = 0, tinnitus is extremely annoying = 100) were obtained. After the rating, CR stimulation (**Figure 1B**) was presented for exactly 16 min. At the end of this stimulation period, the participants were asked to indicate the mean tinnitus loudness and annoyance during the stimulation period on the VAS-L and VAS-A. The stimulus presentation was followed by a 2-min-long resting period with eyes closed, followed by a final VAS-L and VAS-A rating between 2 and 4 minutes after the stimulation. The order of the experimental sessions—whether regular aCR first or noisy aCR first—was pseudorandomly counterbalanced across subjects. The subjects thus underwent both types of aCR. The sequence of events in a typical experimental session is also illustrated in **Figure 1C**. Since the VAS-A and -L scores were measured

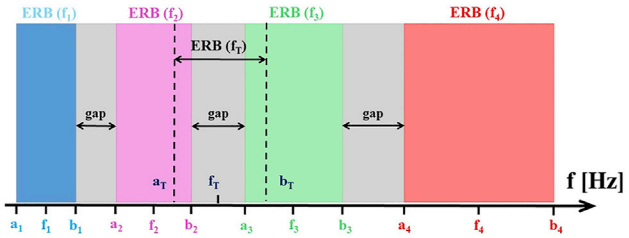

FIGURE 2 | The alignment of CR tones, tinnitus tone f_T and corresponding ERBs in the case when the ERBs of neighboring CR tones are non-overlapping. The symbols used to designate the band edges and center frequencies of the ERBs around the center frequencies of each of the four original CR tones and f_T . The gaps between the ERBs centered at the CR tones are illustrated by gray stripes.

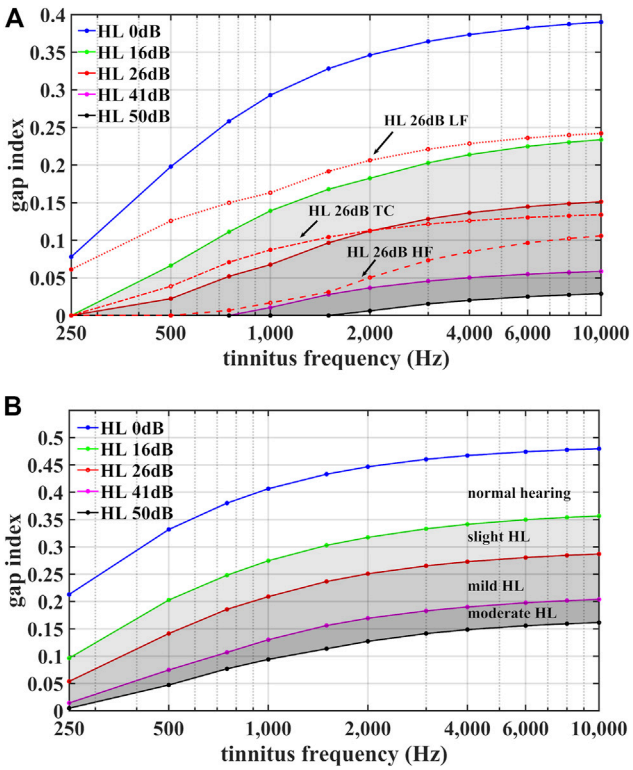

FIGURE 3 | Illustration of the range of possible gap index values for regular aCR stimulation **(A)** and for noisy aCR stimulation **(B)**. The gap indices $g(f_T, h)$ from **Eq. 9 (A)** and $\overline{g}(f_T, h)$ from **Eq. 17 (B)** are plotted against tinnitus frequency f_T for homogenous hearing loss of 0 dB ("HL 0 dB"), 16 dB ("HL 16 dB"), 26 dB ("HL 26 dB"), 41 dB ("HL 41 dB"), 50 dB ("HL 50 dB") at all corresponding CR tones, delineating ranges of maximum gap index for normal hearing as well as slight, mild, and moderate hearing loss. Additionally, for regular aCR in part **(A)**, we plot curves "HL 26 dB LF," "HL 26 dB HF," and "HL 26 dB TC," to demonstrate how alternatively shaped audiograms with hearing loss in the lower-frequency, higher-frequency, and tinnitus-centered regions, respectively, affect the gap index. Despite all audiograms having average hearing loss of 26 dB, the shape of the audiogram is of critical importance in determining the gap index.

both for the right and left ears, we used their arithmetic mean values normalized to their baseline values (Adamchic et al., 2017). Since the values were normalized to their baseline, the final score used in the analysis is a proportion (with 1.0 indicating a score unchanged from baseline). From this point on, all reference to VAS-A and VAS-L refers to the normalized score unless indicated otherwise. All subjects' normalized VAS-L and VAS-A scores during and after therapy for regular and noisy aCR can be found in **Supplementary Table S2**.

ERB Concept for Acoustic Stimulation

In the present study, we used a frequency scale based on the equivalent rectangular bandwidth (ERB) of the auditory filter, as determined from masking experiments using notched noise or spectrally rippled noise with human listeners (Moore and Glasberg, 1983; Glasberg and Moore, 1990). The average value of the ERB for young listeners with normal audiometric thresholds measured at moderate sound levels is denoted as ERB_N. Its value in Hz is given by

TABLE 1 | Multiple linear regression models using tinnitus duration, gap index, and residual variance of 5-PTA to gap index as predictor variables. The primary outcome variable chosen was VAS-L during therapy. The additional variables of VAS-L after therapy and VAS-A during and after therapy are also shown. Findings are shown for both regular aCR and noisy aCR. *B* (*SE*) represents unstandardized beta with standard error in parentheses.

VAS-L during therapy					
Regular aCR (n =18, R^2 = 0.582, F(3,14) = 6.490, p =0.006[a])	***B* (*SE*)**	**β**	**Partial**	**Part**	***p*-value**
Constant	0.595 (0.162)				0.003[a]
Duration	0.002 (0.001)	0.350	0.415	0.295	0.110
Gap index	–2.175 (0.754)	–0.499	–0.611	–0.499	0.012[a]
Residual variance of 5-PTA	0.020 (0.014)	0.295	0.359	0.249	0.172
Noisy aCR (n =18, R^2 = 0.551, F(3,14) = 5.730, p =0.009[a])	***B* (*SE*)**	**β**	**Partial**	**Part**	***p*-value**
Constant	1.097 (0.238)				<0.001[a]
Duration	0.001 (0.001)	0.216	0.268	0.187	0.315
Gap index	–2.657 (0.786)	–0.609	–0.670	–0.605	0.004[a]
Residual variance of 5-PTA	0.016 (0.014)	0.240	0.296	0.208	0.265
VAS-L AFTER THERAPY					
Regular aCR (n =18, R^2 = 0.442, F (3,14) = 3.696, p =0.038[a])	***B* (*SE*)**	**β**	**Partial**	**Part**	***p*-value**
Constant	0.642 (0.129)				<0.001[a]
Duration	0.002 (0.001)	0.511	0.499	0.431	0.049[a]
Gap index	–1.020 (0.600)	–0.339	–0.413	–0.339	0.111
Residual variance of 5-PTA	0.004 (0.011)	0.085	0.095	0.071	0.726
Noisy aCR (n =18, R^2 = 0.437, F (3,14) = 3.617, p =0.040[a])	***B* (*SE*)**	**β**	**Partial**	**Part**	***p*-value**
Constant	1.022 (0.251)				0.001[a]
Duration	0.001 (0.001)	0.277	0.304	0.240	0.252
Gap index	–2.125 (0.828)	–0.518	–0.566	–0.515	0.022[a]
Residual variance of 5-PTA	0.010 (0.015)	0.151	0.172	0.131	0.524
VAS-A DURING THERAPY					
Regular aCR (n =18, R^2 = 0.674, F(3,14) = 9.633, p =0.001[a])	***B* (*SE*)**	**β**	**Partial**	**Part**	***p*-value**
Constant	0.647 (0.162)				0.001[a]
Duration	0.002 (0.001)	0.357	0.466	0.301	0.069
Gap index	–2.726 (0.750)	–0.555	–0.697	–0.555	0.003[a]
Residual variance of 5-PTA	0.025 (0.014)	0.319	0.426	0.269	0.100
Noisy aCR (n =18, R^2 = 0.530, F(3,14) = 5.270, p =0.012[a])	***B* (*SE*)**	**β**	**Partial**	**Part**	***p*-value**
Constant	0.968 (0.244)				0.001[a]
Duration	0.001 (0.001)	0.276	0.328	0.238	0.215
Gap index	–2.424 (0.806)	–0.554	–0.626	–0.551	0.009[a]
Residual variance of 5-PTA	0.016 (0.015)	0.234	0.284	0.203	0.286
VAS-A AFTER THERAPY					
Regular aCR (n =18, R^2 = 0.699, F(3,14) = 10.841, p <0.001[a])	***B* (*SE*)**	**β**	**Partial**	**Part**	***p*-value**
Constant	0.689 (0.140)				<0.001[a]
Duration	0.003 (0.001)	0.489	0.600	0.412	0.014[a]
Gap index	–2.566 (0.649)	–0.580	–0.726	–0.580	0.001[a]
Residual variance of 5-PTA	0.011 (0.012)	0.153	0.230	0.129	0.392
Noisy aCR (n =18, R^2 = 0.449, F(3,14) = 3.804, p =0.035[a])	***B* (*SE*)**	**β**	**Partial**	**Part**	***p*-value**
Constant	1.090 (0.254)				<0.001[a]
Duration	0.001 (0.001)	0.260	0.289	0.224	0.278
Gap index	–2.360 (0.838)	–0.562	–0.601	–0.559	0.014[a]
Residual variance of 5-PTA	0.007 (0.015)	0.105	0.122	0.091	0.652

[a]*Denotes statistically significant result for alpha level <0.05.*

$$ERB_N = 24.7 \cdot (0.00437 \cdot f + 1), \quad (1)$$

where f is the center frequency in Hz (Glasberg and Moore, 1990). This equation provides a good prediction of *ERB* values estimated psychoacoustically using masking experiments for center frequencies spanning almost the entire range of human hearing from about 50 to 15,000 Hz (Zhou, 1995). The edges of the ERB-wide frequency intervals were estimated at low sensation

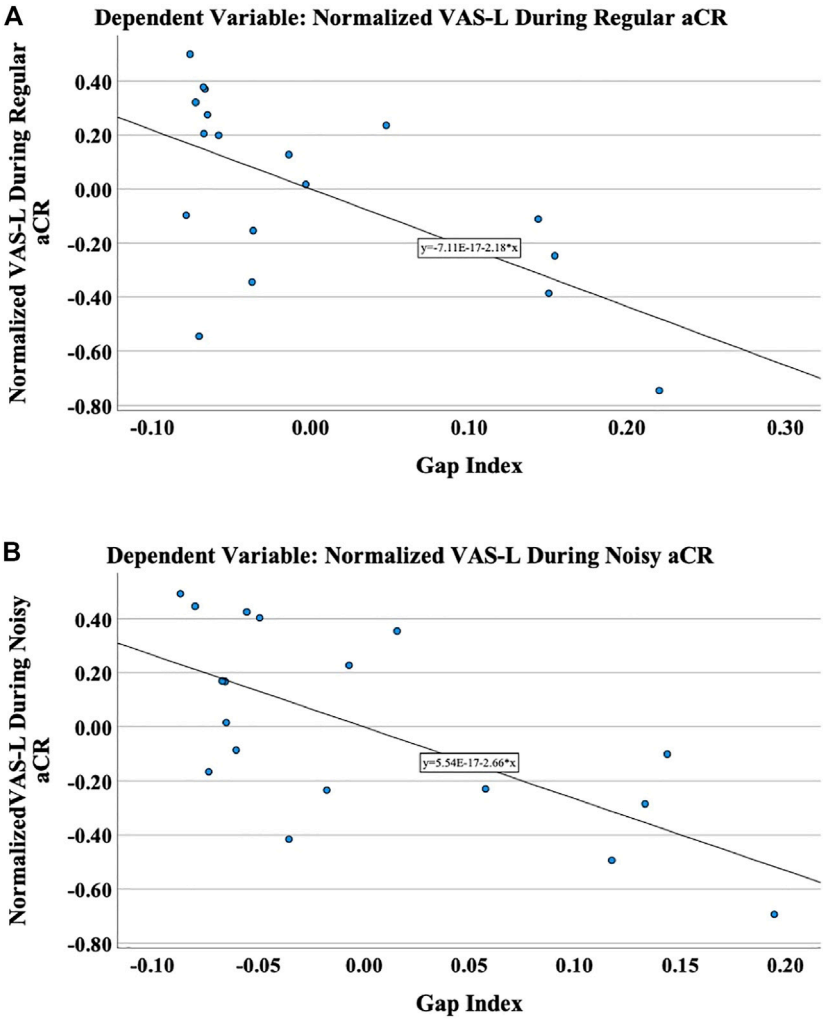

FIGURE 4 | The primary outcome variable was chosen to be the normalized VAS-L during therapy. These are the partial regression plots demonstrating the relationship of the residuals of the normalized VAS-L to the residuals of the gap index after regressing on the residual variance of 5-PTA during **(A)** regular aCR and **(B)** noisy aCR. It should be noted that partial regression plots demonstrate the residuals of the represented variables, rather than the variables themselves.

levels using data presented by Moore and others, where the value of the ERB was provided for center frequencies 2,000, 4,000, and 6,000 Hz and audiometric thresholds from 0 to 80 dB HL (Moore et al., 1999). From these data, the following equation was generated for hearing loss h in the range of 0–50 dB HL (Tass et al., 2019):

$$ERB(h) = ERB_N \cdot (1 + h/50\ dB\ HL), \tag{2}$$

The values of frequencies at the upper edges a_T and lower edges b_T of the ERB-wide band centered around f_T are defined by

$$a_T = f_T - 0.5 \cdot ERB\big(h\big(f_T\big)\big), \tag{3}$$
$$b_T = f_T + 0.5 \cdot ERB\big(h\big(f_T\big)\big), \tag{4}$$

Analogously, the frequencies at the upper and lower edges of the *ERB* band centered at the frequency of CR tone j, a_j, and b_j, read

$$a_j = f_j - 0.5 \cdot ERB\big(h\big(f_j\big)\big), \tag{5}$$
$$b_j = f_j + 0.5 \cdot ERB\big(h\big(f_j\big)\big), \tag{6}$$

Figure 2 illustrates the alignment of CR tones $f_1, \ldots f_4$, tinnitus tone f_T together with the corresponding ERBs for the case when the ERBs of neighboring CR tones are not overlapping.

Gap Index for Psychophysical ERBs

Gaps and Overlaps for Regular aCR Stimulation

For subjects with normal hearing, neighboring ERBs of CR tones do not overlap for tinnitus frequencies f_T greater than 560 Hz (Tass et al., 2019). With increasing hearing impairment, the width of the gaps between the CR tone ERBs may decrease or even vanish (Tass et al., 2019). To quantify the spacing of the CR tones, we introduce different quantities measuring gaps and overlaps. To this end, we introduce the *relative gap* between $ERB\big(f_j\big)$ and $ERB\big(f_k\big)$, where $f_j < f_k$, by

$$G(f_j, f_k) = \frac{G_{abs}(f_j, f_k)}{ERB(f_k)} = \frac{a_k - b_j}{ERB(f_k)}, \quad (7)$$

where $G_{abs}(f_j, f_k)$ denotes the absolute gap between $ERB(f_j)$ and $ERB(f_k)$, where $f_j < f_k$. $G(f_j, f_T) > 0$ means that $ERB(f_j)$ and $ERB(f_k)$ do not overlap and are separated by a gap, whereas $G(f_j, f_k) < 0$, if $ERB(f_j)$ and $ERB(f_k)$ overlap. $G(f_j, f_k) = 0$ if both ERBs touch each other, so that the edges of $ERB(f_j)$ and $ERB(f_k)$ coincide.

For regular aCR stimulation, the *mean relative gap* between all pairs of neighboring ERBs, $ERB(f_j)$ and $ERB(f_{j+1})$ (with $j = 1, 2, 3$), reads

$$\overline{G} = \sum_{j=1}^{3} G(f_j, f_{j+1}), \quad (8)$$

For regular aCR stimulation, the entire frequency range spanned by the ERBs centered around four CR tones is given by the *ERB span* $E = [a_1, b_4]$ (**Figure 2**). As an alternative means to assess the spacing of the CR tone ERBs, we introduce the *gap index g* by

$$g = \left[\sum_{j=1}^{3} \left[G_{abs}(f_j, f_{j+1}) \right]_+ \right] / (b_4 - a_1), \quad (9)$$

where $[\ldots]_+$ is defined by

$$[x]_+ = \begin{cases} x : x > 0 \\ 0 : x \le 0 \end{cases}.$$

Thus, the gap index provides us with the percentage of E covered by the gray stripes as shown in **Figure 2**.

As shown in **Supplementary Figure 1A**, the relative gap $G(f_j, f_{j+1})$ is highly correlated with the gap index (with the r ranging from 0.92 to 0.99, depending on which tone pair is assessed), regardless of whether the relative gap is negative, zero, or positive. Further, as shown in **Supplementary Figure 2A**, the mean relative gap $\overline{G}$ between all pairs of neighboring ERBs is also highly correlated with the gap index g ($r = 0.99$). This motivates the use of the gap index as a summary index of the spacing of the ERBs of all four CR tones, rather than the behavior of individual pairwise ERBs.

In addition, we determine the number of gaps (i.e., gray stripes in **Figure 2**) between the four ERBs belonging to the regular aCR tones. To this, in analogy to **Eq. 7** we determine whether there is a gap between $ERB(f_j)$ and $ERB(f_k)$, where $f_j < f_k$, by

$$H(j,k) = \begin{cases} 1 : a_k - b_j > 0 \\ 0 : else \end{cases}, \quad (10)$$

$H(j,k) = 1$ if there is a gap between $ERB(f_j)$ and $ERB(f_k)$ and 0 else. To count the number of gaps between neighboring ERBs belonging to the regular aCR tones, we introduce the *gap count c* is then defined by

$$c = \sum_{j=1}^{3} H(j, j+1), \quad (11)$$

$c(f_T, h)$ can attain integer values between 0 and 3. **Supplementary Figure 3A** demonstrates the relationship between the gap count c and the gap index g ($r = 0.94$).

Gap index and gap count quantify the overall spacing of the entire ERB arrangement of the CR therapy tones. In addition, as an alternative means to describe the spatial CR tone arrangement, we use the tinnitus $ERB(f_T)$ as reference. To assess to which extent the tinnitus $ERB(f_T)$ is covered by $ERB(f_j)$ of the CR therapy tones $j = 1, 2, 3, 4$, we determine the *relative overlap between* the tinnitus $ERB(f_T)$ and the CR tone $ERB(f_j)$

$$O(f_j, f_T) = \begin{cases} (b_j - a_T)/ERB(f_T) : f_j < f_T \\ (b_T - a_j)/ERB(f_T) : f_j > f_T \end{cases}, \quad (12)$$

$O(f_j, f_T) > 0$ means that $ERB(f_T)$ and $ERB(f_j)$ overlap, whereas $O(f_j, f_T) < 0$ corresponds to $ERB(f_T)$ and $ERB(f_j)$ being separated by a gap. $O(f_j, f_T) = 0$ if $ERB(f_T)$ and $ERB(f_j)$ touch each other with coincident ERB edges.

With this the *mean relative overlap* between the tinnitus $ERB(f_T)$ and all other CR tone ERBs, $ERB(f_1), \ldots, ERB(f_4)$, reads

$$\overline{O}(f_T) = \sum_{j=1}^{4} O(f_j, f_T), \quad (13)$$

As shown in **Supplementary Figure 4A**, the relative overlap and the gap index are highly correlated (r ranges from −0.99 to −0.95, depending on which tone pair is assessed). As shown in **Supplementary Figure 5A**, the mean relative overlap is also highly correlated with the gap index ($r = -0.98$). Thus, the overlaps of the CR tone ERBs with the tinnitus ERB are also captured by the gap index.

The advantage of using the gap index, a single, integral spacing measure for all CR tones (rather than, for example, multiple such metrics for single ERB pairs) is that the gap index reflects the spacing of CR tone ERBs in their entirety and enables a comprehensive correlation to different clinical outcome measures. It also captures the relationship of CR tone ERBs to the tinnitus ERB.

Gaps and Overlaps for Noisy aCR Stimulation

To determine the mean gap between all pairs of CR tone frequencies f_j and f_k, we first determine the *relative gap* defined by **Eq. 7** according to

$$G_N(c_m, c_n) = \frac{a_n - b_m}{ERB(c_n)}, \quad (14)$$

for $c_m \in S_j$ and $c_n \in S_k$, and a_n and b_n denote the lower and upper edge of $ERB(c_n)$ (see **Figure 2**).

With this, the *mean relative gap* between all pairs of neighboring CR frequencies f_j and f_{j+1} $(j = 1, 2, 3)$ for noisy aCR stimulation reads

$$\overline{G}_N(f_j, f_{j+1}) = \sum_{c_m \in S_j,\, c_n \in S_k} G(c_m, c_n), \quad (15)$$

For noisy aCR stimulation, the ERB span depends on the lowest and highest CR tone of the respective noisy aCR cycle (see *Stimulation Protocols and Symptom Scoring*). To determine the gap index for noisy aCR stimulation, for each realization of noisy aCR cycles we consider the percentage ERB span consisting of gaps in

between the CR tone ERBs and average over all (equally frequent) possible realizations, where the set of realizations is given by

$$\begin{aligned}\mathcal{R} &= \left\{\left(f_j, f_k, f_l, f_m\right)\right\}_{j=1,2,3;k=4,5,6;l=7,8,9;m=10,11,12} \\ &=: \left\{(j,k,l,m)\right\}_{j=1,2,3;k=4,5,6;l=7,8,9;m=10,11,12}\end{aligned} \tag{16}$$

(see Stimulation Protocols and Symptom Scoring). To this end, we use **Eq. 7** for the absolute gap $G_{abs}(f_j, f_k)$ between $ERB(f_j)$ and $ERB(f_k)$ and calculate the gap index $g(f_T, h)$ for each single realization (j,k,l,m). Denoting the gap index for realization (j,k,l,m) by $g(f_T, h, j, k, l, m)$, the *gap index for noisy aCR* reads

$$\overline{g}(f_T, h) = \frac{1}{81}\sum\nolimits_{j=1,2,3;k=4,5,6;l=7,8,9;m=10,11,12} g(f_T, h, j, k, l, m), \tag{17}$$

The relationship of relative gap to gap index for noisy aCR is shown in **Supplementary Figure 1B** (r ranges from 0.93 to 0.98 depending on which tone pair is assessed) and mean relative gap to gap index for noisy aCR in **Supplementary Figure 2B** ($r = 0.999$).

For noisy aCR stimulation, we additionally determine the *gap count*

$$\overline{c}(f_T, h) = \frac{1}{81}\sum\nolimits_{j=1,2,3;k=4,5,6;l=7,8,9;m=10,11,12} c(f_T, h, j, k, l, m), \tag{18}$$

To this end, we replace the term for the gap, $a_k - b_j$, by the corresponding Heaviside function $H(j,k)$ (**Eq. 10**). **Supplementary Figure 3B** demonstrates the relationship between the gap count $\overline{c}$ and the gap index $\overline{g}$ ($r = 0.97$).

In addition, we describe the spatial CR tone arrangement by using the tinnitus $ERB(f_T)$ as reference. To assess to which extent the tinnitus $ERB(f_T)$ is covered by $ERB(c_m)$, in analogy to **Eq. 12**, we determine the *relative overlap between* the tinnitus $ERB(f_T)$ and $ERB(c_m)$

$$O(c_m, f_T) = \begin{cases} (b_m - a_T)/ERB(f_T): & c_m < f_T \\ (b_T - a_m)/ERB(f_T): & c_m > f_T \end{cases}, \tag{19}$$

For noisy aCR stimulation, the *mean relative overlap* between all three realizations of a CR frequency f_j and the tinnitus $ERB(f_T)$ reads

$$O_N\left(f_j, f_T\right) = \sum\nolimits_{c_m \in S_j} O(c_m, f_T), \tag{20}$$

With this the *mean relative overlap* between the tinnitus $ERB(f_T)$ and all other CR tone ERBs, $ERB(f_1), \ldots, ERB(f_4)$, reads

$$\overline{O}_N(f_T) = \sum\nolimits_{j=1}^{4} O_N\left(f_j, f_T\right), \tag{21}$$

The relative overlap vs. gap index for noisy aCR is shown in **Supplementary Figure 4B** (r ranges from −0.97 to −0.95 depending on which tone pair is assessed). The mean relative overlap vs. gap index for noisy aCR is shown in **Supplementary Figure 5B** ($r = -0.97$). As is the case with regular CR, the gap index once again represents a single measure that captures multiple relationships among the noisy aCR tone ERBs and between the noisy aCR tone ERBs to the tinnitus ERB.

Spacing of CR Tones

According to the American Speech-Language-Hearing Association (ASHA), the hearing thresholds relevant to our study can be classified with the following descriptors: normal hearing (0–15 dB), slight hearing loss (16–25 dB), mild hearing loss (26–40 dB), and moderate hearing loss (41–55 dB) (Goodman, 1965; Clark, 1981). Due to deterioration in estimates of the ERB width beyond hearing thresholds of 50 dB, we do not plot severe-to-profound hearing loss here. Nine of the eighteen subjects had at least one threshold above 50 dB in at least one ear at the frequencies included in the 5-PTA.

To illustrate how the range of possible gap index values for aCR stimulation depends on tinnitus frequency f_T and hearing loss, we plot the gap index against tinnitus frequency f_T, assuming homogenous hearing loss, where 0, 16, 26, and 41 dB hearing loss applies to all corresponding CR frequencies, respectively ("HL 0dB", . . ., "HL 41dB" in **Figure 3A**). In these cases, $h(f_1), \ldots, h(f_4) =$ 0, 16, 26, and 41 dB, respectively. This is to illustrate maximum ranges of the gap index belonging to normal hearing as well as slight, mild, and moderate homogenous hearing loss. Analogously, we plot the same curves for noisy aCR stimulation (**Figure 3B**). The maximum range of possible gap index values increases with increasing tinnitus frequency and begins to broaden even for milder degrees of homogenous hearing loss. The tinnitus frequency-dependent increase is more pronounced for aCR stimulation than for noisy aCR stimulation. In general, the values of the gap index for aCR stimulation are smaller than for noisy aCR stimulation.

However, the gap index not only depends on the average hearing loss in the vicinity of the tinnitus frequency f_T (i.e., the frequency range between f_1, the lowest CR tone, and f_4, the highest CR tone) but may strongly vary depending on the actual shape of the audiogram in that frequency range. For illustration, for aCR stimulation we consider different types of non-homogenous hearing impairment. For this, we introduce the mean hearing impairment belonging to all four CR tones by

$$\overline{h}(f_T) = \frac{1}{4}\sum\nolimits_{j=1}^{4} h\left(f_j\right).$$

We consider different shapes of (model) audiogram with the same mean $\overline{h}(f_T)$ as for the homogenous hearing impairment at 26 dB shown in **Figure 3A**:

On average 26 dB hearing loss:

For $\overline{h}(f_T) = 26$ dB we consider three different cases with non-homogenous (model) hearing impairment (**Figure 3A**):

1) Lower-frequency hearing loss ("HL 26 dB LF"): $h(f_1) = h(f_2) = 50$ dB, $h(f_3) = 4$ dB, $h(f_4) = 0$ dB.
2) Higher-frequency hearing loss ("HL 26 dB HF"): $h(f_4) = h(f_3) = 50$ dB, $h(f_2) = 4$ dB, $h(f_1) = 0$ dB.
3) Tinnitus-centered hearing loss ("HL 26 dB TC"): $h(f_3) = 50$ dB, $h(f_2) = 14$ dB, $h(f_1) = h(f_4) = 0$ dB.

As shown in **Figure 3A**, the lower-frequency (model) hearing impairment has the greatest gap values, even exceeding the HL 16 dB curve for homogenous hearing impairment. Conversely,

for frequencies between 800 Hz and 1,500 Hz the gap index of the higher-frequency (model) hearing impairment approaches gap index values of the HL 41 dB curve for homogenous hearing impairment. Similar audiogram-shape dependent variations of the gap index were also observed for $\overline{h}(f_T) = 16$ dB and $\overline{h}(f_T) = 41$ dB, as described in the Supplementary Methods. In summary, the gap index does not simply depend on the average hearing impairment around f_T. The gap index rather strongly depends on the actual shape of the audiogram in the vicinity of the tinnitus frequency f_T.

Calculation of Gap Index

To compute the distances between adjacent ERBs and the overall gap index (**Eq. 9**, above) for the aCR tones used in the clinical study, we used the following procedure:

1) The audiogram of every tinnitus patient was linearly interpolated on a logarithmic frequency axis.
2) The frequencies of the tones used for regular CR stimulation and for noisy aCR stimulation were computed for every tinnitus patient, and the hearing thresholds at the frequencies of the stimulation tones were interpolated from the audiometric thresholds.
3) The edges of the ERB-wide frequency intervals centered at the frequencies of CR tones were estimated using **Eqs. 5**, **6**.
4) The gaps between the ERBs centered at the neighboring CR tones were calculated using **Eq. 7** for every tinnitus patient.
5) The values of the gap index were calculated using **Eq. 9** for every tinnitus patient in the case of regular aCR stimulation and **Eq. 17** for noisy aCR stimulation.

a) Notably, if the tinnitus frequency was the same in both ears, the gap index for both ears was calculated with the mean values of the linearly interpolated audiograms of both ears.
b) However, if the tinnitus frequency was different between the ears, the gap index was initially calculated for each ear separately (using the individual thresholds for each ear). Then, the two indices for the ears were averaged for the final gap index.

Statistical Analysis

All statistical analyses were performed using IBM SPSS Statistics (2020).

Primary Analysis

VAS-L score during stimulation was chosen as the primary outcome variable. This was motivated by several factors. Firstly, the most pronounced clinical effect seen in Adamchic et al., 2017 was the acute effect on loudness and annoyance. Stimulation-induced reduction of VAS-L and VAS-A was quite similar (Adamchic et al., 2017). However, tinnitus loudness appears to be the more elementary measure as opposed to tinnitus annoyance, the latter possibly prone to complex psychological factors (Hiller and Goebel, 2007; Guimaraes et al., 2014), such as a high degree of self-attention and somatic attention (Newman et al., 1997). Additionally, the score during stimulation rather than after stimulation was chosen as the primary outcome variable. The goal of CR stimulation is to induce long-lasting effects. However, this requires stimulation of sufficient duration. Based on the 2012 proof-of-concept study (Tass et al., 2012a), we could not expect to induce full-scale effects after only 16 min. In addition, it is not known to which extent the required stimulus duration depends on factors like disease duration. Onset and time course of neuronal plastic changes may depend on several factors. From computational studies in simple neural networks, we know that acute after-effects reflect the CR stimulation-induced changes and reduction of synaptic weights (Khaledi-Nasab, 2021). However, we focus on the most pronounced acute effects that may be less dependent on several other factors intrinsic to patients. Thus, overall, the VAS-L score during stimulation may be a relatively "purer" metric of stimulus efficacy less dependent on patient-specific factors, more so than the VAS-A score during or after stimulation, or VAS-L score after stimulation.

The primary analysis thus included linear regression models to determine the effects of tinnitus duration, gap index, and 5-PTA on the VAS-L score during regular and noisy aCR. Bivariate correlations amongst the predictor variables demonstrated multicollinearity of the gap index and 5-PTA. For aCR, the gap index and 5-PTA had an $r = -0.659$ for regular aCR. The gap index and 5-PTA had an $r = -0.705$ for noisy aCR. This indicates that higher 5-PTA is correlated with lower gap indices, as would be expected due to broadening of ERBs with increasing threshold. Because the 5-PTA is a function of the patient's underlying hearing loss and cannot be modified when selecting CR parameters, we chose the gap index as the more preferred predictor variable in this study over 5-PTA. To that end, we calculated the residual variance of 5-PTA toward the response variable of gap index for both regular aCR and noisy aCR. Residual variance is the unexplained variance between 5-PTA and the gap index. This method enabled us to correct for multicollinearity between these predictor variables. Of note, patient age was not included in the regression models, as hearing loss has a known significant impact on cochlear tuning, while age may have a smaller impact (Lutman et al., 1991). The bivariate correlation between the two variables of age and 5-PTA demonstrated an $r = 0.635$. Thus, 5-PTA was preferentially selected over age to minimize further multicollinearity, considering the known smaller effect of age on cochlear tuning relative to the effect of hearing loss.

Gap index, tinnitus duration, and residual variance of 5-PTA (calculated from the relationship to the gap index of either regular or noisy aCR) were included in the models with the VAS-L during therapy as the primary outcome variable.

Secondary Analyses

Additionally, we chose to perform secondary analyses that were exploratory in nature and therefore had no formal hypotheses. The secondary analyses were performed with the outcome variables of VAS-L after stimulation, as well as VAS-A during and after stimulation. Furthermore, the mean relative overlap and mean relative gap were also assessed as

part of the secondary analyses. As in the primary analysis, the 5-PTA was residualized in all secondary analyses to account for multicollinearity.

RESULTS

Primary Analysis

As shown in **Table 1**, in the linear models for VAS-L during both regular and noisy aCR, the gap index was the only significant predictor variable. Partial regression plots for the primary analysis are shown in **Figure 4**. It should be noted that partial regression plots demonstrate the residuals of the represented variables, rather than the variables themselves. For this reason, the *y*-axis in each subfigure of **Figure 4** represents the residual of VAS-L during CR, and the *x*-axis represents the residual of the gap index after removing the linear effects of the residual variance of 5-PTA. The slope of each plot is the same as the unstandardized beta coefficient (*B*) for the gap index for each multiple linear regression, the values of which can be found in **Table 1**.

Secondary Analyses

Gap Index

As shown in **Table 1** and **Supplementary Table 6**, in the linear models for VAS-L after regular aCR, only the duration was a significant predictor variable. However, in noisy aCR, the gap index was once again significant. In looking at VAS-A during therapy, the gap index was significant for both regular and noisy aCR. In looking at the VAS-A after therapy, both the duration and gap index were significant for regular aCR, while only the gap index was significant for noisy aCR.

Mean Relative Gap

As shown in **Supplementary Table 4** and **Supplementary Table 6**, the findings for the mean relative gap were very similar to those seen with the gap index. The mean relative gap was a significant predictor variable for all models except the VAS-L after regular aCR, in which only the duration was significant. For VAS-A after regular and noisy aCR, both the duration and mean relative gap were significant.

Mean Relative Overlap

As shown in **Supplementary Table 5** and **Supplementary Table 6**, for VAS-L during regular aCR, only the residual variance of 5-PTA was significant. For VAS-L during noisy aCR, the mean relative overlap was significant. For VAS-L after regular aCR, the duration was trending toward significance, while in noisy aCR, the duration was again trending, with mean relative overlap as significant. For VAS-A during regular aCR, the mean relative overlap and residual variance of 5-PTA were significant. For VAS-A during noisy aCR, only the mean relative overlap was significant. For VAS-A after regular and noisy aCR, the duration and mean relative overlap were both significant.

Tone Spacing Relationships

Some additional findings from observing tone spacing relationships are described herein. Notably, only for regular aCR do the pairwise relative gaps increase with increasing tone frequency, as seen in **Supplementary Figure 1** (i.e., in (A), $G(1,2) < G(2,3) < G(3,4)$ on average, while in (B), $G(1,2) < G(3,4) < G(2,3)$. Additionally, when looking at the relative overlap, as in **Supplementary Figure 4**, for regular aCR, even at large values of the gap index, there is overlap of the ERBs for tones 2 and 3 with the tinnitus ERB. In noisy aCR, however, the ERBs for tones 2 and 3 do not overlap with the tinnitus ERB.

DISCUSSION

Overall Findings

Coordinated reset was developed computationally to lead to desynchronization of populations of neurons with abnormal degrees of coincident firing (Tass, 2003; Tass and Popovych, 2012). However, the optimal values of overlap of spatial stimulation profiles for aCR—leading to maximal desynchronization and clinical benefit—remain an unknown in clinical practice. Several lines of evidence suggest that stimulus amplitudes and the intimately associated parameter of spatial stimulation profiles can have major impacts on the degree of desynchronization achievable. Tass et al. demonstrated that CR-DBS with one-third the stimulus amplitude of conventional DBS leads to more pronounced clinical effects in parkinsonian monkeys (Tass et al., 2012b). Additional computational studies have demonstrated the presence of the "spacing principle," whereby spaced CR stimulation at weaker intensities can effectively induce anti-kindling (Popovych et al., 2015).

This study aims to shed light on the impact of tone spacing on clinical efficacy of regular and noisy aCR, as measured by the changes to self-reports of tinnitus loudness and annoyance during and after stimulation. The existing tone paradigms were transformed into an ERB-scale, which allowed for an analysis of the impact of aCR spatial stimulation profiles on clinical outcome. The gap index—or fraction of the target spectral range uncovered by stimulation—was introduced as a measure of spacing between adjacent auditory filters. We carefully analyzed several possible metrics, as described in the Methods, and found the gap index to be a useful composite measure that captures multiple relationships, both among the therapeutic tones and also between the therapeutic tones and the tinnitus frequency.

To that end, several multiple linear regression models were developed, using tinnitus duration, the gap index, and residual variance of 5-PTA (after controlling for multicollinearity with the gap index) as predictor variables. The primary outcome variable was VAS-L during therapy, with additional secondary analyses performed on the response variables of VAS-L after therapy and VAS-A during and after stimulation with the two CR paradigms. The gap index was found to be the primary predictor variable for the primary outcome variable of VAS-L during regular aCR and

during noisy aCR. This suggests that, as the gap index becomes smaller, i.e., the ERBs corresponding to the CR tones have less space between them, there is a decrease in the response to treatment, with higher symptom scores during and after stimulation. Thus, higher gap indices—and thus loosely spaced CR tones—are associated with a more pronounced treatment response in the acute stage. These results hold true when controlling for both tinnitus duration and 5-PTA.

When examining VAS-L after regular aCR, only the duration was significant. When examining VAS-A after regular aCR, both gap index and duration were significant. The results of these exploratory analyses suggest that having had tinnitus for longer duration had a possible negative impact on therapeutic efficacy for the acute after-effect. In contrast, in a prospective, randomized, single-blind, placebo-controlled 12-week proof of concept study in 63 patients with chronic tonal tinnitus, up to 50 dB hearing loss and tinnitus duration characteristics comparable to the sample considered here, it was shown that tinnitus duration was not a confounding factor for patients treated with aCR stimulation for 4–6 hours per day (Tass et al., 2012a). Hence, while the acute effects studied in this paper may depend on tinnitus duration, long-term effects of aCR stimulation may evolve irrespective of tinnitus duration. The results of this study are applicable specifically to the acute effects of aCR during short, 16-min epochs. With these results in hand, it will be important to assess whether loosely spaced CR tones will also be favorable in a chronic stimulation setting, with the goal of inducing plastic changes furthering sustained long-term desynchronization and corresponding symptom relief. With regards to the other indices considered—mean relative gap and mean relative overlap—there were fewer models in which the VAS scores were explained solely by those variables, as summarized in **Supplementary Table 6**.

Of note, acute desynchronizing effects (obtained during stimulation) are not necessarily predictive of long-term desynchronizing effects emerging after cessation of stimulation. For instance, a theoretical study in spiking neuronal networks with STDP receiving periodic stimulation revealed complex and counterintuitive stimulus-response relationships between acute (de)synchronization during stimulation and sustained, long-lasting (de)synchronization emerging as time evolves after cessation of stimulation (Kromer and Tass, 2020). In particular, synchronization during stimulation may be followed by long-lasting desynchronization, and desynchronization during stimulation may end up in long-lasting synchronization. From a computational standpoint, acute desynchronizing effects of CR stimulation are favorable but not predictive of long-term desynchronization (Manos et al., 2018; Kromer and Tass, 2020), for which reason the gap index is not necessarily predictive of long-term effects.

There are some important differences between regular and noisy aCR that are worth mentioning. First, regular and noisy aCR differ slightly with respect to acute after-effects. In the original Adamchic et al., 2017 study, while both stimulation protocols caused significant after-effects on tinnitus loudness, only noisy aCR led to a significant reduction of tinnitus annoyance after the end of stimulation. From an electrophysiologic standpoint, regular aCR caused a significantly longer and stronger decrease of the delta band power, longer and stronger increase of alpha band power, and significantly longer decrease of gamma band power (Adamchic et al., 2017). However, interestingly in the window of 80–90 s after stimulation, the reduction in gamma band power is superior after noisy aCR. There is evidence to suggest that the gamma band is more pertinent to the loudness of the tinnitus percept (Van Der Loo et al., 2009), so once again, this may be why only noisy aCR showed a statistically significant acute after-effect in VAS-L after therapy, while regular aCR does not (and hence also why the gap index is only a significant predictor for VAS-L after noisy aCR).

These electrophysiologic differences suggest a likely underlying mechanistic difference. The two protocols also differ with respect to long-term effects. While noisy aCR does have an acute on-effect, this effect is not long-lasting. After cessation of stimulation, only regular aCR has a lasting off-simulation effect, while noisy aCR does not (Tass et al., 2012a). Because regular and noisy aCR demonstrate marked differences in the duration of effect as well as in electrophysiologic changes induced, it stands to reason that the underlying mechanism of the two protocols may be different. For example, as described in (Adamchic et al., 2017), the reduction of delta band power after the end of regular aCR was more pronounced and lasted longer than that after noisy aCR. Noisy aCR may behave similar to a masker, suppressing the tinnitus via feed-forward inhibition rather than strictly via long-lasting desynchronization (Roberts, 2007), though this is not known. Despite the possible differences in underlying mechanism between regular and noisy aCR, we found in this study that wider ERB spacing was found to be beneficial for both regular and noisy aCR. The reason for this is yet unknown. One possibility is that wider ERB spacing in noisy aCR leads to a greater degree of masking. As shown in **Supplementary Figure 5**, the mean relative overlap of CR tones 2 and 3 is negative for noisy aCR, indicating greater spacing. Evidence suggests that masking may be most efficient for sounds of frequency just below the tinnitus frequency (Terry et al., 1983). With a higher degree of spacing between tones, it may be that the functional spectrum of noisy aCR is wider on average, thus possibly contributing to greater residual inhibition, but this is speculative and requires further investigation. Furthermore, as was seen in (Tass et al., 2012a), the pitch of patients' tinnitus tended to shift downward over the course of therapy in regular aCR. One possible explanation for this may be evident from the relative gaps. As seen in **Supplementary Figure 1**, in regular aCR, the pairwise relative gaps increase with increasing tone frequency in regular aCR (i.e., in (A), $G(1,2) < G(2,3) < G(3,4)$ on average), while in noisy aCR this is not true (i.e., in (B), $G(1,2) < G(3,4) < G(2,3)$ on average). This may contribute to the lowering of the tinnitus pitch with therapy which has been observed with regular aCR only, on account of a possible downshifting of the tinnitus focus due to disproportionately

effective desynchronization at higher stimulus frequencies in regular aCR.

Additional studies are required to validate the findings of this acute effects clinical study. To that end, there are several important considerations discussed herein that impact the interpretation of these results and the design of future experiments. Firstly, the ERB model itself utilizes several assumptions, which may limit the generalizability of this approach to specific subgroups of tinnitus patients. Secondly, various cochlear nonlinearities can impact the frequency specificity and thus the frequency-to-place match of auditory tonotopy which are unaccounted for in the existing ERB-transformation of CR tones. Thirdly, peripheral estimations of frequency selectivity are reasonable but imperfect representations of cortical tuning, i.e., the ERB model represents the behavior at the level of the basilar membrane more closely than it may represent the auditory cortex in full, which is more difficult to probe non-invasively. And finally, ascertaining an accurate pitch match is a necessity of aCR in order to determine the correct f_T around which to place the therapeutic tones, whether using fixed spacing or ERB-based spacing. Each of these considerations is discussed in detail in the **Supplementary Discussion**.

Limitations of the ERB Model as Applied to Tinnitus

Auditory filter widths tend to broaden in individuals with cochlear deficits (Florentine et al., 1980; Glasberg and Moore, 1986), with the bandwidth typically increasing with increasing threshold. As described in **Eq. 2**, the ERB widths for hearing-impaired listeners can be estimated as a function of threshold at a given center frequency. However, there are some limitations to this approach. Firstly, this relationship does not hold for thresholds greater than 50 dB HL (Moore et al., 1999). Secondly, the relationship between ERB width and center frequency is best established for frequencies from 2,000 to 6,000 Hz (Moore et al., 1999), thus it is harder to comment on relationships outside of this spectral range. The tinnitus frequency in this cohort ranged from 675 to 9,800 Hz. Of the 36 ears across 18 patients, seven ears had a tinnitus pitch match between 2,000 and 6,000 Hz.

Notably, there is a weak correlation between threshold elevation on audiometry and the widening of the filter bandwidth, as there is variability on an individual level in the degree of broadening and in the asymmetry of the filter, possibly due to varying patterns of cochlear damage (Moore, 1995). This points to a need for measuring the ERB directly rather than estimating it from the absolute threshold, as was done in **Eq. 2**, in order to attain truly perceptually relevant tone spacing for aCR in any given individual.

Furthermore, the analysis was done on previously acquired data. As a result, it was not possible to manipulate the spacing of CR tones independently of the hearing thresholds, for which reason the 5-PTA demonstrated multicollinearity, i.e., high intercorrelation, with the gap index, mean relative gap, and mean relative overlap. In each of these multiple linear regressions, the 5-PTA variable was residualized to help reduce the effect of multicollinearity, as described in *Primary Analysis*. This involves regressing the two predictor variables and using the resulting residual variance in the overall multiple linear regression instead of one of the original predictors. However, this is a statistical estimation of the residual variance of the 5-PTA, and as a result, it is not possible within the framework of this re-analysis to definitively eliminate the relationship of hearing loss to each of these measures of tone spacing. In the future, additional experiments would require a within-subject approach to vary the tone spacing on the frequency axis (rather than the estimated ERB axis alone) while holding the underlying hearing thresholds constant in order to eliminate the effect of hearing loss on the ERB spacing arrangements. Ultimately, on account of these limitations, direct measurements of auditory filters may be required in individual patients rather than estimations based on tinnitus pitch and hearing thresholds. In the **Supplementary Methods**, we describe several methods by which the ERB widths may be directly measured in future studies. Additionally, in the **Supplementary Discussion**, we describe in further detail several other limitations and considerations unique to the ERB model, as introduced in *Overall Findings*.

Recommendations for Future Studies

Based on the results of this study, we hypothesize that a larger gap index—and thus more loosely spaced CR tones—may improve the ability of tinnitus patients to respond positively to aCR acutely. Follow-up studies would involve the direct measurement of the ERBs of the auditory filters centered at the therapeutic tone frequencies, such as with one or more of the "rapid" methods described above. A first experiment may involve traditional, fixed spacing aCR compared head-to-head with aCR with some specified larger gap index between the ERBs of the therapeutic tones, on both an acute and chronic stimulation basis. Furthermore, our study at present was limited to the analysis of self-reported questionnaire data. Subsequent experiments should consider electrophysiologic measures of desynchronization as well, to assess the power changes that may result from different ERB-based aCR paradigms.

As a result of the afore mentioned cochlear nonlinearities and the related effect of stimulus level used to probe the auditory system's frequency selectivity, it is evident that the desynchronization ability of individual CR tones may depend on more than simply the degree of overlap or gap between the corresponding ERBs. Upward and/or downward spread of masking, as well as lateral suppression, may have additional effects on CR efficacy, dependent on the magnitude and perhaps directionality of the individual inter-tone effects. As an example, if in fact there is pathologic downward spread of masking in SNHL, then higher frequency tones above f_T may themselves to some extent mask the tinnitus frequency. High-frequency CR tones may in theory also decrease the efficacy of lower-frequency CR tones. The inverse could be seen in excess upward spread of masking. To parse out these effects, follow-up experiments in tinnitus subjects may involve pairs of tones above and below the tinnitus frequency. The distance between the CR tones themselves and the distance between the CR tones and f_T could be varied systematically in order to determine degree of subjective tinnitus relief as well as degree of electrophysiologic desynchronization resulting from various spacing configurations. Considering as well that CR tones may be susceptible to the effects of forward masking, in which a probe tone is masked by

a preceding masker tone, the temporal spacing of CR—in addition to frequency spacing—may also be an avenue of further exploration.

It should be noted that when reversing the residualization procedure in the methods, such that the residual variance of the gap index is calculated toward the 5-PTA, the model yields the same adjusted R^2 and p-value as the original analysis, as shown in **Supplementary Table 3**. However, the only significant predictor variable now is the 5-PTA, rather than the residual variance of the gap index. From this, one could ask whether the hearing loss is the true predictor variable of the effect on VAS-L during aCR, rather than the tone spacing driving the effect. However, as shown in **Figure 3A**, the gap index does not simply depend on the average hearing impairment around f_T. The gap index strongly depends on shape of the audiogram around f_T. To that end, several studies will be necessary in further disentangling the impact of hearing loss versus the impact of tone spacing on clinical outcome.

As shown in **Figure 3A**, the largest values of the gap index are, on average, for normal hearing, and the gap span (or the range of gap values dependent on the hearing impairment) increases with increasing f_T. If normal hearing is more favorable, rather than inherently larger gap indices, we could provide a normal hearing subject with a relatively high f_T, such as on the order of 8 kHz, regular CR tones (in which the predicted gap index would be low for this patient). If the acute effect is favorable with significant tinnitus suppression during therapy, it may be that the absence of hearing impairment, rather than the tone spacing, is associated with clinical improvement. Further, if we were to provide wider tone spacing to this subject (essentially the spacing one would expect for an individual with moderate hearing loss) and the patient does not have clinical benefit, again this would suggest that the absence of hearing impairment is associated with improved outcomes, rather than loosely spaced tones on the ERB scale. The same effect should be observable throughout the f_T range. However, due to the fact that the gap span increases with increasing f_T, we hypothesize that the difference between regular CR tone spacing and the mimicked hearing impairment spacing would be greatest when f_T is on the higher end of the spectrum (such as in the aforementioned hypothetical patient with an f_T of 8 kHz).

In an additional related experiment, one could test a patient with moderate hearing loss. With hearing loss, the gap index tends to decrease. To compensate for hearing impairment, we could increase the spacing and thereby the gap index. If the patient has a clinical reduction in tinnitus loudness during CR, this could mean the tone spacing is the more salient predictor than the hearing loss. In each of these cases, whether normal hearing or moderate hearing loss, we could provide the aCR tone spacing expected in the opposite scenario to differentiate the effects of hearing threshold and tone spacing. Furthermore, it would be of immense utility to test patients whose audiograms demonstrate hearing loss above the f_T, hearing loss below the f_T, and hearing loss in the vicinity of f_T, thereby directly measuring outcomes with differently shaped audiograms, as was done in **Figure 3A** for the 26 dB hearing loss.

Overall, the results of this study are a first step in the clinical optimization of tone spacing for aCR in order to obtain maximal anti-kindling and long-term therapeutic benefit. Broader spatial stimulation of CR tones, as indicated by higher gap indices, may result in improved relief from tinnitus loudness and annoyance in the acute stage of therapy. Additional studies are required to determine electrophysiologic correlation of these findings, to assess the impacts of chronic stimulation, and to correlate measured rather than estimated auditory filter widths with symptom and electrophysiologic data.

DATA AVAILABILITY STATEMENT

The original contributions presented in the study are included in the article/**Supplementary Material**, further inquiries can be directed to the corresponding author.

ETHICS STATEMENT

The studies involving human participants were reviewed and approved by the Ethics Committee of Cologne University's Faculty of Medicine. The patients/participants provided their written informed consent to participate in this study.

AUTHOR CONTRIBUTIONS

TM, AS, KP, and PT drafted and refined the article. TM, KP, JY, SH, and PT performed data and statistical analyses on the patient data. MF and IA performed a critical reading of the article. All authors have read and approved the article.

FUNDING

This study was funded with the support of the Binns Family Foundation.

ACKNOWLEDGMENTS

TM acknowledges the generous support of the T32DC015209 training grant from the National Institutes of Health/National Institute on Deafness and Other Communication Disorders.

SUPPLEMENTARY MATERIAL

The Supplementary Material for this article can be found online at: https://www.frontiersin.org/articles/10.3389/fnetp.2021.734344/full#supplementary-material

REFERENCES

Adamchic, I., Langguth, B., Hauptmann, C., and Tass, P. A. (2014a). Abnormal Cross-Frequency Coupling in the Tinnitus Network. *Front. Neurosci.* 8, 284. doi:10.3389/fnins.2014.00284

Adamchic, I., Hauptmann, C., and Tass, P. A. (2012). Changes of Oscillatory Activity in Pitch Processing Network and Related Tinnitus Relief Induced by Acoustic CR Neuromodulation. *Front. Syst. Neurosci.* 6, 18. doi:10.3389/fnsys.2012.00018

Adamchic, I., Toth, T., Hauptmann, C., and Tass, P. A. (2014b). Reversing Pathologically Increased EEG Power by Acoustic Coordinated Reset Neuromodulation. *Hum. Brain Mapp.* 35, 2099–2118. doi:10.1002/hbm.22314

Adamchic, I., Toth, T., Hauptmann, C., Walger, M., Langguth, B., Klingmann, I., et al. (2017). Acute Effects and After-Effects of Acoustic Coordinated Reset Neuromodulation in Patients with Chronic Subjective Tinnitus. *NeuroImage: Clin.* 15, 541–558. doi:10.1016/j.nicl.2017.05.017

Angelini, L., De Tommaso, M., Guido, M., Hu, K., Ivanov, P. Ch., Marinazzo, D., et al. (2004). Steady-state Visual Evoked Potentials and Phase Synchronization in Migraine Patients. *Phys. Rev. Lett.* 93, 038103. doi:10.1103/PhysRevLett.93.038103

Bashan, A., Bartsch, R. P., Kantelhardt, J. W., Havlin, S., and Ivanov, P. C. (2012). Network Physiology Reveals Relations between Network Topology and Physiological Function. *Nat. Commun.* 3, 702. doi:10.1038/ncomms1705

Bhatt, J. M., Lin, H. W., and Bhattacharyya, N. (2016). Prevalence, Severity, Exposures, and Treatment Patterns of Tinnitus in the United States. *JAMA Otolaryngol. Head Neck Surg.* 142, 959–965. doi:10.1001/jamaoto.2016.1700

Bi, G.-Q., and Poo, M.-M. (1998). Synaptic Modifications in Cultured Hippocampal Neurons: Dependence on Spike Timing, Synaptic Strength, and Postsynaptic Cell Type. *J. Neurosci.* 18, 10464–10472. doi:10.1523/jneurosci.18-24-10464.1998

Bjørk, M., and Sand, T. (2008). Quantitative EEG Power and Asymmetry Increase 36 H before a Migraine Attack. *Cephalalgia* 28, 960–968.

Chittka, L., and Brockmann, A. (2005). Perception Space-The Final Frontier. *Plos Biol.* 3, e137. doi:10.1371/journal.pbio.0030137

Clark, J. G. (1981). Uses and Abuses of Hearing Loss Classification. *Asha* 23, 493–500. Retrieved from: https://www.researchgate.net/publication/16145943.

Eggermont, J. J., and Tass, P. A. (2015). Tinnitus and Neural Plasticity (Tonndorf Lecture at XIth International Tinnitus Seminar, Berlin, 2014). *Hearing Res.* 319, 1–11. doi:10.1016/j.heares.2014.10.002

Fletcher, H. (1940). Auditory Patterns. *Rev. Mod. Phys.* 12, 47–65. doi:10.1103/revmodphys.12.47

Florentine, M., Buus, S., Scharf, B., and Zwicker, E. (1980). Frequency Selectivity in Normally-Hearing and Hearing-Impaired Observers. *J. Speech Lang. Hear. Res.* 23, 646–669. doi:10.1044/jshr.2303.646

Gerstner, W., Kempter, R., Van Hemmen, J. L., and Wagner, H. (1996). A Neuronal Learning Rule for Sub-millisecond Temporal Coding. *Nature* 383, 76–78. doi:10.1038/383076a0

Glasberg, B. R., and Moore, B. C. J. (1986). Auditory Filter Shapes in Subjects with Unilateral and Bilateral Cochlear Impairments. *The J. Acoust. Soc. America* 79, 1020–1033. doi:10.1121/1.393374

Glasberg, B. R., and Moore, B. C. J. (1990). Derivation of Auditory Filter Shapes from Notched-Noise Data. *Hearing Res.* 47, 103–138. doi:10.1016/0378-5955(90)90170-t

Goodman, A. (1965). Reference Zero Levels for Pure-Tone Audiometer. *Asha* 7, 1.

Guimarães, A. C., De Carvalho, G. M., Monteiro Zappelini, C. E., Mezzalira, R., Stoler, G., Paschoal, J. R., et al. (2014). Study of the relationship between the degree of tinnitus annoyance the presence of hyperacusis☆☆Please cite this article as: Guimarães AC, Carvalho GM, Voltolini MM, Zappelini CE, Mezzalira R, Stoler G, et al. Study of the relationship between the degree of tinnitus annoyance and the presence of hyperacusis. Braz J Otorhinolaryngol. 2014;80:24-8. *Braz. J. Otorhinolaryngol.* 80, 24–28. doi:10.5935/1808-8694.20140007

Hammond, C., Bergman, H., and Brown, P. (2007). Pathological Synchronization in Parkinson's Disease: Networks, Models and Treatments. *Trends Neurosciences* 30, 357–364. doi:10.1016/j.tins.2007.05.004

Hauptmann, C., and Tass, P. A. (2007). Therapeutic Rewiring by Means of Desynchronizing Brain Stimulation. *Biosystems* 89, 173–181. doi:10.1016/j.biosystems.2006.04.015

Henry, J. A., Dennis, K. C., and Schechter, M. A. (2005). General Review of Tinnitus. *J. speech, Lang. hearing Res.* 48, 1204–1235. doi:10.1044/1092-4388(2005/084)

Hiller, W., and Goebel, G. (2007). When Tinnitus Loudness and Annoyance Are Discrepant: Audiological Characteristics and Psychological Profile. *Audiol. Neurotol* 12, 391–400. doi:10.1159/000106482

IBM SPSS Statistics (2020). *IBM Statistics for Windows*. Armonk, NY: IBM Corp.

Ivanov, P. C., Bartsch, R. P., and Bartsch, R. P. (2016). Focus on the Emerging New fields of Network Physiology and Network Medicine. *New J. Phys.* 18. doi:10.1088/1367-2630/18/10/100201

Khaledi-Nasab, A. (2021). Long-lasting Desynchronization Effects of Coordinated Reset Stimulation Improved by Random Jitters. *Front. Physiol.* 12, 719680. doi:10.3389/fphys.2021.719680

Kromer, J. A., and Tass, P. A. (2020). Long-lasting Desynchronization by Decoupling Stimulation. *Phys. Rev. Res.* 2, 033101. doi:10.1103/physrevresearch.2.033101

Langers, D. R., De Kleine, E., and Van Dijk, P. (2012). Tinnitus Does Not Require Macroscopic Tonotopic Map Reorganization. *Front. Syst. Neurosci.* 6, 2–15. doi:10.3389/fnsys.2012.00002

Lenz, F. A., Kwan, H. C., Martin, R. L., Tasker, R. R., Dostrovsky, J. O., and Lenz, Y. E. (1994). Single Unit Analysis of the Human Ventral Thalamic Nuclear Group. *Brain* 117, 531–543. doi:10.1093/brain/117.3.531

Lutman, M. E., Gatehouse, S., and Worthington, A. G. (1991). Frequency Resolution as a Function of Hearing Threshold Level and Age. *J. Acoust. Soc. America* 89, 320–328. doi:10.1121/1.400513

Lysyansky, B., Popovych, O. V., and Tass, P. A. (2011). Desynchronizing Anti-Resonance Effect of m:n ON-OFF Coordinated Reset Stimulation. *J. Neural Eng.* 8, 036019. doi:10.1088/1741-2560/8/3/036019

Manos, T., Zeitler, M., and Tass, P. A. (2018). How Stimulation Frequency and Intensity Impact on the Long-Lasting Effects of Coordinated Reset Stimulation. *Plos Comput. Biol.* 14, e1006113. doi:10.1371/journal.pcbi.1006113

Markram, H., Lübke, J., Frotscher, M., and Sakmann, B. (1997). Regulation of Synaptic Efficacy by Coincidence of Postsynaptic APs and EPSPs. *Science* 275, 213–215. doi:10.1126/science.275.5297.213

Meikle, M., and Taylor-Walsh, E. (1984). Characteristics of Tinnitus and Related Observations in over 1800 Tinnitus Clinic Patients. *J. Laryngol. Otol.* 98, 17–21. doi:10.1017/s1755146300090053

Mišić, B., Betzel, R. F., Nematzadeh, A., Goñi, J., Griffa, A., Hagmann, P., et al. (2015). Cooperative and Competitive Spreading Dynamics on the Human Connectome. *Neuron* 86, 1518–1529. doi:10.1016/j.neuron.2015.05.035

Moore, B. C. J., and Glasberg, B. R. (1983). Suggested Formulae for Calculating Auditory-filter Bandwidths and Excitation Patterns. *J. Acoust. Soc. America* 74, 750–753. doi:10.1121/1.389861

Moore, B. C. J., Vickers, D. A., Plack, C. J., and Oxenham, A. J. (1999). Inter-relationship between Different Psychoacoustic Measures Assumed to Be Related to the Cochlear Active Mechanism. *J. Acoust. Soc. America* 106, 2761–2778. doi:10.1121/1.428133

Moore, B. C. (1995). *Perceptual Consequences of Cochlear Damage*. Oxford University Press.

Newman, C. W., Wharton, J. A., and Jacobson, G. P. (1997). Self-focused and Somatic Attention in Patients with Tinnitus. *J. Am. Acad. Audiol.* 8, 143–149.

Nini, A., Feingold, A., Slovin, H., and Bergman, H. (1995). Neurons in the Globus Pallidus Do Not Show Correlated Activity in the normal Monkey, but Phase-Locked Oscillations Appear in the MPTP Model of Parkinsonism. *J. Neurophysiol.* 74, 1800–1805. doi:10.1152/jn.1995.74.4.1800

Nondahl, D. M., Cruickshanks, K. J., Huang, G.-H., Klein, B. E. K., Klein, R., Javier Nieto, F., et al. (2011). Tinnitus and its Risk Factors in the Beaver Dam Offspring Study. *Int. J. Audiol.* 50, 313–320. doi:10.3109/14992027.2010.551220

O'Dea, R., Crofts, J. J., and Kaiser, M. (2013). Spreading Dynamics on Spatially Constrained Complex Brain Networks. *J. R. Soc. Interf.* 10, 20130016. doi:10.1098/rsif.2013.0016

Ortmann, M., Müller, N., Schlee, W., and Weisz, N. (2011). Rapid Increases of Gamma Power in the Auditory Cortex Following Noise Trauma in Humans. *Eur. J. Neurosci.* 33, 568–575. doi:10.1111/j.1460-9568.2010.07542.x

Pfeifer, K. J., Kromer, J. A., Cook, A. J., Hornbeck, T., Lim, E. A., Mortimer, B. J., et al. (2021). Coordinated Reset Vibrotactile Stimulation Induces Sustained

Cumulative Benefits in Parkinson's Disease. *Front. Physiol.* 12, 200. doi:10.3389/fphys.2021.624317

Popovych, O. V., and Tass, P. A. (2012). Desynchronizing Electrical and Sensory Coordinated Reset Neuromodulation. *Front. Hum. Neurosci.* 6, 58. doi:10.3389/fnhum.2012.00058

Popovych, O. V., Xenakis, M. N., and Tass, P. A. (2015). The Spacing Principle for Unlearning Abnormal Neuronal Synchrony. *PLoS One* 10, e0117205. doi:10.1371/journal.pone.0117205

Reed, G. F. (1960). An Audiometric Study of Two Hundred Cases of Subjective Tinnitus. *Arch. Otolaryngol. - Head Neck Surg.* 71, 84–94. doi:10.1001/archotol.1960.03770010088009

Roberts, L. E. (2007). "Residual Inhibition," in *Progress in Brain Research*. Editors B. Langguth, G. Hajak, T. Kleinjung, A. Cacace, and A. R. Møller (Elsevier), 487–495. doi:10.1016/s0079-6123(07)66047-6

Savastano, M. (2004). Characteristics of Tinnitus: Investigation of over 1400 Patients. *J. Otolaryngol.* 33, 248–253. doi:10.2310/7070.2004.03057

Schlee, W., Weisz, N., Bertrand, O., Hartmann, T., and Elbert, T. (2008). Using Auditory Steady State Responses to Outline the Functional Connectivity in the Tinnitus Brain. *PLoS ONE* 3, e3720. doi:10.1371/journal.pone.0003720

Silchenko, A. N., Adamchic, I., Hauptmann, C., and Tass, P. A. (2013). Impact of Acoustic Coordinated Reset Neuromodulation on Effective Connectivity in a Neural Network of Phantom Sound. *NeuroImage* 77, 133–147. doi:10.1016/j.neuroimage.2013.03.013

Syrkin-Nikolau, J., Neuville, R., O'day, J., Anidi, C., Miller Koop, M., Martin, T., et al. (2018). Coordinated Reset Vibrotactile Stimulation Shows Prolonged Improvement in Parkinson's Disease. *Mov Disord.* 33, 179–180. doi:10.1002/mds.27223

Tass, P. A., Silchenko, A. N., and Popelka, G. R. (2019). Acoustic Coordinated Reset Therapy for Tinnitus with Perceptually Relevant Frequency Spacing and Levels. *Sci. Rep.* 9, 13607–13616. doi:10.1038/s41598-019-49945-w

Tass, P. A. (2003). A Model of Desynchronizing Deep Brain Stimulation with a Demand-Controlled Coordinated Reset of Neural Subpopulations. *Biol. Cybernetics* 89, 81–88. doi:10.1007/s00422-003-0425-7

Tass, P. A., Adamchic, I., Freund, H.-J., Von Stackelberg, T., and Hauptmann, C. (2012a). Counteracting Tinnitus by Acoustic Coordinated Reset Neuromodulation. *Restor Neurol. Neurosci.* 30, 137–159. doi:10.3233/rnn-2012-110218

Tass, P. A., and Majtanik, M. (2006). Long-term Anti-kindling Effects of Desynchronizing Brain Stimulation: a Theoretical Study. *Biol. Cybern* 94, 58–66. doi:10.1007/s00422-005-0028-6

Tass, P. A., and Popovych, O. V. (2012). Unlearning Tinnitus-Related Cerebral Synchrony with Acoustic Coordinated Reset Stimulation: Theoretical Concept and Modelling. *Biol. Cybern* 106, 27–36. doi:10.1007/s00422-012-0479-5

Tass, P. A., Qin, L., Hauptmann, C., Dovero, S., Bezard, E., Boraud, T., et al. (2012b). Coordinated Reset Has Sustained Aftereffects in Parkinsonian Monkeys. *Ann. Neurol.* 72, 816–820. doi:10.1002/ana.23663

Tass, P. A. (2017). Vibrotactile Coordinated Reset Stimulation for the Treatment of Neurological Diseases: Concepts and Device Specifications. *Cureus* 9, 1. doi:10.7759/cureus.1535

Terry, A. M. P., Jones, D. M., Davis, B. R., and Slater, R. (1983). Parametric Studies of Tinnitus Masking and Residual Inhibition. *Br. J. Audiol.* 17, 245–256. doi:10.3109/03005368309081485

Tunkel, D. E., Bauer, C. A., Sun, G. H., Rosenfeld, R. M., Chandrasekhar, S. S., Cunningham, E. R., Jr., et al. (2014). Clinical Practice Guideline. *Otolaryngol. Head Neck Surg.* 151, S1–S40. doi:10.1177/0194599814545325

Van Der Loo, E., Gais, S., Congedo, M., Vanneste, S., Plazier, M., Menovsky, T., et al. (2009). Tinnitus Intensity Dependent Gamma Oscillations of the Contralateral Auditory Cortex. *PloS one* 4, e7396. doi:10.1371/journal.pone.0007396

Wang, J., Nebeck, S., Muralidharan, A., Johnson, M. D., Vitek, J. L., and Baker, K. B. (2016). Coordinated Reset Deep Brain Stimulation of Subthalamic Nucleus Produces Long-Lasting, Dose-dependent Motor Improvements in the 1-Methyl-4-Phenyl-1,2,3,6-Tetrahydropyridine Non-human Primate Model of Parkinsonism. *Brain Stimulation* 9, 609–617. doi:10.1016/j.brs.2016.03.014

Wong, R. K., Traub, R. D., and Miles, R. (1986). Cellular Basis of Neuronal Synchrony in Epilepsy. *Adv. Neurol.* 44, 583–592.

Zhou, B. (1995). Auditory Filter Shapes at High Frequencies. *J. Acoust. Soc. America* 98, 1935–1942. doi:10.1121/1.413313

Conflict of Interest: TM serves as a consultant for Spiral Therapeutics for work unrelated to this study. PT is an employee inventor of the underlying patent WTO 10 2016 009 874.0. AS and PT are (current and former, respectively) employees of Forschungszentrum Jülich GmbH.

The remaining authors declare that the research was conducted in the absence of any commercial or financial relationships that could be construed as a potential conflict of interest.

Publisher's Note: All claims expressed in this article are solely those of the authors and do not necessarily represent those of their affiliated organizations, or those of the publisher, the editors and the reviewers. Any product that may be evaluated in this article, or claim that may be made by its manufacturer, is not guaranteed or endorsed by the publisher.

frontiers in Network Physiology

ORIGINAL RESEARCH
published: 08 March 2022
doi: 10.3389/fnetp.2022.840829

Linear and Nonlinear Directed Connectivity Analysis of the Cardio-Respiratory System in Type 1 Diabetes

Michele Sorelli[1,2†], *T. Noah Hutson*[3†], *Leonidas Iasemidis*[3] *and Leonardo Bocchi*[1,4*]

[1]European Laboratory for Non-Linear Spectroscopy, University of Florence, Florence, Italy, [2]Department of Physics and Astronomy, University of Florence, Florence, Italy, [3]Department of Translational Neuroscience, Barrow Neurological Institute, Phoenix, AZ, United States, [4]Department of Information Engineering, University of Florence, Florence, Italy

In this study, we explored the possibility of developing non-invasive biomarkers for patients with type 1 diabetes (T1D) by quantifying the directional couplings between the cardiac, vascular, and respiratory systems, treating them as interconnected nodes in a network configuration. Towards this goal, we employed a linear directional connectivity measure, the directed transfer function (DTF), estimated by a linear multivariate autoregressive modelling of ECG, respiratory and skin perfusion signals, and a nonlinear method, the dynamical Bayesian inference (DBI) analysis of bivariate phase interactions. The physiological data were recorded concurrently for a relatively short time period (5 min) from 10 healthy control subjects and 10 T1D patients. We found that, in both control and T1D subjects, breathing had greater influence on the heart and perfusion with respect to the opposite coupling direction and that, by both employed methods of analysis, the causal influence of breathing on the heart was significantly decreased ($p < 0.05$) in T1D patients compared to the control group. These preliminary results, although obtained from a limited number of subjects, provide a strong indication for the usefulness of a network-based multi-modal analysis for the development of biomarkers of T1D-related complications from short-duration data, as well as their potential in the exploration of the pathophysiological mechanisms that underlie this devastating and very widespread disease.

Keywords: directional connectivity, type 1 diabetes (T1D), dynamical Bayesian inference, directed transfer function (DTF), cardio-respiratory system

OPEN ACCESS

Edited by:
Luca Faes,
University of Palermo, Italy

Reviewed by:
Mirjana M. Platiša,
University of Belgrade, Serbia
Mario Lavanga,
Aix-Marseille Université, France
Luiz Eduardo Virgilio Silva,
Children's Hospital of Philadelphia, United States

***Correspondence:**
Leonardo Bocchi
leonardo.bocchi@unifi.it

[†]These authors have contributed equally to this work and share first authorship

Specialty section:
This article was submitted to Information Theory, a section of the journal Frontiers in Network Physiology

Received: *21 December 2021*
Accepted: *14 February 2022*
Published: *08 March 2022*

Citation:
Sorelli M, Hutson TN, Iasemidis L and Bocchi L (2022) Linear and Nonlinear Directed Connectivity Analysis of the Cardio-Respiratory System in Type 1 Diabetes. Front. Netw. Physiol. 2:840829. doi: 10.3389/fnetp.2022.840829

INTRODUCTION

Type 1 diabetes (T1D) is a chronic condition affecting roughly 5% of the world's diabetic population (Ogurtsova et al., 2017), which is estimated to reach 642 million (95% CI: 521–829 million) by 2040 (it was 151 million in 2000 (Wild et al., 2004)) with dramatic social and financial implications. T1D is associated with pathogenetic mechanisms that lead to the apoptosis of pancreatic beta cells and, thus, to an inadequate production of the insulin hormone. There is no currently available cure for T1D, and its clinical care is focused primarily on the normalization of blood glucose levels for averting the onset of long-term complications including cardiovascular disease and renal failure. The treatment of diabetic-related chronic complications accounts for a considerable percentage [about 80% in the

TABLE 1 | Physiological frequency ranges in microvascular perfusion signals.

Oscillation	Nominal range (Hz)
Cardiac	(0.6, 2.0)
Respiratory	(0.145, 0.6)
Myogenic	(0.052, 0.145)
Sympathetic	(0.021, 0.052)
Endothelial (NO-dependent)	(0.0095, 0.021)
Endothelial (NO-independent)	(0.005, 0.0095)

TABLE 2 | Study participants: general characteristics.

Characteristics		Control	T1D	*p*-value
Gender	(M/F)	7/3	5/5	0.361$^{\alpha}$
Age	(years)	26.7 ± 1.5	29.7 ± 13.3	1.000$^{\beta}$
Smokers	(Y/N)	1/9	4/6	0.121$^{\alpha}$
Heart rate	(bpm)	70.7 ± 7.2	74.1 ± 9.5	0.406$^{\beta}$
Breathing rate	(Hz)	0.25 ± 0.06	0.28 ± 0.03	0.149$^{\beta}$
LDF cardiac power	(%)	90.6 ± 6.6	91.7 ± 7.8	0.450$^{\beta}$
T1D duration	(years)	-	13.8 ± 10.0	-
HbA1c	(%)	-	7.5 ± 1.1	-

α: via *Pearson's* χ^2 *test.*
β: via *Mann-Whitney* U *test.*

United Kingdom (Ogurtsova et al., 2017)] of the total medical costs of diabetes mellitus. Studies show that timing of medical intervention is key to reducing effects of comorbidities of T1D, with earlier interventions resulting in lower disease impact (Doria et al., 2012). Thus, there would be benefits to patients and healthcare systems alike from development of novel diagnostic techniques for early and non-invasive detection of T1D-related complications. Such diagnostic regimes could also have implications in outpatient monitoring and disease progression assessment.

The complex function of the cardiovascular system is realized by the synergistic activity of self-sustained cardiac, respiratory, and vascular oscillators (Ticcinelli et al., 2017), which is deemed to convey the necessary adaptability to sudden variations in the metabolic requirements of the organism or to changing environmental conditions (Penzel et al., 2017). There is a wide variety of clinically available devices for non-invasively monitoring the physiological systems that may be impacted by the progression of T1D. Such systems generate oscillatory modes that span a wide range of characteristic time scales, which can be isolated and separately characterized by means of established time-frequency representation (TFR) techniques (Clemson et al., 2016). In this regard, the wavelet transform (WT) analysis of laser Doppler flowmetry (LDF) signals of microvascular perfusion (Stefanovska et al., 1999) has contributed to the identification of myogenic (Aalkjaer et al., 2011), neurogenic (Söderström et al., 2003) and endothelial (Kvandal et al., 2006) frequency ranges in the microcirculatory vasomotion, in addition to the ones of the extrinsic cardiac and respiratory components (Stefanovska and Hozic, 2000) transmitted to the distal microvascular beds (**Table 1**). This, in turn, has enabled the non-invasive assessment of the underlying vasomotor mechanisms in pathological states.

Furthermore, the wavelet cross-spectrum (Clemson et al., 2016) and the phase coherence of bivariate data, (Sheppard et al., 2012; Tankanag et al., 2014; Perrella et al., 2018), along with statistical properties translated from information theory [e.g., Granger causality (Granger, 1969) and transfer entropy (Vejmelka and Palus, 2008; Sabesan et al., 2009)], have been used to gain insights into the presence of significant relations between oscillatory sources, and to determine the existence of a mutual physiological coordination, e.g., the well-known synchronous modulation of the heartbeat period by the breathing rhythm, produced at the respiratory centers located within the medulla oblongata and pons of the brainstem (Eckberg, 2003). However, beyond the effects manifested in the oscillators' phase dynamics, the fundamental functional mechanisms underlying these interactions can be probed via more sophisticated techniques, able to provide information about the directional strength of the coupling and hence about the causality of the interaction (Rosenblum and Pikovsky, 2001; Palus and Stefanovska, 2003; Faes et al., 2004). Since the cardiovascular system must handle time-varying conditions, the employed methods should be capable of capturing non-stationary functional couplings. The dynamical Bayesian inference (DBI) technique, more recently introduced by Stankovski et al. (2012), seeks to account for such non-stationarities. In DBI, the cardiovascular system is modelled as a network of phase oscillators coupled by time-dependent functions, which are identified dynamically through a Bayesian estimation framework within subsequent time windows of the oscillators' phase time series. Several researchers have employed DBI to investigate potential changes in the direct and indirect coupling between the cardiac, respiratory and vasomotor activities; their studies have detected a reduction in the respiratory sinus arrhythmia with ageing (Shiogai et al., 2010; Iatsenko et al., 2013; Stankovski et al., 2014; Ticcinelli et al., 2015; Ticcinelli et al., 2017), and a weakening of the coupling between the microvascular myogenic vasomotion and the central cardiac and respiratory oscillations in the elderly population and in primary hypertension (Ticcinelli et al., 2017). Since metabolic diseases, such as obesity and diabetes, have been recognized as models of accelerated ageing, the aforementioned alterations may also be present in subjects diagnosed with T1D.

Non-stationary metrics of time-frequency activity could elucidate stochastic coupling but require an adequate number of data points over stationary windows for inferences to be statistically significant. Linearly modelling the data may provide a valuable alternative. Multivariate autoregressive (MVAR) models have been used for describing interactions between time series originating from different nodes within a network (Baccalá et al., 2007; Vlachos et al., 2017). In detail, MVAR-based parametric techniques can be utilized to elucidate inter-node connections via coherence-based measures of implicit causality. One such measure is the directed transfer function (DTF), a frequency-domain descriptor of directed network connectivity with fundamental implications from Granger causality (Baccalá et al., 2007). DTF measures cascaded direct and indirect interactions, emphasizes source-based outflow and has been employed in several neuroscience applications (Kamiński et al., 2001; Blinowska et al., 2013; Kamiński and Blinowska, 2014;

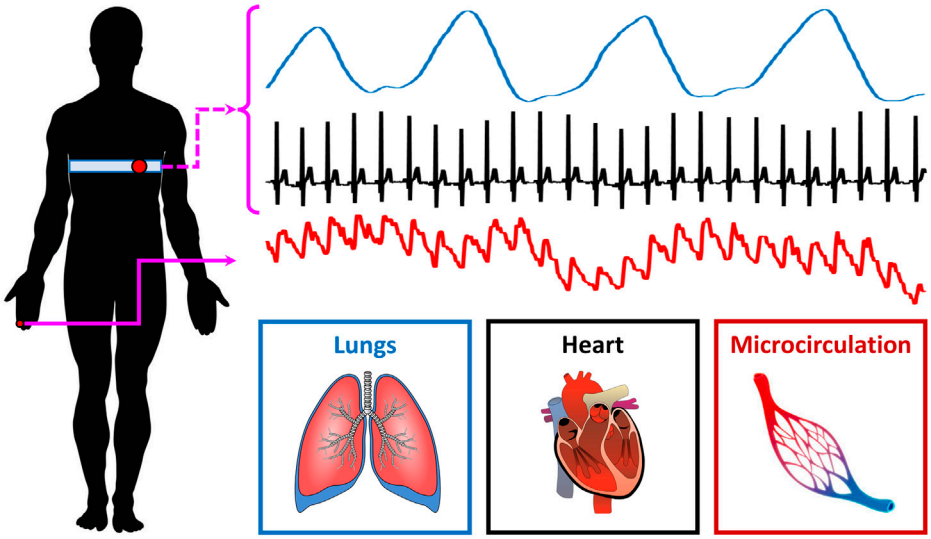

FIGURE 1 | Experimental recording setup.

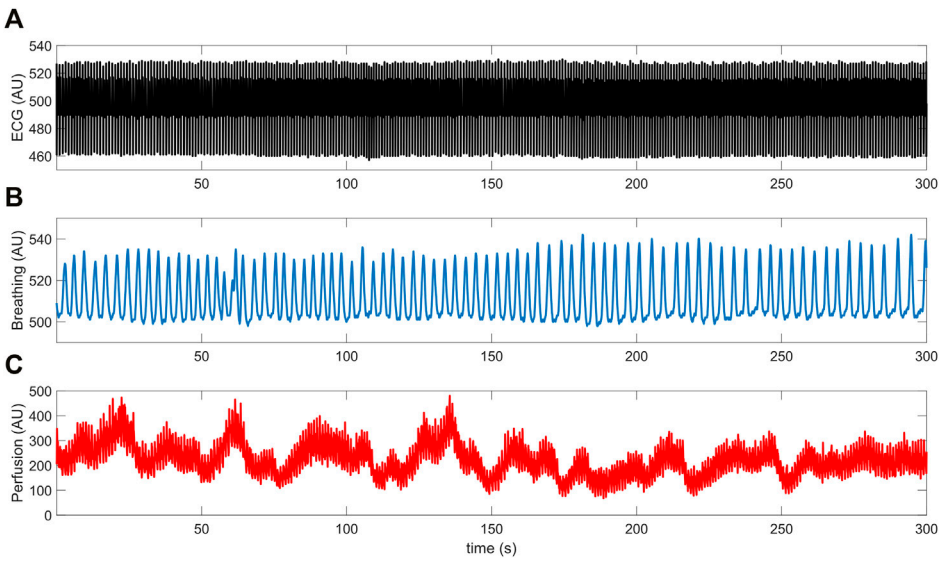

FIGURE 2 | Example of **(A)** ECG, **(B)** breathing and **(C)** LDF perfusion signals recorded from a young control subject.

Vlachos et al., 2017; Adkinson et al., 2018; Hutson et al., 2018). DTF and other MVAR-based measures of directional connectivity may also be applied to the evaluation of the directional coupling between the cardiac, respiratory, and peripheral blood flow systems. The utility of these measures in neuro-cardio-respiratory network interactions has been shown lately in animal studies of sudden unexpected death in epilepsy (SUDEP), a condition that involves potential failure of central control units of cardiac and respiratory behavior (Hutson et al., 2020).

Employing directed connectivity measures to quantify the inter-modulation of the biological oscillations originating from separate but interconnected systems could have valuable diagnostic potential for assessing the deterioration of the cardiovascular and respiratory function in prevalent high-risk conditions such as T1D. According to the results of a recent review article (Klein et al., 2010), adult subjects diagnosed with type 2 diabetes are characterized by reduced respiratory parameters, which appear to be inversely related to blood glucose levels and the time since the initial diagnosis. This review has linked chronic hyperglycemia and inflammation, autonomic neuropathy, microangiopathy of the pulmonary arterioles, and stiffening of the lung parenchyma to the possible biological mechanisms underlying the lung function

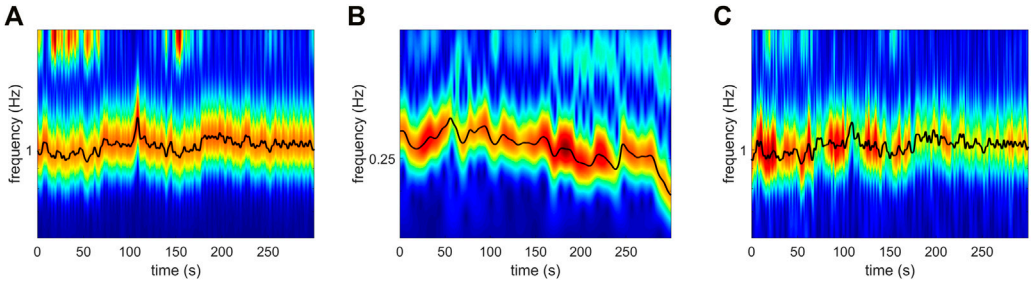

FIGURE 3 | Time-frequency ridges of the **(A)** ECG, **(B)** breathing and **(C)** LDF perfusion signals shown in **Figure 2**. Ridges were estimated by means of the adaptive parametric approach developed in (Iatsenko et al., 2016).

impairment. This may then result in a detrimental impact on the mutual physiological coupling between the breathing and heart function. In light of the above, in the present study we employed the DBI and DTF frameworks with the aim to non-invasively detect characteristics of the potential decline of connectivity in the cardio-respiratory oscillatory network in a preliminary, relatively small group of healthy controls and patients diagnosed with T1D.

MATERIALS AND METHODS

Experimental Setup and Subjects

10 healthy controls (age: 26.7 ± 1.5 years; M/F: 7/3) and 10 T1D patients (age: 29.7 ± 13.3 years; M/F: 5/5) were recruited for the present study. Research activities were carried out in accordance with the guidelines of the Declaration of Helsinki of the World Medical Association: the included subjects received detailed information on the research protocol and its purpose and signed an informed consent form. The general characteristics of the participants are summarized in **Table 2**; one control subject (i.e., 10%) and four T1D subjects (40%) were smokers. ECG, breathing and microvascular perfusion signals were simultaneously recorded. Microvascular perfusion was measured on the distal phalanx of the right forefinger using a Periflux 5,000 laser Doppler flowmetry (LDF) system (Perimed AB, Sweden). The time constant of the output low-pass filter of the instrument was set to 0.03 s in order to preserve pulse waveforms. The heart and spontaneous respiratory activities were instead monitored by means of a BioHarness 3.0 wearable chest strap sensor (Zephyr Technology, United States) and transmitted to a PC *via* Bluetooth. A graphical illustration of the recording setup is shown in **Figure 1**.

The above three signals were concurrently recorded and digitized at a sampling frequency of 250 Hz (being synchronized through a dedicated data acquisition software). Each recording session lasted 5 min and took place in thermally stable conditions (T ≈ 23°C) following a preliminary acclimatization time interval of 10 min. During signal acquisition, subjects were seated in a chair with back support and leaned their right forearm on a table; furthermore, they were instructed to carefully avoid abrupt movements to prevent the displacement of the LDF probe and thus the introduction of motion-related artifacts in the recorded perfusion signals. An example of the raw signals acquired from a young control individual is shown in **Figure 2**.

The mean breathing rate of all subjects was inside the nominal physiological range, that is (0.145, 0.6) Hz (**Table 1**). Furthermore, LDF perfusion signals recorded from the pathological group did not exhibit a significantly different (p = 0.450) power within the nominal frequency range of the cardiac rhythm (0.6, 2) Hz. However, T1D subjects included a larger proportion of smokers and were on average older than the control subjects. Nevertheless, these differences did not reach statistical significance according to Pearson's χ^2 and Wilcoxon rank-sum tests, respectively.

Dynamical Bayesian Inference

The functional physiological interaction between cardiac and respiratory processes was investigated by means of the dynamical Bayesian inference (DBI) technique (Duggento et al., 2012; Stankovski et al., 2012). This method regards the cardio-respiratory system as a network of coupled self-sustained nonlinear phase oscillators and uses a Bayesian inference scheme to dynamically estimate their time-evolving coupling strength and causality (i.e., the direction of interactions). Myogenic, sympathetic, and endothelial microvascular oscillations (**Table 1**) were not considered in the present study, due to the insufficient duration of the recorded signals. A comprehensive description of the approach can be found elsewhere (Duggento et al., 2012; Stankovski et al., 2012; Iatsenko et al., 2013; Clemson et al., 2016; Ticcinelli et al., 2017). Briefly, in DBI, the phase dynamics of two interacting oscillatory processes p_1 and p_2 is modelled as follows:

$$\dot{\varphi}_1(t) = \omega_1(t) + d_1(\varphi_2, t) + k_1(\varphi_1, \varphi_2, t) + \varepsilon_1(t) \qquad (1)$$

where $\omega_1(\cdot)$ is the natural frequency of the first oscillator, $d_1(\cdot)$ and $k_1(\cdot)$ are the coupling functions that describe the direct and indirect driving of the second oscillator (with the acceleration/deceleration of the first oscillator's phase φ_1 depending on the second's φ_2), whereas the stochastic term, $\varepsilon(\cdot)$, represents the noise (usually assumed to be Gaussian and white (Stankovski et al., 2012)). Since the above coupling functions are hypothesized to be 2π-periodic, the right-hand side of **Eq. 1** can be decomposed into a linear combination of Fourier basis functions $\Phi_n = \exp[i(n_1\varphi_1 + n_2\varphi_2)]$:

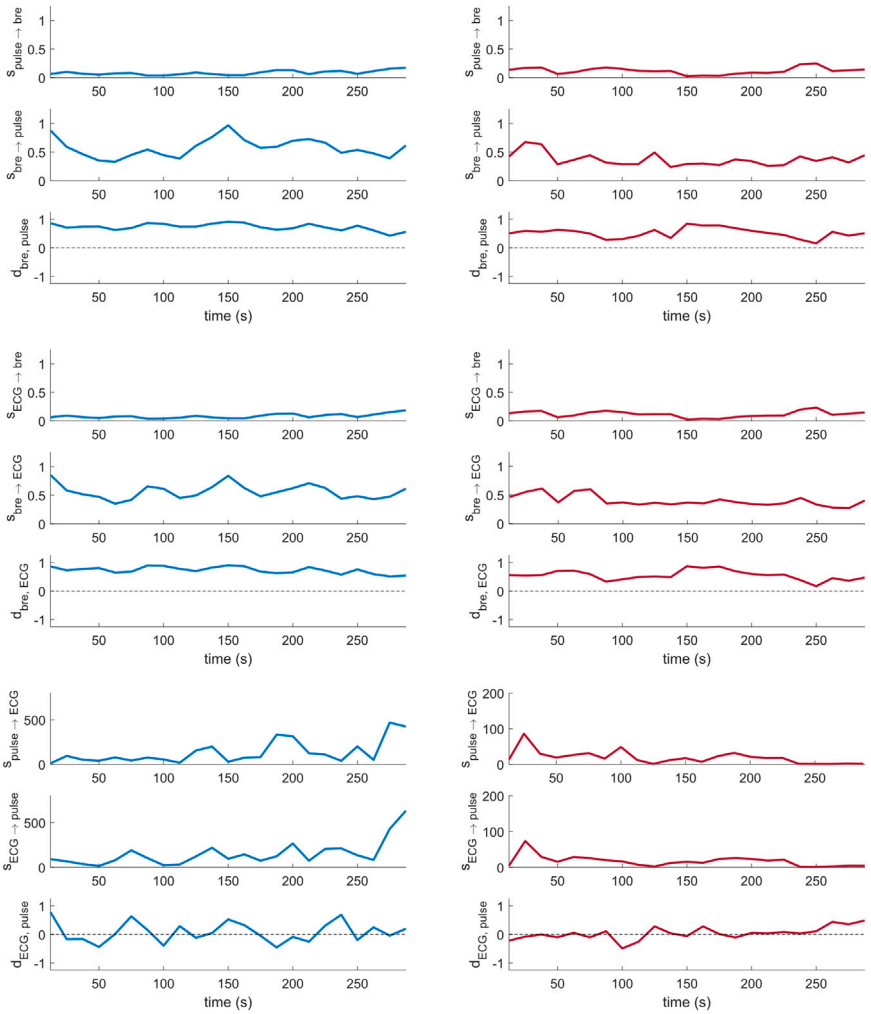

FIGURE 4 | Cardio-respiratory directional coupling strength parameters estimated *via* DBI (**Eqs 4**, **5**; two per panel), and respective directionality indices (**Eq. 6**; one per panel) obtained from a control subject (left) and a T1D patient (right).

$$\dot{\varphi}_1(t) = \sum_{n=-N}^{N} c_{1,n} \cdot \Phi_{1,n}(\varphi_1, \varphi_2) + \varepsilon_1(t) \tag{2}$$

where N is the order of the expansion and $\Phi_{i,0} = 1$ (where $i = 1, 2$). In general, the DBI technique sequentially applies the Bayesian theorem to adjacent time windows of the oscillators' instantaneous phases, $\varphi_i(t)$, in order to infer the bank of time-varying parameters $c_{i,n}$ characterizing the functional interaction between the underlying physiological processes, and the noise term, ε_i. The inferred $c_{i,n}$ values are then used to estimate a dynamic index of directional coupling strength and directionality of influence. In the present study, DBI analysis was based on the related Matlab toolbox developed by the research group on Nonlinear and Biomedical Physics at Lancaster University (http://www.physics.lancs.ac.uk/research/nbmphysics/diats/tfr/).

In detail, DBI analysis usually requires the extraction of the instantaneous frequency of the oscillations of interest, in order to track their characteristic time-dependent phase $\varphi_i(t)$. In this regard, an adaptive parametric ridge reconstruction scheme (Iatsenko et al., 2016) was applied to the time-frequency representation (TFR) of the acquired signals in order to isolate the breathing and cardiac oscillatory components. In the present study, the cardiac component was isolated from both the ECG and the LDF signals of cutaneous perfusion. The adjustable parameters of the algorithm, which respectively tune the tolerance to deviations from the component's mean rate of frequency change and mean frequency, were set to their default value of 1. The wavelet transform (WT) was adopted as TFR technique because of its logarithmic frequency resolution (Stefanovska et al., 1999); specifically, a Morlet wavelet with central frequency $f_0 = 1$ was chosen as the mother function:

$$\gamma_m(t) = \frac{1}{\sqrt{2\pi}} \left(e^{i2\pi t} - e^{-\frac{(2\pi)^2}{2}} \right) e^{-t^2/2} \tag{3}$$

Prior to the application of the WT, signals were downsampled to 50 Hz, detrended by means of a third order polynomial fit, and band-passed inside the cardiac and respiratory frequency

TABLE 3 | Median coupling strength values obtained from 100 inter-subject surrogates.

Interaction	DBI connectivity	Median surrogates (N_w = 2,300)
Lungs ↔ Pulse	$s_{pulse\rightarrow bre}$	0.08
	$s_{bre\rightarrow pulse}$	0.24
Lungs ↔ Heart	$s_{ECG\rightarrow bre}$	0.09
	$s_{bre\rightarrow ECG}$	0.19
Heart ↔ Pulse	$s_{pulse\rightarrow ECG}$	0.28
	$s_{ECG\rightarrow pulse}$	0.25

intervals listed in **Table 1**, to remove the influence of components lying outside the physiological range of interest. The discretization of the frequency domain was performed with a density of 128 voices/octave, which enabled the extraction of smooth ridge curves. DBI was then applied to consecutive overlapping windows of the original time series, with an overlap factor of 50%. The window width was set so as to include approximately five cycles of the slowest oscillatory component for inference of the coupling parameters $c_{i,n}$, as reported in (Iatsenko et al., 2015; Clemson et al., 2016). For the analysis of cardio-respiratory interactions, this resulted in the adoption of 23 overlapping windows of 25 s. Thus, the lowest frequency we could theoretically observe was 1/25 s = 0.04 Hz. The characteristic time-frequency ridges extracted from the signals in **Figure 2** are shown in **Figure 3**.

As done by Iatsenko et al. (2013) and Ticcinelli et al. (2017), a Fourier decomposition up to the second order (i.e., $N = 2$) was chosen for the phase dynamics model expressed in **Eq. 1**. Moreover, the propagation constant p_w, that weights the diffusion of information between consecutive data windows w (Stankovski et al., 2012), was set to an arbitrary value of 0.2. Iatsenko et al. (2013) have nonetheless reported that this internal parameter of the DBI algorithm does not significantly affect the outcome of the Bayesian inference. The Euclidean norm of the coupling parameters $c_{i,n}$ estimated within each data window w was finally used to quantify the overall influence (including direct and indirect couplings) of the phase of the second oscillator on the first one's, and vice versa, yielding the following directional coupling strength signals:

$$s_{1\rightarrow 2}(w) = \sqrt{\sum_{n=-N}^{N} \left(c_{1,n}(w)\right)^2} \tag{4}$$

$$s_{2\rightarrow 1}(w) = \sqrt{\sum_{n=-N}^{N} \left(c_{2,n}(w)\right)^2} \tag{5}$$

where w indicates the dependence of the coupling coefficients on the particular time window.

Furthermore, a directionality index $d_{1,2}$ ($d_{1,2} \in [-1, +1]$) was estimated from each window w, in order to quantify the dynamic asymmetry of the bi-directional interaction:

$$d_{1,2}(w) = \frac{s_{1\rightarrow 2}(w) - s_{2\rightarrow 1}(w)}{s_{1\rightarrow 2}(w) + s_{2\rightarrow 1}(w)} \tag{6}$$

This index, proposed by Rosenblum and Pikovsky (2001) has been used in the recent literature for detecting the predominant direction of influence between the cardiac and respiratory oscillators (Stankovski et al., 2012; Iatsenko, et al., 2013; Ticcinelli, et al., 2017). Namely, if $d_{1,2} \in (0, +1]$, then the first oscillator drives the second more than the other way around; conversely, if $d_{1,2} \in [-1, 0)$, the second drives the first one. However, as reported in (Duggento et al., 2012), directional coupling strengths $s_{i\rightarrow j}(w)$ obtained via DBI represent an overall estimate of the combined phase relationships between the analyzed time series. Thus, spurious non-zero values can be inferred even when no functional interaction exists between the underlying oscillatory processes. This is why the reliability of $s_{i\rightarrow j}(w)$ should be ascertained by surrogate testing, i.e., rejecting directional coupling strengths below a specified acceptance threshold estimated from an adequately large set of surrogate interactions. In this regard, we adopted the inter-subject surrogate approach followed by Toledo et al. (2002) and Ticcinelli et al. (2017) validating our coupling strength estimates against the median value obtained from 100 unique combinations of randomly selected inter-group signals and subjects. Each of the 100 surrogate datasets was composed of mutually independent time series recorded from different individuals (e.g., ECG from control subject A, breathing from T1D patient B, LDF perfusion from control C). This technique allowed us to exclude from further consideration any directional couplings whose strength was equivalent to the one which might have arisen from chance or bias.

Directed Transfer Function

Multivariate autoregressive (MVAR) modelling of the data within short-time segments, each data window aligned in time with concurrent ones from more than one time series, is recommended for network connectivity analysis assuming that these signals are recorded from different parts of a multi-dimensional, linear and wide-sense stationary system. For each window, the estimated array of MVAR model coefficients can then be further analyzed in the frequency domain and, depending on different types of normalization utilized, provides frequency-specific measures of directional functional connectivity between the nodes of the assumed network configuration of the system (Baccalá et al., 2007). We have successfully employed such measures in network analyses of intracranial EEG (iEEG) (Vlachos et al., 2017; Adkinson et al., 2018), and magnetoencephalographic (MEG) recordings (Krishnan et al., 2015) from patients with focal epilepsy for localization of their epileptogenic focus, as well as the assessment of the dynamics of brain's network connections *en route* to a life-threatening neurological event, status epilepticus (T. N. Hutson et al., 2018). In the current study we fitted a MVAR model to each of 60-s consecutive non-overlapping data segments from the three recorded signals (ECG, breathing, perfusion) over 5 min. By using a 60-s time window, our frequency resolution is 1/60 s = 0.017 Hz = 0.05 Hz/3, and thus the lowest frequency we can deal with moving the analysis in the frequency domain is three times less than the 0.05 Hz, the lowest frequency in the frequency band of (0.05, 2) Hz we are interested in here. Thus, the MVAR model was of dimension D = 3 [i.e., the data to be fitted were placed in three-dimensional column vectors $X(t)$], and of

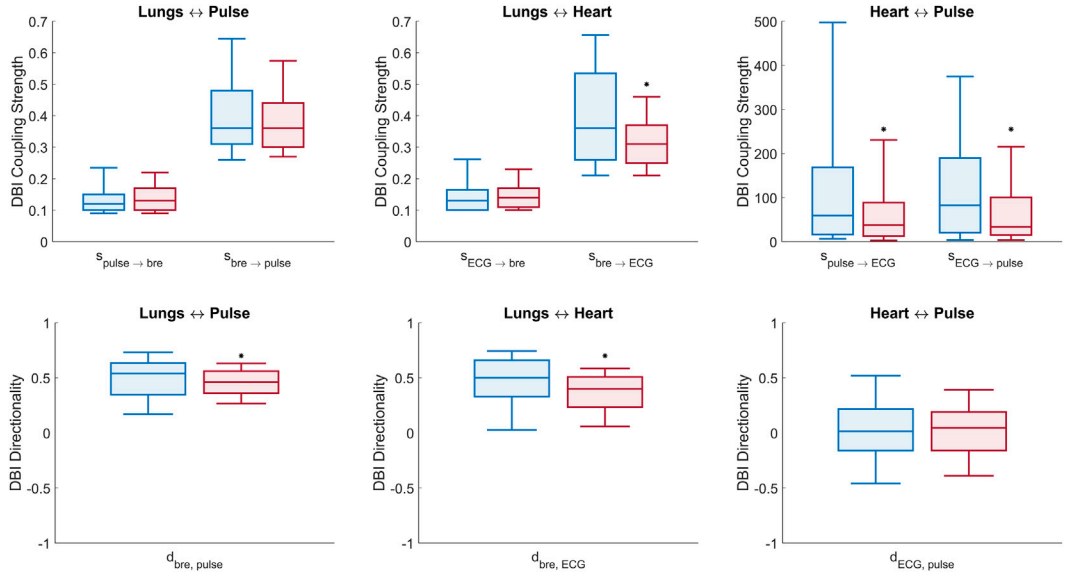

FIGURE 5 | Box plots of DBI measures of connectivity (**Eqs 4–6**). Top panel: comparison of all (six) cardio-respiratory coupling parameters estimated with DBI for the control (blue) and T1D (red) groups. Bottom panel: comparison of the (three) directionality indices per pair interaction for the control (blue) and T1D (red) groups. Statistically significant decreases, identified by one-tailed Wilcoxon rank-sum tests, are denoted by (*) above the respective boxes.

order M = 7 per subject. Also, the window length of 60 s (15,000 data points x three channels = 45,000 data points) is enough for a confident estimation of the 7 × 3 × 3 = 63 MVAR parameters as we are using more than 100 times as many data points as we have parameters to fit.

For each set of three 60-s running windows extracted at the same time from all three signals, the model linearly fits the data in the column vectors $X(t)$ as follows:

$$X(t) = \sum_{\tau=1}^{M} \boldsymbol{A}(\tau) X(t-\tau) + E(t) \tag{7}$$

where the time index t is from 1 to N, with N being the number of data points per time series within a time window (N = 15,000), M is the order of the model (M = 7), and τ is increasing in steps of the time delay between samples (we used τ = 1, that is, in time units, equal to the sampling period 1/(250 Hz) = 4 ms). Matrices $A(\tau)$ contain the model's coefficients, whereas the fitting error values are the components of the vector E (in the ideal MVAR model fit, E is multivariate Gaussian white noise). The coefficients of the MVAR model were estimated via the Vieira-Morf partial correlation method. Taking the discrete Fourier Transform of both sides of **Eq. 7** and rearranging, we have: $[I - \sum_{\tau=1}^{p} \boldsymbol{A}(\tau) e^{-i2\pi f\tau}] \cdot X(f) = E(f)$, where I is the unitary matrix. Then, by defining:

$$\bar{\boldsymbol{B}}(f) = \begin{cases} I - \sum_{\tau=1}^{p} \boldsymbol{A}_{ij}(\tau) e^{-\mathbf{i}2\pi f\tau}, \; for\, i = j \\ -\sum_{\tau=1}^{p} \boldsymbol{A}_{ij}(\tau) e^{-\mathbf{i}2\pi f\tau}, \; for\, i \neq j \end{cases} \tag{8}$$

where $\mathbf{i} = \sqrt{-1}$ in the exponents of **Eq. 8**, the directed transfer function (DTF) can be derived by utilizing the transfer matrix, $H(f)$, defined as:

$$H(f) = \bar{B}^{-1}(f) \tag{9}$$

Specifically, DTF is estimated via the following equation:

$$DTF_{j\to i}(f) = \frac{|H_{ij}(f)|^2}{\sum_{k=1}^{D} |H_{ik}(f)|^2} \tag{10}$$

The statistical significance of the DTF values of each interaction derived from each 60-s window was determined. The statistical criteria for inferring the statistical significance and confidence interval of the derived frequency-domain Granger causality-based connectivity measures are recent and have been discussed by a small number of researchers. In this study, we have followed an asymptotic analysis for evaluation of the connectivity measures from the MVAR modelling of our data (Baccalá et al., 1997; Baccalá et al., 2016). In detail, the significance of the connectivity measures $DTF_{j\to i}(f)$ at a specific frequency f between two nodes i and j was tested according to the following null hypothesis:

$$H_0: \left|DTF_{j\to i}(f)\right|^2 = 0 \quad \forall i, j \in \{1, \ldots, D\} \tag{11}$$

Rejecting H_0 at a specified significance level (typically α = 0.05) also required to reject non-statistically significant DTF values. Confidence intervals for the existing connections were estimated by determining the asymptotic distribution of DTF according to (Toppi et al., 2016). Only the thus identified statistically significant DTF values (ssDTF) were further analyzed in this study. Analogously to the DBI

TABLE 4 | Median of statistically significant ($p < 0.05$, vs. surrogates) DBI coupling strengths and directionality indices per interaction in controls and T1D patients. The statistical significance of the differences observed between the groups was estimated by one-tailed Wilcoxon rank-sum tests comparing the null hypothesis H_0 (medians in the two groups are equal) to two alternative hypotheses: H_{1a}, the median of controls being greater than that of T1D; and H_{1b}, the median of T1D being greater than that of controls. The *p*-values for each of the two performed Wilcoxon tests (last two columns) refer to the probability of accepting hypothesis H_0 to be true over the alternative hypotheses H_{1a} or H_{1b}.

Interaction	DBI connectivity	Median (controls)	Median (T1D)	*p*-value H_{1a}	*p*-value H_{1b}
Lungs ↔ Pulse	$s_{pulse\to bre}$	0.120	0.134	0.949	0.051
	$s_{bre\to pulse}$	0.361	0.363	0.326	0.674
	$d_{bre,\ pulse}$	0.539	0.455	0.011[a]	0.990
Lungs ↔ Heart	$s_{ECG\to bre}$	0.127	0.140	0.887	0.113
	$s_{bre\to ECG}$	0.360	0.314	<0.001[a]	1.000
	$d_{bre,\ ECG}$	0.503	0.396	<0.001[a]	0.999
Heart ↔ Pulse	$s_{pulse\to ECG}$	59.21	37.51	<0.001[a]	0.999
	$s_{ECG\to pulse}$	82.86	33.44	<0.001[a]	1.000
	$d_{ECG,\ pulse}$	0.013	0.042	0.556	0.445

[a]*Statistically significant at $\alpha = 0.05$ level (one-tailed Wilcoxon rank-sum test).*

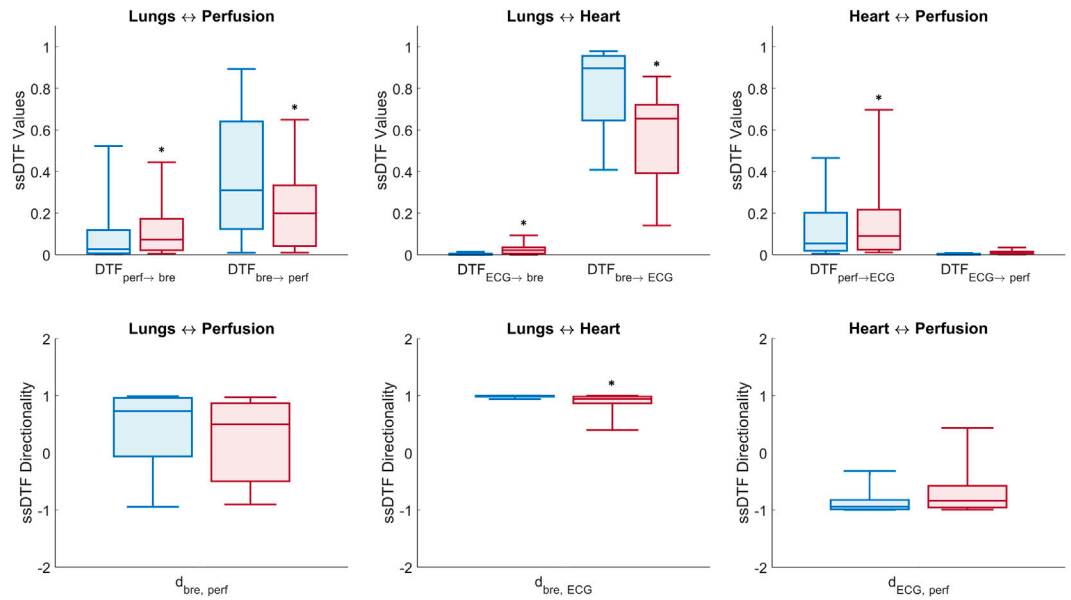

FIGURE 6 | Box plots of DTF measures of connectivity in the (0.05, 2) Hz frequency band (**Eqs 10**, **12**). Top panel: median ± first and third quartiles of ssDTF values across all directed interactions for control (blue) and T1D (red) groups. Bottom panel: directionality indices per pair interaction for the control (blue) and T1D (red) groups (*) above boxes denotes *p*-value < 0.05 estimated from non-parametric one-tailed Wilcoxon rank-sum tests comparing T1D and control groups.

analysis, an index of directionality was finally obtained from the ssDTF estimates as follows:

$$d_{i,j}(f) = \frac{ssDTF_{i\to j}(f) - ssDTF_{j\to i}(f)}{ssDTF_{i\to j}(f) + ssDTF_{j\to i}(f)} \tag{12}$$

RESULTS

Dynamical Bayesian Inference

Figure 4 shows sample coupling strength signals of the time-evolving pairwise interactions among peripheral pulse, respiratory and ECG signals, estimated using DBI in a control subject and a T1D patient. Directional coupling strength estimates below the corresponding median values of the surrogates reported in **Table 3** (100 surrogate subjects, for a total of N_w = 2,300 windows), were rejected. Also, only those windows for which both directional coupling strengths per paired interaction were found to be statistically significant according to the above rule were further considered in the statistical analysis of the directionality index, $d_{i,j}$. The overall results of the DBI analysis of the control and pathological groups including their statistical comparison (*p*-values) are shown in **Figure 5** and summarized in **Table 4**. Statistically significant differences

TABLE 5 | Median of statistically significant ($p < 0.05$, vs. surrogates) DFT values (ssDTF) and directionality indices aggregated over subsequent time windows, and averaged over the frequency range (0.05, 2) Hz. The statistical significance of the differences observed between the control and T1D groups is also illustrated as in **Table 4**.

Interaction	DTF connectivity	Median (controls)	Median (T1D)	p-value H_{1a}	p-value H_{1b}
Lungs ↔ Perfusion	$ssDTF_{perf\rightarrow bre}$	0.027	0.074	0.982	0.019[a]
	$ssDTF_{bre\rightarrow perf}$	0.310	0.129	0.031[a]	0.970
	$d_{bre,\,perf}$	0.729	0.276	0.084	0.918
Lungs ↔ Heart	$ssDTF_{ECG\rightarrow bre}$	0.002	0.011	1.000	<0.001[a]
	$ssDTF_{bre\rightarrow ECG}$	0.897	0.634	<0.001[a]	1.000
	$d_{bre,\,ECG}$	0.992	0.954	<0.001[a]	1.000
Heart ↔ Perfusion	$ssDTF_{perf\rightarrow ECG}$	0.055	0.121	0.998	0.002[a]
	$ssDTF_{ECG\rightarrow perf}$	0.002	0.006	0.763	0.258
	$d_{ECG,\,perf}$	−0.940	−0.865	0.646	0.379

[a]*Statistically significant at $\alpha = 0.05$ level (one-tailed Wilcoxon rank-sum test).*

between the two groups were detected by means of one-tailed Wilcoxon rank-sum tests for independent samples.

Lungs–Heart interaction. Compared to controls, T1D patients exhibited a significant reduction in the directionality index $d_{bre,\,ECG}$ ($p < 0.001$), which reflects a lowered asymmetry of the cardio-respiratory interaction in the pathological group. This was due to a weakened influence of the breathing activity on the cardiac rhythm, as expressed by the statistically significant decrease in the directional coupling strength $s_{bre\rightarrow ECG}$ ($p < 0.001$; **Table 4**, row 4). Conversely, the directional coupling from the heart to the lungs was not significantly different between the two groups (**Table 4**, row 5).

Lungs–Pulse interaction. T1D patients also exhibited a significant decrease in the $d_{bre,pulse}$ index ($p = 0.011$), which indicates a higher symmetry of the interaction between the breathing activity and the cardiac oscillatory mode of the LDF signals. However, in this case, none of the corresponding directional coupling strengths was significantly different between the compared subjects (**Table 4**, rows 1 and 2).

Heart–Pulse interaction. With respect to the healthy group, T1D patients were characterized by significantly lowered directional coupling strengths, $s_{pulse\rightarrow ECG}$ ($p < 0.001$; **Table 4**, row 7) and $s_{ECG\rightarrow pulse}$ ($p < 0.001$; **Table 4**, row 8). However, no statistically significant difference emerged in the overall directionality of influence, as expressed by the $d_{ECG,pulse}$ index across the control and pathological groups (**Table 4**, row 9).

Directed Transfer Function

The statistically significant DTF values (ssDTF) of directional connectivity estimated per interaction from MVAR modelling (six directional interactions between the three recorded signals) were aggregated over all windows (60-s non-overlapping data segments) and subjects within the same group (control or T1D) and averaged over the physiologically relevant frequency band (0.05, 2) Hz. The median and quartiles of the ssDTF values obtained from the control and T1D groups are shown in **Figure 6**. It is relevant to highlight that MVAR modelling evaluate signals across identical frequencies over the entire physiological range of interest, in contrast to DBI which is based on the extraction of the specific time-varying frequency component of the cardiac pulsatility, within an effectively tighter range. Therefore, in this section interactions involving LDF signals are denoted as "perfusion", rather than "pulse". From **Figure 6**, we make the following statistically significant observations about the assessed directional interactions: "Perfusion→Breathing", "Perfusion→ECG" and "ECG→Breathing" connectivity strengths are elevated in T1D subjects compared to controls. Conversely, the "Breathing→ECG" interaction in T1D is lower than the controls'. It is also noteworthy that "Breathing→ECG" is significantly higher in connectivity than "ECG→Breathing" for both T1D and controls. Also, the "Perfusion→ECG" coupling is higher than "ECG→Perfusion" in both groups.

Statistically significant directional interactions ($p < 0.05$) between the network nodes for each pair of recorded signals are reported in **Table 5** (columns 3 and 4) together with their directionality index $d_{i,j}$. Inter-group comparisons were conducted via one-tailed Wilcoxon rank-sum statistical tests, whose p-values are also included in **Table 5** (last two columns).

Lungs–Heart interaction. In agreement with the results from the DBI method, DTF shows that T1D patients exhibit a statistically significant reduction ($p < 0.001$) in the directional coupling strength from the lungs to the heart, as well as in the directionality index $d_{bre,\,ECG}$, compared to controls. The latter is due to a statistically significant increase ($p < 0.001$) in the directional strength $ssDTF_{ECG\rightarrow bre}$ observed in the pathological group, with a parallel significant decrease ($p < 0.001$) in $ssDTF_{bre\rightarrow ECG}$ (**Table 5**, rows 4–6).

Lungs–Perfusion interaction. Similarly to the DBI analysis, the DTF measures of connectivity showed a decrease in the $d_{bre,pulse}$ index of T1D patients compared to the one estimated from the control group (0.729 vs. 0.276), implying a lowered asymmetry of the interaction between breathing and LDF signals. However, this decrease was not as significant ($p = 0.084$) as the one estimated via DBI ($p = 0.011$). This outcome is due to the mixed results (decrease with $p = 0.031$, and increase with $p = 0.019$) related to the directional coupling strengths $ssDTF_{bre\rightarrow perf}$ and $ssDTF_{perf\rightarrow bre}$, respectively (**Table 5**, rows 1 and 2).

Heart–Perfusion interaction. T1D patients exhibited increased connectivity compared to the controls in both directions, with the difference in the "Perfusion→ECG" coupling reaching statistical significance ($p = 0.002$) (**Table 5**, rows 7 and 8). The above trends contributed to a diminished absolute value of the directionality index $d_{ECG,perf}$ in the pathological group, which implies a more balanced interaction with respect to controls (**Table 5**, row 9).

Finally, within each group, a few interesting features were also observed from the DTF results in relation to the difference in the strength of the directional couplings per interaction. In particular, in both control subjects and T1D patients, the median coupling strengths from the lungs to the heart and from the lungs to the microcirculation were considerably higher than in the opposite direction (the same outcome of the DBI analysis). However, the inter-group differences in the directional strengths between heart and microcirculation were contradictory with respect to the DBI analysis, which associated a higher level of bidirectional connectivity to the control group (**Table 5**, columns 3 and 4).

DISCUSSION

Towards the goal of developing reliable and non-invasive biomarkers for T1D, we employed both nonlinear (bivariate) and linear (multivariate) measures to assess possible impairments in the coupling strength and directionality of influence between three representative nodes of the cardiovascular and respiratory systems (heart, lungs, microcirculation) in patients diagnosed with T1D compared to control subjects. The two adopted methods can capture equivalent or different features in the communication between the nodes of a physiological network because of their different capabilities, that is: linearity (DTF) vs. nonlinearity (DBI) in the data; multivariate (DTF) vs. bivariate (DBI) data analysis; measure of connectivity between signals at the same frequency (DTF) vs. different frequencies (DBI). Employing these two techniques, we did identify impairments (by both or one of the approaches) in the functional directional interactions between heart, lungs, and microcirculation in T1D patients. In detail, an impairment was defined as a statistically significant difference ($p < 0.05$) in the directional coupling strengths between the respective nodes, compared to the homologous estimate obtained from the control group (i.e., rejection of the null hypothesis H_0).

Regarding the functional interactions between heart and lungs, DBI, the nonlinear framework, revealed a significantly reduced ($p < 0.001$) influence of the respiratory activity on the phase of the cardiac rhythm in the T1D group. A similar, statistically significant ($p < 0.001$) finding also emerged from the linear network analysis, using DTF. Moreover, the imbalance in the two communication channels from the lungs to the heart and vice versa, as captured by the directionality index, was also highly significantly different in both methods ($p < 0.001$). It is well known that the phase of the respiratory activity directly influences the action of the heart pump, as breathing-related changes in the intrathoracic volume alter the cardiac pre-load, thus affecting cardiac filling, post-load and other circulatory variables. Furthermore, respiration gates the timing of autonomic motoneuron firing (Eckberg, 2003), thus modulating the peripheral autonomic nervous system's outflow to the heart, an indirect cardio-respiratory coupling occurring via neuronal control (Iatsenko et al., 2013; Kralemann et al., 2013). Therefore, our finding of a reduced driving relationship of the lungs to the heart in T1D patients could be related to autonomic neuropathy, vascular degeneration or lung tissue stiffening, common co-morbidities associated with diabetes mellitus (Klein et al., 2010).

An analogous decrease of the influence of respiration on the microvascular perfusion in the T1D group compared to controls was observed by DTF analysis ($p = 0.031$) but could not be verified by DBI ($p > 0.05$). However, like for the lungs-heart interaction, the imbalance in the directional coupling strengths between lungs and microcirculation, as reflected by the directionality index, was significantly less ($p = 0.011$) in T1D than in controls as shown by DBI as well as by DTF, though without reaching a statistical significance level ($p = 0.084$). Also, regarding the DBI analysis of phase interactions, it is notable that control subjects exhibited similar statistics with respect to the evaluation of breathing and ECG signals. This result would be in line with previous findings by Jamšek and Stefanovska on the coupling information among cardiac and respiratory processes which propagates to the distal microvascular beds (Jamšek and Stefanovska, 2007), and can be characterized through the analysis of LDF signals recorded non-invasively from the skin.

In T1D subjects, the DBI analysis highlighted a significantly decreased communication in both directions between the ECG and the microvascular pulse signal extracted from LDF signals. This finding, however, could not be validated by DTF too. It is noteworthy that these directional interactions were associated with significantly higher coupling strength values (**Table 4**). This could be due to the way DBI evaluates causal relationships and what it can capture. In this case, DBI basically assesses the phase coupling between ECG and pulse signals that, although recorded at different anatomical locations, originate from the same source, representing the electrical and mechanical activities of the heart, respectively (Kralemann et al., 2013).

Finally, the estimated directional couplings from the lungs to the heart and microvasculature, via either the DBI or DTF methods, were considerably higher than the ones from the heart and vasculature towards the lungs, in both control subjects and T1D patients. Since this outcome was common in both groups, it cannot be used as a biomarker for T1D. However, it agrees with the findings of Palus and Stefanovska (2003), which have shown that the respiratory process drives the heart activity at all breathing frequencies, whether paced or spontaneous, and may shed more light on the involved physiological mechanisms *en route* to a better understanding of the cardio-respiratory system.

A potential limitation of this study is the availability and analysis of signals from only a small number of nodes (lungs, heart, microcirculation) in the network under investigation. Both DTF and DBI measure the global (direct and indirect) interactions between two nodes A and B, the indirect interactions from A to B or from B to A occurring through other node(s) C that we may not have access to in the network (Kamiński et al., 2001; Baccalá et al., 2016). In this regard, it is established that each respiratory cycle is tightly controlled by four separate control centers in the pons and medulla (Smith et al., 1991; Hilaire and Pásaro, 2003; Dampney, 2017), which cannot operate without central intervention from the brain, and direct feedback from the heart. Furthermore, central

autonomic neural control has a well-known role in the low- and high-frequency variability of the heart rate (Shaffer and Ginsberg, 2017). Thus, ignoring the brain (EEG) and investigating this complex neuro-cardio-respiratory network from only three nodes (lungs, heart, microcirculation) could have skewed the level of the estimated bivariate interactions in both T1D and control groups. However, the comparative statistical analysis of each measure across the two groups may take care of this skewness if it were in the same direction in both groups, per interaction.

In summary, we found that in both control and T1D subjects, breathing had greater influence on the heart and peripheral microvascular perfusion, compared to the opposite directional couplings and that, by both the employed methods of connectivity analysis, the causal influence of the respiratory activity on the heart was significantly decreased ($p < 0.05$) in T1D patients compared to the control group. These preliminary results can be linked to established comorbidities of T1D and, although obtained from a limited number of subjects, provide a strong indication for the usefulness of a network-based multimodal analysis for the development of biomarkers from short-duration data, and for monitoring the disease and T1D-related complications over time, as well as its potential in the exploration of the pathophysiological mechanisms that underlie this devastating and very widespread disease.

DATA AVAILABILITY STATEMENT

The raw data supporting the conclusion of this article will be made available by the authors, without undue reservation.

ETHICS STATEMENT

Ethical review and approval was not required for the study on human participants in accordance with the local legislation and institutional requirements. Written informed consent to participate in this study was provided by the participants' legal guardian/next of kin.

AUTHOR CONTRIBUTIONS

MS collected and shared data with United States site, conceptualized and performed the dynamical Bayesian inference, in addition to compiling and preparing results for publication. TH conceptualized and performed the directed transfer function analysis in addition to compiling and preparing results for publication. LI gave input and expertise on signal processing and analysis, and assisted with full preparation and review of the manuscript. LB provided expertise on data, disease state, and analytical decisions in addition to preparation and review of the manuscript. All authors contributed to review and revision of results and final manuscript.

FUNDING

This work was supported by grants from United States's National Science Foundation (NSF EPSCoR grant OIA 1632891 to LI) and Fondazione Cassa di Risparmio di Firenze (grants number 2015.0914 and 2017.0800).

REFERENCES

Aalkjaer, C., Boedtkjer, D., and Matchkov, V. (2011). Vasomotion - What Is Currently Thought? *Acta Physiol.* 202, 253–269. doi:10.1111/j.1748-1716.2011.02320.x

Adkinson, J. A., Karumuri, B., Hutson, T. N., Liu, R., Alamoudi, O., Vlachos, I., et al. (2018). Connectivity and Centrality Characteristics of the Epileptogenic Focus Using Directed Network Analysis. *IEEE Trans. Neural Syst. Rehabil. Eng.* 27 (1), 22–30. doi:10.1109/TNSRE.2018.2886211

Baccalá, L. A., de Brito, C. S., Takahashi, D. Y., and Sameshima, K. (1997). Unified Asymptotic Theory for All Partial Directed Coherence Forms. *Philos. Trans. A. Math. Phys. Eng. Sci.* 371, 20120158. doi:10.1098/rsta.2012.0158

Baccalá, L. A., Sameshima, K., and Takahashi, D. (2007). "Generalized Partial Directed Coherence," in 2007 15th International Conference on Digital Signal Processing, Cardiff, UK, 1-4 July 2007, 3, 163–166. doi:10.1109/icdsp.2007.4288544

Baccalá, L. A., Takahashi, D. Y., and Sameshima, K. (2016). Directed Transfer Function: Unified Asymptotic Theory and Some of its Implications. *IEEE Trans. Biomed. Eng.* 63 (12), 2450–2460. doi:10.1109/tbme.2016.2550199

Blinowska, K. J., Kamiński, M., Brzezicka, A., and Kamiński, J. (2013). Application of Directed Transfer Function and Network Formalism for the Assessment of Functional Connectivity in Working Memory Task. *Philos. Trans. A. Math. Phys. Eng. Sci.* 371, 20110614. doi:10.1098/rsta.2011.0614

Clemson, P., Lancaster, G., and Stefanovska, A. (2016). Reconstructing Time-Dependent Dynamics. *Proc. IEEE* 104 (2), 223–241. doi:10.1109/jproc.2015.2491262

Dampney, R. (2017). Central Mechanisms Regulating Coordinated Cardiovascular and Respiratory Function. *Oxford Res. Encyclopedia Neurosci.* 1, 1–27. doi:10.1093/acrefore/9780190264086.013.64

Doria, A., Niewczas, M. A., and Fiorina, P. (2012). Can Existing Drugs Approved for Other Indications Retard Renal Function Decline in Patients with Type 1 Diabetes and Nephropathy? *Semin. Nephrol.* 32 (5), 437–444. doi:10.1016/j.semnephrol.2012.07.006

Duggento, A., Stankovski, T., McClintock, P. V., and Stefanovska, A. (2012). Dynamical Bayesian Inference of Time-Evolving Interactions: from a Pair of Coupled Oscillators to Networks of Oscillators. *Phys. Rev. E Stat. Nonlin Soft Matter Phys.* 86, 061126. doi:10.1103/PhysRevE.86.061126

Eckberg, D. L. (2003). The Human Respiratory Gate. *J. Physiol.* 548 (2), 339–352. doi:10.1113/jphysiol.2002.037192

Faes, L., Porta, A., Cucino, R., Cerutti, S., Antolini, R., and Nollo, G. (2004). Causal Transfer Function Analysis to Describe Closed Loop Interactions between Cardiovascular and Cardiorespiratory Variability Signals. *Biol. Cybern.* 90 (6), 390–399. doi:10.1007/s00422-004-0488-0

Granger, C. W. J. (1969). Investigating Causal Relations by Econometric Models and Cross-Spectral Methods. *Econometrica* 37 (3), 424–438. doi:10.2307/1912791

Hilaire, G., and Pásaro, R. (2003). Genesis and Control of the Respiratory Rhythm in Adult Mammals. *News Physiol. Sci.* 18, 23–28. doi:10.1152/nips.01406.2002

Hutson, T., Pizarro, D., Pati, S., and Iasemidis, L. D. (2018). Predictability and Resetting in a Case of Convulsive Status Epilepticus. *Front. Neurol.* 9, 172–178. doi:10.3389/fneur.2018.00172

Hutson, T. N., Rezaei, F., Gautier, N. M., Indumathy, J., Glasscock, E., and Iasemidis, L. (2020). Directed Connectivity Analysis of the Neuro-Cardio- and Respiratory Systems Reveals Novel Biomarkers of Susceptibility to SUDEP. *IEEE Open J. Eng. Med. Biol.* 1, 301–311. doi:10.1109/ojemb.2020.3036544

Iatsenko, D., Bernjak, A., Stankovski, T., Shiogai, Y., Owen-Lynch, P. J., Clarkson, P. B., et al. (2013). Evolution of Cardiorespiratory Interactions with Age. *Philos. Trans. A. Math. Phys. Eng. Sci.* 371, 20110622. doi:10.1098/rsta.2011.0622

Iatsenko, D., McClintock, P. V. E., and Stefanovska, A. (2016). Extraction of Instantaneous Frequencies from Ridges in Time-Frequency Representations of Signals. *Signal. Process.* 125, 290–303. doi:10.1016/j.sigpro.2016.01.024

Iatsenko, D., McClintock, P. V. E., and Stefanovska, A. (2015). Linear and Synchrosqueezed Time-Frequency Representations Revisited: Overview, Standards of Use, Resolution, Reconstruction, Concentration, and Algorithms. *Digital Signal. Process.* 42, 1–26. doi:10.1016/j.dsp.2015.03.004

Jamšek, J., and Stefanovska, A. (2007). "The Cardio-Respiratory Couplings Observed in the LDF Signal Using Wavelet Bispectrum," in Proceedings of the 29th Annual International Conference of the IEEE EMBS, Lyon, France, 22-26 Aug. 2007, 2007, 4072–4075. doi:10.1109/IEMBS.2007.4353228

Kamiński, M., Ding, M., Truccolo, W. A., and Bressler, S. L. (2001). Evaluating Causal Relations in Neural Systems: Granger Causality, Directed Transfer Function and Statistical Assessment of Significance. *Biol. Cybern* 85 (2), 145–157. doi:10.1007/s004220000235

Kamiński, M., and Blinowska, K. J. (2014). Directed Transfer Function Is Not Influenced by Volume Conductionâ€"inexpedient Pre-Processing Should Be Avoided. *Front. Comput. Neurosci.* 8, 61. doi:10.3389/fncom.2014.00061

Klein, O. L., Krishnan, J. A., Glick, S., and Smith, L. J. (2010). Systematic Review of the Association between Lung Function and Type 2 Diabetes Mellitus. *Diabetic Med.* 27 (9), 977–987. doi:10.1111/j.1464-5491.2010.03073.x

Kralemann, B., Frühwirth, M., Pikovsky, A., Rosenblum, M., Kenner, T., Schaefer, J., et al. (2013). *In Vivo* cardiac Phase Response Curve Elucidates Human Respiratory Heart Rate Variability. *Nat. Commun.* 4, 2418. doi:10.1038/ncomms3418

Krishnan, B., Vlachos, I., Wang, Z. I., Mosher, J., Najm, I., Burgess, R., et al. (2015). Epileptic Focus Localization Based on Resting State Interictal MEG Recordings Is Feasible Irrespective of the Presence or Absence of Spikes. *Clin. Neurophysiol.* 126 (4), 667–674. doi:10.1016/j.clinph.2014.07.014

Kvandal, P., Landsverk, S. A., Bernjak, A., Stefanovska, A., Kvernmo, H. D., and Kirkebøen, K. A. (2006). Low-Frequency Oscillations of the Laser Doppler Perfusion Signal in Human Skin. *Microvasc. Res.* 72, 120–127. doi:10.1016/j.mvr.2006.05.006

Ogurtsova, K., da Rocha Fernandesda, J. D. R., Huang, Y., Linnenkamp, U., Guariguata, L., Cho, N. H., et al. (2017). IDF Diabetes Atlas: Global Estimates for the Prevalence of Diabetes for 2015 and 2040. *Diabetes Res. Clin. Pract.* 128, 40–50. doi:10.1016/j.diabres.2017.03.024

Palus, M., and Stefanovska, A. (2003). Direction of Coupling from Phases of Interacting Oscillators: An Information-Theoretic Approach. *Phys. Rev. E Stat. Nonlin Soft Matter Phys.* 67 (2), 055201. doi:10.1103/PhysRevE.67.055201

Penzel, T., Porta, A., Stefanovska, A., and Wessel, N. (2017). Recent Advances in Physiological Oscillations. *Physiol. Meas.* 38 (5), E1–E7. doi:10.1088/1361-6579/aa6780

Perrella, A., Sorelli, M., Giardini, F., Frassineti, L., Francia, P., and Bocchi, L. (2018). Wavelet Phase Coherence between the Microvascular Pulse Contour and the Respiratory Activity. *World Congress Med. Phys. Biomed. Eng.* 68 (2), 311–314. doi:10.1007/978-981-10-9038-7_58

Rosenblum, M. G., and Pikovsky, A. S. (2001). Detecting Direction of Coupling in Interacting Oscillators. *Phys. Rev. E* 64 (4), 045202. doi:10.1103/PhysRevE.64.045202

Sabesan, S., Good, L. B., Tsakalis, K. S., Spanias, A., Treiman, D. M., and Iasemidis, L. D. (2009). Information Flow and Application to Epileptogenic Focus Localization from Intracranial EEG. *IEEE Trans. Neural Syst. Rehabil. Eng.* 17 (3), 244–253. doi:10.1109/tnsre.2009.2023291

Shaffer, F., and Ginsberg, J. P. (2017). An Overview of Heart Rate Variability Metrics and Norms. *Front. Public Health* 5, 258. doi:10.3389/fpubh.2017.00258

Sheppard, L. W., Stefanovska, A., and McClintock, P. V. (2012). Testing for Time-Localized Coherence in Bivariate Data. *Phys. Rev. E Stat. Nonlin Soft Matter Phys.* 85, 046205–046282. doi:10.1103/PhysRevE.85.046205

Shiogai, Y., Stefanovska, A., and McClintock, P. V. (2010). Nonlinear Dynamics of Cardiovascular Ageing. *Phys. Rep.* 488 (2–3), 51–110. doi:10.1016/j.physrep.2009.12.003

Smith, J. C., Ellenberger, H. H., Ballanyi, K., Richter, D. W., and Feldman, J. L. (1991). Pre-Bötzinger Complex: A Brainstem Region that May Generate Respiratory Rhythm in Mammals. *Science* 254 (5032), 726–729. doi:10.1126/science.1683005

Söderström, T., Stefanovska, A., Veber, M., and Svensson, H. (2003). Involvement of Sympathetic Nerve Activity in Skin Blood Flow Oscillations in Humans. *Am. J. Physiology-Heart Circulatory Physiol.* 284, H1638–H1646. doi:10.1152/ajpheart.00826.2000

Stankovski, T., Duggento, A., McClintock, P. V., and Stefanovska, A. (2012). Inference of Time-Evolving Coupled Dynamical Systems in the Presence of Noise. *Phys. Rev. Lett.* 109 (2), 024101–024105. doi:10.1103/PhysRevLett.109.024101

Stankovski, T., McClintock, P. V. E., and Stefanovska, A. (2014). "Cardiorespiratory Coupling Functions, Synchronization and Ageing," in 2014 8th Conference of the European Study Group on Cardiovascular Oscillations (ESGCO), Trento, Italy, 25-28 May 2014. doi:10.1109/esgco.2014.6847579

Stefanovska, A., Bracic, M., and Kvernmo, H. D. (1999). Wavelet Analysis of Oscillations in the Peripheral Blood Circulation Measured by Laser Doppler Technique. *IEEE Trans. Biomed. Eng.* 46 (10), 1230–1239. doi:10.1109/10.790500

Stefanovska, A., and Hožič, M. (2000). Spatial Synchronization in the Human Cardiovascular System. *Prog. Theor. Phys. Suppl.* 139, 270–282. doi:10.1143/PTPS.139.270

Tankanag, A. V., Grinevich, A. A., Kirilina, T. V., Krasnikov, G. V., Piskunova, G. M., and Chemeris, N. K. (2014). Wavelet Phase Coherence Analysis of the Skin Blood Flow Oscillations in Human. *Microvasc. Res.* 95, 53–59. doi:10.1016/j.mvr.2014.07.003

Ticcinelli, V., Stankovski, T., Iatsenko, D., Bernjak, A., Bradbury, A. E., Gallagher, A. R., et al. (2017). Coherence and Coupling Functions Reveal Microvascular Impairment in Treated Hypertension. *Front. Physiol.* 8, 749. doi:10.3389/fphys.2017.00749

Ticcinelli, V., Stankovski, T., McClintock, P. V. E., and Stefanovska, A. (2015). "Ageing of the Couplings between Cardiac, Respiratory and Myogenic Activity in Humans," in 37th Annual International Conference of the IEEE Engineering in Medicine and Biology Society (EMBC), Milan, Italy, 25-29 Aug. 2015. doi:10.1109/embc.2015.7320093

Toledo, E., Akselrod, S., Pinhas, I., and Aravot, D. (2002). Does Synchronization Reflect a True Interaction in the Cardiorespiratory System? *Med. Eng. Phys.* 24, 45–52. doi:10.1016/S1350-4533(01)00114-X

Toppi, J., Mattia, D., Risetti, M., Formisano, R., Babiloni, F., and Astolfi, L. (2016). Testing the Significance of Connectivity Networks: Comparison of Different Assessing Procedures. *IEEE Trans. Biomed. Eng.* 63 (12), 2461–2473. doi:10.1109/TBME.2016.2621668

Vejmelka, M., and Palus, M. (2008). Inferring the Directionality of Coupling with Conditional Mutual Information. *Phys. Rev. E* 77 (2), 026214. doi:10.1103/PhysRevE.77.026214

Vlachos, I., Krishnan, B., Treiman, D. M., Tsakalis, K., Kugiumtzis, D., and Iasemidis, L. D. (2017). The Concept of Effective Inflow: Application to Interictal Localization of the Epileptogenic Focus from iEEG. *IEEE Trans. Biomed. Eng.* 64 (9), 2241–2252. doi:10.1109/tbme.2016.2633200

Wild, S., Roglic, G., Green, A., Sicree, R., and King, H. (2004). Global Prevalence of Diabetes: Estimates for the Year 2000 and Projections for 2030. *Diabetes Care* 27 (5), 1047–1053. doi:10.2337/diacare.27.5.1047

Conflict of Interest: The authors declare that the research was conducted in the absence of any commercial or financial relationships that could be construed as a potential conflict of interest.

Publisher's Note: All claims expressed in this article are solely those of the authors and do not necessarily represent those of their affiliated organizations, or those of the publisher, the editors and the reviewers. Any product that may be evaluated in this article, or claim that may be made by its manufacturer, is not guaranteed or endorsed by the publisher.

frontiers in Network Physiology

ORIGINAL RESEARCH
published: 24 March 2022
doi: 10.3389/fnetp.2022.844607

Body Weight Control Is a Key Element of Motor Control for Toddlers' Walking

Jennifer N. Kerkman, Coen S. Zandvoort, Andreas Daffertshofer† and Nadia Dominici*†*

Department of Human Movement Sciences, Faculty of Behavioural and Movement Sciences, Amsterdam Movement Science Institute (AMS) and Institute for Brain and Behaviour Amsterdam (iBBA), Vrije Universiteit Amsterdam, Amsterdam, Netherlands

New-borns can step when supported for about 70–80% of their own body weight. Gravity-related sensorimotor information might be an important factor in developing the ability to walk independently. We explored how body weight support alters motor control in toddlers during the first independent steps and in toddlers with about half a year of walking experience. Sixteen different typically developing children were assessed during (un) supported walking on a running treadmill. Electromyography of 18–24 bilateral leg and back muscles and vertical ground reaction forces were recorded. Strides were grouped into four levels of body weight support ranging from no (<10%), low (10–35%), medium (35–55%), and high (55–95%) support. We constructed muscle synergies and muscle networks and assessed differences between levels of support and between groups. In both groups, muscle activities could be described by four synergies. As expected, the mean activity decreased with body weight support around foot strikes. The younger first-steps group showed changes in the temporal pattern of the synergies when supported for more than 35% of their body weight. In this group, the muscle network was dense with several interlimb connections. Apparently, the ability to process gravity-related information is not fully developed at the onset of independent walking causing motor control to be fairly disperse. Synergy-specific sensitivity for unloading implies distinct neural mechanisms underlying (the emergence of) these synergies.

Keywords: motor development, muscle synergies, muscle networks, gravity, toddlers

OPEN ACCESS

Edited by:
Plamen Ch. Ivanov, Boston University, United States

Reviewed by:
Robert Hristovski, Saints Cyril and Methodius University of Skopje, North Macedonia
Sergi Garcia-Retortillo, Boston University, United States

****Correspondence:***
Nadia Dominici
n.dominici@vu.nl
Andreas Daffertshofer
a.daffertshofer@vu.nl

†These authors have contributed equally to this work

Specialty section:
This article was submitted to Systems Interactions and Organ Networks, a section of the journal Frontiers in Network Physiology

Received: *28 December 2021*
Accepted: *10 February 2022*
Published: *24 March 2022*

Citation:
Kerkman JN, Zandvoort CS, Daffertshofer A and Dominici N (2022) Body Weight Control Is a Key Element of Motor Control for Toddlers' Walking. Front. Netw. Physiol. 2:844607. doi: 10.3389/fnetp.2022.844607

INTRODUCTION

Gravity greatly affects early motor development as body weight control is of great importance for human locomotion (Dietz and Duysens, 2000; Duysens et al, 2000). New-borns can generate coordinated alternations of the lower limbs (Thelen and Fisher, 1983; Thelen et al, 1987; Dominici et al., 2011) but are not able to walk unsupported, yet. Since they can step when they only have to support about 20–40% of their own body weight, the integration of loading-related information to oppose gravity and the ability to control the own body weight appears crucial.

Loading of the limbs influences the walking pattern. It arguably modulates the efferent output (Harkema et al., 1997) *via* the activation of Ib-afferents that appears in weight acceptance muscles (Finch et al, 1991), i.e., in extensors. In adults, it enhances the activity of (anti-gravity) muscles during stance and delays the initiation of the swing phase (Duysens and Pearson, 1980). When adults are unloaded, muscle activity and kinetics change, while kinematic and spatiotemporal parameters are merely affected (Ivanenko et al, 2002; Ivanenko et al., 2004; Apte et al, 2018). In contrast, toddlers show clear changes in their kinematic coordination during their first independent steps, when supported for more than 30% of their body weight (Dominici et al, 2007). This suggests that the

reduction in gravity affects motor control during walking in toddlers differently than in adults (Ivanenko et al, 2007). Like in adults, in infants unloading may elongate the stance phase duration of walking (Pang and Yang, 2000) and infant stepping already renders adaptation to loading and other environmental changes (e.g., external perturbations, walking in different directions or at different speeds; Lam et al, 2003; Lam and Yang, 2000; Pang and Yang, 2000; Thelen and Cooke, 1987; Yang et al, 2005; Yang et al, 1998). Infants that are responsive to load changes tend to acquire functional motor skills at very young age (Vaal et al., 2000). This suggests the importance of early neurodevelopment to integrate load-related sensory information (Chang et al, 2006; Lacquaniti et al, 2012).

Stepping movements of infants are thought to emanate from embryonic interneurons in locomotor spinal circuitry (Forssberg, 1985; Lacquaniti et al., 2012). Inhibition of these spinal networks by descending cortico-spinal input appears mandatory to refine muscle activity (McGraw, 1940; Harkema et al., 1997; Grillner, 2011; Petersen et al., 2012; Vasudevan et al, 2016). Yet, whether this inhibition includes the sensorimotor integration of load-related information is unclear. If it does, one has to realise that neuromaturation is not completed at birth (McGraw, 1940; Berger et al, 1987; Vaughan et al, 2003), which may—in fact—explain why cortical control seems limited at a young age and the effect of unloading is different between toddlers and adults.

During the first year of life, motor behaviour develops gradually towards independent walking (McGraw, 1940). This development is accompanied by an increase in the number of locomotor muscle synergies from two to four, a number that persists in adults (Dominici et al., 2011). Locomotor muscle synergies are orchestrated patterns of co-activations in (groups of) muscles that are often considered essential for interlimb coordination, in particular, during walking. Here, we forward the hypothesis that the maturation of the cortico-spinal tract and, especially, that of afferent loading-related feedback are paramount for the emergence and control of the two supplementary locomotor synergies.

The contribution of neural circuits to motor control can be summarised as a network with a modular structure of neural structures and pathways. Network analysis has proven successful when mapping structural and functional connectivity in the brain (Sporns and Betzel, 2016), studying more general anatomy (Esteve-Altava et al, 2015; Molnar et al, 2017; Murphy et al., 2018; Powell et al., 2018) and unravelling physiologically interacting subsystems (Jeong et al, 2000; Bashan et al, 2012; Faes et al., 2014; Ivanov et al, 2016) or basic physiologic states (Liu et al, 2015; Ivanov et al, 2017; Rizzo et al, 2020). Casting such a diversity of subsystems in a network provides a comprehensive overview of many to many interactions (Bassett and Sporns, 2017; Balagué et al, 2020). Networks may "rewire" through changes in the task, coordination, or evolutional development (Lacquaniti et al, 2013) and, hence, can serve as an excellent means to identify corresponding changes in the (interactions of the) subsystems.

We altered body weight support (BWS) and explored its influence on motor output in toddlers at the onset of walking and in children about 6 months after their first independent steps. By this, we zoomed in on body weight control during the first experience of independent walking. We employed synergy analysis and determined the minimal number of locomotor muscle synergies. Expectedly, around the occurrence of the first independent steps, the two supplementary locomotor muscle synergies emerge and settle. We constructed functional networks with multi synergy-specific layers, so called muscle synergy networks (Kerkman et al, 2020). While traditional synergy analysis combines muscle groups by their co-activation, combining a set of synergies into a network provides direct insight into the interaction between them. As such, it allows for an encompassing study of functional changes in muscle activity during a transition in physiological coupling (Bashan et al, 2012; Ivanov et al., 2014).

We investigated the temporal activation patterns of locomotor muscle synergies as a function of BWS and complemented the analysis by muscle synergy networks to detail changes in spatial representation between groups. All children were likely to show a mature motor output that we expected to turn towards less mature temporal patterns in the presence of high BWS because of the unloading-induced lack of sensory feedback. This primarily applied to the younger, first-steps group. We predicted changes to mainly occur in the two just emerged (or still emerging) locomotor synergies (Dominici et al., 2011), in particular by their altered strength (or amplitude). We anticipated changes in muscle activation to be also visible in the spatial representation, or synergies' weightings, given the known changes in co-contraction within and between the legs around the onset of independent walking (Yang et al., 1998). Accordingly, we expected that muscle synergies were accompanied by densely connected networks containing several (functional) clusters associated with the BWS level.

MATERIALS AND METHODS

Participants

Sixteen typically developing children were included in this study (age range between 10.9 and 23.1 months, all born at term). Children were divided into two groups based on their walking experience, the FS and FS+ groups. In the FS group, we included toddlers during their first independent steps (within 3 weeks of walking experience) and in the FS+ group toddlers with around 6 months of walking experience. Seven children were measured two times (**Supplementary Table A.1**). Subjects visited the BabyGaitLab of the Department of Human Movement Sciences, Vrije Universiteit Amsterdam, wore a diaper during all measurements and walked without shoes. Familiarisation time was incorporated such that children had time to get comfortable to the lab and the experimenters. Ethical approval conform the Declaration of Helsinki was obtained at the Faculty of Behavioural and Movement Sciences (VCWE-2016–082) and parents signed the informed consent after a written and verbal explanation of the study.

To assess the first independent steps, we established regular contact with the parents that were monitoring their child's walking ability. Recording sessions were scheduled as soon as

the parents reported that the child was able to walk independently for at least four consecutive steps. This moment was defined as "walking onset" with which we determined the corresponding "walking age" (**Supplementary Table A.1**). We recorded the first unsupported steps in fourteen toddlers, (FS group, mean age 14.1, range (10.9–17.2) months old), and nine children were recorded about 6 months after the first independent steps (FS+ group, mean age 19.6, range (16.5–23.1) months old).

Setup

The experimental procedure was adapted to the children such that one experimenter and one parent were located next the child to reduce the risks of falling and to make sure that the child always felt comfortable. Children were encouraged to make steps while supported by their hands or their trunk above a running treadmill. An additional weighting trial was recorded during each session while the child was standing or sitting quietly on the non-running treadmill for at least 2 seconds.

Treadmill speed was tuned to elicit stepping movements and adjusted to a comfortable speed for the child based on his/her walking capacity; mean walking speed 0.7 ± 0.3 and 1.0 ± 0.3 km/h for the FS and FS+ group, respectively. To assess the influence of body support on the motor output, we recorded trials while an experimenter firmly supported the child's trunk with both hands while sitting on a bench behind the child and applied an approximately constant vertical force during several consecutive strides on the treadmill (**Supplementary Figure A.1 A**). In addition, the forearm of the experimenter holding the toddlers were supported to guarantee that an approximately constant vertical force was applied during consecutive strides and limit the possibility of imposing movements on the toddlers (**Supplementary Figure A.1 B**). Manual unloading was previously used in infants (Thelen and Cooke, 1987; Yang et al, 1998; Lam and Yang, 2000; Pang and Yang, 2000; Lam et al, 2003; Yang et al, 2005; Dominici et al., 2007; Vasudevan et al, 2016). It is a natural strategy adopted by parents to support their children during walking and avoids potential changes in the walking patterns through external equipment. The amount of body unloading was varied trial by trial to cover a wide range of levels from low until high level of BWS. Whenever feasible, additional trials were recorded while the experimenter held one or two hands or the trunk to stabilise the body during walking and supplied only limited vertical force, which was typically less than 20% of the body weight.

Data Acquisition

Kinematic and video data were collected with a Vicon motion capture system (10 Vicon Vero v2.2 cameras and Vue Vicon camera, Oxford, UK) and sampled at 100 Hz. Vertical ground reaction forces were recorded with a force plate and sampled at 1 kHz (N-Mill 60 × 150 cm, Motek Medical BV, Amsterdam, the Netherlands). Force sensors with a sensitivity of 3N were installed in the force platform to measure low body weight values.

Electromyography (EMG) was recorded of 18–24 bilateral leg and back muscles. The following set of muscles was recorded simultaneously from both body sides: tibialis anterior (TA), gastrocnemius medialis (GM), gastrocnemius lateralis (GL), soleus (SOL), rectus femoris (RF), vastus medialis (VM), vastus lateralis (VL), biceps femoris (BF), semitendinosus (SEM), tensor fascia latae (TFL), gluteus maximus (GLM), erector spinae recorded at L2 (ES). The skin was cleaned with alcohol and micro golden Cometa golden disc-electrodes pairs (acquisition area of 4 mm^2) were placed at the approximate location of the muscle with an inter-electrode distance of 10 mm. To minimise movement artefacts, pre-amplified EMG sensor units were attached with double tape to the skin of the child and fixed with elastic gauzes. EMG data were recorded using Cometa Mini Wave Wireless EMG system (Cometa srl, Italy) and sampled at 2 kHz after online band-pass filtering between 10 and 500 Hz. EMG, kinematic, force and video data were synchronised online.

Data Analysis

Kinematics

We analysed the video recordings frame by frame to identify the foot strike and foot off events of both feet. A gait cycle was defined from the right leg starting with the foot strike (0%) to the consecutive strike of the right foot (100%). We considered a sequence of strides successful if at least three consecutive strides were present. The first and last stride in each sequence as well as jumps or other interruptions were excluded from subsequent analyses.

Body Weight Support

The vertical force data were low pass filtered (12th order bi-directional Butterworth filter, cut-off frequency at 20 Hz) and the average amount of force was computed per gait cycle. We specified the amount of external BWS as the percentage reduction of the mean vertical force during a stride compared to the estimated body weight that we determined during the weighting trial. In our previous work (Dominici et al., 2007), we showed significant differences in foot coordination when toddlers were supported for more than 30% of their body weight, while adults and older children showed only minimal changes. Based on these results, four levels of BWS were selected. Per subject, gait cycles were hence grouped into four different BWS levels: no (<10%), low (10–35%), medium (35–55%) and high (55–95%) support (**Supplementary Table A.1**).

Electromyography

EMG signals were visually inspected and pre-processed by linearly interpolating ±150 ms epochs around peaks that exceeded ten times the signal's standard deviation. These data were high-pass filtered (30 Hz) with a second order bi-directional Butterworth filter and notch filtered (fourth order) to remove the power line artefact. Subsequently, EMG envelopes were extracted as modulus of the analytic signal (Myers et al., 2003; Boonstra and Breakspear, 2012). We applied a low-pass filter (second order Butterworth filter, cut-off frequency at 5 Hz) to obtain the slow-temporal changes in muscle activity. Finally, envelopes were time normalised to 200 samples per gait cycle (Ivanenko et al., 2005; Cappellini and Ivanenko, 2006; Dominici et al., 2011) and scaled to the mean amplitude per muscle of the low level of support (10–35% BWS). For every BWS level, we used the bilateral EMG

patterns for all individual subjects and pooled all gait cycles of all subjects to determine the grand averages for both groups.

Muscle Synergies

Muscle synergies were estimated using non-negative matrix factorisation (NNMF, Lee and Seung, 1999) by a multiplicative update algorithm over one to seven synergies. Briefly, NNMF decomposes the original EMG matrix into (small number of) temporal patterns and weighting coefficients:

$$EMG = \sum_{i=1}^{n} P_i \cdot W_i + error$$

where P represents the temporal activation patterns of the synergies (n × s matrix, where n denotes a pre-defined number of synergies, n ≤ m, where m is the number of muscles) and W the synergies' weighting coefficients (m × n matrix).

Per group, we estimated muscle synergies for the grand-averaged EMG activities of the four BWS levels and concatenated them to obtain a (s × k) × m matrix, where s = 200 is the number of samples, m = 24 the number of muscles and k = 4 the levels of body weight support, yielding a 800 × 24 matrix. In this form, our NNMF resulted in temporal patterns per BWS level and fixed synergies' weighting coefficients across the levels of support. We also decomposed the original EMG signals for all individual subjects, for which we used the averaged EMG activities per subject for every BWS level; the corresponding results can be found in **Supplementary Figure A.2**. The reconstruction quality of the synergies was determined as the contribution of the synergies to the Frobenius norm λ of the original signal (EMG):

$$\lambda^{(n)} = \left(1 - \frac{\|EMG - W^{(n)}P^{(n)}\|_F^2}{\|EMG\|_F^2}\right) \times 100\%$$

The number of synergies was selected such that the reconstruction of the synergies should exceed 88% of the Frobenius norm of the original signal per level of support (Zandvoort et al, 2019; Kerkman et al., 2020; Bach et al., 2021).

For every resulting synergy, the mean amplitude of the temporal pattern was determined for every BWS level relative to the no-support level to assess changes in the amount of muscle activity across the gait cycle. We normalised the amplitude of the temporal pattern to the maximum value over the gait cycle to discard amplitude effects and to verify whether changes in the temporal pattern were induced by a change in the waveform itself. An enlarged normalised amplitude indicated a longer peak duration of the temporal pattern. Finally, to quantify the similarity between temporal patterns independent of amplitude, we estimated the circular cross correlation (Oppenheim et al., 2001) between different levels of support.

Muscle Synergy Networks

Network analysis (Bullmore and Sporns, 2009; Betzel and Bassett, 2017) was performed to compare the spatial representation of the muscle synergies between groups (Boonstra et al., 2015; Kerkman et al., 2018; Murphy et al., 2018). We constructed muscle networks (Kerkman et al., 2020) for which we first scaled the synergies' weightings coefficients by the sum of the integrals of the temporal patterns to correct for overall amplitude effects. Using the outer product of the scaled synergies' weightings, we obtained a 24 × 24 connectivity matrix per synergy. A bipartite muscle network (Murphy et al., 2018) was created, in which muscles served as nodes and where edges were given as the afore-defined weighted appearance of two muscles in the same synergy (i.e., the elements of the connectivity matrix). The connectivity matrices of all synergies were thresholded with an absolute threshold of $5{\cdot}10^{-5}$ and we determined the density and the transitivity of every synergy network (Kerkman et al., 2020). Network density and transitivity served to quantify (changes of) network topology in terms of the number and clustering of connections, respectively (Rubinov and Sporns, 2010).

RESULTS

Effect of Body Weight Support on Muscle Activity

The mean muscle activity over subjects per level of support showed a decreased amplitude and increased duration of the peak activity of several—mainly upper leg—muscles active at the foot strikes when weight support was increased (**Figure 1**). This effect was most pronounced in the FS group between low and medium BWS.

Effect of Body Weight Support on Muscle Synergies

For both groups, four synergies were required to cover 88% or more of the original signal's Frobenius norm (**Table 1**).

Toddlers in the FS group displayed four synergies, of which two were primarily active during the right (S1) and left foot strike (S3), while the other two were active during the stance phase of the right (S2) and left leg (S4, **Figure 2A**). These right and left synergies appeared to be symmetric by mean of contributions of muscles of the right and left side (**Figure 2B**). The mean amplitude of the foot strike synergies decreased incrementally with respect to no support with unloading: −17, −39 and −49%, and −36, −51 and −62% for S1 and S3, respectively, whereas the mean amplitude in S2 mainly increased (+13, +6 and −2%) and in S4 remained almost constant between low, medium and high support (+25, +23 and +22%, respectively; **Figure 2C**). Next to the change in amplitude, the shape of the temporal patterns of S3 and S4 changed substantially: The circular cross correlation between no and high and low and high support decreased to 0.959 and 0.944 in S3, and in S4 between no and medium to 0.969 and between no and high support to 0.934 (**Figure 2E**). These changes seemingly reflected an elongated peak duration (**Figure 2D**).

The FS+ group also showed four synergies, which were like those in the FS group (**Figure 3**). Again, there was a foot strike synergy for both right and left leg (S1 and S3) and two synergies active during the right and left stance phase (S2 and S4). The mean amplitude of the temporal pattern decreased compared to

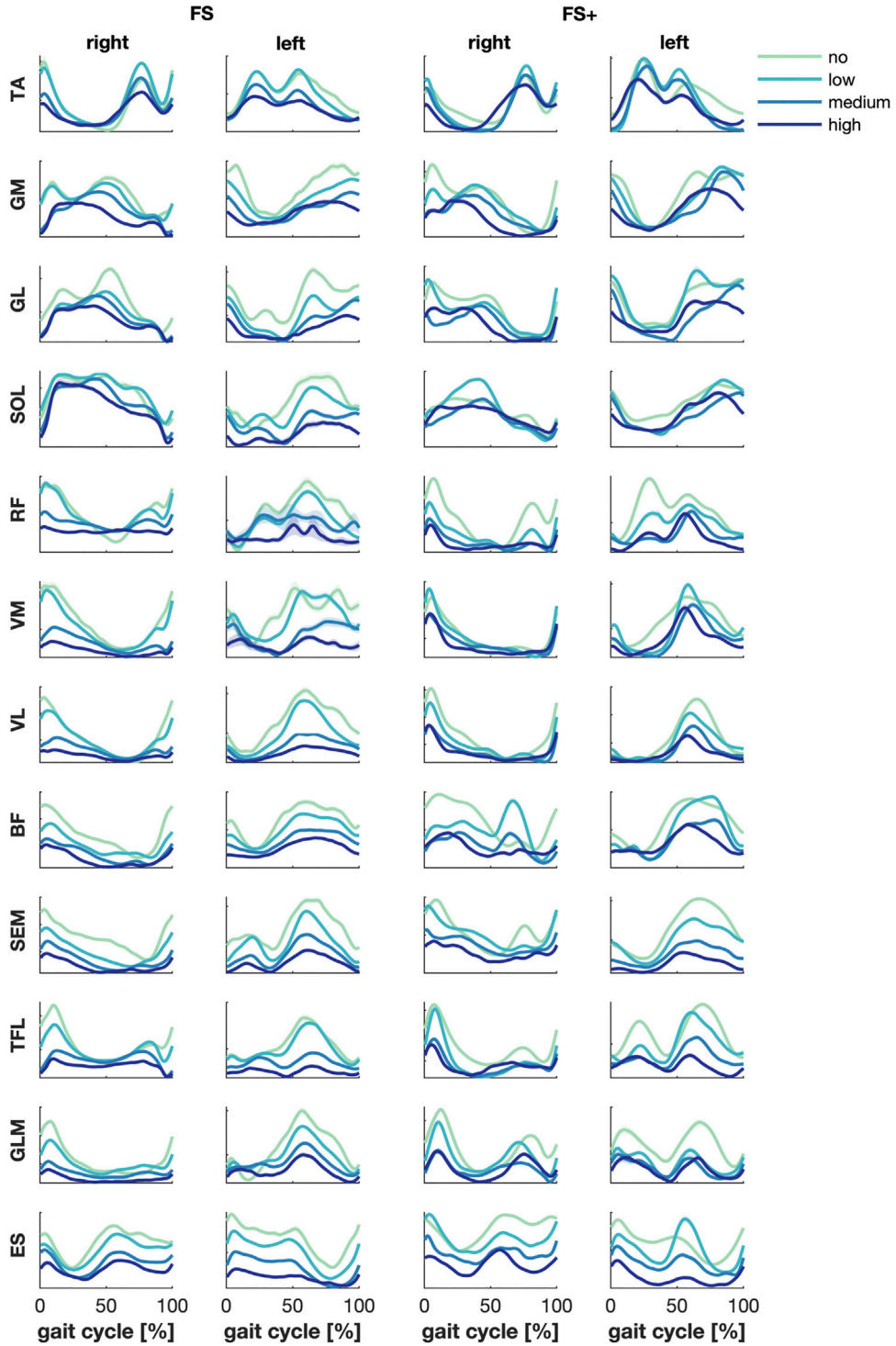

FIGURE 1 | Muscle activities—grand average per group. Green, cyan, blue and dark blue represent no, low, medium, and high body weight support, respectively. Error patches represent the standard errors of the mean, which turned out very small.

the no BWS condition in S1 and S3 (−18, −37 and −49%, and −19, −44 and −67% in S1 and S3, respectively), while the mean amplitude of S2 and S4 increased (+8, +7 and +14%, and +2, +7, and +25%) in low, medium and high BWS, respectively. The similarity in shape of the temporal patterns (circular cross correlation) decreased to a minimum of 0.966 in S3 between no and high BWS, which implies that the temporal pattern barely changed in waveform in the FS+ group.

TABLE 1 | Contribution of the synergies to the Frobenius norm (λ) of the original concatenated EMGs. λ was computed across all conditions as well as per level of support.

Group	# of synergies	Across conditions (%)	No (%)	Low (%)	Medium (%)	High (%)
FS	4	89	88	89	90	92
FS+	4	89	89	88	90	90

Effect of Body Weight Support on Muscle Synergy Networks

The spatial representation of the muscle synergies of both groups revealed similarities in their muscle networks (**Figures 2F** and **3F**). Yet, their network characteristics differed: the number of connections (density) of one muscle to another, i.e., whether muscles were active in the same synergy, was larger in FS compared to FS+ across synergies: +9, +70, +10 and +45%. Especially in the foot strike synergies (S1 and S3), we found a larger number of interlimb connections in the FS compared to the FS+ group. The transitivity was higher in FS compared to FS+ in all synergies except of S3 indicating more clusters in the synergy networks in toddlers at the onset of walking (cf. **Table 2**).

DISCUSSION

For the currently study, we asserted the importance of body weight control in the development of independent walking. As expected, we found adaptations in temporal patterns of the muscle synergies when toddlers around their first independent steps were supported. We also found differences between the spatial representation between toddlers at the onset of walking and with half a year of walking experience. The motor pattern of these toddlers were similar to those of older children and adults as reported in the literature (Ivanenko et al., 2004; Ivanenko et al., 2005; Yokoyama et al, 2016). Both groups revealed four synergies with separate foot strike and stance phase synergies; the mean amplitude of the foot strike synergies decreased with increasing body weight support. It seems that, at the onset of walking, the coordination of muscle activity is reasonably developed allowing for independent walking, presuming a sufficient amount and quality of sensory feedback. However, the shape of the temporal pattern of the left foot strike and left stance phase synergies changed in toddlers at their first independent steps suggesting that the motor pattern in toddlers depends on the amount of support, while this dependency may be absent in older children, similar to adults (Ivanenko et al., 2004). Differences in spatial representation identified here demonstrated higher connectivity in the FS group compared to the FS+ group. This might have been caused by increased co-contractions and less specified contributions of muscles to the muscle synergies. The changes and differences arguably imply that the ability to control the body weight is a key element in the development of independent walking in children. In addition, the large number of interlimb connections found in the FS group are compatible with the idea that spinal network of interneurons project to multiple motor neurons pools, including distant motor neurons pools (Levine et al., 2014; Takei et al., 2017; Hug et al., 2021). These spinal networks seem to be largely involved in the coordination of toddler's muscle activity during their first independent steps. Our results are in line with recent studies showing task-specific connectivity in the neuromuscular system during postural and walking tasks (Boonstra et al., 2015; Conway et al., 1995; Farmer et al., 1993; Kerkman et al., 2018; 2020).

Even when toddlers are only able to walk a few steps unsupported, four muscle synergies suffice to explain muscle activities during walking. This agrees with findings in older children and adults (Dominici et al., 2011). Here, the shapes of the temporal patterns were consistent across BWS levels. The amplitudes of the foot strike synergies, however, were clearly affected by BWS. This was probably due to a decrease in muscle effort to support the own body weight. It seems that the primary walking pattern is present at the onset of walking but that it can be modulated to account for body weight control requirements.

Despite the growing interest in the application of BWS in pediatric rehabilitation until now just few studies investigated the effect of body weight unloading in young children. We found changes in the muscle synergies of toddlers at the onset of independent walking in the shape of some of the temporal patterns when supported for more than 35%. This indicates that unloading affects motor control in these children. When unloaded, the available gravity-related information that can be transferred via Ib-afferents is reduced (Harkema et al., 1997; Pang and Yang, 2000). In toddlers at the onset of independent walking, the sensitivity and gain of the load-receptors might not be fully developed, and the motor system may not be able to account for a change in body weight support by modulating the gain of the feedback. The inability to integrate these load changes is supported by the observed overshoot of the foot in the swing phase in this age group (Dominici et al., 2007). When toddlers are unloaded for more than one third of their body weight, the information received by the neuromuscular system seems insufficient to preserve the primary motor pattern for walking, while this effect on motor control disappears in older children and adults when unloaded (Ivanenko et al., 2004).

BWS training has shown positive effects in the rehabilitation after stroke (Sale et al., 2012; Moraru and Onose, 2014) and spinal cord injury (Hubli and Dietz, 2013), and in the presence of Parkinson's disease (Miyai et al., 2000; Picelli et al., 2013). In children with cerebral palsy, however, appear less promising (Damiano and DeJong 2009; Mutlu et al., 2009; Willoughby et al., 2009). Whether or not the diversity of finding in this degenerative disease has been cause by the age range of include patients remain opaque. Our results suggest that targeting load-regulating mechanisms in children should be most effective at very early age.

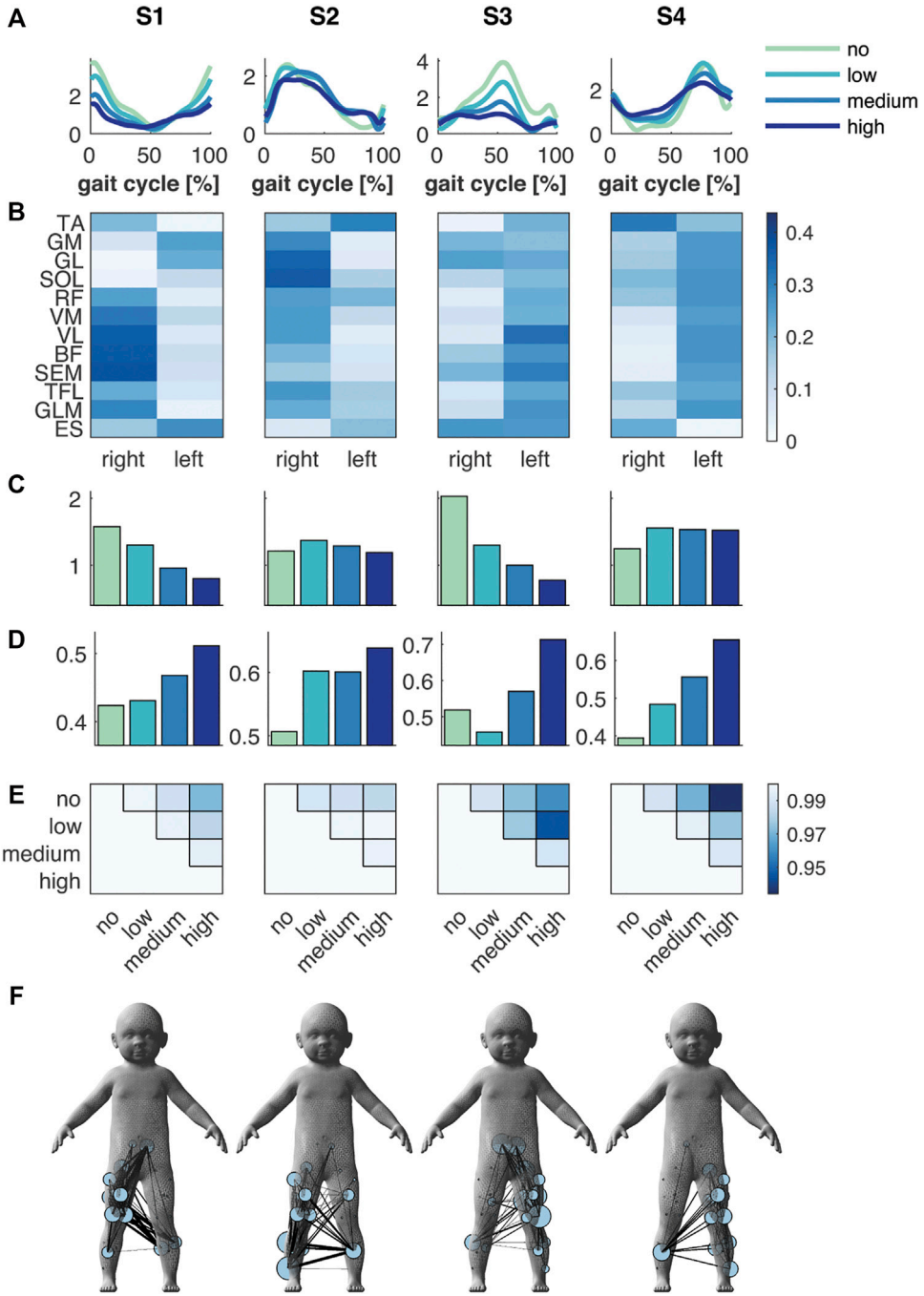

FIGURE 2 | Muscle synergies and muscle synergy network in the FS group. **(A)** Temporal patterns and **(B)** synergies' weighting coefficients. **(C)** Mean amplitude and **(D)** normalised mean amplitude of the synergy temporal pattern over the gait cycle, and **(E)** the circular cross correlation between the temporal pattern of the different levels of support. **(F)** Muscle synergy network on the toddler's body mesh (MakeHuman 2018) based on the synergies' weightings; node size represents the muscle degree and edge thickness the connection strength between muscles. Green, cyan, blue and dark blue represent no, low, medium, and high body weight support, respectively, in **(A,C,D)**.

Striking is that only the newly developed synergies that are active during the foot strikes decreased in amplitude when unloaded. This suggests a phase-specific effect of body weight unloading, which has also been found in adults (Finch et al., 1991; Harkema et al., 1997; Sylos-Labini et al, 2014). The foot strike synergies may have a different origin than the stance phase synergies and they may be differently controlled. This supports a synergy-specific sensitivity for changes in the amount of body weight control. Some synergies may need proprioceptive feedback in the modulation of the synergy,

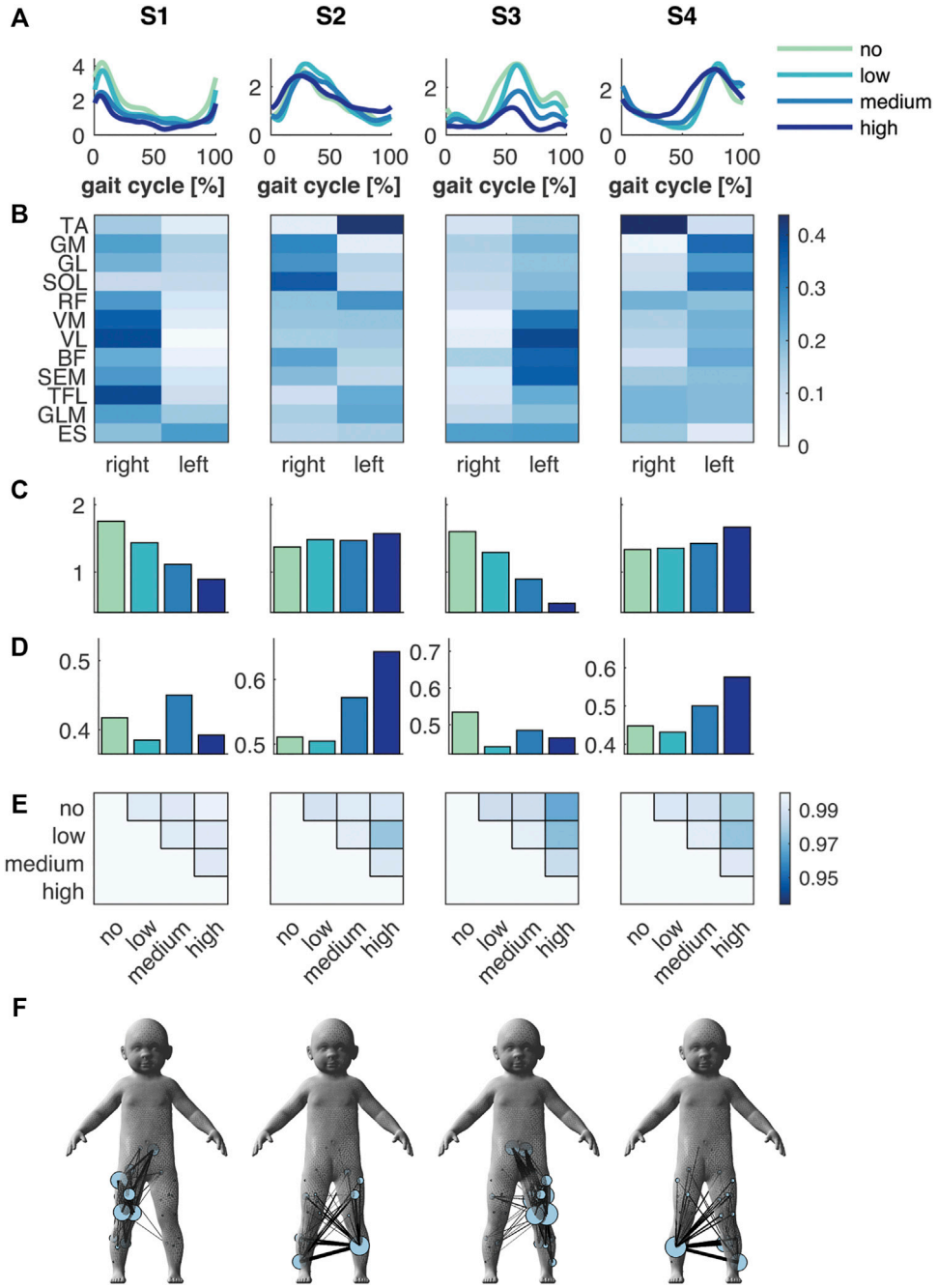

FIGURE 3 | Muscle synergies and muscle synergy network in the FS+ group. **(A)** Temporal patterns and **(B)** synergies' weighting coefficients. **(C)** Mean amplitude and **(D)** normalised mean amplitude of the synergy temporal pattern over the gait cycle, and **(E)** the circular cross correlation between the temporal pattern of the different levels of support. **(F)** Muscle synergy network on the toddler's body mesh (MakeHuman 2018) based on the synergies' weightings; node size represents the muscle degree and edge thickness the connection strength between muscles. Green, cyan, blue and dark blue represent no, low, medium, and high body weight support, respectively, in **(A,C,D)**.

while others operate without any proprioceptive or supra-spinal input (Grillner, 1973; Harkema et al., 1997) and, hence, remain largely unaltered despite of weight-bearing experiences during the first year (Yang et al, 2019). Cortico-muscular coherence found during the double support phase (Roeder et al., 2018) may suggest that the foot strike synergies are cortically controlled, while the other synergies may be controlled by brainstem and spinal networks (Labini et al., 2011; Lacquaniti et al., 2012). This arguably points at distinct neural origins of the synergies with different functions and sensitivities for gravity-related information.

TABLE 2 | Network density and transitivity per synergy for FS and FS+ Transitivity is 10^{-5}.

Group	Network metric	S1	S2	S3	S4
FS	density	0.21	0.23	0.28	0.21
FS+		0.19	0.13	0.15	0.15
FS	transitivity	7.9	5.2	4.6	5.2
FS+		5.8	3.8	5.5	2.8

By comparing toddlers at the onset of walking and half a year later, we found a changed spatial representation with a less densely connected muscle network in the younger group. Despite of similar muscle synergy activity patterns, the muscle clustering, and the contribution of muscles within the synergies evolved after a child started to walk independently. Yet, this reorganisation did not merely result from unloading (**Supplementary Figure A.3**), and changes in the networks were not consistent across synergies (e.g., no increased density in FS in all synergies). Hence, they could be the result of a combination of a decrease in co-contraction (Teulier et al, 2012) and a phase-specific reorganisation of muscle clustering.

Limitations

The children involved in the current study were small, yielding limited space for EMG electrodes. Recall that we recorded multi-EMGs were recorded simultaneously. Potentially that may jeopardise data quality due to electrical crosstalk between adjacent muscles. However, the small size of the EMG electrodes used in our recordings and the chosen interelectrode distance should have minimised the pickup from adjacent muscles. Although it is not possible to separate co-activation from crosstalk in nearby muscles, muscle synergy analysis can identify whether a muscle is activated independent from a nearby muscle even in the presence of such crosstalk. Previous studies reported that if crosstalk did exist, it would likely have affected only the synergies' weighting coefficients and not the number of muscle synergies or the temporal patterns (Ivanenko et al., 2004; Chvatal and Ting, 2013). Despite a proper skin preparation and EMG electrodes attachment, motion artefacts were still observed during foot strike in some of the lower limb muscles (TA, SOL). A pre-processing step was performed to the EMG signals to minimise these artefacts.

Muscle synergies are often estimated per subject (e.g., Ivanenko et al., 2004; Dominici et al., 2011). We must admit that in our toddlers' group, it was quite difficult to collect EMG data from all muscles with sufficient steps in the four different BWS levels. To accommodate this, we averaged all steps across subjects. One may question the degree to which this grand average is representative for muscle synergies at single subject level. As expected, the single subject results were variable. Yet, when temporal patterns and synergies' weightings coefficients were averaged over subjects, the results revealed similar temporal and spatial characteristics compared to the grand average results (**Supplementary Figure A.2**).

CONCLUSION

Our results confirm that the ability for toddlers to control their own body weight is important in motor control during walking. Being at the onset of walking implies that the motor system can control independent walking. Yet, control processes continue to undergo modifications, arguably to integrate sensory feedback. Here, this was reflected in an amplitude decrease of the foot strike synergies when supported, i.e., a synergy-specific sensitivity of unloading. This can be a result of distinct neural mechanisms that may underlie the formation of synergies. Toddlers at the onset of walking showed a reorganisation of the spatial grouping of the muscles presumably due to immature motor control resulting in high co-contraction and less muscle-specific activity during the gait cycle. Unloading-induced motor adaptation was pronounced in these children when supported for more than 35% of their body weight. Apparently, motor control at the onset of walking is not fully developed, yet, and is modulated by loading-related feedback stressing its importance in the motor development of independent walking.

DATA AVAILABILITY STATEMENT

The data that support the findings of this study are available on request from the corresponding authors.

ETHICS STATEMENT

The studies involving human participants were reviewed and approved by the Faculty of Behavioural and Movement Sciences, Vrije Universiteit Amsterdam (VCWE-2016-082). Written informed consent to participate in this study was provided by the participants' legal guardian/next of kin.

AUTHOR CONTRIBUTIONS

JK, AD, and ND designed the experiment. JK, CZ, and ND conducted the recordings. JK analysed the data. The first draft of the manuscript was written by JK and all authors commented on previous versions of the manuscript. All authors read and approved the final manuscript.

FUNDING

This project has received funding from the European Research Council (ERC) under the European Union's Horizon 2020 research and innovation programme under grant agreement No. 715945 Learn2Walk and from the Dutch Organisation for Scientific Research (NWO) VIDI grant (016.156.346 FirSTeps).

ACKNOWLEDGMENTS

We would like to thank Annike Bekius with her help during data acquisition and the parents and children for their participation in the study.

SUPPLEMENTARY MATERIAL

The Supplementary Material for this article can be found online at: https://www.frontiersin.org/articles/10.3389/fnetp.2022.844607/full#supplementary-material

REFERENCES

Apte, S., Plooij, M., and Vallery, H. (2018). Influence of Body Weight Unloading on Human Gait Characteristics: a Systematic Review. *J. Neuroengineering Rehabil.* 15 (1), 53. doi:10.1186/s12984-018-0380-0

Bach, M. M., Daffertshofer, A., and Dominici, N. (2021). Muscle Synergies in Children Walking and Running on a Treadmill. *Front. Hum. Neurosci.* 15, 637157. doi:10.3389/fnhum.2021.637157

Balagué, N., Hristovski, R., Almarcha, M., Garcia-Retortillo, S., and Ivanov, P. C. (2020). Network Physiology of Exercise: Vision and Perspectives. *Front. Physiol.* 11, 611550. doi:10.3389/fphys.2020.611550

Bashan, A., Bartsch, R. P., Kantelhardt, J. W., Havlin, S., and Ivanov, P. C. (2012). Network Physiology Reveals Relations between Network Topology and Physiological Function. *Nat. Commun.* 3 (702), 10–1038. doi:10.1038/ncomms1705

Bassett, D. S., and Sporns, O. (2017). Network Neuroscience. *Nat. Neurosci.* 20 (3), 353–364. doi:10.1038/nn.4502

Berger, W., Quintern, J., and Dietz, V. (1987). Afferent and Efferent Control of Stance and Gait: Developmental Changes in Children. *Electroencephalography Clin. Neurophysiol.* 66 (3), 244–252. doi:10.1016/0013-4694(87)90073-3

Betzel, R. F., and Bassett, D. S. (2017). Generative Models for Network Neuroscience: Prospects and Promise. *J. R. Soc. Interf.* 14 (136), 20170623. doi:10.1098/rsif.2017.0623

Boonstra, T. W., and Breakspear, M. (2012). Neural Mechanisms of Intermuscular Coherence: Implications for the Rectification of Surface Electromyography. *J. Neurophysiol.* 107 (3), 796–807. doi:10.1152/jn.00066.2011

Boonstra, T. W., Danna-Dos-Santos, A., Xie, H.-B., Roerdink, M., Stins, J. F., and Breakspear, M. (2015). Muscle Networks: Connectivity Analysis of EMG Activity during Postural Control. *Sci. Rep.* 5, 17830. doi:10.1038/srep17830

Bullmore, E., and Sporns, O. (2009). Complex Brain Networks: Graph Theoretical Analysis of Structural and Functional Systems. *Nat. Rev. Neurosci.* 10 (3), 186–198. doi:10.1038/nrn2575

Cappellini, G., Ivanenko, Y. P., Poppele, R. E., and Lacquaniti, F. (2006). Motor Patterns in Human Walking and Running. *J. Neurophysiol.* 95 (6), 3426–3437. doi:10.1152/jn.00081.2006

Chang, C.-L., Kubo, M., Buzzi, U., and Ulrich, B. (2006). Early Changes in Muscle Activation Patterns of Toddlers during Walking. *Infant Behav. Development* 29 (2), 175–188. doi:10.1016/j.infbeh.2005.10.001

Chvatal, S. A., and Ting, L. H. (2013). Common Muscle Synergies for Balance and Walking. *Front. Comput. Neurosci.* 7, 48. doi:10.3389/fncom.2013.00048

Conway, B. A., Halliday, D. M., Farmer, S. F., Shahani, U., Maas, P., Weir, A. I., et al. (1995). Synchronization between Motor Cortex and Spinal Motoneuronal Pool during the Performance of a Maintained Motor Task in Man. *J. Physiol.* 489 (3), 917–924. doi:10.1113/jphysiol.1995.sp021104

Damiano, D. L., and DeJong, S. L. (2009). A Systematic Review of the Effectiveness of Treadmill Training and Body Weight Support in Pediatric Rehabilitation. *J. Neurol. Phys. Ther. JNPT* 33 (1), 27–44. doi:10.1097/npt.0b013e31819800e2

Dietz, V., and Duysens, J. (2000). Significance of Load Receptor Input during Locomotion: a Review. *Gait & Posture* 11 (2), 102–110. doi:10.1016/s0966-6362(99)00052-1

Dominici, N., Ivanenko, Y. P., Cappellini, G., d'Avella, A., Mondì, V., Cicchese, M., et al. (2011). Locomotor Primitives in Newborn Babies and Their Development. *Science* 334 (6058), 997–999. doi:10.1126/science.1210617

Dominici, N., Ivanenko, Y. P., and Lacquaniti, F. (2007). Control of Foot Trajectory in Walking Toddlers: Adaptation to Load Changes. *J. Neurophysiol.* 97 (4), 2790–2801. doi:10.1152/jn.00262.2006

Duysens, J., Clarac, F., and Cruse, H. (2000). Load-regulating Mechanisms in Gait and Posture: Comparative Aspects. *Physiol. Rev.* 80 (1), 83–133. doi:10.1152/physrev.2000.80.1.83

Duysens, J., and Pearson, K. G. (1980). Inhibition of Flexor Burst Generation by Loading Ankle Extensor Muscles in Walking Cats. *Brain Res.* 187 (2), 321–332. doi:10.1016/0006-8993(80)90206-1

Esteve-Altava, B., Diogo, R., Smith, C., Boughner, J. C., and Rasskin-Gutman, D. (2015). Anatomical Networks Reveal the Musculoskeletal Modularity of the Human Head. *Sci. Rep.* 5, 8298. doi:10.1038/srep08298

Faes, L., Nollo, G., Jurysta, F., and Marinazzo, D. (2014). Information Dynamics of Brain-Heart Physiological Networks during Sleep. *New J. Phys.* 16 (10), 105005. doi:10.1088/1367-2630/16/10/105005

Farmer, S. F., Bremner, F. D., Halliday, D. M., Rosenberg, J. R., and Stephens, J. A. (1993). The Frequency Content of Common Synaptic Inputs to Motoneurones Studied during Voluntary Isometric Contraction in Man. *J. Physiol.* 470 (1), 127–155. doi:10.1113/jphysiol.1993.sp019851

Finch, L., Barbeau, H., and Arsenault, B. (1991). Influence of Body Weight Support on normal Human Gait: Development of a Gait Retraining Strategy. *Phys. Ther.* 71 (11), 842–855. doi:10.1093/ptj/71.11.842

Forssberg, H. (1985). Ontogeny of Human Locomotor Control I. Infant Stepping, Supported Locomotion and Transition to Independent Locomotion. *Exp. Brain Res.* 57 (3), 480–493. doi:10.1007/bf00237835

Grillner, S. (2011). Human Locomotor Circuits Conform. *Science* 334 (6058), 912–913. doi:10.1126/science.1214778

Grillner, S. (1973). *Locomotion in the Spinal catControl of Posture and Locomotion*. Boston, MA: Springer, 515–535. doi:10.1007/978-1-4613-4547-3_42

Harkema, S. J., Hurley, S. L., Patel, U. K., Requejo, P. S., Dobkin, B. H., and Edgerton, V. R. (1997). Human Lumbosacral Spinal Cord Interprets Loading during Stepping. *J. Neurophysiol.* 77 (2), 797–811. doi:10.1152/jn.1997.77.2.797

Hubli, M., and Dietz, V. (2013). The Physiological Basis of Neurorehabilitation - Locomotor Training after Spinal Cord Injury. *J. NeuroEngineering Rehabil.* 10, 5. doi:10.1186/1743-0003-10-5

Hug, F., Avrillon, S., Sarcher, A., Del Vecchio, A., and Farina, D. (2021). Networks of Common Inputs to Motor Neurons of the Lower Limb Reveal Neural Synergies that Only Partly Overlap with Muscle Innervation. *bioRxiv*. doi:10.1101/2021.10.13.460524

Ivanenko, Y. P., Cappellini, G., Dominici, N., Poppele, R. E., and Lacquaniti, F. (2005). Coordination of Locomotion with Voluntary Movements in Humans. *J. Neurosci.* 25 (31), 7238–7253. doi:10.1523/JNEUROSCI.1327-05.2005

Ivanenko, Y. P., Dominici, N., and Lacquaniti, F. (2007). Development of Independent Walking in Toddlers. *Exerc. Sport Sci. Rev.* 35 (2), 67–73. doi:10.1249/JES.0b013e31803eafa8

Ivanenko, Y. P., Grasso, R., Macellari, V., and Lacquaniti, F. (2002). Control of Foot Trajectory in Human Locomotion: Role of Ground Contact Forces in Simulated Reduced Gravity. *J. Neurophysiol.* 87 (6), 3070–3089. doi:10.1152/jn.2002.87.6.3070

Ivanenko, Y. P., Poppele, R. E., and Lacquaniti, F. (2004). Five Basic Muscle Activation Patterns Account for Muscle Activity during Human Locomotion. *J. Physiol.* 556 (1), 267–282. doi:10.1113/jphysiol.2003.057174

Ivanov, P. C., Bartsch, R. P., and Bartsch, R. P. (2016). Focus on the Emerging New fields of Network Physiology and Network Medicine. *New J. Phys.* 18 (10), 100201. doi:10.1088/1367-2630/18/10/100201

Ivanov, P. C., P, Ch., and Bartsch, R. P. (2014). "Network Physiology: Mapping Interactions between Networks of Physiologic Networks," in *Networks of Networks: The Last Frontier of Complexity*. Editors G. D'Agostino and A. Scala (Cham: Springer International Publishing), Chapter10, 203–222. doi:10.1007/978-3-319-03518-5_10

Ivanov, P. C., Lin, A., Bartsch, R. P., and Bartsch, R. P. (2017). "Network Physiology: From Neural Plasticity to Organ Network Interactions," in *Physics, Engineering and the Life Sciences*. Editors G. Mantica, R. Stoop, and S. Stramaglia (Cham: Springer), 145–165. doi:10.1007/978-3-319-47810-4_12

Jeong, H., Tombor, B., Albert, R., Oltvai, Z. N., and Barabási, A.-L. (2000). The Large-Scale Organization of Metabolic Networks. *Nature* 407 (6804), 651–654. doi:10.1038/35036627

Kerkman, J. N., Bekius, A., Boonstra, T. W., Daffertshofer, A., and Dominici, N. (2020). Muscle Synergies and Coherence Networks Reflect Different Modes of Coordination during Walking. *Front. Physiol.* 11 (11), 751. doi:10.3389/fphys.2020.00751

Kerkman, J. N., Daffertshofer, A., Gollo, L. L., Breakspear, M., and Boonstra, T. W. (2018). Network Structure of the Human Musculoskeletal System Shapes Neural Interactions on Multiple Time Scales. *Sci. Adv.* 4 (6), eaat0497. doi:10.1126/sciadv.aat0497

Labini, F. S., Ivanenko, Y. P., Cappellini, G., Gravano, S., and Lacquaniti, F. (2011). Smooth Changes in the EMG Patterns during Gait Transitions under Body Weight Unloading. *J. Neurophysiol.* 106 (3), 1525–1536. doi:10.1152/jn.00160.2011

Lacquaniti, F., Ivanenko, Y. P., d'Avella, A., Zelik, K. E., and Zago, M. (2013). Evolutionary and Developmental Modules. *Front. Comput. Neurosci.* 7, 61. doi:10.3389/fncom.2013.00061

Lacquaniti, F., Ivanenko, Y. P., and Zago, M. (2012). Development of Human Locomotion. *Curr. Opin. Neurobiol.* 22 (5), 822–828. doi:10.1016/j.conb.2012.03.012

Lam, T., Wolstenholme, C., and Yang, J. F. (2003). How Do Infants Adapt to Loading of the Limb during the Swing Phase of Stepping? *J. Neurophysiol.* 89 (4), 1920–1928. doi:10.1152/jn.01030.2002

Lamb, T., and Yang, J. F. (2000). Could Different Directions of Infant Stepping Be Controlled by the Same Locomotor central Pattern Generator? *J. Neurophysiol.* 83 (5), 2814–2824. doi:10.1152/jn.2000.83.5.2814

Lee, D. D., and Seung, H. S. (1999). Learning the Parts of Objects by Non-negative Matrix Factorization. *Nature* 401 (6755), 788–791. doi:10.1038/44565

Levine, A. J., Hinckley, C. A., Hilde, K. L., Driscoll, S. P., Poon, T. H., Montgomery, J. M., et al. (2014). Identification of a Cellular Node for Motor Control Pathways. *Nat. Neurosci.* 17 (4), 586–593. doi:10.1038/nn.3675

Liu, K. K. L., Bartsch, R. P., Lin, A., Mantegna, R. N., and Ivanov, P. C. (2015). Plasticity of Brain Wave Network Interactions and Evolution across Physiologic States. *Front. Neural Circuits* 9, 62. doi:10.3389/fncir.2015.00062

McGraw, M. B. (1940). Neuromuscular Development of the Human Infant as Exemplified in the Achievement of Erect Locomotion. *J. Pediatr.* 17 (6), 747–771. doi:10.1016/S0022-3476(40)80021-8

Miyai, I., Fujimoto, Y., Ueda, Y., Yamamoto, H., Nozaki, S., Saito, T., et al. (2000). Treadmill Training with Body Weight Support: Its Effect on Parkinson's Disease. *Arch. Phys. Med. Rehabil.* 81 (7), 849–852. doi:10.1053/apmr.2000.4439

Molnar, J., Esteve-Altava, B., Rolian, C., and Diogo, R. (2017). Comparison of Musculoskeletal Networks of the Primate Forelimb. *Sci. Rep.* 7 (1), 10520. doi:10.1038/s41598-017-09566-7

Moraru, E., and Onose, G. (2014). Current Issues and Considerations about the central Role of Rehabilitation Therapies in the Functional Recovery of Neurological Impairments after Stroke in Adults. *J. Med. Life* 7, 368–372.

Murphy, A. C., Muldoon, S. F., Baker, D., Lastowka, A., Bennett, B., Yang, M., et al. (2018). Structure, Function, and Control of the Human Musculoskeletal Network. *Plos Biol.* 16 (1), e2002811. doi:10.1371/journal.pbio.2002811

Mutlu, A., Krosschell, K., and Spira, D. G. (2009). Treadmill Training with Partial Body-Weight Support in Children with Cerebral Palsy: a Systematic Review. *Dev. Med. Child. Neurol.* 51 (4), 268–275. doi:10.1111/j.1469-8749.2008.03221.x

Myers, L. J., Lowery, M., O'Malley, M., Vaughan, C. L., Heneghan, C., St Clair Gibson, A. A., et al. (2003). Rectification and Non-linear Pre-processing of EMG Signals for Cortico-Muscular Analysis. *J. Neurosci. Methods* 124 (2), 157–165. doi:10.1016/S0165-0270(03)00004-9

Oppenheim, A. V., Buck, J. R., and Schafer, R. W. (2001). *Discrete-Time Signal Processing*. Vol. 2. Upper Saddle River, NJ: Prentice Hall.

Pang, M. Y. C., and Yang, J. F. (2000). The Initiation of the Swing Phase in Human Infant Stepping: Importance of Hip Position and Leg Loading. *J. Physiol.* 528 (2), 389–404. doi:10.1111/j.1469-7793.2000.00389.x

Petersen, T. H., Willerslev-Olsen, M., Conway, B. A., and Nielsen, J. B. (2012). The Motor Cortex Drives the Muscles during Walking in Human Subjects. *J. Physiol.* 590 (10), 2443–2452. doi:10.1113/jphysiol.2012.227397

Picelli, A., Melotti, C., Origano, F., Neri, R., Waldner, A., and Smania, N. (2013). Robot-assisted Gait Training versus Equal Intensity Treadmill Training in Patients with Mild to Moderate Parkinson's Disease: a Randomized Controlled Trial. *Parkinsonism Relat. Disord.* 19, 605–610. doi:10.1016/j.parkreldis.2013.02.010

Powell, V., Esteve-Altava, B., Molnar, J., Villmoare, B., Pettit, A., and Diogo, R. (2018). Primate Modularity and Evolution: First Anatomical Network Analysis of Primate Head and Neck Musculoskeletal System. *Sci. Rep.* 8 (1), 2341. doi:10.1038/s41598-018-20063-3

Rizzo, R., Zhang, X., Wang, J. W. J. L., Lombardi, F., and Ivanov, P. C. (2020). Network Physiology of Cortico-Muscular Interactions. *Front. Physiol.* 11, 558070. doi:10.3389/fphys.2020.558070

Roeder, L., Boonstra, T. W., Smith, S. S., and Kerr, G. K. (2018). Dynamics of Corticospinal Motor Control during Overground and Treadmill Walking in Humans. *J. Neurophysiol.* 120 (3), 1017–1031. doi:10.1152/jn.00613.2017

Rubinov, M., and Sporns, O. (2010). Complex Network Measures of Brain Connectivity: Uses and Interpretations. *NeuroImage* 52 (3), 1059–1069. doi:10.1016/j.neuroimage.2009.10.003

Sale, P., Franceschini, M., Waldner, A., and Hesse, S. (2012). Use of the Robot Assisted Gait Therapy in Rehabilitation of Patients with Stroke and Spinal Cord Injury. *Eur. J. Phys. Rehabil. Med.* 48, 111–121.

Sporns, O., and Betzel, R. F. (2016). Modular Brain Networks. *Annu. Rev. Psychol.* 67, 613–640. doi:10.1146/annurev-psych-122414-033634

Sylos-Labini, F., Lacquaniti, F., and Ivanenko, Y. P. (20142014). Human Locomotion under Reduced Gravity Conditions: Biomechanical and Neurophysiological Considerations. *Biomed. Res. Int.* 2014, 1–12. doi:10.1155/2014/547242

Takei, T., Confais, J., Tomatsu, S., Oya, T., and Seki, K. (2017). Neural Basis for Hand Muscle Synergies in the Primate Spinal Cord. *Proc. Natl. Acad. Sci. USA* 114 (32), 8643–8648. doi:10.1073/pnas.1704328114

Teulier, C., Sansom, J. K., Muraszko, K., and Ulrich, B. D. (2012). Longitudinal Changes in Muscle Activity during Infants' Treadmill Stepping. *J. Neurophysiol.* 108 (3), 853–862. doi:10.1152/jn.01037.2011

Thelen, E., and Cooke, D. W. (1987). Relationship between Newborn Stepping and Later Walking: a New Interpretation. *Developmental Med. Child Neurol.* 29 (3), 380–393. doi:10.1111/j.1469-8749.1987.tb02492.x

Thelen, E., and Fisher, D. M. (1983). The Organization of Spontaneous Leg Movements in Newborn Infants. *J. Mot. Behav.* 15 (4), 353–372. doi:10.1080/00222895.1983.10735305

Thelen, E., Skala, K. D., and Kelso, J. S. (1987). The Dynamic Nature of Early Coordination: Evidence from Bilateral Leg Movements in Young Infants. *Developmental Psychol.* 23 (2), 179–186. doi:10.1037/0012-1649.23.2.179

Vaal, J., Van Soest, A. J. K., and Hopkins, B. (2000). Spontaneous Kicking Behavior in Infants: Age-Related Effects of Unilateral Weighting. *Dev. Psychobiol.* 36 (2), 111–122. doi:10.1002/(sici)1098-2302(200003)36:2<111::aid-dev3>3.0.co;2-h

Vasudevan, E. V., Patrick, S. K., and Yang, J. F. (2016). Gait Transitions in Human Infants: Coping with Extremes of Treadmill Speed. *PLoS One* 11 (2), e0148124. doi:10.1371/journal.pone.0148124

Vaughan, C. L., Langerak, N. G., and O'Malley, M. J. (2003). Neuromaturation of Human Locomotion Revealed by Non-dimensional Scaling. *Exp. Brain Res.* 153 (1), 123–127. doi:10.1007/s00221-003-1635-x

Willoughby, K. L., Dodd, K. J., and Shields, N. (2009). A Systematic Review of the Effectiveness of Treadmill Training for Children with Cerebral Palsy. *Disabil. Rehabil.* 31 (24), 1971–1979. doi:10.3109/09638280902874204

Yang, J. F., Lament, E. V., and Pang, M. Y. C. (2005). Split-belt Treadmill Stepping in Infants Suggests Autonomous Pattern Generators for the Left and Right Leg in Humans. *J. Neurosci.* 25 (29), 6869–6876. doi:10.1523/JNEUROSCI.1765-05.2005

Yang, J. F., Stephens, M. J., and Vishram, R. (1998). Infant Stepping: a Method to Study the Sensory Control of Human Walking. *J. Physiol.* 507 (3), 927–937. doi:10.1111/j.1469-7793.1998.927bs.x

Yang, Q., Logan, D., and Giszter, S. F. (2019). Motor Primitives Are Determined in Early Development and Are Then Robustly Conserved into Adulthood.

Proc. Natl. Acad. Sci. USA 116 (24), 201821455. doi:10.1073/pnas.1821455116

Yokoyama, H., Ogawa, T., Kawashima, N., Shinya, M., and Nakazawa, K. (2016). Distinct Sets of Locomotor Modules Control the Speed and Modes of Human Locomotion. *Sci. Rep.* 6, 36275. doi:10.1038/srep36275

Zandvoort, C. S., van Dieën, J. H., Dominici, N., and Daffertshofer, A. (2019). The Human Sensorimotor Cortex Fosters Muscle Synergies through Cortico-Synergy Coherence. *NeuroImage* 199, 30–37. doi:10.1016/j.neuroimage.2019.05.041

Conflict of Interest: The authors declare that the research was conducted in the absence of any commercial or financial relationships that could be construed as a potential conflict of interest.

Publisher's Note: All claims expressed in this article are solely those of the authors and do not necessarily represent those of their affiliated organizations, or those of the publisher, the editors and the reviewers. Any product that may be evaluated in this article, or claim that may be made by its manufacturer, is not guaranteed or endorsed by the publisher.

frontiers in Network Physiology

ORIGINAL RESEARCH
published: 24 March 2022
doi: 10.3389/fnetp.2022.845495

The Fractal Tapestry of Life: II Entailment of Fractional Oncology by Physiology Networks

Bruce J. West [1,2]*

[1]Center for Nonlinear Science, Univesity of North Texas, Denton, TX, United States, [2]Office for Research and Innovation, North Carolina State University, Rayleigh, NC, United States

This is an essay advocating the efficacy of using the (noninteger) fractional calculus (FC) for the modeling of complex dynamical systems, specifically those pertaining to biomedical phenomena in general and oncological phenomena in particular. Herein we describe how the integer calculus (IC) is often incapable of describing what were historically thought to be simple linear phenomena such as Newton's law of cooling and Brownian motion. We demonstrate that even linear dynamical systems may be more accurately described by fractional rate equations (FREs) when the experimental datasets are inconsistent with models based on the IC. The Network Effect is introduced to explain how the collective dynamics of a complex network can transform a many-body noninear dynamical system modeled using the IC into a set of independent single-body fractional stochastic rate equations (FSREs). Note that this is not a mathematics paper, but rather a discussion focusing on the kinds of phenomena that have historically been approximately and improperly modeled using the IC and how a FC replacement of the model better explains the experimental results. This may be due to hidden effects that were not anticapated in the IC model, or to an effect that was acknowledged as possibly significant, but beyond the mathematical skills of the investigator to Incorporate into the original model. Whatever the reason we introduce the FRE used to describe mathematical oncology (MO) and review the quality of fit of such models to tumor growth data. The analytic results entailed in MO using ordinary diffusion as well as fractional diffusion are also briefly discussed. A connection is made between a time-dependent fractional-order derivative, technically called a distributed-order parameter, and the multifractality of time series, such that an observed multifractal time series can be modeled using a FRE with a distributed fractional-order derivative. This equivalence between multifractality and distributed fractional derivatives has not received the recognition in the applications literature we believe it warrants.

Keywords: fractals, fractional calculus, oncology, networks, multifractals

OPEN ACCESS

Edited by:
Plamen Ch. Ivanov,
Boston University, United States

Reviewed by:
Paul Bogdan,
University of Southern California, United States
Pedro Carpena,
University of Malaga, Spain

***Correspondence:**
Bruce J. West
brucejwest213@gmail.com

Specialty section:
This article was submitted to Systems Interactions and Organ Networks, a section of the journal Frontiers in Network Physiology

Received: *29 December 2021*
Accepted: *07 February 2022*
Published: *24 March 2022*

Citation:
West BJ (2022) The Fractal Tapestry of Life: II Entailment of Fractional Oncology by Physiology Networks. Front. Netw. Physiol. 2:845495. doi: 10.3389/fnetp.2022.845495

INTRODUCTION

All phenomena are equally susceptible of being calculated, and all that is necessary, to reduce the whole of nature to laws similar to those which Newton discovered with the aid of the calculus, is to have a sufficient number of observations and a mathematics that is complex enough (Marquis de Cordorcet, 2022).

The modern science of medicine, like many other non-physical disciplines, has been guided in its early mathematical development by the successful mechanical models of physics. That strategy has proven to be extraordinarily successful, even surviving the introduction of fractals into its modeling, until quite recently. The true complexity of medical networks has been revealed with the development and implementation of ever more sensitive sensors and mathematically sophisticated data processing techniques (Niu et al., 2021). These developments have led to a divergence of the modeling strategies appropriate for the physical sciences from those for the life sciences.

Complex phenomena in any of the science disciplines have complicated and intricate behaviors, typically balancing randomness against order, with no consensus among scientists or poets as to what constitutes a reasonable scientific measure of complexity. Any list of traits of complexity is arbitrary and idiosyncratic and mine consists of eight traits which is recorded in *Where Medicine Went Wrong* (West, 2006). It would not serve our purpose to reproduce the details of that list here except to note that it contained such things as the number of time-dependent variables, along with the nonlinear relations among them, a dependence on their environment, scaling is space and time, and a mixture of order and randomness.

Recognizing the different ways each of these complexity properties are treated in the physical, social, and life sciences, led to further divergences of the modeling strategies developed for each. Therefore, we review how far the fractional calculus (FC) or alternatively fractional dynamics (FD) has taken us into the non-mechanical interpretation of medicine. On the one hand, network science has had a significant growth spurt over the last 2 decades with the recognition of its utility in describing the dynamic behavior of all manner of complex phenomena. This includes the recent establishing of new journal on Network Physiology (Ivanov, 2021). On the other hand, although the developers of network science have put such topics as scaling (Schmitt and Ivanov, 2007), renormalization group theory, fractal statistics (Bernaola-Galván et al., 2012), and other ostensibly esoteric mathematical tools into their bag of tricks, they have been slow to incorporate FD and the FC as a primary modeling strategy. Hopefully, the present essay will help to rectify that situation.

This essay is an unapologetic advocacy for the use of FC in the effective modeling of complex phenomena in biology and medicine. What emerges herein is the increasing importance of criticality (West, 2020), the cooperative nature of networks in healthy physiologic behavior (West et al., 2014), and the importance of the FC in characterizing the dynamics of living networks (West et al., 2008; West and Grigolini, 2021). In particular, we examine how and why the dynamic behavior of such pathologies as cancer may lend themselves to description by the FC (Nasrolahpour, 2018).

Historical Perspective

The present paper is the sequel to *The Fractal Tapestry of Life: A review of Fractal Physiology* (West, 2021). The prequel contains a critique of the reliance that physiology theory has had on the mechanical models of physics for its development, pointing out the extraordinarily success this strategy has enjoyed, see for example (Ruch and Patton, 1979). However, with the introduction of fractals by Mandelbrot (Mandelbrot, 1977) into the modeling strategy of science and engineering, the true complexity of physiological networks was revealed and led to the parting of the ways for the modeling strategies appropriate for the physical sciences from those for the life sciences. In the prequel we emphasized how far the fractal concept has taken us in the non-mechanical interpretation of physiology since the term *fractal physiology* was coined by Bassingthwaighte et al. (Bassingthwaighte et al., 1994) a quarter century ago. The prequel drew largely from papers published in the *frontiers in Physiology*, *Fractal Physiology* over my 2 decade tenure as its founding editor. The intent of that review was to demonstrate how far the modeling community has come in accepting fractals as a part of natural history.

As done in the prequel, the discussion presented herein draws inspiration for its rationale from Daniel Kahneman's book, *Thinking, fast and slow* (Kahneman, 2011). Kahneman is a psychologist who was awarded the 2002 Noble Prize in Economics, suggesting that disciplinary borders, between economics and psychology in that case, are self-imposed barriers not supported by experiments done on the phenomena being studied. One consequence of the psychology experiments done and interpreted by him and his long time friend and collaborator Amos Tversky was that the historical assumptions about how humans make decisions, and in particular, how economic decisions on which microeconomics was based, had to be reexamined and some needed to be abandoned altogether. The assumption of strict rationality in humans, foundational to modern economic theory, turned out to be at odds with the empirical findings (Ariely, 2008).

The purpose of the present work is to demonstrate that we are now entering a new era in medicine, or rather in the mathematical modeling of medical phenomena, and what that entails for the future. It is useful to recall that in the *Principia* Newton introduced motion as a central idea of mechanics into physics, and although he never used the term *fluxion*, his word for a differential, in this major work he drew inspiration from his new mathematics to explore its implications. It was the mathematical notion of a differential that led Newton to identify motion as the central concept in celestial mechanics. He communicated this using the scientific language of the day, that being geometry, which explains some of the more torturous geometric arguments one finds in that remarkable book. His use of the differential historically guided the mechanics-based development of quantitative physiologic models, with some extraordinary successes, see, e.g., (Ruch and Patton, 1979) for a comprehensive discussion of the IC modeling of physiological systems.

On the other hand, this new era of medicine argues against relying on borrowing as a strategy for model building. It is not much of a stretch to say that typical phenomena in the life sciences are significantly more complex than those typically addressed in the physical sciences. Consequently, how one incorporates this complexity into the dynamic description of living cells, tissue and organs is uniquely defined by the

phenomenon being considered (Magin, 2006; West et al., 2008). It is also the case that the way in which complexity enters the mathematical model determines the sensitivity of the model's reaction to changes in parameter values. In other words the complexity of the phenomenon being modeled determines the degree of disruption that can be tolerated without the network degenerating into pathological behavior.

It is also the case that the standard training of the life scientist relies less on mathematical formalism, a reliance that enabled the success of the physical scientist in constructing useful physics-based mathematical models. However, scientists from both the physical and medical camps saw, almost immediately, the benefit of the fractal concepts for their respective domains of interest after it was introduced by Mandelbrot (Mandelbrot, 1977). But unlike Newton, who was working to understand a clearly observed physical phenomenon, Mandelbrot was attempting to understand not just the way we model change in the physical world, but change in every scientific discipline. To accomplish this ambitious goal he introduced the fractal concept through an endless succession of exemplars, including mathematical measures, noise, error, stellar matter, turbulence, statistics, polymers, and so on. These and many other applications of his ideas were based on his phenomenal intuition, using a kind of mathematics that neither the physical nor life sciences had seen before, much less implemented in the understanding of complex phenomena. Consequently, scientists in each discipline began developing fractal models based on what was needed to understand the unique processes and phenomena in their respective areas of study. It was equally clear that the fractal behavior of phenomena in living systems is the norm, and not the exception it seemed to be, at first, in the physical sciences (Mandelbrot, 1982).

In general, the complexity of a phenomenon molds the characteristics of the function used to describe its behavior. This is particularly true in describing how a function describing a phenomenon changes in time. The Weierstrass function, although expressed as an infinite Fourier series, does not have a finite integer derivative and was for that reason chosen by Richardson (Richardson, 1926) to describe the diffusion of a passive scalar in the turbulent flow of a fluid. It has been shown (Rocco and West, 1999) that such a function can have a finite fractional derivative, even when its integer derivative diverges. So what does this divergence property entail? It was determined during the last quarter century that an amazing number of familiar medical phenomena are described by fractal functions (West, 2006; West, 2021). Subsequently, it was argued that the equations of motion for such complex phenomena must be fractional, since a fractal function does not have integer-value derivatives and consequently cannot have Newtonian equations of motion (West, 2016). Thus, this essay is devoted to the whys and ways the FC enters into the dynamics of medicine and provides insight into certain medical pathologies including MO (Durrett, 2013).

THE NETWORK EFFECT

The new millennium has witnessed the blossoming of two quite different strategies for the mathematical modeling of the complex dynamics of large collections of interacting elements that appear in medicine, those being network science (West et al., 2014; Barabasi, 2016; Newman, 2018) and the fractional calculus (Podlubny, 1999; West et al., 2003a; Magin, 2006). The adoption of the network science strategy for the study of complex phenomena such as epidemic spreading of diseases (Pastor-Satorras et al., 2015), neuronal avalanches (Hernandez-Urbina et al., 2016), and social dynamics (Bak, 1996; Castellano et al., 2009; Mahmoodi et al., 2017) is a consequence of the fact that these networks are composed of many simple, interconnected, and dynamically interacting elements (West, 2014). In a similar way, the popularity of the FC in research has grown in the modeling of processes characterized by long-term memory as well as spatial heterogeneity (Herrmann, 2011; West, 2016). This FC popularity stems from its particular mathematical formulation, based on various definitions of non-local differentiation and integration operators and its utility in describing the dynamics of fractal phenomena, both in space and time. Therefore, since the effects of spatial heterogeneity and memory are frequently observed in biological, social, and artificial networks (Magin, 2016; Meerschaert et al., 2017), the application of FC in the domain of complex networks is a natural step toward providing novel analytical tools that are capable of addressing research questions arising in the field of medicine, such as *fractional dynamics* (FD). For example, FD has been used to model the complex dynamics in biological tissue (Magin, 2010) and biomedicine (Nasrolahpour, 2017; Nasrolahpour, 2018), as well as in the growth of cancer cells (Valentim et al., 2021), the signal decay in MRIs (Magin, 2016), and finally in the bizarre statistical fluctuations in dilute suspensions of algae and bacteria (Zaid et al., 2011), to name a few applications that are subsequently discussed.

At the turn of the 20th century the foundation of biology started moving from the concept of homeostasis, which is compatible with the physical notion of regression to equilibrium, to the concept of homeodynamics, which involves periodicity (Lloyd et al., 2001; Tu and McKnight, 2006), chaos and complexity (Guzm´an et al., 2017). As far as the important biological role of periodicity is concerned, we invite the readers to consult the excellent review paper of Strogatz (Strogatz, 2000), which reveals a connection between homeodynamics and neurophysiology.

Despite how simple the basic elements of complex networks are assumed to be, such as in cooperative behavior of animals (Flack et al., 2018), in the flow of highway traffic (Bette et al., 2017), or in the cascades of load shedding on power grids (Yang et al., 2017), the network dynamics are invariably characterized by rich self-organized emergent behavior (West and Grigolini, 2021). However, in most cases solving a network of coupled nonlinear equations to describe the behavior of a network composed of N units is at best labor intensive and at worst it is intractable. Consequently, the primary focus of investigations into the behavior of complex networks has been on their global behavior (Dorogovtsev et al., 2008). This approach travels the path taken by classical statistical physics, starting from insights

of Maxwell and Boltzmann that the description of the state of a gas or a solid could only be achieved over the scale of the entire system (Toda et al., 2004).

In the same way, the ability to portray the global behavior of a complex network is not free but comes at the price of not being able to quantify the Newtonian dynamics of the components of which it is composed. Typically, one attempts to infer the global dynamics by averaging the behavior of single elements within the system, following a bottom-up approach of mean field theory (Turalska and West, 2018). Turalska and West (Turalska and West, 2018) addressed the issue of depicting global dynamics by turning the question around and rather than joining the behaviors of single elements within the dynamic network, they asked whether it is possible to construct a description of the dynamics of the individual elements from information provided about the network's global behavior. They approach the problem by considering statistical properties of the global variable.

Frequently, the macro, or coarse-grained, variables observed in complex networks display emergent properties of scale invariance in space and/or in time. This scale invariance is manifest by, for example, the inverse power law (IPL) scaling of waiting-time probability density functions (PDFs) that reveals the variability of the time intervals between events. These time intervals are manifest in heart rate variability (HRV), in stride interval variability (SIV) and breath interval variability (BIV), or in the occurrence of brainquakes (West and Grigolini, 2021). The IPLs that characterize the emergent macroscopic behavior are reminiscent of particle dynamics near a critical point, where a dynamic network undergoes a phase transition (Christensen and Moloney, 2005). However, despite the mathematical advances made by the renormalization group approach and self-organized criticality theories that have shown how scale-free phenomena emerge at critical points, the issue of determining how the emergent properties influence the micro-dynamics of individual units, such as the growth of a single cell within a network of cells, whether healthy or pathological, is still in its nascent phase.

The Entailment of Network Dynamics

Grinstein et al. (1985) demonstrated that any discrete network, whose dynamics are defined in terms of local interactions, having symmetric transitions between states and random fluctuations originating from a thermal bath or internal dynamics is a member of the Ising universality class. One such dynamic complex network is given by the decision making model (DMM) (Bianco et al., 2008; Turalska et al., 2009; Turalska et al., 2011) and for clarity of discussion this is the dynamic model we implement in this section. Each individual unit of the DMM is a stochastic oscillator that statistically dithers between the two states, +1 and -1. The dynamics are modeled on a two-dimensional lattice and defined in terms of the probability of an individual at lattice point i to be in either state, by the coupled two-state master equation:

$$\frac{d\mathbf{p}^{(i)}(t)}{dt} = \mathbf{G}_i(t)\mathbf{p}^{(i)}(t), \tag{1}$$

$$\mathbf{p}^{(i)}(t) \equiv \begin{pmatrix} p_1^{(i)}(t) \\ p_2^{(i)}(t) \end{pmatrix}, \tag{2}$$

where $\mathbf{p}^{(i)}(t)$ is the probability of the element $i = 1, 2, \ldots, N$ within the network at the time t is normalized such that $p_1^{(i)}(t) + p_2^{(i)}(t) = 1$ for every i and changes with the fundamental transition rate $g_0 < 1$ between states. The matrix of time-dependent coupling rates for individual i is given by:

$$\mathbf{G}_i(t) = \begin{pmatrix} -g_{12}^{(i)}(t) & g_{21}^{(i)}(t) \\ -g_{21}^{(i)}(t) & g_{22}^{(i)}(t) \end{pmatrix}; \tag{3}$$

where the individual transition rates are:

$$\begin{aligned} g_{12}^{(i)}(t) &= g_0 \exp\left[-\frac{K}{M^{(i)}}\left(M_1^{(i)}(t) - M_2^{(i)}(t)\right)\right], \\ g_{21}^{(i)}(t) &= g_0 \exp\left[\frac{K}{M^{(i)}}\left(M_1^{(i)}(t) - M_2^{(i)}(t)\right)\right], \end{aligned} \tag{4}$$

and $0 \le K < \infty$ is the strength of the interaction. On the regular two-dimensional lattice considered here the number of nearest neighbors is given by $M^{(i)} = 4$ and $0 \le M_{1,2}^{(i)}(t) \le 4$ denotes the count of nearest neighbors in states $s_i(K,t) = \pm 1$ at time t for every individual i. The probability that the single unit in isolation changes its state corresponds to the case of $K = 0$. When the coupling constant $K > 0$, a unit in state +1 (-1) makes a transition to the state -1 (+1) faster or slower according to whether $M_1^{(i)}(t) < M_2^{(i)}(t)$ or $M_1^{(i)}(t) > M_2^{(i)}(t)$, respectively.

This DMM network is defined by N such coupled equations, which gives rise to the problem of finding an analytic solution to a highly nonlinear network (Turalska et al., 2011) containing $2N$ dynamic variables. Given this number of dynamic variables extensive numerical calculations are supplemented by an analytic formulation of the evolution of a global variable. As depicted in **Figure 1B**, the global behavior of the model is defined by the fluctuations of the mean field variable:

$$\xi(K,t) = \frac{1}{N}\sum_{i=1}^{N} s_i(K,t), \tag{5}$$

which shows a pronounced transition as a function of the control parameter K as it passes through the critical value $K = K_c$. The network dynamics for various quantities are depicted in the figure for the control parameter being subcritical ($K < K_c$), critical ($K = K_c$) and supercritical ($K > K_c$). While in **Figure 1A** a typical single element appears to be essentially unchanged by its interactions with the rest of the network elements. On the other hand, the global variable shifts from a configuration dominated by randomness (subcritical) to one in which strong interactions give rise to long-lasting majority states (supercritical) shown in **Figure 1B**. Note that the source of the random fluctuation in the DMM is the finite size of the network, having a strength of $1/\sqrt{N}$ and has nothing to do with the thermal fluctuations arising in the modeling of phase transitions in physics phenomena such as the freezing of water or magnetization (West et al., 2014).

To characterize the changes in temporal properties of the network elements and those of the emergent properties of the

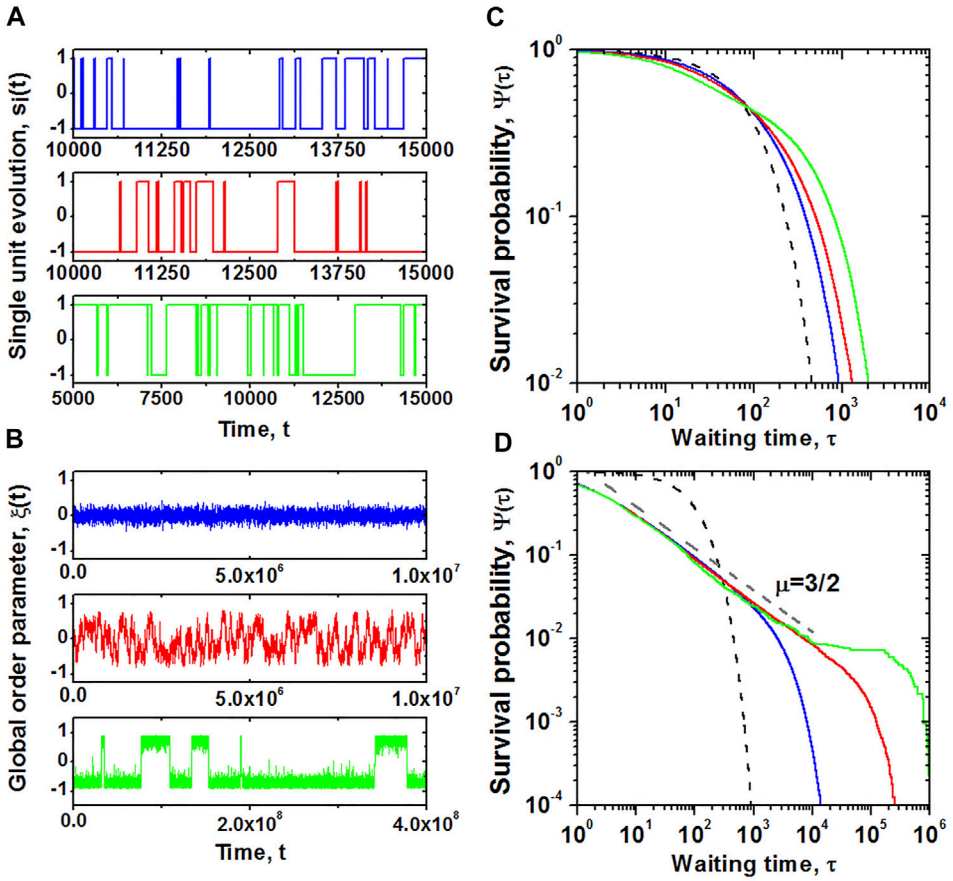

FIGURE 1 | Behavior of a discrete, two-state dynamic unit on a two-dimensional lattice. Temporal evolution and corresponding survival probability $\Psi(\tau)$ for the transitions between two states for the single unit $s_i(t)$ of the network, presented on panels **(A,C)**, respectively, are compared with the behavior and statistical properties of the global order parameter $\xi(t)$, shown on panels **(B,D)**. Simulations were performed on a lattice of size $N = 50 \times 50$ nodes, with periodic boundary conditions, for $g_0 = 0.01$ and increasing values of the control parameter K. Blue, red, and green lines correspond to $K = 1.50$, 1.70, and 1.90, respectively. The critical value of the control parameter is $K_C \approx 1.72$. Black dashed line on the plots of $\Psi(\tau)$ denotes an exponential distribution, with the decay rate g_0. From (Turalska and West, 2018) with permission.

macro variables, we evaluate the survival probability function $\Psi(\tau)$, where τ is the time interval between consecutive events. These events are defined as changes of state or crossings of the zero-axis, for a single element or the global variable, respectively. These calculations reveal a modest deviation of the survival probability function for a single individual from the exponential form, $\Psi(\tau) = exp(-g_0\tau)$, that characterizes a single non-interacting element, as shown in **Figure 1C**. The network's influence on the behavior of the individual appears to induce only a small change in the behavior of the latter. Despite this apparently small change in the individual's behavior, the global variable changes dramatically, manifesting IPL statistics, as depicted in **Figure 1D**.

In this last panel three different aspects of dynamic behavior are revealed. The potential for the global variable is bimodal with the height of the barrier between the two potential minima determined by the parameter K. The dynamics are given by a Langevin equation with the strength of the random fluctuations driving the network from one well to the other decreasing with the size of the network as $1/\sqrt{N}$. The subcritical and critical domains have dominant IPL survival probabilities trailing off into exponentials for long times. In the supercritical domain (green curve) a new phenomenon emerges called the *Kramers shoulder*. In his study of chemical reactions involving two states Kramers determined that the process becomes ergodic for times larger than what is now called the Kramers time, which increases exponentially with the size of the network, see West et al. (2014) for a detailed discussion.

Thus, to what extent are individual opinions within a complex network influenced by the network dynamics?

Complex Network Subordination

To determine the network's influence on the dynamics of the individual unit we adapt a subordination argument, and relate the time scale of the macro variable $\xi(K, t)$ to the time scale of the micro variable $s_i(t)$ following the arguments presented in (Turalska and West, 2018). The notion of different clocks associated with different aspects of a complex network dynamics dates back to the middle of the 19th century where the two clocks defined subjective and objective times and were

used to justify the empirical Weber-Fechner law (Fechner, 1860). More recently, due to the availability of time resolved datasets, life science has begun adopting the notion of multiple clocks to distinguish between cell-specific and organ-specific clocks in biology, which is analogous to person-specific and group-specific clocks in sociology. While the global activity of an organ, such as the brain or the heart, might be characterized by quite regular, often periodic behaviors, the activity of single neurons or pacemaker cells demonstrate burstiness and noisiness. Thus, because of the stochastic behavior of the clocks, a transformation between clock times is necessary. An example of such a probabilistic transformation is the subordination procedure, see for example (Feller, 1966).

The two-state master equation for a DMM single isolated individual in discrete time n in steps of $\Delta\tau$ can be written in terms of the single variable:

$$\varphi(n+1) - \varphi(n) = -g_0 \Delta\tau \varphi(n) \tag{6}$$

in the notation $\varphi(n) = \varphi(n\Delta\tau) \equiv p_1(n\Delta\tau) - p_2(n\Delta\tau)$ being the difference in probabilities for the typical individual to assume one of two states. The solution to this discrete equation is after n ticks of the individual's clock is:

$$\varphi(n) = (1 - g_0\Delta\tau)^n \varphi(0), \tag{7}$$

which, in the limit $g_0\Delta\tau \ll 1$, becomes an exponential. However, when the individual interacts with the other members of a network, the dynamics are no longer simple. Assuming a renewal property for events, an event being a transition from one state to the other, so that each event is independent of every other event, one can relate the discrete time of the unit to the clock time of the network using subordination theory.

Introducing subordination, we define the discrete index n as the *operational* time of the individual that is connected to the *chronological* time t recorded by the ticking of the network's clock in which the global behavior is observed. If each tick of the discrete clock n is thought of as an event, then the relation between the operational time and the continuous chronological time can be given by the waiting-time PDF of those events in chronological time $\psi(t)$. The chronological time lies in the interval $(n-1)\Delta\tau \le t \le n\Delta\tau$ for each operational tick and consequently the equation for the average dynamics of the individual probability difference is given by (Pramukkul et al., 2013):

$$\langle \varphi(t) \rangle = \sum_{n=1}^{\infty} \int_0^t \Psi(t-t') \psi_n(t') \varphi(n) dt'. \tag{8}$$

Every tick of the operational clock is an event and occurs in chronological time at the drawing from the renewal waiting-time PDF $\psi(t)$ determined by the derivative of the survival probability. The empirically determined analytic expression for the survival probability from the numerical simulation of DMM is:

$$\Psi(t) = \left(\frac{T}{T+t}\right)^{\mu-1} e^{-\epsilon t}. \tag{9}$$

The dominant behavior of the empirical survival probability is IPL as indicated in **Figure 1D**. However, at early times the probability of not making a transition approaches the constant value of unity, whereas at late times the probability of not making a transition in a given time decays exponentially. It is in the middle range, where the survival probability is IPL. The extent of the IPL range of the survival probability is determined by the empirical values of T, μ and ϵ and from **Figure 1D** the value of ϵ is seen to become smaller as the control parameter K increases. The IPL functional form of the PDF results from the behavior of the survival probability $\Psi(\tau)$ of the global variable depicted in **Figure 1D** with $\mu = 3/2$.

Using a renewal theory argument Pramukkul et al. (2013) show that **Eq. 8** expressed in terms of Laplace transform variables indicated by $\hat{f}(u)$ for the time-dependent function $f(t)$ has the form:

$$\langle \hat{\varphi}(s) \rangle = \frac{\varphi(0)}{u + \epsilon + \lambda_0 \hat{\Phi}(u+\epsilon)} \tag{10}$$

where $\lambda_0 \equiv g_0\Delta\tau$ and $\hat{\Phi}(u+\epsilon)$ is the Laplace transform of the Montroll-Weiss memory kernel (Pramukkul et al., 2013):

$$\hat{\Phi}(u+\epsilon) = \frac{(u+\epsilon)\hat{\psi}(u+\epsilon)}{1 - \hat{\psi}(u+\epsilon)}. \tag{11}$$

Note that u is replaced by $u + \epsilon$ in the Laplace transforms, because the exponential truncation of the empirical survival probability shifts the index on the Laplace transform operation. The asymptotic behavior of an individual in time is determined by considering the waiting-time PDF as $u + \epsilon \to 0$:

$$\hat{\psi}(u+\epsilon) \approx 1 - \Gamma(1-\alpha) T^{\alpha} (u+\epsilon)^{\alpha} \; ; \; 0 < \alpha = \mu - 1 < 1, \tag{12}$$

so that **Eq. 10** reduces to:

$$\langle \hat{\varphi}(u) \rangle = \frac{\varphi(0)}{u + \epsilon + \lambda^{\alpha} (u+\epsilon)^{1-\alpha}}. \tag{13}$$

The inverse Laplace transform of **Eq. 13** yields the tempered non-integer rate equation:

$$(\partial_t + \epsilon)^{\alpha} \langle \varphi(t) \rangle = -\lambda^{\alpha} \langle \varphi(t) \rangle, \tag{14}$$

where the operator $\partial_t^{\mu-1}[\cdot]$ is the Caputo fractional derivative For the moment we define the Caputo fractional derivative in terms of its Laplace transform:

$$\mathcal{LT}\left[\partial_t^{\alpha}[f(t)]; u\right] = u^{\alpha} \hat{f}(u) - u^{\alpha-1} f(0),$$

where $f(0)$ is the initial value of $f(t)$ and $\hat{f}(u)$ is its Laplace transform for $0 < \alpha = \mu - 1 < 1$ (West, 2016) and:

$$\lambda T = \left[g_0 \Delta\tau / \Gamma(2-\mu)\right]^{\frac{1}{\mu-1}}. \tag{15}$$

Note that due to the dichotomous nature of the states that $\langle \varphi(t) \rangle$ is the average opinion of the individual $s_i(t)$.

A technique for obtaining the solution of the asymptotic fractional master equation **Eq. 14** is given in the following section in some detail. For the moment we solve the equation for a randomly chosen unit within the social network and obtain

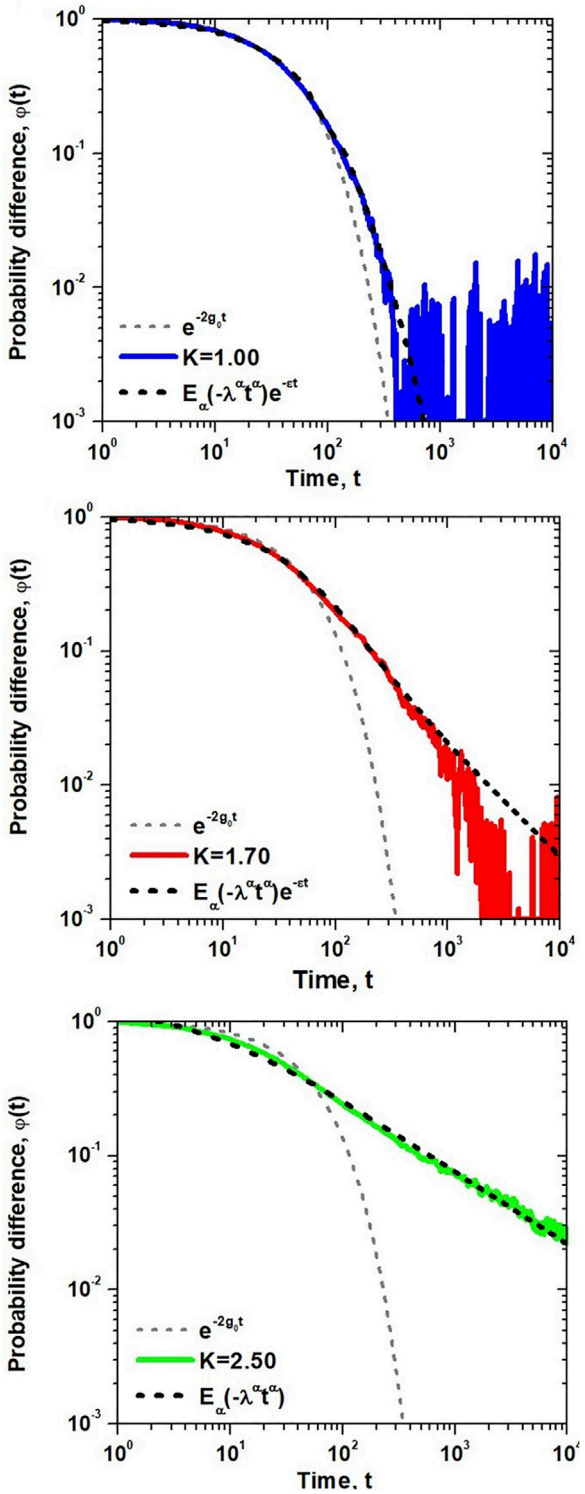

FIGURE 2 | The probability difference $\langle \varphi(t) \rangle$ estimated as an average over an ensemble of 10^4 independent realizations of single element trajetories. Each trajectory corresponds to evolution of a randomly selected node within a $N = 100 \times 100$ lattice network, with $g_0 = 0.01$ and the same initial condition $s_i(0) = 1$. The parameter values for the numerical data are given in **Figure 1** and from top to bttom $K = 1.0, 1.7, 2.5$, respectively. The fit of the

(*Continued*)

FIGURE 2 | exponentially truncated MLF to the numerical calculations over the time interval [a,b] yields the parameter values: $K = 1.0$, $\epsilon = 4 \times 10^{-3}$, $\lambda = 1.47 \times 10^{-2}$, $\alpha = 0.892$ [1, 300]; $K = 1.70$, $\epsilon = 1.4 \times 10^{-11}$, $\lambda = 2.06 \times 10^{-2}$, $\alpha = 0.805$, [1, 10^3]; $K = 2.50$, $\epsilon = 5.58 \times 10^{-12}$, $\lambda = 2.93 \times 10^{-2}$, $\alpha = 0.558$ [1, 10^4]. Adapted from (Turalska and West, 2018) with permission.

an exponentially attenuated Mittag–Leffler function (MLF) (Turalska and West, 2018):

$$\langle \varphi(t) \rangle = \varphi(0) E_\alpha(-(\lambda t)^\alpha) \exp[-\epsilon t]. \tag{16}$$

and the MLF is defined by the series:

$$E_\alpha(z) \equiv \sum_{n=0}^{\infty} \frac{z^n}{\Gamma(n\alpha + 1)}, \; \alpha > 0. \tag{17}$$

The MLF is a stretched exponential at early times and an IPL at late times, with $\alpha = \mu - 1$ being the IPL index in both domains (West et al., 2003a). The MLF will be discussed more fully in subsequent sections.

Comparisons With Numerics

We test the above solution against the numerical simulations of the dynamic network consisting of $N = 10^4$ units on a two-dimensional lattice with nearest-neighbor interactions in all three regions of DMM dynamics; subcritical, critical and supercritical. The time-dependent average opinion of a randomly chosen individual is presented in **Figure 2**, where the average is taken over 10^4 independent realizations of the dynamics in the three regimes.

A comparison with the exponential form of $\langle \varphi(t) \rangle$ for an isolated individual depicted by the dashed line segment depicted in **Figure 2** indicates that the influence of the network on the individual's dynamics clearly persists for increasingly longer times with increasing values of the control parameter within the network. The parameters μ and λ of **Eq. 16** obtained through fitting numerical results of **Figure 2** with the MLF are summarized in the table given in **Figure 3**. It is evident that the influence of the network dynamics on the individual is greatest at long times. The deviation of the analytic solution to the FRE from the numerical calculation is evident for values of the control parameter at and below the critical value. The analytic prediction is least reliable at extremely long times in the subcritical domain. Consequently, the response of the individual to the group, mimics the group's behavior most closely when the control parameter is equal to or greater than the critical value.

Complex Networks Entail Fractional Space Diffusion Equations

Herein the subordination procedure provides an equivalent description of the average dynamics of a single individual within a complex network in terms of a linear fractional stochastic rate equation (FSRE). The fractional dynamics given by **Eq. 14** is solved exactly, determining that the Poisson statistics of the isolated individual, becomes attenuated Mittag–Leffler

	K=1.00	K=1.70	K=2.50
μ	1.9139	1.8081	1.5339
λ	0.0211	0.0232	0.0864
R^2	0.9968	0.9989	0.9890

FIGURE 3 | The probability difference $\langle \varphi(t) \rangle$ of **Figure 2** is fitted with the MLF using an algorithm developed by Podlubny (Gorenflo et al., 2002). Assuming $T = 0.10$, $\Delta\tau = 1$ and $g_0 = 0.01$ the parameters of analytic solution are $\mu = 3/2$ and $\lambda = 0.031\,8$. The mean-square goodness of fit R^2 is discussed in (Turalska and West, 2018).

statistics, due to the interaction of that individual with the other members of the complex dynamic network. The numerical simulation of the network dynamics consisting of ten thousand nonlinearly interacting units collapses onto a one-dimensional fractional dissipative rate equation for a typical single unit. Note that the average influence of the other 9,999 units in the nonlinear dynamic network on the unit of interest is predicted by the MLF solution of the linear FRE without linearizing the dynamics. Let me say this again *the FRE is an exact representation of the complete response of a typical unit to the rest of the nonlinear dynamic network without linearizing the dynamics.* The effect of the other 9,999 units on the typical one is two-fold giving rise to an attenuated MLF dynamics with an attenuation rate ε and the noninteger-order derivative α, apparently without approximation.

> As Pointed out in West (West, 2016): The results in this section provide a partial answer to a question in sociophysics identified by Kulakolwski and Nawojczyk (Kulakolwski and Nawojczyk, 2008) concerning how empirical regularities such as prejudice or tolerance can be derived from global social properties such as entropy or temperature. We can interpret their use of the nomenclature "temperature" as the control parameter in the DMM network. Here again we have demonstrated how the state of the network, as described by the global dynamics, can influence the decision making behavior of the individual.

This quote can be recast in the form where sociophysics is replaced by medical biophysics and the same partial answers can be obtained for how the empirical regularities such that the ubiquity of IPL statistics can be derived from global properties of physiological networks. We shall pursue this more fully in subsequent sections.

We conjecture that the behavior of the individual units are generic, given that the DMM network dynamics belong to the Ising universality class. Members of this universality class share the critical temporal behavior (West et al., 2014) driving the subordination process. It is the renewal property of the event statistics, which through the subordination process, gives rise to the linear fractional master equation for the typical unit's dynamics. The solution to the tempered FRE manifests a subsequent robust behavior of the individual. It remains to determine just how robust the behavior of the individual is relative to control signals that might be used to manage healthy dynamics, as well as any pathologies that arises in the dynamics over the lifetime of the living network.

Thus, a unit's simple random behavior, when isolated, is replaced with behavior that could serve a more adaptive role in social and medical networks. Think of the difference in the dynamics of an isolated pacemaker cell and that of the sinus node, the heart's natural pacemaker. One might consider the solution to the following FSRE:

$$(\partial_t + \epsilon)^\alpha \xi(t) = -\lambda^\alpha \xi(t) + V(t), \tag{18}$$

and $V(t)$ represents parasympathetic and sympathetic fluctuating signals from the autonomic nervous system and $\xi(t)$ is the mean field electrical output of the sinus node. The two branches of the nervous system are in an on-going tug-of-war in driving the sinus node, one decreasing and the other increasing the heart's rate thereby producing the HRV time series in healthy subjects.

We close this section with the observation that the aggregate effect of the network dynamics is to reduce the $2N$ – dimensional master equation description of the nonlinear evolution of the probability to a 1 – dimensional description of the linear fractional dynamics of the global variable. Therefore, **Eq. 18** is a generic representation of such dynamics with the formal solution in Laplace space:

$$\hat{\xi}(u) = \frac{(u+\epsilon)^{\alpha-1}\xi(0)}{(u+\epsilon)^\alpha + \lambda^\alpha} + \frac{\hat{V}(u)}{(u+\epsilon)^\alpha + \lambda^\alpha}, \tag{19}$$

where the homogeneous solution $\xi_h(t)$ is obtained from **Eq. 16**:

$$\xi_h(t) = \xi_h(0) E_\alpha(-(\lambda t)^\alpha) \exp[-\epsilon t], \tag{20}$$

and the complete time-dependent solution is obtained by Laplace inversion to be (West et al., 2003a):

$$\xi(t) = \xi_h(t) + \int_0^t dt' (t-t')^{\alpha-1} E_{\alpha,\alpha}(-[\lambda(t-t')]^\alpha) \exp[-\epsilon(t-t')] V(t'), \tag{21}$$

where we have introduced the generalized MLF:

$$E_{\alpha,\beta}(z) \equiv \sum_{n=0}^{\infty} \frac{z^n}{\Gamma(n\alpha+\beta)}, \ \alpha, \beta > 0. \tag{22}$$

The formalism represented here in the solution given by **Eq. 21** is probably overwhelming if you are seeing it for the first time. So for the sake of clarity let us take a step back and systematically

prepare the ground for solving differential equations involving noninteger operators before interpreting the above solution. The take away message from introducing such FDEs is that the solution to a ten thousand component master equation using IDEs has been expressed as a global variable solution to an appropriate FDE. As a medical application consider a tissue consisting of a large number of cells and what a practitioner could do with a model that exploited such a startling mathematical simplification.

APPLICATIONS OF FRACTIONAL CALCULUS

Since the time of Newton science has accepted the explanation that the myriad kinds of motions of the objects in the physical world around us are determined by energy. Electrical energy provides the power that runs social media, the internet and lights our cities; chemical energy supplies the power to drive the engines in our transportation systems, and solar energy is converted by photosynthesis into the foods we eat. Physics provides a detailed description of how changes in energy over spatial intervals produce forces, which moves things around. A kite pulling at its tether, the invariant order of the colors in a rainbow, moon rise, and sunset, all have their causal explanations in terms of forces. But the force laws, even when generalized to continuous media such as fluids, are not able to explain everything. We talk of individuals exerting forces on one another, of stress in a relationship or in the work place. Is the latter force merely an analogue of the mechanical forces and thereby lacking material substance, or is it something more? Or are the dynamics of living networks really no different from those for inanimate matter?

We do not have complete answers to such profound questions, but what we can say is that models using IC from theoretical physics when applied to the complex phenomena of social and life sciences have, by and large, been disappointing. Here we argue that much of the disappointment encountered in the development and application of models outside the physical sciences has been the result of the simplifying assumptions made. Very often the simplifying assumption were known to be wrong but were necessary to satisfy the known properties of the mathematics used to construct the models. Other times the assumptions were idealizations that although not entirely accurate, were thought to capture the dominant characteristic of the phenomenon being investigated, and therefore the idealized model was wrong, but conveyed the truth. This is not unlike the children stories in *Aesop's Fables* that teach abstract lessons in ethics and morality in a language children can understand.

The purpose here is not to belittle the mathematical techniques used in the past to understand the unifying nature of physical laws, but rather to highlight the fact that the only way we can formulate questions is by means of language and mathematics is the language of science: for Galileo the language was geometry and algebra; for Newton and scientists for the following three centuries the language was primarily the differential calculus. Consequently, much of what is presented is concerned with the mental map of the world we construct from such mathematics. An exhaustive treatment of the social implications of the limit concept has been treated by Amir Alexander in his remarkable book *Infinitesimal, How a Dangerous Mathematical Theory Shaped the Modern World* (Alexander, 2014):

> On 10 August 1,632, five men in flowing black robes convened in a somber Roman palazzo to pass judgment on a simple proposition: that a continuous line is composed of distinct and infinitely tiny parts. The doctrine would become the foundation of calculus, but on that fateful day the Jesuit fathers ruled that it was forbidden. With the stroke of a pen they launched a war for the very soul of the modern world.

This dramatic depiction of the dispute over a mathematical concept lay at the heart of what was the Catholic Church's role in interpreting how we humans were to understand the world in which we live. It is not my purpose here to present Alexander's brilliant historical arguments on how the concepts of continuity and limit became a fundamental theological issue. Instead I wish to emphasize that then, as now, our understanding of the world is based on the language we use to describe it and which necessarily determines how we can think about it. Our mental models of the world and its events are all we have, so when we embark on scientific investigations it is in our fundamental interest to refine those models as best we can.

This is where the FC enters the discussion. It is not surprising that colleagues should ask about noninteger differentials and integrals and they did so in Newton's lifetime, asking Leibniz the cofounder of the differential calculus if such noninteger operators could be defined. Other than these technical questions addressed in private letters the noninteger aspect of the calculus was mostly ignored by the social, physical, and life scientists, intermittently emerging from the shadows of formalism with an application over the centuries. The international scientific community saw no need for a new calculus. As a body, the science community tacitly agreed that the ordinary differential calculus, along with the analytic functions entailed by solving the equations resulting from Newton's force law, are all that was required to provide a scientific description of the macroscopic physical world.

As pointed out elsewhere (West, 2020) the evidence is all around us that the domain of application of Newton's view of the physical world is contracting dramatically. This is one result of the increase in sensitivity of diagnostic tools, advances in data processing techniques, and expanded computational capabilities, which have all contributed to the broadening of science in ways that have pushed many phenomena from borderline interest to center stage. These curious complex processes are now catalogued under the heading of fractal scaling phenomena and their impact has nowhere been more

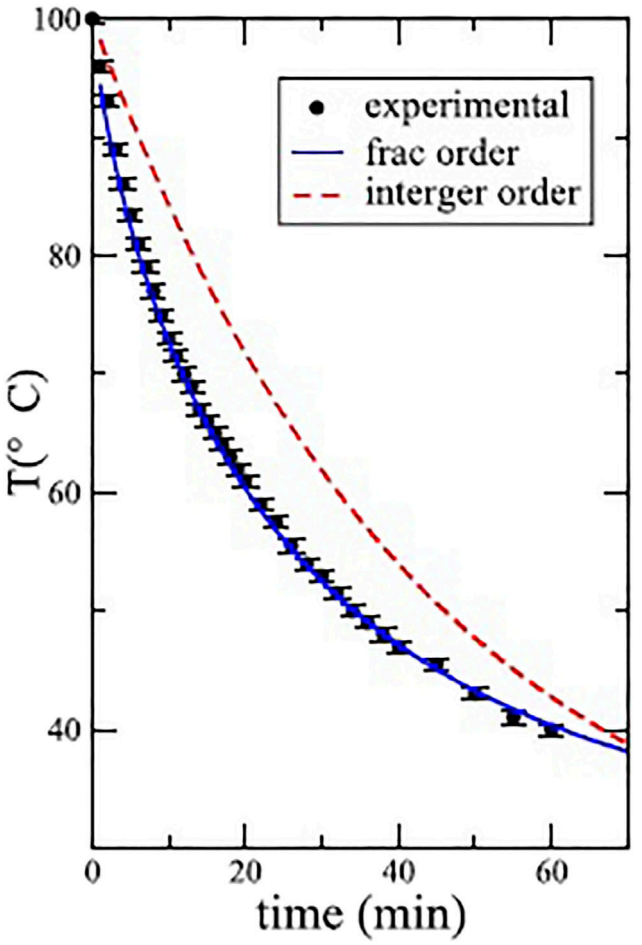

FIGURE 4 | Comparison of the experimental cooling data with solutions using the Caputo derivative in **Eq. 25** with $\alpha = 0.79$ and the exponential for 300 ml of water. Adapted from Mondol et al. (2018) with permission.

emphatic than in medical science (West, 2016). The understanding of the fundamental dynamics underlying such scaling requires the new mathematical perspective obtained using fractional operators and such descriptions have apparently ushered in the sunset for much of what remains of Newton's world view.

Fractional Differential Equations

FC is concerned with the quantitative analysis of functions using non-integer-order operators that generalize the traditional meaning of integration and differentiation. The non-integer order of a FC operator can be a real number, a complex number, or even the function of a variable, as we shall see. But this is less an essay on mathematics, than it is a presentation of the remarkable scientific utility of the FC, whose scope is intended here for medical scientists who recognize the need for such methods but may be less interested in learning the formal details of the methodology. So let us begin by examining well-accepted, simple, linear, dynamic processes that turn out to be not so simple.

Newtonian Cooling

We begin with an example presented by Mondol et al. (Mondol et al., 2018) who used a FDE to examine Newton's linear cooling law. This law states that the rate of heat loss from a body is directly proportional to the difference in the temperatures between that of the body at time t denoted as $T(t)$ and that of its surroundings T_a given by the IRE:

$$\frac{dT(t)}{dt} = -\lambda[T(t) - T_a], \tag{23}$$

with loss rate λ, provided the temperature difference is not too large and the nature of the radiating surface remains the same throughout the time of the cooling process. The prediction of this law is that cooling proceeds at a constant rate from the initial temperature of the object T_0 to the ambient temperature T_a and is exponential in time:

$$T(t) = T_0 e^{-\lambda t} + T_a\left(1 - e^{-\lambda t}\right), \tag{24}$$

since it is the solution to a linear rate equation. This solution allows the medical examiner to unambiguously establish the time of death in every television murder mystery ever made. However, in the real world Mondol et al. determined experimentally that the cooling problem is not so simple and does in fact depend more subtilely on the properties of the objects being cooled.

In general, they replace Newton's cooling equation with the FRE:

$$\partial_t^\alpha [T(t)] = -\lambda[T(t) - T_a], \tag{25}$$

where again the ambient temperature is T_a. Notice also that the solution to cooling equation given by **Eq. 25** using a Caputo noninteger derivative $\partial_t^\alpha[\cdot]$ has the same form as **Eq. 24** with the exponential replaced with a MLF:

$$T(t) = T_0 E_\alpha(-\lambda t^\alpha) + T_a[1 - E_\alpha(-\lambda t^\alpha)], \tag{26}$$

a complete discussion of this solution is given elsewhere (West, 2016; Mondol et al., 2018). In **Figure 4** the dashed curve depicts the "best" exponential solution to Newton's cooling law, which clearly deviates from the experimental data given for 300 ml of water. The solution to the FRE is given by **Eq. 26** and is depicted by the solid curve, fitting the experimental data extremely well.

Of course, this is just one example selected from the many experimental results Mondol et al. present. These IRE and FRE predictions compared to the experimental datasets emphasize the error one can make in modeling even familiar linear dynamic phenomena that one has no reason to believe are not simple. But this is a cautionary tale. One should consider every phenomenon to be complex or nonsimple until it is verified by both experiment and theory to be simple. In the case of an object cooling over time the nonsimplicity has to do with memory that is built into the definition of the FC derivatives irrespective of their detailed forms. Mondol et al. (Mondol et al., 2018) demonstrate experimentally that some cooling phenomena are represented by Newton's law of cooling, others

by the Caputo noninteger form as in the example shown in **Figure 4** and still others by the Reiman-Liouville form of the FC derivative operator, both of which will be defined in due course. The need for the fractional (noninteger) differential is explained in the following manner (Mondol et al., 2018):

> Thus, it is all about taking rate of change of a variable. . .with respect to fractional differential of time which defines Δt, the "window of observation." While the classical differential is Δt^{α} with $\alpha = 1$, the fractional differential is Δt^{α} with $\alpha < 1$. . .(thus) the fractional differential will always be greater than classical differential as $\Delta t \rightarrow 0$. This makes the "window of observation" to view complex dynamics effectively larger, as compared to Δt . . .as we make Δt go from milli, to micro, to pico. . .the fractional differential . . .grows, helping us to view the dynamics which may be complex with several relaxation processes and relaxation rates, better.

They go on to say that if the dynamics is governed by a unique cooling rate, there is no need to increase the viewing window by using a fractional (noninteger) differential and Newton's cooling law prevails. Thus, if you are convinced that the process you are dealing with is linear, but the data deviate systematically from any linear IDE model you have examined, the deviation may be the result of non-locality and not a nonlinearity. The questions you need to answer is which calculus Nature has chosen for the dynamics of the phenomena under investigation and why?

Brownian Motion

The only exposure to stochastic processes that typically resonates with non-mathematically oriented scientists is the phenomenon of Brownian motion. The phenomenon was observed by the botonist Robert Brown in 1827, who studied the erratic motion of a pollen mote suspended in a fluid using a microscopic. He hoped that his observation would explain the 'life force' he thought at first he was observing, which he admittedly did not accomplish. Of course, it turned out that he was watching the reaction of the pollen mote to the thermal motion of the invisible molecules of the ambient fluid as explained by Einstein in his 1905 paper on diffusion (Einstein, 1905). In a 1907 sequel to this paper Einstein speculated, after informally hearing of these early experiments, that Brown could well have been observing a diffusive process (Einstein, 1907). This off-hand remark in a published paper was sufficient to insure Brown's scientific immortality.

Einstein did however recognize a problem with his formulation of what is now known as Brownian motion. If $X(t)$ is the instantaneous position of a free Brownian particle its mean-square displacement (MSD) from its initial position is predicted by Einstein's theory to be $X(0)$:

$$\langle \Delta X(t)^2 \rangle = \langle [X(t) - X(0)]^2 \rangle = 2Dt, \tag{27}$$

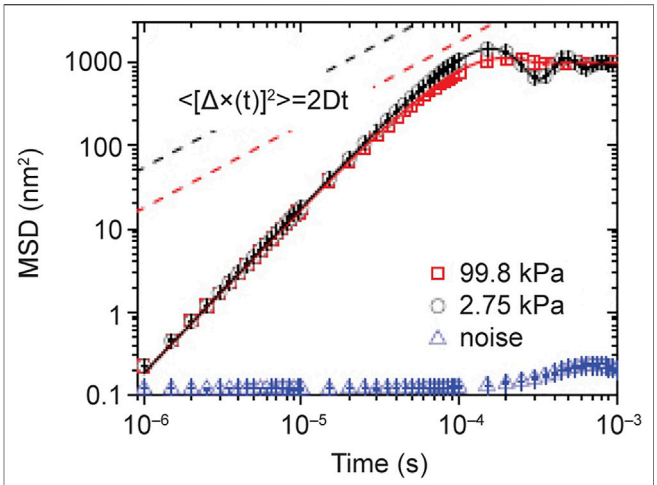

FIGURE 5 | The MSDs of a 3 *μm* silica bead trapped in air at 99.98 *kPa* (red squares) and 2.75 *kPa* (black circle). They are calculated from 4×10^7 measurements for each pressure. The "noise" signal (blue triangles) is recorded when there is no particle in the optical trap. The solid lines are the theoretical predictions of **Eq. 31**. The prediction of Eistein's theory of free Brownian motion in the diffusive regime is shown in dashed lines for comparison. From (West, 2016) with permission originally published by (Li and Raizen, 2013).

where D is the diffusion coefficient and t is the time. Without going into the underling physics of molecular diffusion we can observe, as did Einstein, that the average velocity $\bar{V}$ over a time t can be estimated using the MSD:

$$\bar{V} = \frac{\overline{\Delta X}}{\Delta t} = \frac{\sqrt{\langle \Delta X(t)^2 \rangle}}{t} = \frac{\sqrt{2D}}{\sqrt{t}}. \tag{28}$$

Consequently, for very short times, where one might expect the estimate to be better, the mean velocity diverges to infinity and therefore cannot represent a real velocity (Einstein, 1907). Using an argument based on the equipartition theorem of statistical physics Einstein concluded (Einstein, 1907):

> We must conclude that the velocity and direction of motion of the particle will be already very greatly altered in the extraordinary short time θ, and, indeed, in a totally irregular manner. It is therefore impossible - at least for ultramicroscopic particles - to ascertain $\sqrt{\overline{V^2}}$ by observation.

As Li and Raizen (2013) point out, it took more than a century for Einstein's conclusions to be experimentally challenged because of the technical difficulties of doing an experiment that can resolve a Brownian particle at times on the order of nanoseconds and within distances on the order of the radius of a hydrogen atom. Li et al. (2010) were able to achieve the incredibly high resolution in space and time necessary to measure the ballistic motion of the Brownian particle between molecular collisions using optical trapping interferometry.

Langevin's theory of Brownian motion (Langevin, 1908), based as it is on dynamic equations and not on probability arguments, is ostensibly valid at all times including for times much smaller than that for diffusion of the Brownian particle. It predicts ballistic motion for such short times and as a consequence the MSD is independent of the diffusion coefficient D and is given directly in terms of the fluid temperature T, Boltzmann's coefficient k_B, and the mass of the Brownian particle M:

$$\langle \Delta X(t)^2 \rangle = \frac{k_B T}{M} t^2, \tag{29}$$

yielding the average velocity:

$$\bar{V} = \frac{\sqrt{\langle \Delta X(t)^2 \rangle}}{t} = \sqrt{\frac{k_B T}{M}}, \tag{30}$$

a well-defined constant.

Li et al. (2010) determined the position and velocity of a 3 μm diameter silicon sphere confined in an air optical trap configured in a vacuum chamber. Without presenting the details of the experiment it is sufficient to note that the optical trap harmonically confines the particle in physical space where it is subject to thermal collisions with the air particles in the chamber. It is evident from **Figure 5** that the measured MSD deviates markedly from Einstein's theory of Brownian motion in the early time regime.

Langevin theory gives the proper ballistic behavior for a harmonic oscillator driven by random noise and the MSD was originally obtained in 1930 by Uhlenbeck and Ornstein (Uhlenbeck and Ornstein, 1930):

$$\langle [X(t) - \langle X(t) \rangle]^2 \rangle = \frac{2k_B T}{M\omega_0^2} \left\{ 1 - e^{-t/\tau_D} \left[\cos \omega_1 t + \frac{\sin \omega_1 t}{2\omega_1 \tau_D} \right] \right\} \tag{31}$$

where τ_D is the diffusion time scale, ω_0 is the resonant frequency of the optical trap and $\omega_1 = \sqrt{\omega_0^2 - (1/2\tau_D)^2}$. Note that the strength of the fluctuations driving the Langevin equation in the experiment are not proportional to the diffusion coefficient but to the temperature of the ambient air in the chamber. This solution is given by the solid curve in **Figure 5** with the parameter values determined from the experiment the fit to the data is excellent.

Like the story of Newton's linear theory of cooling the present tale of Brownian motion does not end here. You may have noticed that Einstein's theory was based on a Brownian particle in water, whereas Langevin's theory is applied to one in air and this highlighted the difference between the two theories at short times. The properties of the ambient fluid turn out to make a tremendous difference in which theory to apply because the momentum relaxation time scale in a liquid phase is 50 times greater than in a gas phase due to the difference in the ambient fluid density. It turns out that neither Einstein nor Langevin got it entirely right, because the dynamics of a freely moving Brownian particle is more subtle than either of them imagined. Brownian motion had been separated into microscopic and macroscopic by both men

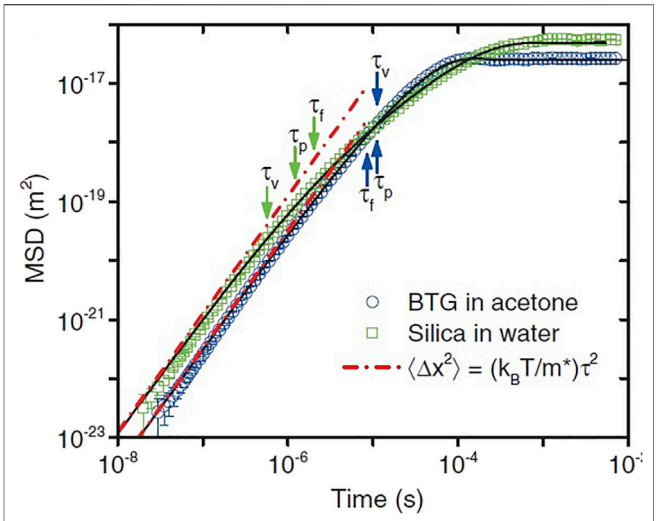

FIGURE 6 | Experimental and theoretical correlation functions from recorded trajectories of two different bead-fluid combinations. Double logarithmic plot of the MSD for an optically trapped barium titanate glass (BTG) bead (3.7 μm diameter) in acetone (blue circles; $\tau_p = 11.0\mu s$, $\tau_f = 8.5\mu s$, $\tau_v = 11.0\mu s$), and a silica bead (2.8 μm in diameter) in water (green squares; $\tau_p = 1.2\mu s$, $\tau_f = 2.01\mu s$, $\tau_v = 0.57\mu s$). The red dashed lines indicate the MSD of a particle moving at constant velocity. Adapted from (Kheifets et al., 2014) with permission.

but the phenomenon actually lives in the in-between world of the mesoscopic.

The force equation used to describe Brownian motion by Langevin is given by the direct application of Newton's Third Law to a spherical particle in water and that turned out to be the wrong approach. The phenomenon is more subtle than that. It requires taking into account the inertia of the ambient fluid. The derivation of the equation for the motion of a heavy spherical particle in a fluid, requires taking into account the back-reaction of the ambient fluid in contact with the Brownian particle. This back-flow of the fluid was first derived in 1885 by Boussinesq (Boussinesq, 1885) and independently 3 years later by Basset (Basset, 1888).

For a spherical particle of radius R in a fluid with a viscosity η the force law is given by (Clercx and Schram, 1992):

$$m^* \frac{dV(t)}{dt} = -\gamma V(t) - U'(X) + \eta(t) - \lambda \int_0^t \frac{d\tau}{\sqrt{t-\tau}} \frac{dV(\tau)}{d\tau}, \tag{32}$$

where $m^* = 1 + 0.5M_0/M$ is the ratio of the mass of the Brownian particle M to its value shifted by half the virtual mass of sphere of the same size in an incompressible fluid M_0; the ordinary Stokes friction with coefficient $\gamma = 6\pi\eta R/M$ is the first term on the right hand side of **Eq. 32**; the second term is a mechanical force modeled by the potential function $U(X)$; the third is the random force generated by the ambient fluid $\eta(t) = f(t)/M$; the final term is the memory associated with the hydrodynamic retardation effects with $\lambda = 6R^2\sqrt{\pi\rho\eta}/M$ and is today called the *Basset force*. Clercx and Schraom (Clercx and Schram, 1992) solve this equation using

Laplace transforms and the time-dependent solution fits experimental data over the entire time domain (Huang et al., 2011).

Mainardi and Pironi (Mainardi and Pironi, 1996) discuss the solution to **Eq.(32)** in terms of a FDE:

$$M\frac{dV(t)}{dt}+\lambda_0\partial_t^{1/2}[V(t)]=-\gamma_0V(t)-U'(X)+\eta(t), \qquad (33)$$

expressed here in terms of the Caputo fractional derivative $\partial_t^{1/2}[\cdot]$ and the parameters λ_0 and γ_0 are known functions of the fluid viscosity coefficient, the particle masses, and the radius of the Brownian particle, see the excellent paper (Mainardi and Pironi, 1996) for details. The optical trap previously used by the scientists in Raizen's lab to measure the instantaneous velocity of a harmonically bound particle in air (Li et al., 2010) and a bead in fluid (Huang et al., 2011) was again employed to test the theoretical predictions and interpretations of the Langevin equation modified to include the Basset force. The fit of theory (Clercx and Schram, 1992) to experiment is excellent (Kheifets et al., 2014) as indicated for the fit to the experimental MSD depicted in **Figure 6** by the solid black line segments.

We note that fractional Brownian motion and fractional diffusion in general has attracted significant attention recently and now techniques have been developed to identify the fractional diffusion equation from datasets (Znaidi et al., 2020). This is part of the vast literature due to space limitations we can only mention in passing.

Inanimate and Living Particles

As emphasized a number of times the FD term in **Eq. 33** is the result of the back-reaction onto the Brownian particle by the ambient fluid flowing around it, inducing the retarded viscous force. The solution to this equation is asymptotically dominated by viscous dissipation and the Brownian particle being 'heavy' accounts for the success of the usual description of Brownian motion without the inclusion of the FD term. However, when the ambient fluid is not homogeneous, or the Brownian particle is not 'heavy', the derivation of the forces acting on the Brownian particle need to be re-examined.

Leptos et al. (2009) conducted experiments on the motion of tracers (Brownian particles) suspended in a living fluid of swimming Eukaryotic micro-organisms of varying concentrations. The interplay between the inanimate Brownian particles and the advection by flows from the swimming micro-organisms results in their displacement having a self-similar PDF with a Gaussian core and exponential tails. Eckhardt and Zammert (2012) re-analyzed these data and obtained an excellent fit to a MLF PDF based on the continuous time random walk (CTRW) model.

A theoretical study of a simplified tracer-swimmer interaction by Zaid et al. (2011) show that the non-Gaussian effect of the tails of the PDF can also arise from a combination of truncated Lévy statistics for the velocity field and the IPL decay of correlations in the ambient fluid. They further show that the dynamics of the PDF leading to the truncated Lévy statistics is given by a fractional diffusion equation, which we discuss subsequently. It is evident that rigorous modeling of Brownian motion in heterogeneous fluids such as microbial suspensions in marine ecologies would potentially benefit from applications of the FDC.

Fractional Brownian Motion and the Fractional Calculus

It occurs to me that the above discussion of Brownian motion contained no mention of the fact that one of Mandelbrot's first formal applications of the fractal concept was to a generalization of this stochastic process. In the paper where Mandelbrot and van Ness (Mandelbrot and van Ness, 1968) introduced the term fractional Brownian motion (*FBM*) they made use of the fractional calculus, but did not think the FC was sufficiently significant to develop further given the context of its utilization and their interpretation of it as a moving average. The fractional operator they used in the definition of *FBM* had been defined by Weyl (1917) in 1917:

$$B_H(t_1)-B_H(t_2)=\frac{1}{\Gamma(\alpha)}\left[\int_{-\infty}^{t_1}\frac{dB(\tau)}{(t_1-\tau)^{1-\alpha}}-\int_{-\infty}^{t_2}\frac{dB(\tau)}{(t_2-\tau)^{1-\alpha}}\right] \qquad (34)$$

where $dB(t)$ is a Wiener process, $\alpha = H + 1/2$ and as they point out the properties of *FBM* corresponding to the Hurst parameter $0 < H < 1/2$, $1/2 < H < 1$, and $H = 1/2$, respectively, differ in many significant ways. This in itself has led to a vast literature some of which are summarized in *Crucial Events* (West and Grigolini, 2021).

Fractional Differential Equation Models of Cell Growth

In the prequel (West, 2021) we discussed the ubiquity of fractal time series, factal dynamics and fractal geometric structure in physiological phenomena. The analysis gave rise to scaling as a way to directly interconnect the very large with the very small, as well as the very fast with the very slow. The prequel closed with a suggestion that the FC is a systematic way to incorporate spatial inhomogeneity into describing how information is transported across a complex dynamic network. That suggestion was augmented by another involving memory effects in physiologic networks being generic (Goldberger et al., 2002) and the FC was also pointed out by Nasrolahpour (Nasrolahpour, 2017) as being the natural way to incorporate memory effects into the modeling of various complex phenomena including the growth of cancer tumors.

He (Nasrolahpour, 2017) proposed a new model which is a member of a class of simple models that have been extensively used to describe the growth of stem and cancer cells. Following up on his comment about the utility of this mathematical technique in modeling cancer cells I found that over the past decade it had become a cottage industry with hundreds of papers being published each year on the modeling of cancer.

The mathematician Durrett (Durrett, 2013) in a personal perspective on cancer modeling pondered that 80% of the problem is figuring out what the appropriate question is in the biological application and what mathematical tools to use in answering it. This is unlike physics where the applications are

typically formulated in such a way that a mathematician may immediately see how s/he might be able to help solve the problem. Or in some cases, like Dirac's introduction of the delta function in quantum mechanics based solely on his intuition of the physics problem, he saw that the problem required the existence of such an object for its solution. The delta function led to the development of new area of mathematics providing justification of that intuition and provides a useful tool to the broader scientific community once they had caught up with Dirac's intuition.

With this in mind I have elected to concentrate the following remarks on those aspects of biology and medicine which I believe provide the reasons for FDE being the appropriate mathematics for oncological modeling. We use the master equation for the size distribution of cancer cell colonies $P(x, t)$, defined as the probability that a single cancer cell gives rise to a colony consisting of x cells at time t. The PDF evolves according to the master equation with nearest neighbor interactions and constant coefficients from (Nasrolahpour, 2017) with a slight change in notation:

$$\frac{dP(x,t)}{dt} = \begin{pmatrix} a & -(a+b)x & b \end{pmatrix} \begin{pmatrix} P(x-1,t) \\ P(x,t) \\ P(x+1,t) \end{pmatrix}, \tag{35}$$

where b is the probability per unit time that a cell dies and a is the probability per unit time a cell divides into 2 cells. The equation for the growth of the average colony size is obtained by multiplying **Eq. 35** by x and summing such that after some algebra we obtain the integer rate equation (IRE) for the average size of the colony:

$$\frac{d\langle x(t)\rangle}{dt} = (a-b)\langle x(t)\rangle, \tag{36}$$

which has the exponential solution for the initial value $P(x, t = 0) = \delta_{x,1}$:

$$\langle x(t)\rangle = e^{(a-b)t}. \tag{37}$$

Nasrolahpour (2018) states without discussion that his new model of cancer replaces the IRE for the average cancer cell colony size with a FRE. Note that this could be viewed as an adaptation to the cancer problem of the DMM social interaction model introduced in **Section 2**. We propose doing that here, but instead of an ansatz we apply the *network effect* argument to the interaction of the cell of interest, the one that gives rise to the cancer colony, and transform the IRE into the FRE:

$$\partial_t^\alpha [\langle x(t)\rangle] = \lambda^\alpha \langle x(t)\rangle. \tag{38}$$

Here we have raised the rate $\lambda = a - b$ to the power of the noninteger derivative α in order to retain the same dimensionality on both sides of the equality. Like most differential equations, integer or fractional, we guess the form of the solution and explicitly determine whether or not it solves the equation of interest. The network effect argument applied to a growing population of cells leads to the FDE given by **Eq. 14** and the solution **Eq. 16** which also solves Eq(38) for $\varepsilon = 0$.

Solving the Linear Fractional Rate Equation

It is time to introduce some of the new mathematics that show how to solve this class of linear FREs. Can we use the Taylor series expansion technique to solve a linear FRE or a more general FDE? The answer is yes, as long as we are sufficiently cautious in doing so. The first caution involves generalizing the Taylor series. We start as with IDEs and introduce a Taylor series for the assumed form of the solution. But with a little thought realize that the Taylor series must be generalized to accommodated the noninteger order of the derivative (West, 2017) in the following way:

$$\langle x(t,\alpha)\rangle = \sum_{n=0}^{\infty} A_n t^{n\alpha}, \tag{39}$$

where we have tagged the proposed solution with the index α to match the FRE that is solves. The noninteger derivative $\partial_t^\alpha[\cdot]$ in the FRE must satisfy the familiar derivative relation from the ordinary calculus:

$$\partial_t^\alpha \left[t^\beta\right] = \frac{\Gamma(\beta+1)}{\Gamma(\beta+1-\alpha)} t^{\beta-\alpha}, \tag{40}$$

when all exponents are integers and $\Gamma(\cdot)$ is a gamma function. This same relation holds when the exponents are not integers (Podlubny, 1999; West et al., 2003a) in which case substituting the generalized Taylor series into the FRE given by **Eq. 38** yields:

$$\begin{aligned} &A_0 \frac{t^{-\alpha}}{\Gamma(1-\alpha)} + A_1 \frac{\Gamma(\alpha+1)}{\Gamma(1)} + A_2 \frac{\Gamma(2\alpha+1)t^\alpha}{\Gamma(\alpha+1)} + \cdots \\ &\quad = \lambda^\alpha \{A_0 + A_1 t^\alpha + \cdots\}. \end{aligned} \tag{41}$$

Equating coefficients of equal powers of time from both sides of the equation yields:

$$A_1 = \frac{\lambda^\alpha A_0}{\Gamma(\alpha+1)};\ A_2 = \frac{\lambda^\alpha \Gamma(\alpha+1) A_1}{\Gamma(2\alpha+1)};\ A_3 = \frac{\lambda^\alpha \Gamma(2\alpha+1) A_2}{\Gamma(3\alpha+1)};\ \text{etc.},$$

all of which can be generated from the compact form:

$$A_n = \frac{\lambda^{n\alpha}}{\Gamma(n\alpha+1)} A_0, \tag{42}$$

and the $n = 0$ term is a tautology. A A_0 term is left over in the process of equating coefficients since the IPL in time given by $t^{-\alpha}$ only appears on the LHS of **Eq. 41** and must be otherwise accounted for in the analysis. This is the second place where we must be cautious.

Collecting the coefficients from **Eq. 42** into the generalized Taylor series after some algebra yields the curious result:

$$\partial_t^\alpha [\langle x(t,\alpha)\rangle] - \frac{t^{-\alpha}}{\Gamma(1-\alpha)} \langle x(0,\alpha)\rangle = \lambda^\alpha \langle x(t,\alpha)\rangle, \tag{43}$$

and since the $n = 0$ term in the generalized Taylor series is not excluded **Eq. 43** is a new FRE. The new FRE explicitly displays the

term that was not canceled when the generalized Taylor series was introduced to solve the original FRE and here the unknown coefficient is identified with initial value of the average cancer colony: $A_0 = \langle x(0,\alpha)\rangle$. With the coefficients inserted into **Eq. 39** the generalized Taylor series yields the exact solution to the revised FRE:

$$\langle x(t,\alpha)\rangle = \langle x(0,\alpha)\rangle \sum_{n=0}^{\infty} \frac{(\lambda t)^{n\alpha}}{\Gamma(n\alpha+1)}. \tag{44}$$

Remarkably the fractional derivative on the LHS of **Eq. 43** has a name, the Riemann-Liouville ($\mathcal{RL}$) fractional derivative (FD), and has a long lineage. To make contact with that long history and for notational clarity we rewrite **Eq. 43**:

$$\mathcal{D}_t^{\alpha}[\langle x(t)\rangle] - \frac{t^{-\alpha}}{\Gamma(1-\alpha)}\langle x(0)\rangle = \lambda^{\alpha}\langle x(t)\rangle, \tag{45}$$

where we have suppressed the α – dependence of the solution and added a new symbol $\mathcal{D}_t^{\alpha}[\cdot]$ to denote the $\mathcal{RL}$-fractional derivative. The exact solution to the $\mathcal{RL}$ FRE is expressed in terms of a series first obtained by the mathematician Mittag–Leffler in the early 20th century and which now bears his name:

$$\langle x(t)\rangle = \langle x(0)\rangle E_{\alpha}([\lambda t]^{\alpha}). \tag{46}$$

The MLF in simplest form is given by the series:

$$E_{\alpha}(z) = \sum_{j=0}^{\infty} \frac{z^j}{\Gamma(j\alpha+1)}, \tag{47}$$

and is here called out explicitly because it appears over and over in both the discussion of applications and in the formal theory of the FDC. Note that the MLF series sums to an exponential for $\alpha = 1$, which accounts for the identical form of the solutions in the linear cooling example. It should also be stressed that like the exponential in the ordinary calculus the MLF appears as the backbone to the solutions of more complicated FDEs, as seen elsewhere (Podlubny, 1999; West, 2016; West, 2017).

Altrock et al. (2015) point out that a branching process is a powerful mathematical tool for the study of cancer population growth. In addition they emphasize that this growth model is based on the assumption that cellular events, such as mutation, replication and death, are independent of one another and is assumed for mathematical simplicity. This independence assumption would be partially removed by taking into account the network effect. The resulting generalization of **Eq. 46** would be the case where, at any time, each cell is fully described by cell-intrinsic probability rates of proliferation, mutation, and death, as well as the parameter of the FRE noninteger order. The latter parameter α provides a measure of the level of internal dependency of the intrinsic dynamic processes.

Tumor Nonlinear Dynamics

In the previous subsection we took advantage of the linear master equation to show how probabilistic arguments can be generalized using the FC for a linear dynamic system. In the present section we take a different tack and instead briefly review a number of growth models that have been borrowed from the social sciences and adapted for the modeling of tumor growth. Each of these borrowed and adapted models is nonlinear and that provides a new degree of difficulty in solving the resulting equations. Recall that the FRE obtained from the network effect took such nonlinearities into account without explicitly linearizing the full dynamics of a network.

The most famous of the nonlinear growth equations was introduced into social science by Verhulst in 1838 in order to provide a rationale for a way to limit the world's population and thereby alay the fears resulting from the dismal forecasts of Maltus, who predicted unflagging exponential population growth that would all too soon quench the world's linearly growing food supply, resulting in world-wide famine. The nonlinear equation of Verhulst has become known as the logistic growth model and as pointed out by Varalta et al. (2014) has been used to successfully describe the growth of populations in both the laboratory and in natural habitats, limiting the growth by influencing factors of competition, mortality and fertility. As more complex effects enter into the modeling, such as interactions within food webs, a number of investigators have generalized the logistic equation using the FC to help slow the convergence to the population's carrying capacity.

Much of the previous work in this regard has been on the numerical simulation of fractional nonlinear growth models (FNGMs) and a number of these numerical methods were used to test analytic results, see e.g., the 51 papers devoted to the *Future Directions in FC Research and Applications* (Meerschaert et al., 2017) as an exemplar of the rigorous mathematics being done in this area.

Fractional Logistic Equation

Varalta et al. (2014) are investigators whose work bridges the gap between the complexity of medicine and the mathematics on which medical models can be based. The Malthusian model of exponential growth flies in the face of observation, whether it is the growth of a population of humans or of cells. What all growth processes have in common is that the population must be continually supplied with nutrients, the individual members must be born and they eventually die. This is the process that Malthus modeled and is incorporated into the master equation **Eq. 35** with a modest generalization in the form of the distribution of possible futures, but with the pessimism of Malthus being the final average outcome. Verhulst introduced the idea that a society has a finite carrying capacity, such that the rate of growth is dependent on the population and this rate goes to zero as the carrying capacity of the population is approached:

$$\frac{dX(t)}{dt} = \lambda[1 - X(t)]X(t), \tag{48}$$

where if $N(t)$ is the instantaneous population and N_T is the carrying capacity (the maximum population the society can maintain) we have $X(t) \equiv N(t)/N_T$. The Verhulst or logistic equation is popular because it: 1) provides a reasonable explanation for why the exponential growth is suppressed; 2)

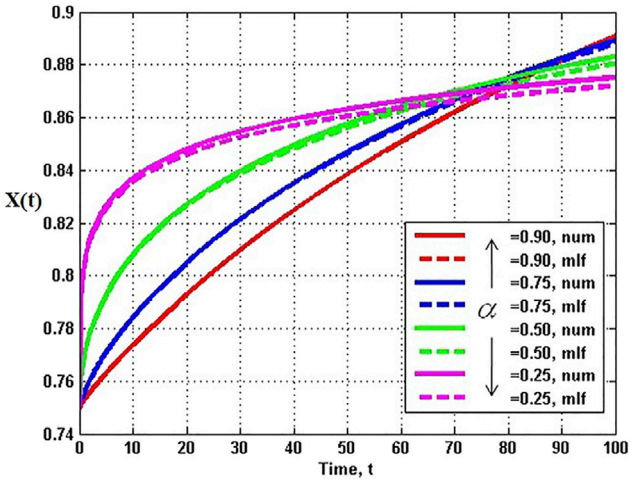

FIGURE 7 | Analytic solutions to the fractional logictic equation (solid) for a number of fractional derivatives are compared to the numerical solutions (dashed) for the values of the fractiona-order α indicated with $X(0) = 0.75$, $\lambda^{\alpha} = 0.1$, and time step 0.001. From (West, 2015) with permission.

the growth is eventually sub-exponential and saturates at a finite value; 3) the logistic equation has an analytic solution.

The analytic solution to the logistic equation is obtained by making the substitution of variables $Y(t) = 1/X(t)$ to obtain the linear growth equation:

$$\frac{dY(t)}{dt} = \lambda[1 - Y(t)], \tag{49}$$

which is solved in terms of $e^{\lambda t}$ and the initial population $X(0)$. Inverting the substitution variable in the solution to this linear equation yields the sigmoidal solution to the logistic equation:

$$X(t) = \frac{X(0)}{e^{-\lambda t} + (1 - e^{-\lambda t})X(0)} \underset{t\to\infty}{\longrightarrow} 1, \tag{50}$$

which asymptotically approaches the carrying capacity, which is 1 in these units.

There are a number of ways to introduce the fractional calculus into the logistic model of growth. One way is through the introduction of the Carleman embedding technique, which follows from the theorem that any finite order nonlinear equation of motion can be replaced by an infinite order set of linear equations (West, 2015). Another is a spectral technique to solve a nonlinear FDE (Turalska and West, 2017). Both these approaches start from the fractional logistic equation:

$$\partial_t^{\alpha}[X(t)] = \lambda^{\alpha}[1 - X(t)]X(t), \tag{51}$$

where one might have used the subordination method introduced in **Section 2.1** to replace the integer order time derivative with the Caputo time derivative. We now know that the fractional derivative in time incorporates memory into the population dynamics. Both the Carleman embedding and spectral techniques yields the same solution to the fractional logistic equation (Turalska and West, 2017):

$$X(t) = \sum_{n=0}^{\infty}\left(\frac{X(0) - 1}{X(0)}\right)^n E_{\alpha}(-n\lambda^{\alpha}t^{\alpha}), \tag{52}$$

which is an expansion over a set of eigen functions given by the MLFs, and the coefficients are in terms of powers of the initial value. Note that asymptotically all the MLFs go to zero except the $n = 0$ term which yields the carrying capacity of the network. The choice $\alpha = 1$ reduces the MLF to the exponential $e^{n\lambda t}$ and the sum over eigen functions in Eq. 52 reduces the solution to the ordinary logistic equation given by **Eq. 50**.

The analytic series solution to the fractional logistic equation given by **Eq. 52** is compared with the numerical integration of the FDE in **Figure 7** each for the same time step and initial condition. It is evident by inspection that the closer the fractional order is to unity the closer the correspondence between the analytic and numerical results. There are some technical issues with this solution which are addressed in (Turalska and West, 2017), but their discussion would take us too far into the mathematical weeds to be of value here.

A very different way of introducing the influence of the FC on the logistic growth is made by (Varalta et al., 2014). They cleverly introduce the fractional derivative into the linear growth of the transformed variable $Y(t)$, which was introduced in **Eq. 49** rather than in the nonlinear equation given by **Eq. 51**. This choice for the insertion of the fractional derivative essentially introduces the network effect into the time rate of change of the population-dependent growth rate:

$$\partial_t^{\alpha}[Y(t)] = \lambda^{\alpha}[1 - Y(t)], \tag{53}$$

rather than into the population dynamics directly. Taking the Laplace transform of the linear equation, after some algebra the Laplace equation can be inverted to yield the solution to the initial value problem:

$$X(t) = \frac{X(0)}{E_{\alpha}(-\lambda^{\alpha}t^{\alpha}) + X(0)[1 - E_{\alpha}(-\lambda^{\alpha}t^{\alpha})]}. \tag{54}$$

However, these solutions are equal when $\alpha = 1$ and MLF becomes an exponential, just as did **Eq. 52** even though these two solutions appear to be very different from one anothe for $\alpha < 1$.

These authors (Varalta et al., 2014) point out that the use of such sophisticated mathematical techniques in the modeling of medical pathologies is of recent vintage, particularly in the study of cancer tumors. They consider this to be one of the reasons that the methods are still finding difficulty in modeling the growth of tumors satisfactorily:

> In the case of tumor dynamics saturation of various types of tumors is not well modeled by the exponential model. For this reason, this model applies only to avascular tumors, i.e., when angiogenesis has not occurred. . .Indeed, tumor cells compete for oxygen and vital resources that is the reason why the logistic model fits well in several cases. . .

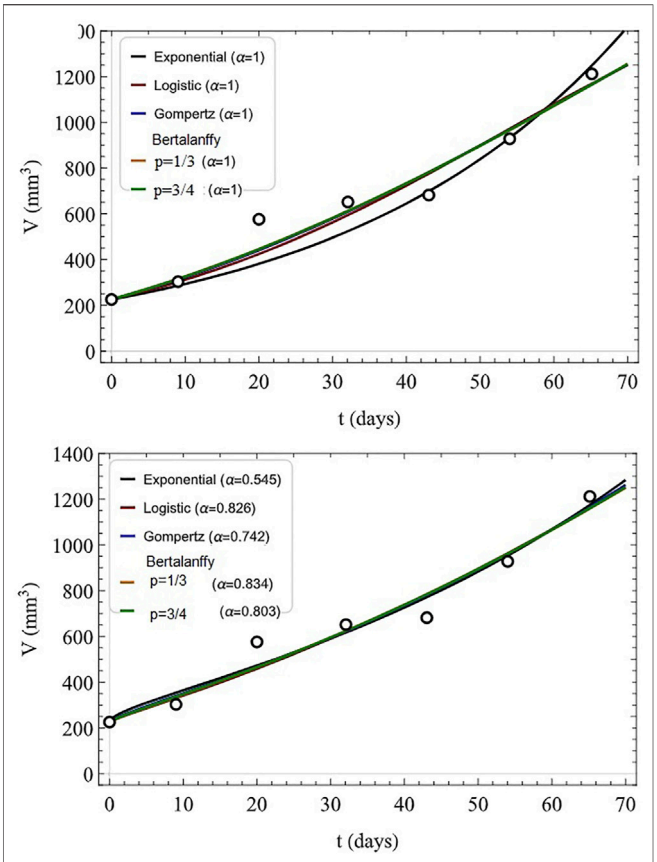

FIGURE 8 | Fitted tumor growth: clinical data (circles), numerical fits to data (first seven data points). The models used are indicated for IDE (top, $\alpha = 1$) and FDE with indicated values of α (bottom). Adapted from (Valentim et al., 2020) with permission.

We can here answer the question as to whether the fractional forms of the logistic equation and that of the linear form in the transformed variable have the same solution. Taking the solution given by Eq(54) and expanding it is an infinite series yields:

$$X(t) = \sum_{n=0}^{\infty} \left(\frac{X(0) - 1}{X(0)} \right)^n [E_\alpha(-\lambda^\alpha t^\alpha)]^n, \tag{55}$$

and the inequality:

$$E_\alpha(-n\lambda^\alpha t^\alpha) \neq [E_\alpha(-\lambda^\alpha t^\alpha)]^n, \tag{56}$$

establishes proof that the solutions given by **Eqs. 52** and **54** are not the same. The relation between the MLFs becomes an equality in the singular case $\alpha = 1$ and the MLF becomes an exponential. However, this does not tell us which of the two models better describes the growth of tumors. In fact since there is no universal law to describe tumor growth these two contenders remain in competition with a host of others, all of which await the detailed fit to extended datasets.

Mathematical Oncology and Fits to Data

Oncology is the branch of medicine that deals with the treatment, diagnosis, and prevention of cancer and the models of tumor growth are within the ever broadening domain of MO. As pointed out by Valentim et al. (2020) all solid cancers originate with the growth of a primary tumor, and the majority of the growth patterns follow a sigmoidal shape determined by the population's growth rate and carrying capacity. They go on to argue that the IDE models for tumor growth possesses certain deductive-reductionistic characteristics that are maintained when such models are generalized to fractional form, for example, the inclusion of memory and heterogeneity effects in fractional MO (FMO).

Valentim et al. (2020) study the deviation in tumor growth from a simple exponential for the analytic solutions for four distinct nonlinear growth models in the IDE as well as the solutions to their fractional generalizations. The FDE and IDE ($\alpha = 1$) models considered have the generic form:

$$\partial_t^\alpha [u(t)] = af(u) - bg(u), \tag{57}$$

here $V(t)$ is the size of the tumor volume at time t, the two functions f and g determine the functional form of the growth: fractional exponential $u = V, f = V, g = 0$; fractional logistic $u = 1/$

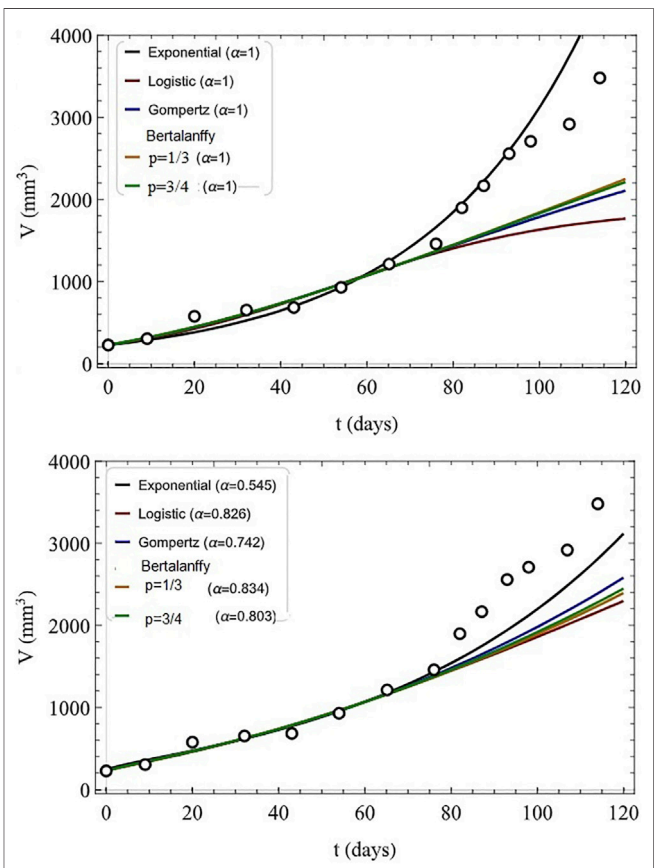

FIGURE 9 | Predicted tumor growth: clinical data (circles). The models used are indicated for IDE (top, $\alpha = 1$) and FDE with indicated values of α (bottom) and the last seven data points are predicted using the model parameters obtained in **Figure 8**. Adapted from (Valentim et al., 2020) with permission.

$V, f = au, g = 1$; fractional Gompertz $u = lnV, f = 0, g = u$; fractional Bertalanffy $u = V^p, f = p, g = pu$ where p is a rational fraction. The solutions to the exponential and logistic forms have been presented in previous sections and the remaining models are solved using the methods discussed and may be expressed in terms of MLFs (Valentim et al., 2020).

The algebraic form of the various solutions are not as important as their flexibility in fitting tumor growth datasets. Such fits are indicated in **Figure 8** where the first seven tumor volume data points are indicated along with fits to the IDE models (top) and their FDE generalizations (bottom).

Using the parameters fit of the first seven data points to the model parameters the prediction of the next seven data points are indicated in **Figure 9** with the IDE models (top) and their FDE generalizations (bottom). Valentim et al. (2020) discuss the relative merits of the modeling of tumor growth using integer versus fractional time derivatives:

> If one also considers fractional models instead of only their classical versions, the indicator for how close the best model replicates experimental data would rise from 67.5 to 88.8% - a very significant improvement. This reveals a major convenience of using fractional models as they keep a higher degree of information regarding the fitted time series, decreasing the chance of misfitting while still maintaining a relatively simple and reductionist form. Such advantage is mainly attributed to the memory effect, a characteristic inherently linked to the definition of fractional operators allowing models to consider not only elements at the evaluation instant but also those occurring before. This feature naturally favors fractional models to describe biological phenomena.

This improvement in the mean-square error supports the interpretation that the FDE models include more information of the cancer time series being fitted than do the IDE models.

In spite of the positive observations made regarding the fractional models it is evident from the comparison with real data that neither the IDE nor FDE models provide an accurate prediction of the asymptotic size of the tumor. On the other hand, even slightly better predictions may improve clinical assessments so the choice of FDE model should be made very carefully (Valentim et al., 2020).

Our intent here is not to argue for the superiority of one numerical fitting technique over another. Rather it is to provide insight provided by a new mechanism available to a FDE model that is not reachable using IDE models. The fitting of the fractional derivative order to the first seven data points provides a mechanism not available to IC fitting procedures. This fitting of the order of the fractional derivative to the early data means that any early change in the internal dynamics can be captured and influences the later system behavior.

The closest analog to this situation in the IC modeling of complex systems is the telegrapher's equation (TE). The diffusion process is generalized in two important respects for telegraphic processes: 1) the TE allows for a finite velocity of information propagation which is infinite in the diffusion equation and 2) the TE at short times describes nearly deterministic wave propagation, whereas at long times the TE supports diffusive behavior.

In the one-dimensional case the MSD for the solution to the time-fractional TE at early times describes wave motion with damping and at late times diffusion with a finite velocity (Masoliver, 2021):

$$\langle X(t)^2 \rangle \begin{cases} \sim t^{2\alpha}, \ t \to 0 \\ \sim t^{\alpha}, \ t \to \infty \end{cases}.$$

For the IC TE we have $\alpha = 1$ and obtain the familiar IC results. When generalized to the fractional order TE with $\alpha < 1$ the solution is a bi-fractal with the fractal dimension halving from one asymptotic time regime ($t \to 0$) to the other ($t \to \infty$). We refer the interested reader to the excellent review by Masoliver (Masoliver, 2021) for details and we shall have more to say on the notion of multifractal behavior and its relation to FC subsequently.

Variable Fractional Order

The fitting of the fractional growth models to the tumor dataset has so far not exploited the full flexibility of the FC. We have replaced the IDE growth models, both linear and nonlinear, with their FDE generalizations. In making these replacements we have used two distinct arguments. One based on the network effect and the other on the time subordination method. We now examine an additional generalization of both these techniques and consider what might make the fractional order of the time derivative itself a function of time, that is, what property of tumor growth would entail:

$$\partial_t^{\alpha}[\cdot] \to \partial_t^{\alpha(t)}[\cdot], \tag{58}$$

where $\alpha(t)$ is a time-dependent fractional order derivative and is called a time profile in (Valentim et al., 2021). Such a time-dependency could incorporate into the growth process the changes in physical characteristics and biomechanical modifications that tumors undergo while advancing toward their malignant final state.

When a mechanical force is applied to a solid body that body changes shape in response to the applied force; these deforming forces are collectively called *stresses* (σ) and the deformation the body undergoes under stress is called *strain* (ε). An object that undergoes deformation can do one of two things after the stress is released. An elastic material object returns to its original shape immediately, whereas a plastic material object will retain its deformation for some length of time including permanently. The branch of physics dealing with study of the dynamics of plastic materials goes by a number of different names including rheology, viscoelasticity and hereditary solid mechanics, all of which address the solution of dynamic stress-strain relations. It is in this context that the time-dependent fractional derivative expressed in **Eq. 60** has been most fully motivated for application in MO (Di Paola et al., 2020; Valentim et al., 2021).

Di Paola et al. (2020) note that the response of a linear viscoelastic material to a generic imposed strain or stress history is obtained by applying Boltzmann's linear superposition principle:

$$\sigma(t) = \int_0^t \Phi(t-\tau)d\varepsilon(\tau), \tag{59}$$

$$\varepsilon(t) = \int_0^t J(t-\tau)d\sigma(\tau), \tag{60}$$

where $\Phi(t)$ is the relaxation function from a constant strain $\varepsilon(t) = \varepsilon_0\Theta(t)$, and $J(t)$ is the creep function for a constant stress $\sigma(t) = \sigma_0\Theta(t)$ and $\Theta(t) = 1$ for $t \geq 0$, and $= 0$, for $t < 0$. Under the linearity assumption these expressions are readily extended to complex FDE form with a constant power law index, see e.g., West et al. (2003a). In the linear regime the creep law is:

$$J(t) = \frac{t^\alpha}{\mathcal{E}_\alpha \Gamma(1+\alpha)}, \tag{61}$$

and the relaxation function is:

$$\Phi(t) = \frac{\mathcal{E}_\alpha t^{-\alpha}}{\Gamma(1-\alpha)}, \tag{62}$$

and $0 < \alpha < 1$ and the standard generalizations to the FC for the stress-strain relations can be made. Note that this is the physical basis for the failure of linear IDEs to describe what appeared to be simple phenomena until the environment was more completely analyzed and found to introduce either memory or spatial heterogeneity into the dynamics.

However even the more familiar arguments breakdown when the dynamics become nonlinear, because in that situation the Boltzmann superposition principle no longer applies. However, if α and $\mathcal{E}_\alpha$ are constant and the nonlinearity involves only the level of stress, the Boltzmann superposition principle holds in a space different from the traditional (ε, σ)-space and the response properties may be represented by the FC operations of constant order. As stated by Di Paola et al. (2020):

> However, for the purpose of handling systems where $\mathcal{E}_\alpha$ and α may change during the time interval of interest new and pertinent fractional calculus tools should be considered rather than variable-order fractional-operators, as obtained from classical fractional operators upon replacing the constant order with a variable one; indeed, these operators implicitly rely on the assumption that the Boltzmann linear superposition holds true in the classical form, which may not be a rigorous assumption in the presence of the nonlinearity associated with changing values of α.

The approach developed by Di Paolo et al. is not presented here due to space constraints, but does warrant a number of additional comments. As they point out their proposed approach is an effective way to build the stress (strain) response of a nonlinear viscoelastic material body having time-dependent fractional order operators to a general imposed strain (stress) history. Throughout the observation time interval it is assumed that the evolution of the parameters α and $\mathcal{E}_\alpha$ are known at each instant of interest.

Here we demonstrate the utility of a time-varying order $\alpha(t)$ using the previously fitted tumor growth dataset. This is done even though such a mathematical description of specific time-dependent tumor features are not known *a priori*. Valentim et al. (2021) use an exploratory approach and capture the 14 data point history of the tumor in the value of the order of the time derivative with a Taylor series:

$$\alpha(t) = \sum_{n=0}^{N} \alpha_n t^n, \tag{63}$$

where the $n = 0$ coefficient corresponds to the fixed-order FC model. The FRE for tumor growth is given by **Eq. 38** with time-varying order and has the MLF solution for the growth of the tumor volume $V(t)$:

$$V(t) = V_0 E_{\alpha(t)}\left(\lambda t^{\alpha(t)}\right), \tag{64}$$

where the MLF has the form defined by **Eq. 47**. The fitting of the MLF solution with time-varying order to the 14 data points is given in **Figure 10** for four consecutive orders of the polynomial in the Taylor series. The variable-order models fit the dataset better than either the solution to the IRE or to the FRE with errors to the fit that decrease with the order of the polynomial N in **Eq. 63**.

Note the two very different strategies for fitting the same dataset in **Figures 9**, **10**. The former uses a nonlinear FRE with a fixed order whose numerical value varies with the model nonlinearity to fit the early time well but does not do well in predicting the tumor volume at late times. The latter multistep experimental model tunes the profile of the time varying order to a third-order polynomial that appears to capture the nuances of the pattern of growth of the tumor volume extremely well. Valentim et al. (2021) emphasize that these latter results indicate the superiority of the proposed strategy for describing experimental data and provides a new perspective for modeling tumor growth. They also explain the difference between a time varying rate of growth $\lambda(t)$ and the variable-order $\alpha(t)$. While it is true that the time variable order does in fact ultimately dictate the time changes in the growth rate the biomedical interpretation of $\alpha(t)$ goes a great deal deeper. A possible source of the time-variability is the fractional stress-strain relations just discussed to take into account the tumor evolution, but in addition how that influence may change during the separate growth stages.

Valentim et al. (2021) make a strong case for interpreting $\alpha(t)$ as a memory index, which may potentially translate the time variation to the activation and/or development of identifiable hallmarks of tumor evolution:

> When $\alpha \approx 1$ tumors follow an exponential increase "programmed" in their original cells (activating hallmarks related to the evasion of growth suppressors and sustainability of proliferative

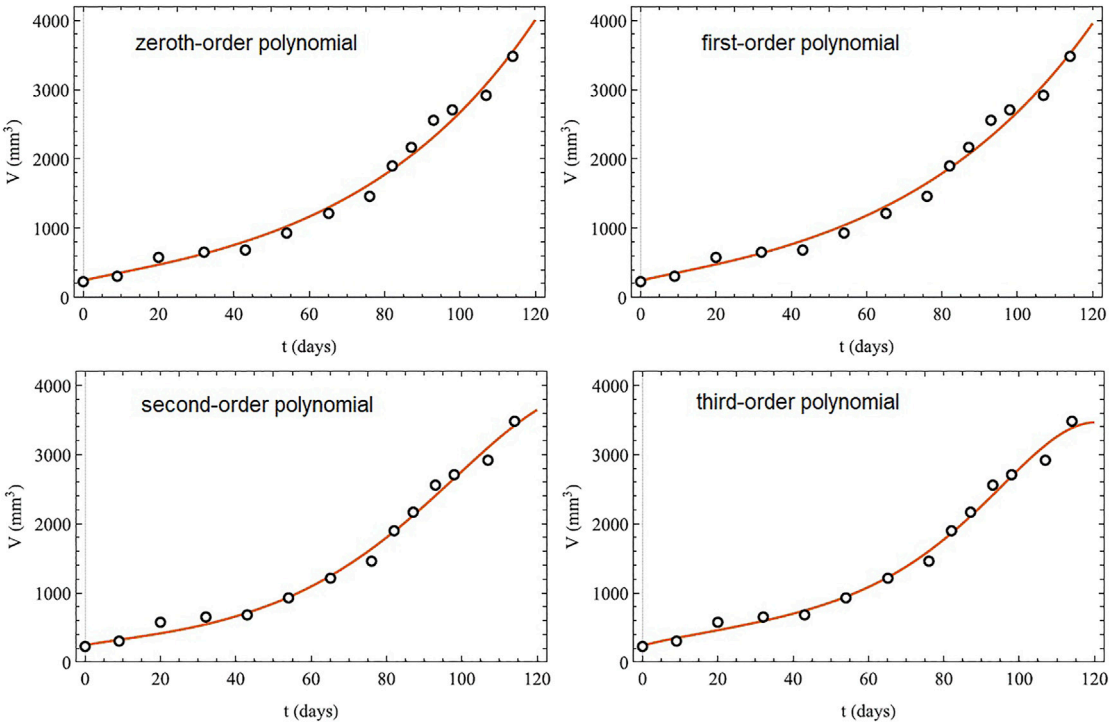

FIGURE 10 | Tumor growth: comparison between clinical data (open circles) and the best-fit variable-order models (solid line segment) given by the MLF solution **Eq. 64** with λ = 0.090 8. The time-varying order is given by the Taylor series with N terms **Eq. 63**. Adapted from (Valentim et al., 2021) with permission.

signaling). On the other hand, when α is lower tumors evolve at a slower growth rate, potentially due to challenges from the microenvironment (e.g., shortage of nutrients, extracellular matrix resistance). In this case, they "forget" (or inactivate) part of their original programming, developing traits suitable to their current evolution stage (hallmarks related to angiogenesis and invasion).

Distributed Fractional Order Derivative and Multifractality

Another of the avenues we have not explored is signal processing and here again Mandelbrot was the first to recognize that signals that are singular at almost every point are encountered everywhere including in physiological datasets. One historical strategy for interpreting a signal in communication theory is to construct the reciprocal integral relations of Fourier and although the method is mathematically unassailable the interpretation of the various derived quantities have been called into question. The basis for these questions is the mutually exclusive treatment of time and frequency in the specification of the signal, that is, the time series is assumed to have infinite length and each frequency is defined for an infinite monochromatic wave train. In the real world, particularly in medicine, all time series are of finite duration and frequencies change over time. The recognition of this limitation of the (time, frequency) -representation of Fourier signals led to the development of the *wavelet transform* method for representing one-dimensional signals as a function of time and frequency (Mallat, 1999).

Here let us define the wavelet transform T_g (a, b) of a time series $X(t)$ with respect to a wavelet g, which is broadly interpreted as being equivalent to a mathematical microscope whose magnification is $1/a$, whose position in the time series is b, and whose optics are given by the choice of the specific wavelet function g (West, 1990). I bring this up here because one can relate this formalism to the FC by applying a wavelet transform to a fractal function, say a function describing the growth of a tumor, as we sketch below.

A fractal function is self-affine and can be generalized by examining the local scaling properties of the function at small scales. Consider an arbitrary point t_0 in the time series $X(t)$:

$$X(t_0, t) = X(t + t_0) - X(t), \tag{65}$$

and the function remains the same up to a scale factor at different length scales. In this case self-affinity at the point $t_0 < t$ means that by scaling the local variable t with a parameter $\lambda > 0$ yields:

$$X(t_0, \lambda t) = \lambda^{\alpha(t_0)} X(t_0, t). \tag{66}$$

The parameter α is the local scaling exponent at t_0 and can be shown to be the fractal dimension of the process being measured $X(t)$. The fact that α is a function of t_0 means that the time series $X(t)$ is multifractal; when the scaling index is independent of t_0 then $X(t)$ is a homogeneous fractal. **Equation 66** was established

using the wavelet transform to construct the scaling relation (West, 1990):

$$T_g(\lambda a, \lambda b + t_0)X(t) = \lambda^{\alpha(t_0)+1/2} T_g(a, b + t_0)X(t), \tag{67}$$

thereby establishing the underlying process to be multifractal.

Halsey et al. (1986) posit that if a dynamic system is partitioned into pieces of size l then the number of times the exponent takes on the value α is:

$$N(l) \sim l^{-f(\alpha)}, \tag{68}$$

where $f(\alpha)$ is the continuous spectrum of singularities of strength α. They go on to show that the generalized fractal dimension D_q can be computed directly from the singularity spectrum:

$$q = \frac{df(\alpha)}{d\alpha} \rightarrow D_q = \frac{1}{q-1}\left[q\alpha - f(\alpha)\right], \tag{69}$$

and consequently the scaling properties of the multifractal is determined by:

$$\alpha = \frac{d}{d\alpha}\left[(q-1)D_q\right]. \tag{71}$$

Measurements of the D_q's and the spectrum of singularities provide global and statistical information of the scaling properties of fractal measures. This information is similar to the power spectral density obtained from the Fourier transform of a time series that quantifies the relative contributions of the underlying frequencies. The function $f(\alpha)$ quantifies the relative contribution of the underlying singularities. Just as the Fourier transform does not keep track in time of the frequencies contributing to a power spectral density, neither does $f(\alpha)$ denote the locations of the singularities. Thus, a multifractal spectrum can only give an indication of the span of dimensions being accessed by the dynamic process and not the order in time at which they occur.

A vast literature has become available on multifractals and their processing techniques over the last quarter century, and there is every indication that the complex dynamics evident in tumor growth from early insights (Baish and Jain, 1998; Nonnenmacher et al., 1993; Losa et al., 1998; ibid, 2002; ibid, 2005; Meakin, 1998) to the development of analytic methods based on multifractal analysis to characterize the emergent properties of complex biological patterns (Balaban et al., 2018) will be facilitated by multifractal data processing techniques (Ivanov et al., 1999; Ivanov et al., 2009).

OM AND DIFFUSION

No discussion of OM would be complete without at least a brief review of the phenomenon of diffusion in a reaction-diffusion type of modeling of cancer growth, even without an extension beyond IDEs to include the fractional derivatives in space as well as in time. An excellent review of diffusion starting from the simple Brownian motion of tracer particles but focusing on the deviations from the laws of Brownian motion is given by Metzler et al. (2014), who provide an overview of different popular anomalous diffusion models paying special attention to their loss of ergodic properties. They highlight several of these models concentrating on the long-time averaged mean squared displacement, showing that the data obtained from time averages are different from ensemble averages. Thus, the workhorse of statistical physics, the ergodic hypothesis, breaks down.

The oncological application of anomalous diffusion is made by Debbouche et al. (2021), who remark that the first mathematical tumor growth models were integer partial differential equation (IPDE) models taking into account tumor, normal and dead cells, nutrition, various inhibitory substances and immune system response. Cells of a healthy organism are mortal with apoptosis being the end of the life cycle, whereas the lack of apoptosis is a main feature of tumor cells.

Here we take a different route and offer various mechanisms that modulate the diffusion process as well as compliment the growth laws already discussed. In this section we are concerned with characterizing the growth of a single species, both in isolation in the presence of other species. The growth of a species in isolation is modeled by means of a growth function which is intended to represent the influence of the fluctuations in the environment on the population. The influences being modeled will, of course, vary from species to species and will often be left quite general in the discussion so as not to unnecessarily limit the applicability of the growth function being used. The total rate of growth of a species is only partly given by such a function. As the population grows in a region of space, it may also migrate into the surrounding territory; also, members in other regions of space may migrate into the given region. This migration may be motivated by the avoidance of competition for common food sources with other species, the depletion of local food stuffs and/or becoming the food source of another species.

Our discussion centers on the three components of the multi-species network: 1) the growth in time of a single species in isolation, 2) the diffusion of that species in space, and 3) the modification of the growth and redistribution (diffusion) of a given species due to its interaction with other species.

Diffusion, Growth and Interactions

The non-homogeneous diffusion equation for the density of cells is given by:

$$\frac{\partial \rho(x,t)}{\partial t} = D\frac{\partial^2 \rho(x,t)}{\partial x^2} + f(x,t), \tag{71}$$

where $\rho(x,t)$ is the concentration of cells at spatial location x and time t and D denotes the diffusion coefficient throughout this chapter. When we consider a specific type of cell the concentration will carry an index to indicate the cell type, and the initial state will be denoted by $\rho(x, t = 0) = \rho_0(x)$. The non-homogeneous term is a growth function for the concentration that we write as:

$$f(x,t) = \rho(x,t)G(\rho), \tag{72}$$

$$G(\rho) \equiv \kappa \frac{1-\rho(x,t)^{\mu}}{\mu}, \tag{73}$$

and logistic growth is identified with $\mu = 1$ and the Gompertz growth with the limit $\mu \to 0$, although the latter equation was developed to model the mortality of the elderly rather than population growth.

The Verhulst and Gompertz models, as well as those with more general forms of $G(\rho)$ were constructed to predict the growth of a single species at a rate κ in a stable environment with limited resources. A growing population can circumvent the saturation inherent in such growth laws ($D = 0$) by redistributing (diffusing $D \neq 0$) into nearby unoccupied territory as the resources become depleted at their existing locations. The diffusion does not stop the saturation but it does retard it. These complementary mechanisms are subsequently discussed in the oncology context.

We can express the self-limiting growth equation by neglecting diffusion and setting $D = 0$ in **Eq. 71**:

$$\frac{dN(t)}{dt} = NG\left(\frac{N}{N_T}\right), \tag{74}$$

and N_T is the carrying capacity of the growth model, i.e., $\rho = N/N_T$. The first restriction we relax here in the discussion of **Eq. 74** is that of the stability of the environment. For example, in the case of human populations, such things as a vacillating economy or war could have extremely large effects on the population; whereas for lower-level biological species, violent weather changes or short-term food shortages could be major influences in the population's growth. Finally, a tumor's environment may disrupt the growth by invading with blood vessels as well as other things. Since it is their unpredictability which all these impacts have in common, the most elementary way to model their effects and still maintain a degree of generality is to assume them to be random. We model these external influences by adding a random forcing term $F(t)$ to the IRE, which we scale to the instantaneous growth rate by choosing the function to be proportional to $N(t)$:

$$\frac{dN(t)}{dt} = NG\left(\frac{N}{N_T}\right) + N(t)F(t). \tag{75}$$

If we introduce a new variable by the transformation:

$$U(t) = \ln\left[N/N_T\right] \; ; \; N = N_T e^{U},$$

then by substituting the new variable into **Eq. 75** we obtain:

$$\frac{dU(t)}{dt} = G\left(e^{U(t)}\right) + F(t), \tag{76}$$

which has the structure of a nonlinear Langevin equation with a deterministic forcing term $G(e^{U(t)})$ and a random force $F(t)$. **Equation 76** may be solved quite generally by means of a finite difference scheme for the deterministic function and a random walk (RW) process for the random force. If the RW is sufficiently simple, then analytic forms for the probability that the population grows to a level $U(t)$ in a time t may be obtained from the nonlinear Langevin equation. To determine the PDF centered on the deterministic growth we must make some assumptions about the RW process generating $F(t)$, that is, about the statistical character of the fluctuating environment. If we assume the random force is generated by a memoryless Wiener process we have:

$$\langle F(t)F(t')\rangle = 2D\delta(t-t'). \tag{77}$$

This assumption enables us to construct the Fokker-Planck equation (FPE) for the PDF:

$$\frac{\partial P(u,t|u_0)}{\partial t} = -\frac{\partial}{\partial u}\left[G(e^{u})P(u,t|u_0)\right] + D\frac{\partial^2 P(u,t|u_0)}{\partial u^2} \tag{78}$$

where $P(u, t|u_0)du$ is the probability that the dynamic variable $U(t)$ is in the phase space interval $(u + du, u)$ at time t given the initial value $U(0) = u_0$.

The FPE may be put in a more recognizable form to physicists by ignoring the dependence on the initial condition and introducing the nonlinear transformation:

$$P(u,t) = \psi(u,t)\exp\left[\frac{1}{2D}\int_0^u G(e^{u'})du'\right], \tag{79}$$

into the FPE to yield:

$$\frac{\partial \psi}{\partial \tau} = \frac{\partial^2 \psi}{\partial \mathcal{U}^2} - \left(\frac{\partial G}{\partial \mathcal{U}} + G^2\right)\psi, \tag{80}$$

where we have scaled the time $\tau = Dt/4$ and the population $u = 2D\mathcal{U}$. Note that this last equation has the form of the Schrödinger equation in Quantum Mechanics and therefore makes available a vast literature on the solution to **Eq. 80** for prescribed forms of $G(e^{u})$. The Verhulst growth law $[G(x) = 1 - x]$ is the analogue of the Morse potential in molecular physics and that of Gompertz corresponds to the harmonic oscillator. The solution to **Eq.80** for these cases, among others, was explored and the equilibrium PDF for the Gompertz case was determined to be Gaussian and that for the Verhulst case to be Poisson (Goel et al., 1971).

Multiple Species

The single species equation of growth was intended to model all the stable environmental effects determining the growth law of a particular cell. We now wish to generalize this expression to include the interaction between multiple kinds of cells. We postulate that a single kind of cell grows in proportion to its instantaneous population with a nonlinear growth rate, which is coupled to all the other cell species in the tissue:

$$\frac{dN_j}{dt} = N_j G_j(N_1, N_2, N_3), \tag{81}$$

here cell type #1 is healthy, #2 is cancerous and #3 is dead. The function $G_j(N_1, N_2, N_3)$ is a normalized growth law for the jth cell type and an interaction function, i.e., the interaction with other cell types has been removed from the fluctuating force of the model just discussed and made explicit. We assume that the

functions $\{G_j\}$ do not depend explicitly on the time, and that there exists a set of equilibrium populations $\{n_j\}$ such that $G_j(n_1, n_2, n_3) = 0$ and none of the equilibrium populations vanish. Consequently in the vicinity of an equilibrium point the growth functions can be expressed as the Taylor series expansions:

$$G_j = \bar{G}_j + \sum_{k=1}^{3}(N_k - n_k)\frac{\partial \bar{G}_j}{\partial N_k} + \sum_{l,k=1}^{3}(N_k - n_k)(N_l - n_l)\frac{\partial^2 \bar{G}_j}{\partial N_k \partial N_l} + \cdots, \tag{82}$$

where $\bar{F}_j(\bar{G}_j = 0)$ is the value of the function calculated at the equilibrium level. Substituting the Taylor series into the rate equation and defining the coefficients:

$$a_k^j \equiv \frac{\partial \bar{G}_j}{\partial N_k}; b_{kl}^j \equiv \frac{\partial^2 \bar{G}_j}{\partial N_k \partial N_l}, \tag{83}$$

gives rise to:

$$\frac{dN_j}{dt} = \sum_{k=1}^{3} a_k^j N_j (N_k - n_k) + \sum_{l,k=1}^{3} b_{kl}^j N_j (N_k - n_k)(N_l - n_l) + \cdots \tag{84}$$

Note that if one neglects the second order and higher terms in the deviation from equilibrium and introduces the constants:

$$\kappa_j = -\sum_{k=1}^{3} a_k^j n_k; a_k^j = a_{jk} \Big/ \beta_j,$$

then **Eq. 85** can be written:

$$\frac{dN_j}{dt} = \kappa_j N_j + \frac{1}{\beta_j}\sum_{k=1}^{3} a_{jk} N_j N_k \tag{85}$$

which is the form of the multi-species interaction modeled by Lotka and Volterra as well as other investigators. In the LV model the quadratic terms are interpreted as binary collisions between species j and k with a_{jk} being positive if j eats (kills) k and negative for the reverse. The $1/\beta_j$ represents exchange rates of the various species so that $(\beta_j/\beta_k)^{-1}$ is the ratio of k's lost (or gained) to j's gained (or lost). Volterra postulated that the coefficient a_{jk} is antisymmetric ($a_{jk} = -a_{kj}$) as required for the eating (killing) order mentioned above, and showed the existence of a constant of the motion for the dynamic system. The Volterra model has, therefore, been shown to be a first approximation to any situation in which the growth rate of a variable is proportional to its instantaneous value when the population is small and in which a steady-state value exists when there are interactions with other species.

Montroll (1972) used the general growth function to extend the LV model to the new form:

$$\frac{dN_j}{dt} = \alpha_j N_j + \frac{1}{\beta_j}\sum_{k=1}^{3} a_{jk} N_j \frac{(N_k^{\mu} - 1)}{\mu}, \tag{86}$$

which becomes the Volterra system when $\mu = 1$ and the linear growth rate is:

$$\alpha_j = \kappa_j + \frac{1}{\beta_j}\sum_{k=1}^{3} a_{jk}.$$

On the other hand, as $\mu \to 0$, after some algebra **Eq. 86** becomes the linear interaction equation in terms of the transformed variable $U_j = \ln(N_j/n_j)$:

$$\frac{dU_j}{dt} = \frac{1}{\beta_j}\sum_{k=1}^{3} a_{jk} U_k, \tag{87}$$

which may be solved by usual methods for linear IREs.

Fisher-Like Equation

We begin the discussion on the effects of diffusion on the growth of a species with a brief review of the classic problem in genetics developed by Fisher (1937). He was interested in the propagation of a virile mutant in a population living in a linear habitat, an example of which would be a species living along a seacoast. He developed his dynamic equations with a RW argument involving finite difference equations defined on a lattice. We skip to the continuous limit of his RW argument and write:

$$\frac{\partial}{\partial t}p(x,t) = D\frac{\partial^2}{\partial x^2}p(x,t) + \kappa p(x,t)\left[1 - p(x,t)\right], \tag{88}$$

which has both the features of self-limited (saturated) growth and diffusion. Here, $p(x, t)dx$ is the relative frequency of the mutant strain in the population at the position x and time t, and κ is the advantage of the mutant strain under conditions of random mating.

Skellam (1951) considered a linear RW in space consisting of computation cells containing a growing population and obtained an equation of the same form as Fisher's, as well as others. A slightly more general form for this diffusion equation was obtained for the population $\rho(x, t) = N_T p(x, t)$ with a finite saturation level N_T, but that equation has proven to be no more amenable to general closed form solution than Fisher's original equation. However, if we can obtain analytic solutions in the region near saturation and another exact solution in a region far from saturation $N_T \gg \rho$ they can be used to bracket the exact solution to Fisher's equation, if it exists. Moreover if the solution to Fisher's equation is continuous, then it must join the two asymptotic solutions at the extremes of population growth.

The direct solution of **Eq. 88** is extremely difficult to obtain due to the nonlinear structure of the equation. Fisher (Fisher, 1937) and Skellam (Skellam, 1952) obtained numerical solutions assuming the form of a diffusion wave $p(x, t) = p(x - vt)$. A more general analytic solution may be obtained in a restricted region, say near saturation. Let us consider the expansion:

$$\frac{\rho(x,t)}{N_T} = e^{\ln\left[\rho(x,t)/N_T\right]} \approx 1 + \ln\left[\rho(x,t)/N_T\right] + \cdots, \tag{89}$$

the first two terms of which give a good representation of the ratio $\rho(x,t)/N_T$ in the region near saturation. Substituting this expansion into **Eq. 88** and introducing the new variable $u(x,t) = \ln\left[\rho(x,t)/N_T\right]$ into the resulting equation yields:

$$\frac{\partial}{\partial t}u(x,t) = D\frac{\partial^2}{\partial x^2}u(x,t) - \kappa u(x,t), \tag{90}$$

It is clear that this equation provides a solution to the Fisher equation near saturation. To obtain a closed form solution, we strain Fisher's example of a linear habitat and require that the population lie along the perimeter L of an island such that $u(x + L, t) = u(x, t)$. With this assumption of periodicity it is straightforward to show that the solution to **Eq. 90** for an initial distribution $u_0(x) = u(x, t = 0)$ is:

$$u(x,t) = e^{-\kappa t}\int_{-\infty}^{\infty}\mathcal{G}(x-x',t)u_0(x')dx', \tag{91}$$

where $\mathcal{G}(x,t)$ is the Gauss distribution solution of the homogeneous diffusion equation and here plays the role of a Greens function.

If we transfer **Eq. 90** back to the population variable ρ, we obtain after a little algebra:

$$\frac{\partial\rho}{\partial t} = D\left[\frac{\partial^2\rho}{\partial x^2} - \frac{1}{\rho}\left(\frac{\partial\rho}{\partial x}\right)^2\right] - \kappa\rho\ln\left(\frac{\rho}{N_T}\right), \tag{92}$$

as the approximate form of the Fisher equation in the region near saturation, whose analytic solution is:

$$\rho(x,t) = \theta\exp\left[e^{-\kappa t}\int_{-\infty}^{\infty}\mathcal{G}(x-x',t)\ln\left[\frac{\rho_0(x')}{N_T}\right]dx'\right]. \tag{93}$$

A similar solution may be found in the region far from saturation $\rho \ll N_T$, that being the solution to the equation:

$$\frac{\partial\rho(x,t)}{\partial t} = D\frac{\partial^2\rho(x,t)}{\partial x^2} + \kappa\rho(x,t). \tag{94}$$

Thus, we are able to bracket the exact solution the Fisher equation even though we do know its analytic form.

Comments on Fractional Diffusion

From previous sections we know that we can introduce memory into the population dynamics through a subordination process and thereby obtain a fractional time diffusion equation (FTDE) of the form:

$$\partial_t^\alpha[\rho(x,t)] = D\frac{\partial^2\rho(x,t)}{\partial x^2}, \tag{95}$$

which is expressed in terms of the Fourier transform of the population $\tilde{\rho}(k,t)$ as:

$$\partial_t^\alpha[\tilde{\rho}(k,t)] = -Dk^2\tilde{\rho}(k,t). \tag{96}$$

Alternatively, the FTDE can be expressed in terms of the Laplace transform of the population $\hat{\rho}(x,s)$ as:

$$s^\alpha\hat{\rho}(x,s) - s^{\alpha-1}\rho_0(x) = D\frac{\partial^2\hat{\rho}(x,s)}{\partial x^2}, \tag{97}$$

where the fractional time derivative is of the Caputo type. The most efficient way to solve the FTDE is to invert the joint Fourier-Laplace transform of the population $\rho^\star(k, s)$ which assumes the form:

$$\rho^\star(k,s) = \frac{s^{\alpha-1}\tilde{\rho}_0(k)}{s^\alpha + Dk^2}. \tag{98}$$

For a point source initial condition $\rho_0(x) = \delta(x)$ we have $\tilde{\rho}_0(k) = 1$ and the inversion of this equation yields:

$$\rho(x,t) = \mathcal{FT}^{-1}\{E_\alpha(-Dk^2t^\alpha); x\}, \tag{99}$$

with the solution to the FTDE in terms of the inverse Fourier transform of the MLF.

We also know from previous discussions that spatial heterogeneity can be introduced into the population dynamics through the network effect and thereby obtain a fractional space diffusion equation (FSDE) of the form:

$$\frac{\partial\rho(x,t)}{\partial t} = D\partial_{|x|}^\beta[\rho(x,t)], \tag{100}$$

where $\partial_{|x|}^\beta[\cdot]$ is the Riesz-Feller fractional derivative (West, 2016). The solution to this FSDE can be expressed in terms of the inverse of the Fourier-Laplace transform:

$$\rho^\star(k,s) = \frac{\tilde{\rho}_0(k)}{s + D|k|^\beta}, \tag{101}$$

where the Fourier transform of the Riesz-Feller fractional derivative in one spatial dimension is $-|k|^\beta$. Inverting **Eq. 101** for the same point source initial condition used previously gives us:

$$\rho(x,t) = \int_{-\infty}^{\infty}\frac{dk}{2\pi}e^{ikx}e^{-D|k|^\beta t}, \tag{102}$$

which is a Lévy stable PDF. Note that when $\alpha = 1$ the MLF in **Eq. 99** becomes an exponential and the PDF reduces to a Gauss PDF which is a $\beta = 2$ Lévy stable form (West, 2017).

It is worth mentioning that the FTDE is a version of (Evangelista and Lenzi, 2018):

$$\partial_t^\alpha[\rho(x,t)] = D\frac{\partial^2\rho(x,t)}{\partial x^2} - \frac{\partial}{\partial x}[F(x,t)\rho(x,t)], \tag{103}$$

$$= \frac{\partial J(x,t)}{\partial x}, \tag{104}$$

where is the influence of the environment is modeled as an external force $F(x, t)$ and $J(x, t)$ is the population current density. A exhaustive mathematical discussion of fractional anomalous diffusion is given by Evangelista and Lenzi in their remarkably timely book (Evangelista and Lenzi, 2018).

CLOSING THOUGHTS

In this all too brief introduction to the growing area of application of the fractional calculus to MO we have covered many mathematical concepts, each new wrinkle capturing a different nuance in the complexity of biomedical phenomena. Rather than

attempting a detailed summary of what has been presented herein, we instead identify and articulate a number of general results. We will then attempt to put these remarks into a larger context and anticipate some of the future research directions that may facilitate the modeling of biomedically complex phenomena and pathologies.

We begin by identifying the most important points covered in this essay:

1) The simple analytic functions of the IC have been shown in the prequel to be insufficient to describe the time dependence of most physiology networks. The notion of fractality was introduced to capture the true complexity of such biomedical networks through fractal geometry, fractal statistics and fractal dynamics.
2) A fractal function diverges when an integer-order derivative is taken, so that such a fractal function cannot be the solution to a Newtonian equation of motion. However, when a fractional-order derivative of a fractal function is taken it results in a new fractal function. Consequently, a time-dependent fractal process can have an equation of motion that is a FDE.
3) The Network Effect is the influence exerted by a complex dynamic network on each member of the network. When the network dynamics is a member of the Ising universality class the interconnected set of IDEs for the probability of an individual being in one of two states during its nonlinear interaction with the other members of the network can be replaced by an equivalent linear FDE.
4) One of the simplest FDEs has a built-in memory resulting from the hidden interaction of the observable with its environment, which is manifest in the non-integer order of the time derivative, as in the network effect. Examples include the deviation of experimental results of Newton's Law of Cooling from predictions using an IRE and the dynamics of the very early time description of Brownian motion also using an IRE.
5) Another simple FDE has a built-in non-locality in space and is the FSDE. The solution to this fractional diffusion equation in space is a Lévy PDF, whose index is given by the order of the spatial fractional derivative. Yet another fractional diffusion equation differs in having a built-in memory and is the FTDE. The solution to this fractional diffusion equation in time is expressed in terms of the inverse Fourier transform of a MLF.
6) The solution to a linear FRE is a MLF for $\alpha < 1$ and becomes an exponential function for $\alpha = 1$. The MLF is the workhorse of the FC just as the exponential is for the IC.
7) A truly complex stochastic dynamic process can have more than one fractal dimension. A multifractal process is characterized by a uni-modal spectrum $f(h)$ peaked at the value of the Hurst exponent $h = H$.
8) The time-dependent fractional-order index $\alpha(t)$ specifies a distributed-order fractional operator. As a sufficiently rich complex process evolves over time its fractal dimension changes to explore the full range of dimensionality $0 < \alpha(t) \leq 1$ through the multifractal spectrum $f(\alpha)$.

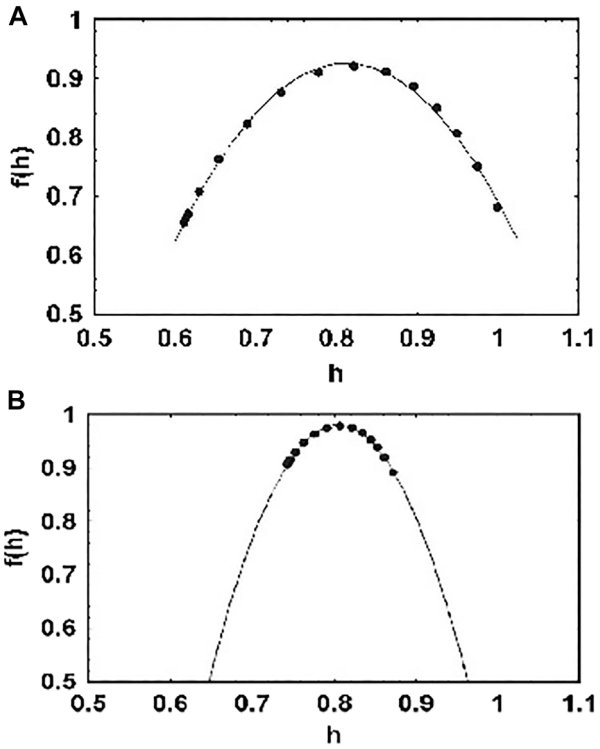

FIGURE 11 | The average multifracal spectrum for middle CBF time series is depicted by *f(h)*. **(A)** The spectrum is the average of 10 time series measurements of five healthy subjects (filled circles). The solid line is the best least-squares fit of the parameters to the predicted spectrum. **(B)** The spectrum is the average of 14 time series measurements of eight migraineurs (filled circles). The solid curve is the best least-squares fit to a predicted spectrum. From (West et al., 2003b) with permission.

The short term goal of this essay has been, in part, to describe how the growth of natural biological phenomena differs from the growth of physical phenomena. We explored this by showing how to incorporate memory effects into the growth process of biological cells by replacing IREs with FREs. The replacement of integer-order with fractional-order derivatives in time required a brief foray into the solving of the FREs that describe the growth of cells over time, including the saturation of growth using Verhulst (logistic) and Gompertz models. Such descriptions are important in order to understand the multiscale processes that emerge when tissues are electrically stimulated or mechanically stressed (Magin, 2010), as well as being pathologically disrupted.

We close these remarks by emphasizing the nexus between distributed-order differentiation and multifractality. The invariance of scale is a property relating time series across multiple scales and has provided a new perspective regarding medicine, physiological phenomena and their associated control systems. The historical engineering paradigm of 'signal-plus-noise' was first replaced by a model of biological time series that had fractal statistics. This however was also shown to be too restrictive when a number of physiological signals were found to be characterized by more than one scaling parameter and

therefore to belong to a class of complex processes known as multifractals. Such multifractal time series appear in the rich healthy variability of both human gait and heart rate (Ivanov et al., 1999; West, 2006; Bogdan et al. 2020).

We use blood flow within the brain as an exemplar of how the multifractal character of health can be described and subsequently explained using the FC. West et al., 2003b) demonstrated that the scaling properties of the time series associated with cerebral blood flow (CBF) significantly differs between that of normal healthy individuals and migraineurs. The CBF time series discussed here is typical of physiologic signals generated by complex self-regulated networks that handle inputs having a broad range of scales. An indirect way of measuring CBF is by monitoring the blood flowing into the brain through the middle cerebral artery. This can be accomplished using an instrument that operates like a radar gun, but instead of scattering electromagnetic waves from your car back to the gun to determine your speed, it scatters acoustic (sound) waves from the fluctuations in the blood back to the gun to determine the flow velocity. The instrument is a transcranial Doppler ultrasonograph and provides a high resolution measurement of middle cerebral artery flow velocity. We look for the signature of the migraine pathology in the scaling properties of the human middle cerebral artery CBF velocity time series.

The properties of monofractals are determined by the local scaling exponent, but as mentioned multifractals are made up of many interwoven subsets with different local scaling exponents. The statistical properties of these subsets are characterized by the spectral distribution of fractal dimensions *f(h)* as depicted in **Figure 11**. In this figure we compare the multifractal spectrum for the middle CBF velocity time series for a healthy group of five subjects and a group of eight migraineurs.

A significant change in the multifractal properties of the middle CBF velocity time series from the control group to that of the migraineurs. is apparent. Namely, the width the multifractal spectrum of the local scaling exponent is vastly constricted, being reduced by a factor of three from 0.038 for the control group to 0.013 for the migraineurs. The multifractal spectrum for migraineurs is centered at 0.81, the same as that of the control group, so the average scaling behavior would appear to be the same. However, the narrowing of the fractal dimension spectrum suggests that the underlying process has lost its flexibility. The advantage of multifractal processes is that they are highly adaptive, so that in this case the brain of a healthy individual adapts to the multifractality of the interbeat interval time series of the heart. We see that the disease, in this case migraine, may be associated with the loss of complexity (Goldberger et al., 1990), due to the narrowing of the spectral width, and consequently the loss of adaptability, thereby suppressing the normal healthy multifractality of CBF time series.

The experimental evidence presented in the prequel supports the interpretation that the greater the complexity of the physiologic time series, as measured by the width of the multifractal spectrum, the healthier the physiological network. In addition, theory (West and Grigolini, 2021) suggests that the information transfer between two coupled networks is from the network with the wider spectrum (greater complexity) to that with the narrower spectrum (lesser complexity). We hypothesize that the multifractal dynamics of oncological processes may be well represented by distributed-order FDEs that captures the loss of complexity in the transition from healthy multifractal physiologic processes with a substantial spectral width to a pathological process with a significantly narrower spectral width. This hypothesis will be the focus of the next essay in this sequence.

To end this essay on a positive note, we briefly mention a number of the topic areas suggested by thoughtful reviewers of the manuscript, which although relevant to the theme of this essay we lacked the skill to incorporate them into the present text. There have been numerous efforts dealing with observability and controllability of physiological networks while considering the FD observed in medicine, see for example, (Bogdan, 2019; Kyriakis et al., 2020). Another is to use what we know concerning the information exchange between complex networks (West et al., 2008; West and Grigolini, 2021) to implement the FC for reducing the risk of closed loop control of blood glucose in artificial pancreas (Ghorbani and Bogdan, 2014), but also in optimal control theory where it may lead to a new branch of control techniques such as time-dependent fractal optimal control.

The acknowledgement of this new perspective is nowhere more evident than in the timely launching of a journal that recognizes the emergening field of Network Physiology (Ivanov et al., 2016; Ivanov, 2021). I wholeheartedly endorse this new journal with but a single reservation, Ivanov's reference to Network Physiology as being 'multi-disciplinary' (Ivanov, 2021). I much prefer the less restrictive term '*trans*-disciplinary', in large part because with the future application of the FC to Network Medicine as well as to Network Physiology will itself generate disciplines that will not fit into our present day taxonomy of scientific disciplines.

DATA AVAILABILITY STATEMENT

The original contributions presented in the study are included in the article/Supplementary Material, further inquiries can be directed to the corresponding author.

AUTHOR CONTRIBUTIONS

This essay is an attempt to introduce the biomedical community to the utility of the fractional calculus as a modeling tool when the ordinary calculus is not adequate. The intent is to step beyond the application of fractals in the description of physiologic networks and show how fractional rate equations capture all manner of complexity and suggest that the dynamics of oncology is fractional.

FUNDING

I have been assured that all fees with regard to this paper will be waived.

REFERENCES

Alexander, A. (2014). *Infinitesimal, How a Dangerous Mathematical Theory Shaped the Modern World*. New York: Scientific American/Farrar , Straus and Giroux, NY.

Altrock, P. M., Liu, L. L., and Michor, F. (2015). The Mathematics of Cancer: Integrating Quantitative Models. *Nat. Rev. Cancer* 15 (12), 730–745. doi:10.1038/nrc4029

Ariely, D. (2008). *Predictably Irrational, the Hidden Forces that Shape Our Decisions*. New York: Harper Collins.

Baish, J. W., and Jain, R. K. (1998). Cancer, Angiogenesis and Fractals. *Nat. Med.* 4, 984. doi:10.1038/1952

Bak, P. (1996). *How Nature Works, the Science of Self-Organized Criticality*. New York: Springer-Verlag.

Balaban, V., Lim, S., Gupta, G., Boedicker, J., and Bogdan, P. (2018). Quantifying Emergence and Self-Organisation of *Enterobacter cloacae* Microbial Communities. *Sci. Rep.* 8, 1246. doi:10.1038/s41598-018-30654-9

Barabasi, A. L. (2016). *Network Science*. Cambridge, UK: Cambridge University Press.

Basset, A. B. (1888). *A Treatise on Hydrodynamics, Vol. 2, Chapt. 22*. Cambridge: Deighton Bell, 285–297.

Bassingthwaighte, J. B., Liebovitch, L. S., and West, B. J. (1994). *Fractal Physiology*. Oxford UK: Oxford University Press.

Bernaola-Galván, P., Oliver, J. L., Hackenberg, M., Coronado, A. V., Ivanov, P. C., and Carpena, P. (2012). Segmentation of Time Series with Long-Range Fractal Correlations. *Eur. Phys. J. B* 85, 211. doi:10.1140/epjb/e2012-20969-5

Bette, H. M., Habel, L., Emig, T., and Schreckenberg, M. (2017). Mechanisms of Jamming in the Nagel-Schreckenberg Model for Traffic Flow. *Phys. Rev. E* 95, 012311. doi:10.1103/PhysRevE.95.012311

Bianco, S., Geneston, E., Grigolini, P., and Ignaccolo, M. (2008). Renewal Aging as Emerging Property of Phase Synchronization. *Physica A: Stat. Mech. its Appl.* 387, 1387–1392. doi:10.1016/j.physa.2007.10.045

Bogdan, P. (2019). Taming the Unknown Unknowns in Complex Systems: Challenges and Opportunities for Modeling, Analysis and Control of Complex (Biological) Collectives. *Front. Physiol.* 10, 1452. doi:10.3389/fphys.2019.01452

Bogdan, P., Eke, A., and Ivanov, P. C. (2020). Editorial: Fractal and Multifractal Facets in the Structure and Dynamics of Physiological Systems and Applications to Homeostatic Control, Disease Diagnosis and Integrated Cyber-Physical Platforms. *Front. Physiol.* 11, 447. doi:10.3389/fphys.2020.00447

Boussinesq, K. (1885). Sur la résistance qu'oppose un fluide indéfini en repos, sans pesanteur, au mouvement varié d'une sphère solide qu'il mouille sur toute sa surface, quand les vitesses restent bien continues et assez faibles pour que leurs carrés et produits soient négligeables. *C.R. Acad. Sci. Paris* 100, 935–937.

Castellano, C., Fortunato, S., and Loreto, V. (2009). Statistical Physics of Social Dynamics. *Rev. Mod. Phys.* 81, 591–646. doi:10.1103/RevModPhys.81.591

Christensen, K., and Moloney, N. R. (2005). *Complexity and Criticality*. London, UK: Imperial College Press.

Clercx, H. J. H., and Schram, P. P. J. M. (1992). Brownian Particles in Shear Flow and Harmonic Potentials: A Study of Long-Time Tails. *Phys. Rev. A.* 46, 1942–1950. doi:10.1103/physreva.46.1942

Debbouche, A., Polovinkina, M. V., Polovinkin, I. P., Valentim, C. A., Jr., and David, S. A. (2021). On the Stability of Stationary Solutions in Diffusion Models of Oncological Processes. *Eur. Phys. J. Plus* 136, 130–148. doi:10.1140/epjp/s13360-020-01070-8

Di Paola, M., Alotta, G., Burlon, A., and Failla, G. (2020). A Novel Approach to Nonlinear Variable-Order Fractional Viscoelasticity. *Phil. Trans. R. Soc. A.* 378, 20190296. doi:10.1098/rsta.2019.0296

Dorogovtsev, S. N., Goltsev, A. V., and Mendes, J. F. F. (2008). Critical Phenomena in Complex Networks. *Rev. Mod. Phys.* 80, 1275–1335. doi:10.1103/RevModPhys.80.1275

Durrett, R. (2013). Cancer Modeling: A Personal Perspective. *Notices Amer. Math. Soc.* 60, 304–309. doi:10.1090/noti953

Eckhardt, B., and Zammert, S. (2012). Non-normal Tracer Diffusion from Stirring by Swimming Microorganisms. *Eur. Phys. J. E* 35, 96. doi:10.1140/epje/i2012-12096-7

Einstein, A. (1907). Theoretische Bemerkungen Über die Brownsche Bewegung. *Z. Elektrotech. Elektrochem.* 13, 41–42. doi:10.1002/bbpc.19070130602

Einstein, A. (1905). Über die von der molekularkinetischen Theorie der Wärme geforderte Bewegung von in ruhenden Flüssigkeiten suspendierten Teilchen. *Ann. Phys.* 322, 549–560. doi:10.1002/andp.19053220806

Evangelista, L. R., and Lenzi, E. K. (2018). *Fractional Diffusion Equations and Anomalous Diffusion*. Cambridge, UK: Cambridge University Press.

Fechner, G. T. (1860). *Elemente der Psychophysik*. Leipzig: Breitkopf and Härtel.

Feller, W. (1966). *An Introduction to Probability Theory and its Applications, Volume II*. New York: J. Wiley & Sons.

Fisher, R. A. (1937). The Wave of Advance of Advantageous Genes. *Ann. Eugen.* 7, 355–369. doi:10.1111/j.1469-1809.1937.tb02153.x

Flack, A., Nagy, M., Fiedler, W., Couzin, I. D., and Wikelski, M. (2018). From Local Collective Behavior to Global Migratory Patterns in white Storks. *Science* 360, 911–914. doi:10.1126/science.aap7781

Ghorbani, M., and Bogdan, P. (2014). Reducing Risk of Closed Loop Control of Blood Glucose in Artificial Pancreas Using Fractional Calculus. *Annu. Int. Conf. IEEE Eng. Med. Biol. Soc.* 2014, 4839–4842. doi:10.1109/EMBC.2014.6944707

Goel, N. S., Maitra, S. C., and Montroll, E. W. (1971). On the Volterra and Other Nonlinear Models of Interacting Populations. *Rev. Mod. Phys.* 43, 241. doi:10.1103/revmodphys.43.231

Goldberger, A. L., Amaral, L. A. N., Hausdorff, J. M., Ivanov, P. C., Peng, C.-K., and Stanley, H. E. (2002). Fractal Dynamics in Physiology: Alterations with Disease and Aging. *Proc. Natl. Acad. Sci.* 99, 2466–2472. doi:10.1073/pnas.012579499

Goldberger, A. L., Rigney, D. R., and West, B. J. (1990). Science in Pictures: Chaos and Fractals in Human Physiology. *Sci. Am.* 262, 42–49. doi:10.1038/scientificamerican0290-42

Gorenflo, R., Loutchko, J., and Luchko, Y. (2002). Computation of the Mittag-Leffler Function and its Derivative. *Fract. Calc. Appl. Anal.* 5, 491–518.

Grinstein, G., Jayaprakash, C., and He, Y. (1985). Statistical Mechanics of Probabilistic Cellular Automata. *Phys. Rev. Lett.* 55, 2527–2530. doi:10.1103/physrevlett.55.2527

Guzm´an, D. A., Flesia, A. G., Aon, M. A., Pellegrini, S., Marin, R. H., and Kembro, J. M. (2017). The Fractal Organization of Ultradian Rhythms in Avian Behavior. *Scientific Rep.* 7, 684.

Halsey, T. C., Jensen, M. H., Kadanoff, L. P., Procaccia, I. B. I., and Shraiman, B. D. (1986). Fractal Measures and Their Singularities: The Characterization of Strange Sets. *Phys. Rev. A.* 33, 1141–1151. doi:10.1103/physreva.33.1141

Hernandez-Urbina, V., Michael Herrmann, J., and Spagnolo, B. (2016). Neuronal Avalanches in Complex Networks. *Cogent Phys.* 3, 1150408. doi:10.1080/23311940.2016.1150408

Herrmann, R. (2011). *Fractional Calculus: An Introduction for Physicists*. New York: World Scientific.

Huang, R., Chavez, I., Taute, K. M., Lukić, B., Jeney, S., Raizen, M. G., et al. (2011). Direct Observation of the Full Transition from Ballistic to Diffusive Brownian Motion in a Liquid. *Nat. Phys* 7, 576–580. doi:10.1038/nphys1953

Ivanov, P. C., Amaral, L. A. N., Goldberger, A. L., Havlin, S., Rosenblum, M. G., Struzik, Z. R., et al. (1999). Multifractality in Human Heartbeat Dynamics. *Nature* 399, 461–465. doi:10.1038/20924

Ivanov, P. C. H., Ma, Q. D., Bartsch, R. P., Hausdorff, J. M., Nunes Amaral, L. A., Schulte-Frohlinde, V., et al. (2009). Levels of Complexity in Scale-Invariant Neural Signals. *Phys. Rev. E Stat. Nonlin Soft Matter Phys.* 79, 041920. doi:10.1103/PhysRevE.79.041920

Ivanov, P. C., Liu, K. K. L., and Bartsch, R. P. (2016). Focus on the Emerging New fields of Network Physiology and Network Medicine. *New J. Phys.* 18, 100201. doi:10.1088/1367-2630/18/10/100201

Ivanov, P. C. (2021). The New Field of Network Physiology: Building the Human Physiolome. *Front. Netw. Physiol.* 1, 711778. doi:10.3389/fnetp.2021.711778

Kahneman, D. (2011). *Thinking, Fast and Slow*. New York, NY: Farrar, Straus and Giroux.

Kheifets, S., Simha, A., Melin, K., Li, T., and Raizen, M. G. (2014). Observation of Brownian Motion in Liquids at Short Times: Instantaneous Velocity and Memory Loss. *Science* 343, 1493–1496. doi:10.1126/science.1248091

Kulakolwski, K., and Nawojczyk, M. (2008). Sociophysics-an Astriding Science. *arXiv:0805.3886vi*.

Kyriakis, P., Pequito, S., and Bogdan, P. (2020). On the Effects of Memory and Topology on the Controllability of Complex Dynamical Networks. *Sci. Rep.* 10, 17346. doi:10.1038/s41598-020-74269-5

Langevin, P. (1908). Comptes Rendus Acad. *Sci. Paris* 146, 530–533.

Leptos, K. C., Guasto, J. S., Gollub, J. P., Pesci, A. I. R. E., and Goldstein, R. E. (2009). Dynamics of Enhanced Tracer Diffusion in Suspensions of Swimming Eukaryotic Microorganisms. *Phys. Rev. Lett.* 103, 198103. doi:10.1103/physrevlett.103.198103

Li, T., Kheifets, S., Medellin, D., and Raizen, M. G. (2010). Measurement of the Instantaneous Velocity of a Brownian Particle. *Science* 328, 1673–1675. doi:10.1126/science.1189403

Li, T., and Raizen, M. (2013). Brownian Motion at Short Time Scales. *Phys. (Berlin)* 525, 281–295. doi:10.1002/andp.201200232

Lloyd, D., Aon, M. A., and Cortassa, S. (2001). Why Homeodynamics, Not Homeostasis? *The Scientific World JOURNAL* 1, 133–145. doi:10.1100/tsw.2001.20

G. A. Losa, D. Merlini, T. F. Nonnenmacher, and E. R. Weibl (Editors) (1998). *Fractals in Biology and Medicine. Vol. II* (Basel: Birkhäuser).

ibid (2002). *Ibid. Vol.III*. Basel: Birkhäuser.

ibid (2005). *Ibid. Vol.IV*. Basel: Birkhäuser.

Magin, R. L. (2006). *Fractional Calculus in Bioengineering*. Redding, CT: Begell House Publishers, Co.

Magin, R. L. (2010). Fractional Calculus Models of Complex Dynamics in Biological Tissues. *Comput. Maths. Appl.* 59, 1586–1593. doi:10.1016/j.camwa.2009.08.039

Magin, R. L. (2016). Models of Diffusion Signal Decay in Magnetic Resonance Imaging: Capturing Complexity. *Concepts Magn. Reson.* 45A, e21401. doi:10.1002/cmr.a.21401

Mahmoodi, K., West, B. J., and Grigolini, P. (2017). Self-organizing Complex Networks: Individual versus Global Rules. *Front. Physiol.* 8, 478. doi:10.3389/fphys.2017.00478

Mainardi, F., and Pironi, P. (1996). The Fractional Langevin Equation: Brrownian Motion Revisited. *Extracta Mathematicae* 11, 140.

Mallat, S. (1999). *A Wavelet Tour of Signal Processing*. 2nd Ed. San Diego, CA: Academic Press.

Mandelbrot, B. B. (1977). *Fractals, Form, Chance and Dimension*. San Francisco: W. H. Freeman.

Mandelbrot, B. B. (1982). *The Fractal Geometry of Nature*. San Francisco: W. H. Freeman.

Mandelbrot, B. B., and van Ness, J. W. (1968). Fractional Brownian Motions, Fractional Noises and Applications. *SIAM Rev.* 10, 422–437. doi:10.1137/1010093

Marquis de Cordorcet (2022). Marquis de Cordorcet. Available at: https://www.goodreads.com/author/quotes/5820660_Nicolas_de_Condorcet.

Masoliver, J. (2021). Telegraphic Transport Processes and Their Fractional Generalization: A Review and Some Extensions. *Entropy* 23 (3), 364. doi:10.3390/e23030364

Meakin, P. (1998). *Fractals, Scaling and Growth Far from Equilibrium*. Combridge: Combridge Univeristy Press.

Meerschaert, M. M., West, B. J., and Zhou, Y. (2017). Future Directions in Fractional Calculus Research and Applications. *Chaos, Solitons and Fractals* 102, 0960–0779. doi:10.1016/j.chaos.2017.07.011

Metzler, R., Jeon, J.-H., Cherstvy, A. G., and Barkai, E. (2014). Anomalous Diffusion Models and Their Properties: Non-stationarity, Non-ergodicity, and Ageing at the Centenary of Single Particle Tracking. *Phys. Chem. Chem. Phys.* 16, 24128–24164. doi:10.1039/c4cp03465a

Mondol, A., Gupta, R., Das, S., and Dutta, T. (2018). An Insight into Newton's Cooling Law Using Fractional Calculus. *J. Appl. Phys.* 123, 064901. doi:10.1063/1.4998236

Montroll, E. M. (1972). Random Walks on Lattices. IV. Continuous-Time Walks and Influence of Absorbing Boundaries. *Am. Math. Soc.* 4, 101.

Nasrolahpour, H. (2017). Fractional Dynamics in Bioscience and Biomedicine and the Physics of Cancer. *bioRxiv*. doi:10.1101/214197

Nasrolahpour, H. (2018). Fractional Dynamics of Cancer Cells and the Future of Research in Biomedicine. *Crj* 6, 16–19. doi:10.11648/j.crj.20180601.13

Newman, M. E. J. (2018). *Networks, an Introduction*. New York, NY: Oxford University Press.

Niu, H., Chen, Y., and West, B. J. (2021). Why Do Big Data and Machine Learning Entail the Fractional Dynamics? *Entropy* 23, 297. doi:10.3390/e23030297

T. F. Nonnenmacher, G. A. Losa, and E. R. Weibl (Editors) (1993). *Fractals in Biology and Medicine. Vol. I* (Basel: Birkhäuser).

Pastor-Satorras, R., Castellano, C., Van Mieghem, P., and Vespignani, A. (2015). Epidemic Processes in Complex Networks. *Rev. Mod. Phys.* 87, 925–979. doi:10.1103/RevModPhys.87.925

Podlubny, I. (1999). *Frational Differential Equations*. San Diego, CA: Academic Press.

Pramukkul, P., Svenkeson, A., Grigolini, P., Bologna, M., and West, B. (2013). Complexity and the Fractional Calculus. *Adv. Math. Phys.* 2013, 1–7. doi:10.1155/2013/498789

Richardson, L. F. (1926). Atmospheric Diffusion Shown on a Distance-Neighbour Graph. *Proc. R. Soc.* 110, 709–723.

Rocco, A., and West, B. J. (1999). Fractional Calculus and the Evolution of Fractal Phenomena. *Physica A: Stat. Mech. its Appl.* 265, 535–546. doi:10.1016/S0378-4371(98)00550-0

T. C. Ruch and H. D. Patton (Editors) (1979). *Physiology and Biophysics*. 19th Edition (Philadelphia and London: W.B. Sanders Co.).

Schmitt, D. T., and Ivanov, P. C. (2007). Fractal Scale-Invariant and Nonlinear Properties of Cardiac Dynamics Remain Stable with Advanced Age: a New Mechanistic Picture of Cardiac Control in Healthy Elderly. *Am. J. Physiology-Regulatory, Integr. Comp. Physiol.* 293, R1923–R1937. doi:10.1152/ajpregu.00372.2007

Skellam, J. G. (1951). Random Dispersal in Theoretical Populations. *Biometrika* 30, 195. doi:10.2307/2332328

Skellam, J. G. (1952). Studies in Statistical Ecology. *Biometrika* 39, 346–362. doi:10.1093/biomet/39.3-4.346

Strogatz, S. H. (2000). From Kuramoto to Crawford: Exploring the Onset of Synchronization in Populations of Coupled Oscillators. *Physica D: Nonlinear Phenomena* 143, 1–20. doi:10.1016/s0167-2789(00)00094-4

Toda, M., Kubo, R., and Saito, N. (2004). *Statistical Physics I: Equilibrium Statistical Mechanics*. Berlin: Springer.

Tu, B. P., and McKnight, S. L. (2006). Metabolic Cycles as an Underlying Basis of Biological Oscillations. *Nat. Rev. Mol. Cel Biol* 7, 696–701. doi:10.1038/nrm1980

Turalska, M., Lukovic, M., West, B. J., and Grigolini, P. (2009). Complexity and Synchronization. *Phys. Rev. E Stat. Nonlin Soft Matter Phys.* 80, 021110. doi:10.1103/PhysRevE.80.021110

Turalska, M., West, B. J., and Grigolini, P. (2011). Temporal Complexity of the Order Parameter at the Phase Transition. *Phys. Rev. E Stat. Nonlin Soft Matter Phys.* 83, 061142. doi:10.1103/PhysRevE.83.061142

Turalska, M., and West, B. J. (2017). A Search for a Spectral Technique to Solve Nonlinear Fractional Differential Equations. *Chaos, Solitons & Fractals* 102, 387–395. doi:10.1016/j.chaos.2017.04.022

Turalska, M., and West, B. J. (2018). Fractional Dynamics of Individuals in Complex Networks. *Front. Phys.* 6, 1–8. doi:10.3389/fphy.2018.00110

Uhlenbeck, G. E., and Ornstein, L. S. (1930). On the Theory of the Brownian Motion. *Phys. Rev.* 36, 823–841. doi:10.1103/physrev.36.823

Valentim, C. A., Oliveira, N. A., Rabi, J. A., and David, S. A. (2020). Can Fractional Calculus Help Improve Tumor Growth Models? *J. Comput. Appl. Maths.* 379, 112964. doi:10.1016/j.cam.2020.112964

Valentim, C. A., Rabi, J. A., David, S. A., and Tenreiro Machado, J. A. (2021). On Multistep Tumor Growth Models of Fractional Variable-Order. *BioSystems* 199, 104294. doi:10.1016/j.biosystems.2020.104294

Varalta, N., Gomes, A. V., and Camargo, R. F. (2014). A Prelude to the Fractional Calculus Applied to Tumor Dynamis. *Tendencias em Matematica Aplicada e Computacional* 15, 211–221.

West, B. J. (2014). A Mathematics for Medicine: The Network Effect. *Front. Physiol.* 5, 456. doi:10.3389/fphys.2014.00456

West, B. J., Turalska, M., and Grigolini, P. (2014). *Network of Echoes: Immitation, Innovation and Invisible Leaders*. New York: Springer.

West, B. J., Bologna, M., and Grigolini, P. (2003). *Physics of Fractal Operators*. New York, NY: Springer.

West, B. J. (2015). Exact Solution to Fractional Logistic Equation. *Physica A: Stat. Mech. its Appl.* 429, 103–108. doi:10.1016/j.physa.2015.02.073

West, B. J. (2016). *Fractional Calculus View of Complexity: Tomorrow's Science*. Boca Raton, FL: CRC Press.

West, B. J., Geneston, E. L., and Grigolini, P. (2008). Maximizing Information Exchange between Complex Networks. *Phys. Rep.* 468, 1–99. doi:10.1016/j.physrep.2008.06.003

West, B. J., and Grigolini, P. (2021). "Crucal Events; Why Are Catastrophes Never Expected?," in *Studies of Nonlinear Phenomena in Life Science-Vol. 17* (Singapore: World Scientific).

West, B. J., Latka, M., Glaubic-Latka, M., and Latka, D. (2003). Multifractality of Cerebral Blood Flow. *Physica A: Stat. Mech. its Appl.* 318, 453–460. doi:10.1016/s0378-4371(02)01377-8

West, B. J. (2017). *Nature's Patterns and the Fractional Calculus*. Berlin/Boston: Walter de Gruyter GmbH.

West, B. J. (1990). Sensing Scaled Scintillations. *J. Opt. Soc. Am. A.* 7, 1074–1100. doi:10.1364/josaa.7.001074

West, B. J. (2020). Sir Isaac Newton Stranger in a Strange Land. *Entropy* 22, 1204. doi:10.3390/e22111204

West, B. J. (2021). The Fractal Tapestry of Life: A Review of Fractal Physiology. *Nonlinear Dyn. Psychol. Life Sci.* 25, 261–296.

West, B. J. (2006). Where Medicine Went Wrong. *Stud. Nonlinear Phenomena Life Sci.* 11, 6175. doi:10.1142/6175

Weyl, H. (1917). Bemerkungen Zum Begriff Er Differentialquotenten Gebrochener Ordnung. *Vierteljahrschrift der Naturforscher Geselschaft in Zürich* 62, 296–302.

Yang, Y., Nishikawa, T., and Motter, A. E. (2017). Small Vulnerable Sets Determine Large Network Cascades in Power Grids. *Science* 358, 3184. doi:10.1126/science.aan3184

Zaid, I. M., Dunkel, J., and Yeomans, J. M. (2011). Lévy Fluctuations and Mixing in Dilute Suspensions of Algae and Bacteria. *J. R. Soc. Interf.* 8, 1314–1331. doi:10.1098/rsif.2010.0545

Znaidi, M. R., Gupta, G., Asgari, K., and Bogdan, P. (2020). Identifying Arguments of Space-Time Fractional Diffusion: Data-Driven Approach. *Front. Appl. Math. Stat.* 6, 14. doi:10.3389/fams.2020.00014

Conflict of Interest: The author declares that the research was conducted in the absence of any commercial or financial relationships that could be construed as a potential conflict of interest.

frontiers | Frontiers in Network Physiology

ORIGINAL RESEARCH
published: 25 April 2022
doi: 10.3389/fnetp.2022.867551

Simulating Multi-Scale Pulmonary Vascular Function by Coupling Computational Fluid Dynamics With an Anatomic Network Model

Behdad Shaarbaf Ebrahimi[1], *Haribalan Kumar*[1], *Merryn H. Tawhai*[1], *Kelly S. Burrowes*[1], *Eric A. Hoffman*[2] *and Alys R. Clark*[1]*

[1]Auckland Bioengineering Institute, University of Auckland, Auckland, New Zealand, [2]Department of Radiology, University of Iowa, Iowa City, IA, United States

The function of the pulmonary circulation is truly multi-scale, with blood transported through vessels from centimeter to micron scale. There are scale-dependent mechanisms that govern the flow in the pulmonary vascular system. However, very few computational models of pulmonary hemodynamics capture the physics of pulmonary perfusion across the spatial scales of functional importance in the lung. Here we present a multi-scale model that incorporates the 3-dimensional (3D) complexities of pulmonary blood flow in the major vessels, coupled to an anatomically-based vascular network model incorporating the multiple contributing factors to capillary perfusion, including gravity. Using the model we demonstrate how we can predict the impact of vascular remodeling and occlusion on both macro-scale functional drivers (flow distribution between lungs, and wall shear stress) and micro-scale contributors to gas exchange. The model predicts interactions between 3D and 1D models that lead to a redistribution of blood between postures, both on a macro- and a micro-scale. This allows us to estimate the effect of posture on left and right pulmonary artery wall shear stress, with predictions varying by 0.75–1.35 dyne/cm^2 between postures.

Keywords: pulmonary circulation, computational fluid mechanics, network flow modelling, lung, computational model

OPEN ACCESS

Edited by:
Susumu Sato,
Kyoto University, Japan

Reviewed by:
Brody Foy,
Harvard Medical School, United States
Rui Carlos Sá,
University of California, San Diego, United States

***Correspondence:**
Alys R. Clark
alys.clark@auckland.ac.nz

Specialty section:
This article was submitted to Networks in the Respiratory System, a section of the journal Frontiers in Network Physiology

Received: *01 February 2022*
Accepted: *25 March 2022*
Published: *25 April 2022*

Citation:
Ebrahimi BS, Kumar H, Tawhai MH, Burrowes KS, Hoffman EA and Clark AR (2022) Simulating Multi-Scale Pulmonary Vascular Function by Coupling Computational Fluid Dynamics With an Anatomic Network Model. Front. Netw. Physiol. 2:867551. doi: 10.3389/fnetp.2022.867551

INTRODUCTION

The pulmonary circulation carries almost the entire cardiac output to the pulmonary alveoli, in order to expose deoxygenated blood to the higher partial pressure of oxygen in the alveolar airspaces. Its function is truly multi-scale, in that blood traverses through vessels of 2–3 cm diameter at the main pulmonary artery Edwards et al. (1998) down to the order of μm diameters in the pulmonary capillaries Fung and Sobin (1969). The distribution of blood flow within this circulation is critical to providing good matching of perfusion to ventilation (air flow) at the alveolar level. This matching is determined by a combination of the effect of gravity acting to deform lung tissue locally, the hydrostatic effect of gravity which acts directly on blood, and a contribution from the anatomic structure of the pulmonary airways and blood vessels Kang et al. (2018). The distribution of perfusion has been demonstrated to be dependent on each of these mechanisms Clark et al. (2011b); Hlastala and Glenny (1999); Hopkins et al. (2007); West et al. (1964), with anatomic structure playing a greater role in the distribution of perfusion than ventilation in the normally functioning

adult lung Clark et al. (2011b); Kang et al. (2018). Overall, the nature of blood flow in the largest and smallest blood vessels is different, and this means that the physics of computational models derived to capture their function relies on different assumptions and biomechanical models. For example, blood flow in the main pulmonary arteries has significant 3-dimensional (3D) complexities, and is functionally altered in patients with pathologies such as pulmonary hypertension Schäfer et al. (2017). In contrast, flow rates and Reynolds numbers are lower in the pulmonary micro-circulation, leading to reduced complexity in flow patterns. However, the pulmonary capillaries directly interact with the expanding alveoli, and are recruited and de-recruited dynamically in response to changes in local air and blood pressure Fung and Sobin (1969); West et al. (1964); Yen et al. (1980).

Several computational models of the branching network of arteries and veins in the pulmonary circulation have been proposed. These range from 3D computational fluid dynamics (CFD) simulations representing the branching network of large arteries Kheyfets et al. (2015); Tang et al. (2011, 2012), through to 1-dimensional (1D) network models that aim to capture the distribution of blood flow within the entire pulmonary circulation Clark et al. (2011b, 2014); Ebrahimi et al. (2021). These models typically target two main areas: 1) wall shear stress (WSS) distribution in pulmonary artery networks which is intimately associated (and correlated) with endothelial dysfunction Kheyfets et al. (2015); Tang et al. (2012), but that cannot be measured experimentally; 2) the major drivers of pulmonary perfusion distribution in the lung in health and disease, and how local perfusion contributes to ventilation-perfusion matching and gas exchange Clark et al. (2014); Kang et al. (2018). 3D CFD is far more accurate in predicting WSS than simplified 1D models. One of the well known challenges of such models is the boundary condition prescription, with small deviations in boundary conditions sometimes yielding large differences in observed velocities Kheyfets et al. (2013). 1D networks on the other hand can well-predict micro-scale perfusion and the impact of vascular structure and gravity on this function, but cannot be used to accurately simulate flow in the major pulmonary arteries Clark et al. (2017). In pathological lungs, this is particularly important, as micro-vascular changes may impact pressure, flow and WSS in the major vessels, and vice versa Wang and Chesler (2011). Previous models have coupled 3D CFD to downstream models via imposed boundary conditions, for example by a structured tree approach Kheyfets et al. (2015), or in other organ systems by using measured values of flow over time from Doppler ultrasound as boundary conditions Oshima et al. (2001); Perktold and Rappitsch (1995). However, no model exists that can predict the multi-scale function in the complex network of the pulmonary vasculature across spatial scales.

Here, we present an integrated model of the pulmonary circulation that includes a 3D representation of the major pulmonary arteries coupled to an anatomically realistic 1D network model that comprises the entire circulation that lies downstream of these major arteries. Importantly, the network model incorporates each of the major contributors to perfusion distribution in the lung (anatomical structure across scales, and gravitational effects), alongside the capability to predict WSS accurately in the major pulmonary arteries.

METHODS

The methodological framework proposed here employs a subject-based model that represents the anatomical structure of an individual's lungs generated from computed tomography (CT) imaging. An illustration of the 3D geometrical model and its connectivity to a 1D network model is shown in **Figure 1**. The methodology is demonstrated in a whole lung with the main pulmonary artery and left and right pulmonary arteries simulated as 3D structures. While the number of generations that may be incorporated into the 3D model is arbitrary, two generations of arteries were chosen in this study to test the hypothesis that posture may impact the distribution and nature of flow between the left and right lungs. The 3D structure is connected to an anatomically-based 1D tree representing morphological branching to the level of the pulmonary acini. For this study, the model geometry was derived from CT images of a healthy adult male (age: 23; weight: 80.9 kg; body mass index: 23.1 kg/m^2) representative of a population of 30 normal subjects aged between 20–30 years old, derived from the Human Lung Atlas Database Hoffman et al. (2004). The subject has the closest lung shape to the mean lung shape for this population determined by a principal component analysis Osanlouy et al. (2020). Functional Residual Capacity (FRC) measured seated was 3.4 L. Imaging was acquired supine with lung volume held constant at 50% of vital capacity.

Model Geometry

The model geometry employed in this study aims to capture the lung shape and the distribution of the largest blood vessels to one generation beyond the sub-segmental level, as measured from CT imaging. The first two generations of blood vessels were represented by their 3D structure, then the centerlines of blood vessels were derived from CT to one generation beyond the segmental level. Blood vessels beyond this level, to the level of the pulmonary acinus are generated as a branching network that is consistent with morphometric data on typical branching structures of pulmonary arteries and veins Burrowes et al. (2005); Horsfield (1978); Horsfield and Gordon (1981); Huang et al. (1996); Tawhai et al. (2004). Lungs, lobes, airways and intra-pulmonary blood vessels were segmented using PASS (Pulmonary Analysis Software Suite, University of Iowa). This study used non-contrast-enhanced imaging, therefore extra-pulmonary blood vessels were segmented manually, starting from the point of attachment of the main pulmonary artery to the heart. Three scales of model geometry were created. The first represents a 3D volume mesh of the first two generations of pulmonary arteries. The second is a spatially distributed network of 1D elements that represents segments of the centerlines of the branching vascular tree. The final scale represents the acinar structure.

Figure 1 provides a schematic of the interface between the 3D volume and the 1D representation of the blood vessel network. A

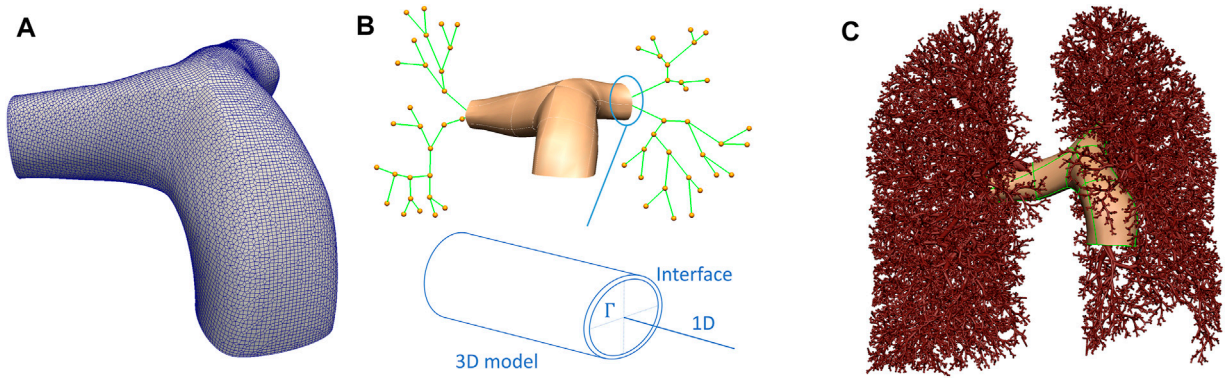

FIGURE 1 | Schematic representation of the 3D/1D model of the pulmonary circulation. **(A)** The 3D model mesh. **(B)** A schematic of how 3D and 1D models are related, including an illustration of the interface, Γ, between the two models. **(C)** Depicts the whole lung model, with the largest blood vessels explicitly meshed in 3D, and the smaller blood vessels represented by elements defined by branch points and their radii.

3D surface model is generated to reflect the vessel surface of the main pulmonary artery and its left and right branches (**Figure 1A**). A centerline representation of the main pulmonary artery and distal branches to one generation beyond the segmental level was extracted, and a 1D network template mesh was manipulated to assign nodal locations to each bifurcation of the pulmonary arteries down to one level beyond the segmental arteries (**Figure 1B**). The surface of the 3D geometry has a bicubic-Hermite element structure, and this is fit to a cloud of datapoints representing the vessel surface by a least squares minimization process - optimizing the sum of squared differences between each surface point and the nearest surface element Fernandez et al. (2004); Tawhai et al. (2009). The surface was converted to a volume mesh using CFMesh (version 1.1, Creative Fields, United Kingdom)—a library implemented in OpenFOAM for mesh generation (Version 7, OpenCFD Ltd.[1]). The meshing process produces hexahedral cells, with polyhedra in the transition zones between cells of various sizes with hexahedral elements at the boundary layers.

To generate a morphological vascular network beyond the major vessels, the volume filling branching algorithm proposed by Tawhai et al. (2004), and presented for the pulmonary blood vessels by Burrowes et al. (2005) was employed. The segmentations of the lobes were converted to a surface data cloud, and a bicubic-Hermite template surface mesh was fitted (following Tawhai et al. (2009)). The surface mesh was filled with an equi-distributed array of datapoints. Using the branching upper vasculature derived from imaging (to one generation beyond the segmental level) as an initial condition, a volume filling algorithm was used to generate branching vessels that fill the volume, and that terminate at ≈ 32,000 terminal blood vessels feeding the pulmonary acini. For simplicity, the pulmonary venous structure is assumed to follow the pulmonary arterial structure except at the pre-segmental level (which is derived manually from imaging). Each blood vessel represented in the 1D network model is described by an element representing its centerline, and its radius.

The acinus is modeled as a 9-generation symmetric network of arterioles and venules that are connected in series, and are connected in parallel by 'sheets' of capillary bed (Clark et al. (2010); Fung and Sobin (1969); Haefeli-Bleuer and Weibel (1988)). This anatomically-based intra-acinar structure has been termed a 'ladder' model (Clark et al. (2010; 2011a)). A symmetric structure is assumed to allow the model solution in ≈30,000 acinar units, and our previous modeling suggests that while within-acinus branching asymmetry impacts sub-acinar heterogeneity in perfusion, its impact on acinar resistance is small Clark et al. (2011a). It allows a direct connection between the capillary structure (which is influenced primarily by local air pressure and inflation), and a physiological stratification of function within them from the most proximal to distal capillary (Read (1969a,b)). The ladder model also facilitates coupling micro-circulatory function to the intra-pulmonary macro-vasculature (which is under the influence of lung tethering pressure, related to elastic recoil) and outwards to the extra-pulmonary vessels with their more complex flow patterns and direct connection to the heart.

3D Computational Fluid Dynamics Simulations

To simulate flow in the pulmonary arteries, the 3D CFD solver OpenFOAM was used. The blood within these arteries was assumed Newtonian, incompressible and laminar. The PimpleFoam solver based on the PIMPLE algorithm was used Passalacqua and Fox (2011). This algorithm combines the PISO (Pressure-Implicit Splitting Operator) Issa (1986) and SIMPLE (Semi-Implicit Method for Pressure-Linked Equations) algorithms Caretto et al. (1973); Ferziger et al. (2002); Jasak (1996); Passalacqua and Fox (2011); Patakar (1980). Outer correction loops are used in the PIMPLE method to specify number of iterations. To guarantee that the explicit sections of the equations converge, outer corrector loops are enabled. In the

[1]www.openfoam.org

PIMPLE algorithm, a dynamic time step technique, allows the time step to vary in relation to the maximum Courant number allowed. Courant number is a dimensionless measure that provides the rate at which data is transported from one cell to another. Adjustable time step is utilized in all of the current simulations, with a maximum Courant number of 1.0. Steady state simulations were performed. Flow inlet boundary conditions were prescribed at the main pulmonary artery (the inlet), and fixed pressure boundary conditions were imposed at each outlet of the 3D model, when not coupled to the 1D model. A mesh dependence analysis on the 3D model was performed to ensure that the mesh resolution does not affect the final results.

To estimate WSS on the pulmonary vasculature, a quantitative metric was chosen that is considered to be independent of the 3D model reconstruction Kheyfets et al. (2015). The WSS magnitude is averaged over the luminal surface (S) of the 3D geometry to define a spatially averaged wall shear stress (SAWSS)

$$\mathrm{SAWSS} = \frac{1}{A}\iint_S \mathrm{WSS}\,\partial S, \tag{1}$$

where A is the total surface area of the luminal surface of the mesh.

1D Network Flow Simulations

The 1D network flow model, that allows for a functional connection between the macro- and micro-vasculatures is based on a compliant electrical analogue described in detail by Clark et al. (2011b) This model is available as an installable library within the lungsim library of Aether.[2] The model incorporates key features of extra-capillary anatomy and blood flow, and employs a sheet flow model for the pulmonary capillaries (derived by Fung Fung and Sobin (1969)) which includes the recruitment and derecruitment of capillary bed in response to air and blood pressures. In each extra-capillary blood vessel the relationship between blood pressure and blood flow ($\dot{Q}$) is described by a modified Poiseuille equation that accounts for the impact of gravity on blood flow

$$\Delta P = \frac{128\mu L}{\pi D^4}\dot{Q} + \rho_b g L\cos\theta, \tag{2}$$

where ΔP is the blood pressure drop along the length of the vessel, μ is the viscosity of blood, L is the axial length of the vessel, D is the diameter of the vessel, ρ_b is the density of blood, g is gravitational acceleration, and θ is the angle the vessel centerline makes with the direction of gravity. The gravitational term is neglected in small intra-acinar vessels where the resistance term dominates. A linear relationship between transmural pressure (P_{tm}), defined as blood minus extra-vascular pressure, is assumed with compliance constant α Clark et al. (2011b); Krenz and Dawson (2003). In vessels with $D < 200\,\mu$m the extra-vascular pressure is defined as alveolar pressure Yen et al. (1980), and in larger vessels, extra vascular pressure is defined as local elastic recoil, which is assumed in this model to vary linearly with gravitational height.

[2]https://github.com/LungNoodle/lungsim

At the level of the capillary sheet, flow depends on the local balance between blood and air pressures, consistent with West's West et al. (1964); West (1999) description of zones of capillary flow in the lungs. With P_{tm} at this scale defined as blood minus air pressure, we are able to define a capillary sheet height H across a range of capillary recruitment conditions

$$H = \begin{cases} 0, & \text{if } P_{tm} < 0, \\ H_0\,(1 + \alpha_c P_{tm}) & 0 \le P_{tm} < P_{CU}, \\ H_{max} = H_0 + \alpha_c P_{tm}, & \text{if } P_{CU} \le P_{tm}, \end{cases} \tag{3}$$

where P_{CU} is defined as an upper bound for pressure beyond which the sheet height remains constant. The relationship between pressure and flow is then defined by

$$\dot{Q} = \frac{SA}{\mu_c f l_c^2}\int H^3 dP_{tm}, \tag{4}$$

where SA is the capillary surface area in any given sheet of capillaries connecting arteriolar to venular circulations, μ_c is the viscosity of capillary blood, f is a constant, l_c is the average path length between arteriole and venule within the capillary sheet. Analytical relationships between $\dot{Q}$ and P are derived in detail by Clark et al. (2010) for conditions relevant to pulmonary capillary perfusion. At each bifurcation in the 1D network, continuity of pressure and conservation of flow (flow into a bifurcation equals flow out) is prescribed. In the absence of coupling to the 3D model, cardiac output is specified as a flow boundary condition at the main pulmonary artery, and a pressure outlet condition is imposed at the main pulmonary veins.

Coupling Method

There are two interfaces connecting the two domains at the outlets of the left and right pulmonary arteries in this model (**Figure 1**), however, any number of interfaces can be defined. At each interface Γ a circle of Willis methodology is employed, following Passerini et al. (2009). Coupling was achieved by prescribing continuity of pressure and flow defined by

$$P_{1D} = \frac{1}{|\Gamma|}\int_\Gamma p_{3D}\,d\gamma, \quad \dot{Q}_{1D} = -\rho\int_\Gamma u_{3D}.n\,d\gamma, \tag{5}$$

where indexes $1D$ and $3D$ represent corresponding domains (**Figure 1B**). γ represents an interface surface segment and u and n are velocity and surface normal vectors.

To solve the coupled system, we solve the two systems iteratively. There is a matching interface in the geometry at the point of intersection between models, and simulations in the 1D model are conducted with boundary conditions imposed at these interface points. The 3D model is simulated by prescribing a boundary condition ($\dot{Q}_{inlet}$) and pressure-outlet boundary conditions (P_i, where i is the number of outlets in the 3D geometry, or interfaces). Solution of 3D governing equations yields corresponding outlet flows ($\dot{Q}_i$). These flows are passed to the 1D network as inlet flow boundary conditions, and the 1D network solution is obtained. The 1D solution yields corrected pressure values (P_i^1) that are passed to the 3D model as outlet boundary conditions for the second coupling iteration, and so on.

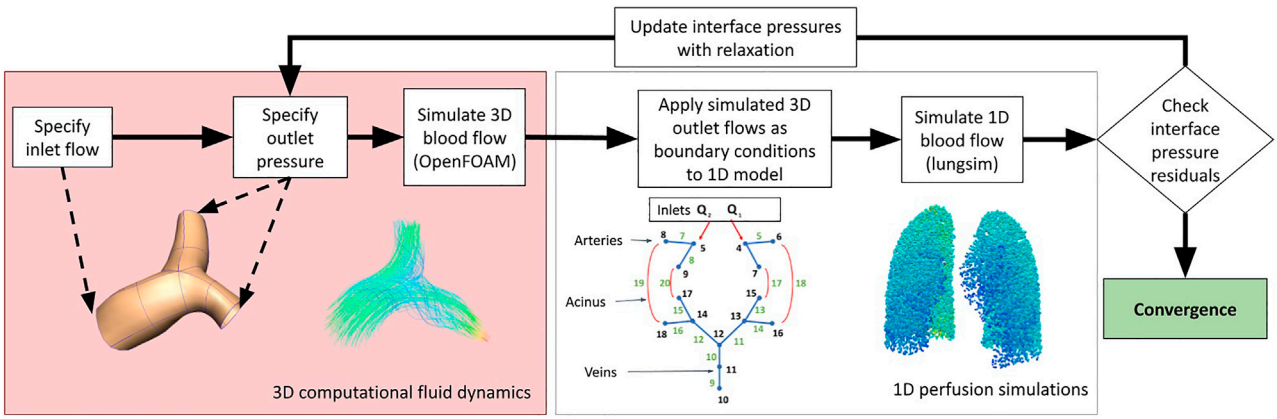

FIGURE 2 | A schematic illustrating the methodologies employed in this study to couple 3D computational fluid dynamic simulations to 1D perfusion in a network model incorporating the multiple scales of function that are important to blood flow in the lungs.

Additionally, at each coupling iteration, the corrected pressure and flow are regularized using an under-relaxation factor

$$\begin{cases} {P_{i1D}}^{k+1} = \lambda {P_{i3D}}^{k} + (1-\lambda){P_{i1D}}^{k}, \text{and,} \\ {Q_{i1D}}^{k+1} = \lambda {Q_{i3D}}^{k} + (1-\lambda){Q_{i1D}}^{k}, \end{cases} \quad (6)$$

where λ is the under-relaxation factor, i is the interface index, and k is the coupling iteration number between domains. The solution procedure is illustrated in **Figure 2**.

Coupling Convergence

Convergence is assumed to have been reached when the pressure and flow at the interface branches are within a specified tolerance between two coupling iterations. Continuity at the 1D-3D domain interface between iterations was used to define error. If we define ϵ, which is a user-defined tolerance, to be the error threshold for convergence, the solution is converged when

$$\sqrt{\sum_i \left(P_i^k - P_i^{k-1}\right)^2} \le \epsilon, \quad (7)$$

is satisfied, with P_i^k being the pressure at interface i after the kth iteration. Here, ϵ is chosen to be 0.1 Pa which is the cumulative error allowed at both interfaces. This threshold ensures that the error is computationally acceptable compared with typical pressure values at this scale (≈2000 Pa in healthy, and higher in hypertensive scenarios).

Model Parameterization and Simulations Conducted

We conduct simulations to assess the behavior of the model under two primary perturbations: 1) the effect of cardiac output within a physiological range, and 2) the effect of posture. Simulations were conducted with boundary conditions at the main pulmonary artery reflecting a mean volumetric flow of 4, 4.8 and 5.6 L/min, in each of zero gravity, prone, supine and upright postures. Primary output metrics were the distribution of acinar perfusion, and SAWSS in the major pulmonary vessels (the main pulmonary artery and the left and right pulmonary arteries). Model parameters and key geometrical features of the model are given in **Table 1**.

Results are presented first for the non-coupled *1D model* (as presented in Clark et al. (2011b)), and *3D model* (full CFD model in major arteries with fixed pressure boundary conditions) to understand non-linearity in the two systems. Then, the full model is presented as the *coupled model*, to analyze how whole lung perfusion simulations behave. The *zero gravity* (0g) coupled model can be interpreted as aligning with existing CFD strategies which assign resistance to outlets depending on the size of these vessels, or estimates for downstream resistances such as structured trees, as they represent the downstream resistance based on anatomy but in the absence of gravitational factors. Comparisons of CFD behaviors against data from the literature are provided in **Supplementary Section S1**.

RESULTS

Mesh Independence

Table 2 shows mesh quality and changes in key output metrics (mean pulmonary artery pressure (mPAP), right pulmonary artery flow (RPA flow), left pulmonary artery flow (LPA flow) and SAWSS) for assessment of mesh independence of solutions. In total, six different mesh densities were generated to assess mesh independence of the model. For cell numbers > 199268 changes in each key output metric with further mesh refinement were < 2% and so this mesh density was selected for further simulations.

Flow-Pressure Relationships of 1D and 3D Model

The 1D and 3D models were first analysed independently to understand the effect of geometry on the flow-pressure relationship (**Figure 3**). The 1D model was solved under baseline parameterization and the pressure differential between the inlet and the outlets to the 3D model was reported, and the 3D model was solved first with fixed and equal pressure boundary

TABLE 1 | A description of model parameters, and geometric features of the 3D model. The parameterization of the 1D network model is described in detail by Clark et al. (2011b), with key parameters outlined here.

Parameter	Description	Value	References & Methodology
A	1D extra-acinar compliance (Pa^{-1})	1.49×10^{-4}	Krenz and Dawson (2003): Derived from 26 studies of distensibility across species
ρ_b	Blood density (kg/m^3)	1050	Pries et al. (1996): Population average across *in vitro* studies
M	Blood viscosity (Pa/s)	0.0035	Pries et al. (1996): Population average across *in vitro* studies
μ_c	Capillary blood viscosity (Pa/s)	0.0019	Fung (1984): Combination of *in vitro* measurements and theoretical derivation
G	Gravitational acceleration (m/s^2)	9.81	
SA	Total capillary surface area (m^2)	65.4	Gehr et al. (1978): Population average derived from electron microscopy
α_c	Capillary sheet compliance (m/Pa)	1.3×10^{-9}	Sobin et al. (1979): Estimate from photomicrographs in *ex vivo* cat lung
F	Numerical factor (no units)	21.6	Fung and Sobin (1972): Theoretical estimation
l_c	Average pathlength from arteriole to venule (m)	1186×10^{-6}	Zhou et al. (2002): Theoretical estimation
H_0	Unstrained capillary sheet height (m)	3.5×10^{-6}	Sobin et al. (1979): Estimate from photomicrographs in *ex vivo* cat lung
H_{max}	Maximum capillary sheet height (m)	7.7×10^{-6}	Sobin et al. (1979): Estimate from photomicrographs in *ex vivo* cat lung
	Strahler diameter ratio (arteries)	1.52	Huang et al. (1996): Fit parameter to produce geometry consistent with vascular casting
	Strahler diameter ratio (veins)	1.56	Huang et al. (1996): Fit parameter to produce geometry consistent with vascular casting
	Main pulmonary artery area (m^2)	7.72×10^{-4}	Derived from CT.
	Left pulmonary artery area (m^2)	3.77×10^{-4}	Derived from CT.
	Right pulmonary	3.54×10^{-4}	Derived from CT.
	3D geometry volume (m^3) artery area (m^2)	7.967×10^{-5}	
	Number of 1D vessel elements	153396	Output from meshing
	Number of interfaces between 1D and 3D	2	User defined
	Number of acinar units	30676	Output from meshing, consistent cwith vascular casting Huang et al. (1996)

TABLE 2 | Mesh quality and independence metrics. Quality metrics are: Number of faces on vessel wall, Maximum cell orthogonality for each mesh, average orthogonality of cells and maximum cell skewness. Key output metrics are: Mean pulmonary artery pressure (mPAP), right pulmonary artery flow (RPA flow), left pulmonary artery flow (LPA flow) and spatially averaged wall shear stress (SAWSS). Percent differences from the most refined mesh (340056 cells) are also reported.

Number of cells	26597	95081	151469	199268	270686	340056
Number wall faces	4178	12035	17421	21645	28151	34345
Average area of s single wall cell (mm^2)	0.029	0.0081	0.0051	0.0039	0.0029	0.0023
Maximum orthogonality	64.49	64.87	64.27	64.69	64.62	64.49
Average orthogonality	9.31	7.32	6.60	6.38	6.21	6.19
Maximum skewness	2.85	3.06	2.83	2.72	2.69	2.70
mPAP (Pa)	2213.0	2211.5	2212.8	2211.8	2211.9	2211.9
mPAP (% difference from refined mesh)	0.05%	–0.02%	0.04%	–0.005%	0.001%	—
RPA flow (L/min)	2.629	2.641	2.711	2.645	2.646	2.645
RPA flow (% difference from refined mesh)	–0.60%	–0.15%	2.50%	–0.002%	0.04%	—
LPA flow (L/min)	2.171	2.159	2.089	2.155	2.154	2.155
LPA flow (% difference from refined mesh)	0.74%	0.19%	–3.06%	0.03%	–0.04%	—
SAWSS ($dyne/cm^2$)	5.29	5.58	5.72	5.85	5.94	5.96
RPA flow (% difference from refined mesh)	–11.2%	–6.38%	–4.03%	–1.85%	–0.34%	-

conditions at the outlets, and again with a 10 Pa pressure differential between LPA and RPA to establish an asymmetry in the model. Both models show non-linear behavior, with the 3D model exhibiting relatively small changes in pressure with increases in flow at low flow rates than at high flow rates. The 1D model shows a flattening off of the relationship between flow and pressure at high flow rates.

When the 1D and 3D models are solved independently, each model also predicts a different distribution of blood flow between LPA and RPA. The 1D model is dominated by downstream effects due to vascular anatomy, capillary recruitment and gravity, and as such across all postures that were simulated, 46.2%–46.9% of flow is predicted to flow to the LPA. In the 3D model, 52.5%–53.2% of the flow is predicted to go through LPA under equal pressure boundary conditions and 28.2%–43% of the cardiac output flows through the LPA under a 10 Pa pressure difference between LPA and RPA outlets, depending on the cardiac output value. This is because the 3D model flow and pressure drop are affected primarily by geometrical detail such as curvature at the bifurcation. This difference between the 1D and 3D model predicted flows simply shows the importance of capturing subject-specific large scale effects into network models of pulmonary perfusion, and vice versa.

Macro-Scale Blood Flow

The coupled model integrates macro-scale flow dynamics from the 3D model with perfusion in smaller blood vessels from the 1D model. This leads to a physiologically meaningful impact of

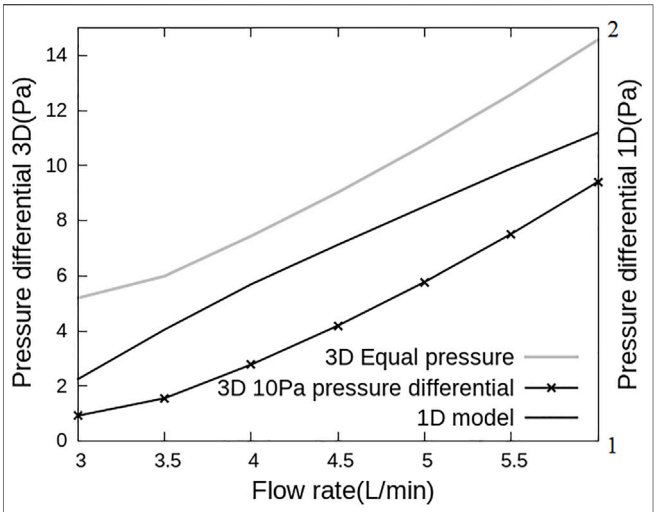

FIGURE 3 | Flow and pressure relationships for the 1D and 3D models used in this work. Pressure differential is defined as the difference in pressure between inlet and LPA outlet. This differential is plotted versus inlet flow rate with 3D model simulations on the primary and 1D model simulations on the secondary axis. The pressure-flow association are different for the two models, with the 3D model dominated by a flow dependent resistance and the 1D model responding to resistance-compliance relationships.

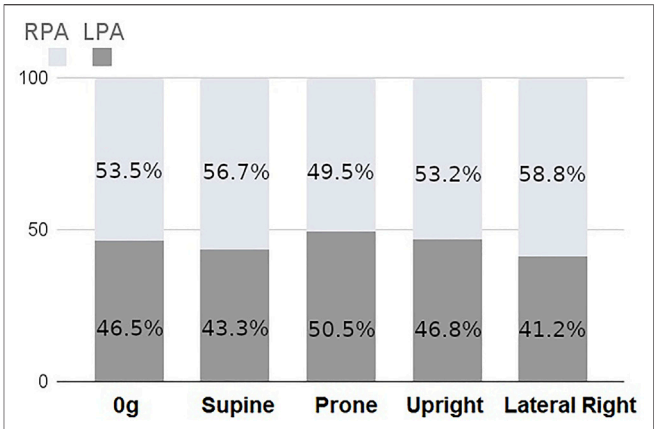

FIGURE 4 | Percentage of total inlet blood flow (cardiac output) between left and right lungs as predicted by the coupled model with a fixed inlet flow of 4.8 L/min. There is a predicted redistribution of flow with posture due to gravitational effects.

gravity arising in the model across scales which is unique to this coupled system. **Figure 4** shows the proportion of the cardiac output that enters the right and left lung in simulations of zero gravity (0g), and in 1g in prone, supine, upright and right-lateral, all with a fixed cardiac output of 4.8 L/min. For reference, in this model the right lung comprises 52.5% of the total lung volume. When model posture is altered there is a redistribution of blood, due to gravitational distribution of lung tissue with respect to the feeding vessels (that arise from the heart) and so the left and right lung flow balance is altered. This redistribution is to the left lung in prone, the right lung in supine and the left lung in left-lateral postures. Trends predicted by the model are consistent with data illustrating left-right flow distribution in the lungs derived from magnetic resonance imaging Wieslander et al. (2019). In zero gravity simulations (and in the 1D model presented by Clark et al. (2011b)) flow is distributed between left and right lungs proportionally to lung volume, with 53.5% of volumetric blood flow to the right lung.

Flow velocity magnitude and streamlines redistribute within the arterial lumen with posture (**Figure 5**). This also translates to a redistribution of shear stress with posture (**Figure 6**), with model predictions of shear stress differing in the LPA and RPA due to their relative size, and flow distribution shifts between the two lungs. Predicted RPA shear stress is typically higher than LPA shear stress, and assuming zero gravity simulations as a reference state (where flow is distributed relative to volume), both the left and right pulmonary arteries can exhibit shifts of up to 0.75 dyne/cm^2 from this reference in between postures. The greatest shift simulated occurs between a prone and right lateral posture with a predicted difference of up to 1.35 dyne/cm^2.

Acinar Scale Perfusion Distribution

The coupled model predicts hemodynamics across spatial scales relevant to the lung. At the acinar scale, there is a known gravitational gradient in perfusion that is important in the matching of perfusion to ventilation. **Figure 7** shows gravitational gradients in perfusion predicted by the coupled model in zero gravity, and under 1g in prone, supine (typically imaged) and upright (typical functional) postures at a fixed cardiac output. Comparisons with the same measures predicted by the 1D model and across different cardiac outputs are presented in **Supplementary Section S2**. Parameters for the right lateral posture are not reported as in this case the entire left lung is non-dependent tissue, and so gradients over the gravitational height become dependent on the lung in question. All predicted perfusion distributions are consistent with the previous model of Clark et al. (2011b), with gravitational gradients (G) in perfusion ranging from 6.80%/cm to 9.10%/cm and coefficient of variation (COV) ranging from 33.3%–47%. These ranges for G and COV have previously been shown to be consistent with imaging studies, when analysed on a spatial scale typical of imaging (e.g., the voxel size in magnetic resonance imaging) Clark et al. (2011b). The coupled model predicts physiologically consistent changes with cardiac output, that is a decrease in G as the gravitationally non-dependent lung vasculature is recruited, and a consistent decrease in COV as perfusion becomes more uniform over the height of the lung.

In general, the coupled model predicts a more heterogeneous distribution of perfusion within the lung than the 1D model previously presented by Clark et al. (2011b). This is due to the balance between resistive properties of the two scales of the model which results in a redistribution of blood flow between the two lungs in the 3D compared with the 1D model. **Figure 8** illustrates the change in the predicted standard deviation of perfusion with gravitational height of the lung in the coupled model compared to the previously published 1D model Clark et al. (2011b). In zero gravity and upright simulations, the left and right lung flow

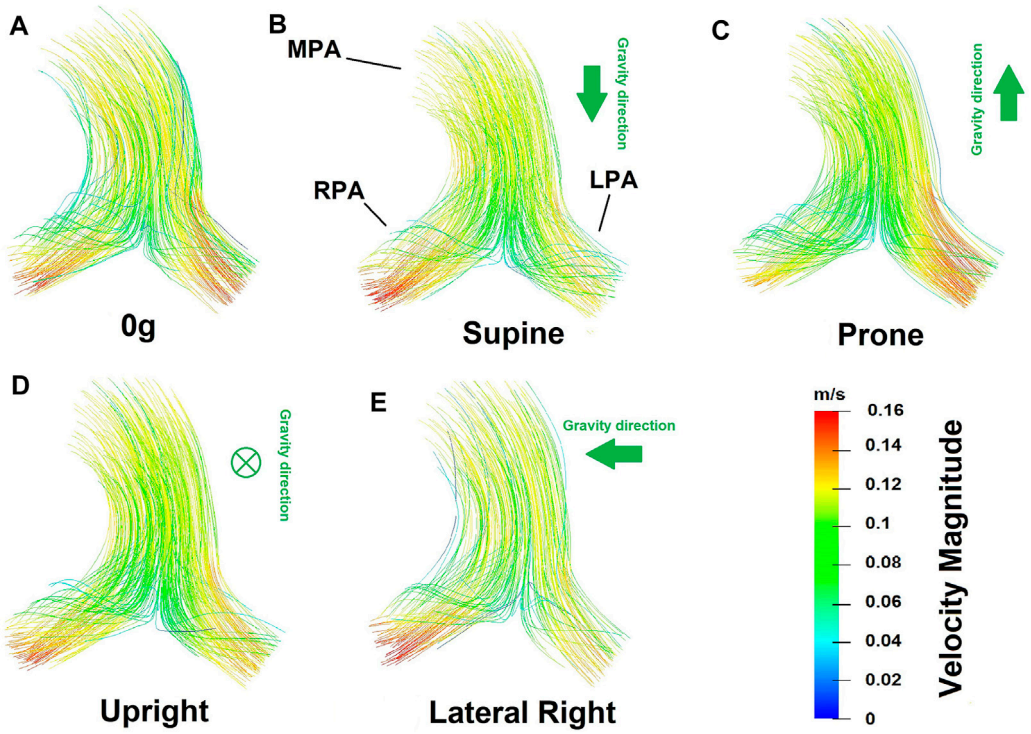

FIGURE 5 | Flow velocity magnitude and streamlines predicted from the coupled model in different postures **(A)** zero gravity, **(B)** supine, **(C)** prone, **(D)** upright and **(E)** lateral right. In these images the viewer is looking down (into the page) at the main pulmonary artery. Therefore in supine simulations gravity is acting downwards with respect to the page, in prone simulations upwards, and in upright simulations into the page. The left-right shifts in blood flow distribution predicted in the model are evident in the flow velocity magnitude.

distributions are approximately equivalent to the relative volume of the two lungs and so the two models predict a similar heterogeneity in perfusion with gravitational height. However, in the supine and prone lungs there is a redistribution of flow meaning that the left and right lungs do not receive a relative flow that matches their volume and so there is overall an increase in heterogeneity as predicted in the 3D model compared to the previously published 1D model. The effect is greater in the gravitationally non-dependent lung which accommodates increases in flow. As overall flow (cardiac output) increases to one lung or the other, the distribution of flow in that lung becomes more uniform, so the impacts of the coupling are most apparent at lower cardiac outputs. In these cases, an increase in acinar perfusion heterogeneity of up to 20% in the coupled model compared to the 1D model is observed, indicating the inter-connectedness between macro-scale and micro-scale function.

DISCUSSION

In this study, we have presented an open-source methodology to couple 3D macrovascular fluid mechanics simulations to an anatomically defined 1D network model of the distal vasculature to allow for multi-scale analysis of pulmonary hemodynamic function. The inclusion of an anatomic network model in this methodology provides unique opportunities to connect the complexity of macro-vascular fluid dynamics with a recruitable capillary bed West et al. (1964); West (1999), that sits within a stratified acinar structure Read (1969b) that responds to gravitational influences West et al. (1964); Hopkins et al. (2007).

Computational fluid dynamics of the pulmonary circulation has been used widely, particularly in the assessment of macro-vascular wall shear stress due to its role in the development of pulmonary hypertensive disease Bordones et al. (2018); Kheyfets et al. (2015); Kong et al. (2018); Tang et al. (2012). As 3D simulations do not typically cover the full vasculature, the choice of outflow boundary conditions is critical, and can significantly impact simulation accuracy Kheyfets et al. (2013). Common boundary conditions employed in models of the pulmonary circulation include zero traction, resistance, and Windkessel (resistance-compliance) which can be adjusted to account for subject-specific variability but do not capture the anatomy or function of the distal micro-vasculature Kheyfets et al. (2013). An alternative is the structured tree approach Kheyfets et al. (2015), which uses an analytical approximation for downstream resistance of each 3D model outlet to characterize the expected pulmonary vascular resistance. This is based on the area of the outlet vessel and expected change in vessel cross-sectional area with generation in a typical pulmonary vascular tree. These structured trees are typically based on the

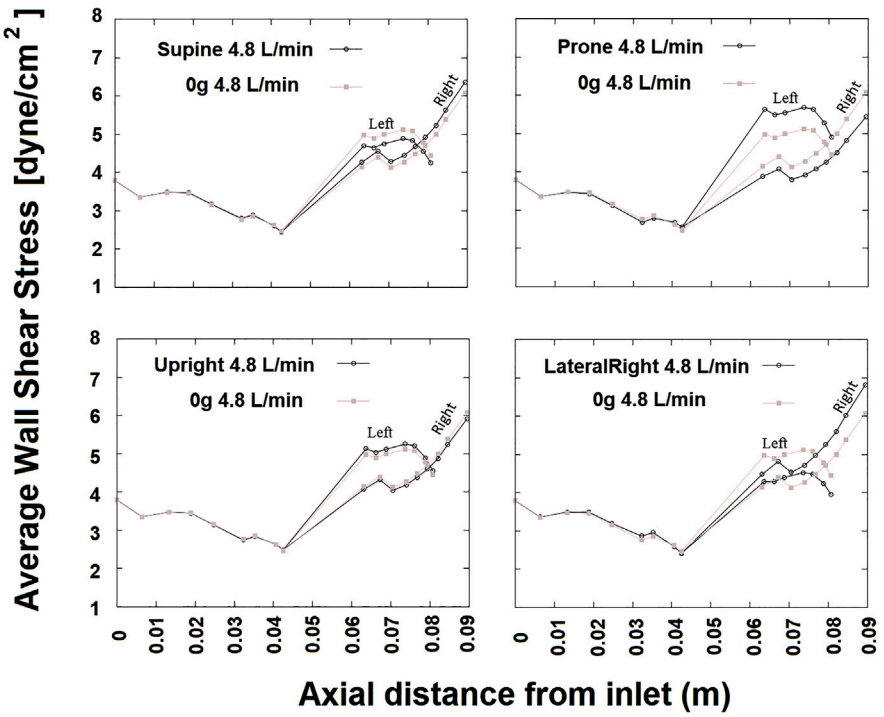

FIGURE 6 | SAWSS (in Pascals) defined in axial planes plotted versus axial distance for cardiac output 4.8 L/min at different postures. Due to presence of the bifurcation, beyond an axial distance of approximately 0.04 m two curves are shown one for left and right. In each plot, results from 0g are shown for reference in gray. The RPA WSS in general is greater than that in the LPA.

same morphometric data against which we have validated our anatomic 1D network model Horsfield (1978); Huang et al. (1996). However, they are not constrained by the shape of the lung nor informed by the function of the recruitable capillary beds in the lung. Zero gravity simulations in our model can be considered as similar to the structured tree approach as they estimate the downstream resistance based on extra-acinar vascular branching and the volume of the lung that is fed by a 3D model outlet.

While the distribution of perfusion in the lung has been simulated in whole lung models, these models typically employ simplified fluid dynamics, assuming arteries to be tubes within which flow is axisymmetric Clark et al. (2011b); Burrowes et al. (2005). While these simplifying assumptions allow for physiological predictions of perfusion within the lung which can be coupled to predictions of gas exchange (Burrowes et al. (2011b); Clark et al. (2014)), they do not hold in the largest pulmonary blood vessels where the flow is complex. In pulmonary hypertension, the flow patterns in the largest pulmonary arteries can exhibit vortices Schäfer et al. (2017). Disruptions to flow patterns due to bifurcations are also common in these larger arteries that have relatively high Reynolds numbers (see for example, **Figure 5**). These flow patterns introduce non-linearities between the flow rate in the major arteries and their resistance (flow dependent resistance, **Figure 3**). Flow dependent resistance is not typically captured in simplified network models of blood flow Clark et al. (2011b, 2014). Some models of airways have included a quasi-empirically derived resistance correction to account for this, but this correction is derived from experimentation and computational fluid dynamics simulations in representative geometries Pedley et al. (1970); Swan et al. (2012). Direct simulation in larger arteries is preferable to capture these effects in a patient specific manner. In addition to non-linearities in 3D models, 1D network models are typically also non-linear, due to their incorporation of vascular compliance and capillary recruitment, which occurs due to the balance of air and blood pressure at the acinar level. Capillaries can be locally collapsed, recruited and distended regionally in the lungs West et al. (1964); West (1999). This leads to a relatively large increase in flow with increases in pressure at low flows (as functional vascular bed is recruited), which then flattens as compliant limits are reached (consistent with whole lung pressure-flow relationships Burrowes et al. (2011a)). Although some simplified boundary conditions (e.g., Windkessel) can capture some of this non-linearity, the model presented here does so with an anatomical and physiological basis which can ultimately enable simulation of patient specific disruptions to resistance and compliance in conditions such as pulmonary hypertension.

Posture is an important consideration in assessing lung function, and it can have important implications in diagnosis and treatment of lung disease. For example, prone posturing has been shown to improve gas exchange in conditions such as respiratory distress syndrome Gattinoni et al. (2001), due to a

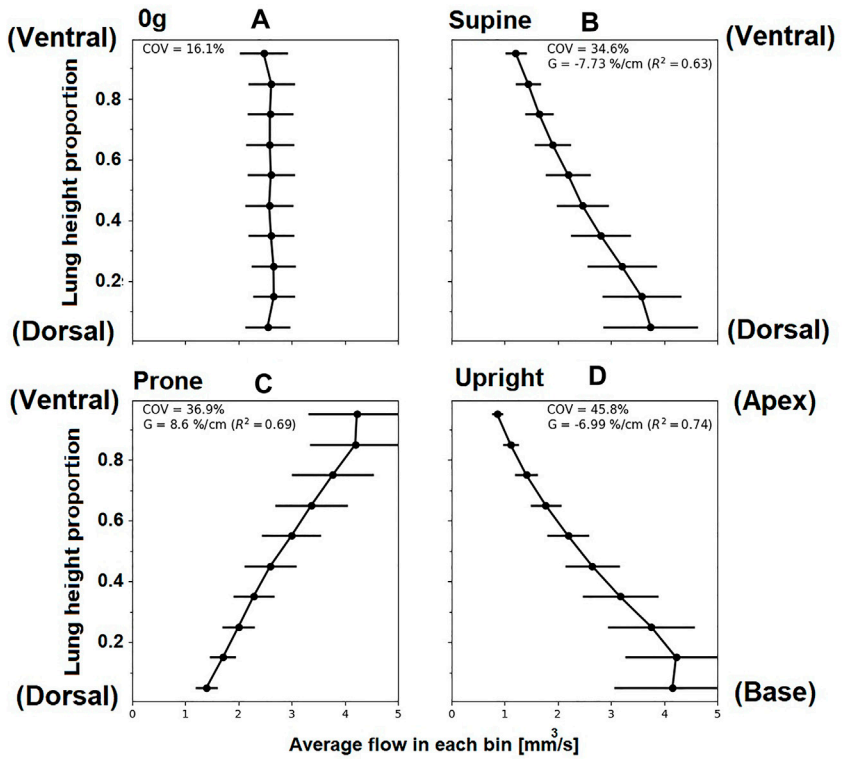

FIGURE 7 | Simulated relationships between acinar perfusion and gravitational height for 4.8 *L*/min cardiac output in different postures. In each case, the coefficient of variation (COV) and the gravitational gradient (G) of perfusion is indicated. Panels show posture **(A)** zero gravity, **(B)** supine, **(C)** prone and **(D)** upright, subsequently. The y-axis shows proportional height in the gravitational direction (cranio-caudal in upright, and ventral-dorsal in supine/prone). For zero gravity (0g), no gravitational gradient is reported since without the presence of gravity this property cannot be defined, ventral dorsal height is plotted and other axes show similar results. Supine and prone show opposite slope direction as the gravity direction is the same but posture is inverted.

redistribution of both ventilation and perfusion with gravity. In pulmonary hypertensive disease, some of the expected gravitational gradients in perfusion may be altered, as remodeling of small arteries and localized occlusion of vessels can lead to loss of vascular reserves and a more gravitationally uniform flow distribution, along with more locally heterogeneous blood flow Lau et al. (2014). The model presented in this study allows for gravitational influences to be investigated, and opens the door for studies that can investigate mechanisms of disruptions to these effects in disease. Here, we have shown that our coupled 3D-1D model can simulate changes in macro-vascular flow dynamics due to posture, simultaneously with predicting micro-vascular perfusion distribution. The volume of the two lungs are not equal, and the right lung has been reported to have 53.6 ± 1.5% of the total lung volume in supine (53.3 ± 1.3% upright) Yamada et al. (2020) reported. This is consistent with 0g simulations of flow distribution, albeit in a single patient-based model, which is distributed in a manner that is consistent with the differential in lung volume (53.4% to the right lung). The distribution changes with simulated posture, with the greatest flow to the right lung being in the lateral posture (58.8% of volumetric flow) and the lowest flow to the right lung being in the prone posture (50.5%) of volumetric flow. These re-distributions are consistent with imaging studies, which also show that with changes in posture, flow does not distribute proportionally to lung volume Wieslander et al. (2019), who showed on average 63% of flow distributing to the right lung in right lateral posture, compared with 52% in prone and 54% in supine. This redistribution of blood in our model is due to the shape of the lung, which means that in different postures there is a different volume of "dependent" tissue (tissue in which blood travels downward from the heart in the direction of gravity). Our previously employed 1D model does not exhibit the same physiological distribution of blood (see **Supplementary Table S1**), and this shows that at the macro-scale flow distribution is driven by both micro-vascular compliance-resistance relationships and the resistance of the upper vasculature. The left-right redistribution of blood with posture is also consistent with trends for higher heterogeneity in perfusion when using coupled model than a 1D model alone, which is consistent with observed perfusion heterogeneity Clark et al. (2011b). The dependence of blood flow distribution on posture does have functional implications for predictions of wall shear stress in computational fluid dynamics models, as imaged posture (usually supine) may not always reflect functional posture (often upright). We estimate that the effect of posture is likely to impact left and right pulmonary artery wall shear stress predictions by 0.75–1.35 dyne/cm^2, which are comparable in magnitude to

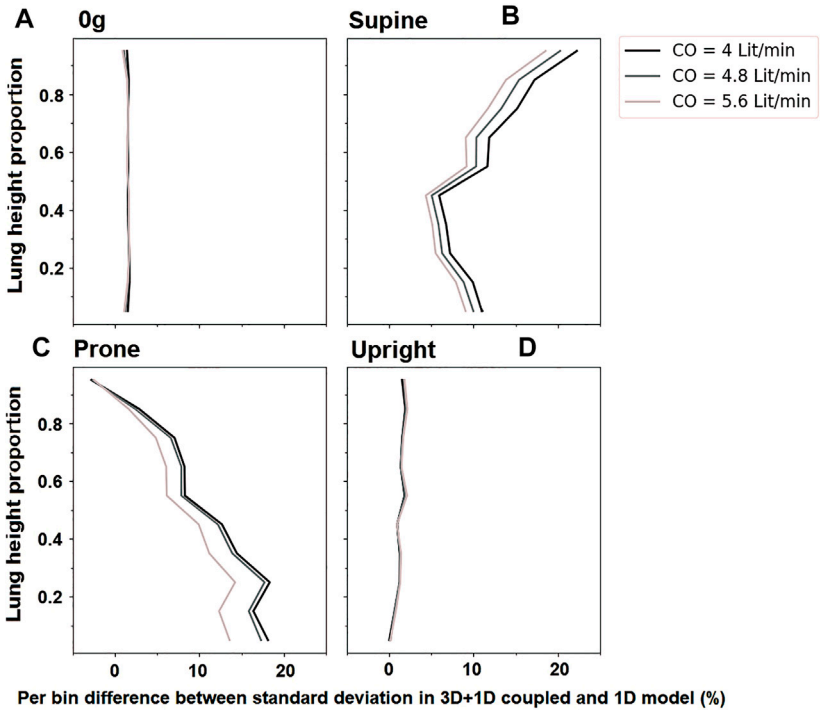

FIGURE 8 | The change in standard deviation of acinar perfusion in simulations of the coupled 3D macro-scale model to a 1D micro-scale model compared to a full 1D simulation as previously published by Clark et al., 2011a. Simulated relationships are shown at different cardiac outputs (4 L/min, 4.8 L/min 5.6 L/min). The y-axis shows proportional height in the gravitational direction (cranio-caudal in upright, and ventral-dorsal in supine/prone). For zero gravity (0g), no gravitational gradient is reported. Standard deviation in different postures is shows as **(A)** For zero-gravity, **(B)** supine, **(C)** prone and **(D)** upright.

differences in time averaged wall shear stress predicted by computational fluid dynamics in patients at risk for or with mild pulmonary hypertension Pillalamarri et al. (2021). The redistribution of left-to-right blood flow with posture in the coupled model has implications for prediction of both flow velocity profiles and wall shear stress in computational fluid dynamics models of the major arteries. Most computational fluid dynamics models, including structured tree models, in essence assume a left-right flow distribution that relates to the relative size of model outlets. Zero gravity simulations reflect these conditions, however, the flow redistribution that our coupled model provides demonstrates that shifts in posture may be functionally important.

Assessment of pulmonary artery hemodynamics can be achieved using imaging techniques such as 4D-cine magnetic resonance imaging (CMRI) and functional magnetic resonance imaging (fMRI). The availability of such imaging to diagnose pulmonary hypertensive disorders can be an issue and also the cost of running such tests can be a burden to some patients. While these imaging modalities can help with understanding the state of disease in some cases, a better understanding of pulmonary artery hemodynamics obtained by computational fluid dynamics could lead to greater insight in conditions such as pulmonary hypertension and tetralogy of Fallot Hu et al. (2020); Schäfer et al. (2017, 2019). Imaging studies of the proximal pulmonary arteries have suggested a relationship between mechanical and flow hemodynamic domains Schäfer et al. (2017). Changes in WSS and viscous energy loss in MPA and RPA have also been observed in disease Hu et al. (2020); Schäfer et al. (2019), and models such as this could provide insight without the need to collect a significant amount of data that can be expensive and more time consuming. The ability of the presented model for patient-specific investigation could provide insights into hemodynamic assessment of both children and adults, where changes in the micro-structure of the lung may influence macro-vascular flow properties. This may occur differently in children compared with adults, with studies suggesting that flow hemodynamics goes through uniform changes in adults with pulmonary arterial hypertension whereas the flow abnormalities are more prevalent in children with pulmonary arterial hypertension Schäfer et al. (2019).

The coupled model presented here provides a strength in its prediction of both macro-vascular flow dynamics and micro-vascular perfusion. This provides a strong framework for future studies of the pathological lung, particularly in pulmonary hypertension. In an acute form of pulmonary hypertension (pulmonary embolism) network models have been used to predict the impact of vascular occlusion on pulmonary vascular resistance, and importantly on gas exchange function Burrowes et al. (2011a,b); Clark et al. (2014). These studies show that the location of a vascular occlusion (for example, does it occlude a region that typically receives a relatively high flow due to gravity?) impacts its functional importance, and that the location of occlusion has differential impacts on vascular

resistance and exchange. Pulmonary embolism can lead to a chronic remodeling of the small pulmonary arteries, and ultimately chronic thromboembolic pulmonary hypertension (CTEPH), in which pulmonary vascular function becomes impaired and heterogeneously distributed Lau et al. (2014). Network models can simulate remodeling in CTEPH Colebank et al. (2021); Ebrahimi et al. (2019, 2021); Qureshi et al. (2014). However, without accurate coupling to macro-vascular models, measurable changes in flow dynamics and shear stress in the largest pulmonary arteries cannot be predicted. While we have used 3D computational fluid dynamics here to predict flow in the main, left and right pulmonary arteries, the methodology employed here is transferable to 3D simulation across scales of interest, for example to the level of segmental arteries. This could provide new insights into the progression of pathologies such as CTEPH in the future.

There are several coupling techniques that can be used to link the large scale (3D) effects and network (1D) flows within a single system. The coupling methodologies can be broadly divided into manual or automatic depending on the method of data transfer between models (one-way or two-way depending on whether both systems mutually influence each other or not). Passerini et al. (2009) proposed a method to simulate the blood flow in the circle of Willis in the brain, which assumed a rigid 3D domain and a compliant 1D model for their biological vessel domains. A Dirichlet-Neumann type mapping of vascular impedance was presented in Vignon-Clementel et al. (2006). A coupled 3D-1D model was first introduced by Formaggia et al. (1999) and followed up by Formaggia et al. (2001, 2002); Urquiza et al. (2006). A number of studies have taken coupling 3D compliant models with a reduced 1D model approach Formaggia et al. (1999, 2001); Urquiza et al. (2006). Their approach included maintaining a continuity of a hemodynamic quantity (flow rate or pressure) at the interface of two models. Blanco et al. (2007) introduced a novel method using variational formulation to minimize the error caused by dimension mismatch in the coupling. Our approach aims to reach an optimal compromise between computational cost and model accuracies across spatial scales.

To demonstrate the methodology we simulated 3D blood flow in the main pulmonary artery and the left and right pulmonary arteries. The number of generations modeled explicitly in CFD studies of the pulmonary arteries ranges from two Bordones et al. (2018); Capuano et al. (2019) to approximately 6 or 7 generations Kheyfets et al. (2015); Tang et al. (2011, 2012). The choice of upper artery CFD geometry depends on the application of the model, and influences simulation time. Although the methodology presented here is applicable to any number of generations in a 3D model, the primary aim of this study was to investigate the distribution of blood flow and wall shear stress predicted by a CFD model coupled to a 1D model that includes the effects of gravity and anatomy. The largest effects in flow distribution are expected to be at the left/right lung scale Wieslander et al. (2019), and flow dependent disruptions are expected to be most significant in the main, left and right pulmonary arteries Schäfer et al. (2017). Capuano et al. (2019) demonstrated that including additional bifurcations to a CFD model of the main pulmonary trunk did not significantly impact predicted flow distributions in the main, left, or right pulmonary arteries. Therefore, a two generation model was appropriate for this application. With this choice of geometry our model is able to be solved on a Desktop computer (Intel(R) Core(TM) i7-7700 CPU @ 3.60 GHz and 32GB RAM), with the 3D CFD model taking approximately 40 min to solve with parallelization on 4 cores, and the 1D model taking approximately 20 min to solve. These solve times can be reduced by using parallelization on high performance computers, and by choosing realistic initial conditions for simulations (for example, as the model approaches convergence, simulations from one iteration can initialize the next). Both 1D and 3D models must be solved at each coupling iteration, however, under normal parameterization this is well within normal solution times for CFD models (e.g., times cited by Tang et al. (2012)), with 25–30 iterations typically required for convergence.

Subject specificity is incorporated into the model via 1) a 3D description of the largest blood vessels, 2) a representation of branching architecture and vascular dimensions in vessels that can be resolved in CT (to one generation beyond the segmental level), and 3) in lung shape and volume. In participants with normal lung function patient-specific boundary conditions are difficult to derive as invasive clinical procedures are infrequent Kheyfets et al. (2015). However, in future studies of pulmonary hypertension inflow boundary conditions could be derived from clinical data including catheter measured flow and pressure profiles Tang et al. (2012), ultrasound Su et al. (2012), or magnetic resonance imaging Tang et al. (2011). An "atlas" based approach Capuano et al. (2019), may also be well-aligned with our modeling methodology. In this approach, statistically derived 3D models of the lungs and their vasculature could be applied with a range of typically measured boundary conditions in cohorts of patients, to understand variability in pulmonary function between groups, without the need to solve patient specific models for each participant in a large cohort.

The model assumes Newtonian behavior of the blood flow in the large arteries in both 1D and 3D models where the shear thinning of blood have no substantial impact, and hence blood viscosity is thought to be constant and irrespective of vessel radius. This assumption is applied in other studies, which have supported the assumption that the effects of non-Newtonian fluid on hemodynamics in the major pulmonary arteries are negligible Gao et al. (2013); Cho and Kensey (1991); Perktold et al. (1991). Non-Newtonian effects in the micro-vasculature are incorporated simply via an effective viscosity that depends on blood vessel size in the acinar structures Clark et al. (2011b). Our model also neglects vessel distensibility in the 3D geometry. In the steady state system that we simulate here, transmural pressure in the macro-vasculature is relatively consistent, and we do not consider the oscillations of blood pressure over a heart beat. Given that the CT imaging is acquired *in vivo* (at physiological pressures and volumes - 50% of vital capacity), this assumption of a rigid macro-vasculature is reasonable. However, more complex fluid structure-interaction models may improve accuracy in the future. A further improvement to the model would be the inclusion of transient changes in the vasculature. Passerini et al. (2009) developed a transient model which included a rigid macro-vasculature and a

compliance-resistance model representing the distal blood vessels in the cerebral vasculature. The rigid vessel assumption could cause mismatch in coupling systems in the transient case, which could be addressed in a similar manner to assess WSS over a heart cycle, perhaps coupled to pulsatile corrections to our 1D steady state network model presented here Clark and Tawhai (2018). Previous CFD studies have suggested that the error in predicted spatially averaged WSS from static versus pulsatile simulations is small Kheyfets et al. (2015). However, pulsatile simulations in the future would provide important insights into dynamic changes in the circulation, which may play a role in response to disease Ebrahimi et al. (2021).

In this study, we introduce a novel 3D/1D coupled model of the pulmonary circulation that operates as a patient-specific model to investigate hemodynamics. An advantage of this model is having an anatomical 1D tree downstream of 3D which makes it provides a subject-based boundary condition to the 3D model. This model has the potential to be applied on a patient-specific manner to interrogate the effects of disease downstream on the upper vasculature. A further advantage of this model is its ability to simulate WSS in the upper vasculature in health and disease under different conditions such as posture and cardiac outputs. The model is designed to provide insights on the pulmonary vasculature to enhance the understanding of disease and help with clinical decision making.

DATA AVAILABILITY STATEMENT

The datasets presented in this study can be found in online repositories. The names of the repository/repositories and accession number(s) can be found below: https://github.com/LungNoodle/lungsim.

ETHICS STATEMENT

The studies involving human participants were reviewed and approved by the University of Iowa Institutional Review Board and Radiation Safety Committees. The patients/participants provided their written informed consent to participate in this study.

AUTHOR CONTRIBUTIONS

BE: Conceived study, derived computational model, data analysis, wrote the first draft of the paper, edited and reviewed the paper draft. HK: Conceived study, contributed to computational model, contributed to computational tool development, data analysis, wrote the first draft of the paper, edited and reviewed the paper draft. MT: Conceived study, contributed to computational model, contributed to computational tool development, edited and reviewed the paper draft. KB: Contributed to computational model, contributed to computational tool development, edited and reviewed the paper draft. EH: Collected Human Lung Atlas data, contributed image analysis tools, interpreted data in a physiological context, edited and reviewed the paper draft. AC: Conceived study, derived computational model, data analysis, contributed to computational tool development, wrote the first draft of the paper, edited and reviewed the paper draft.

FUNDING

This research was funded by the New Zealand Ministry of Business, Innovation and Employment's Catalyst Strategic fund, the Medical Technologies Centre of Research Excellence (Flagship 1, MT principal investigator) and AC was supported by a Royal Society Te Apārangi Rutherford Discovery Fellowship (14-UOA-019). Imaging was supported, in part, by NIH R01HL112986.

SUPPLEMENTARY MATERIAL

The Supplementary Material for this article can be found online at: https://www.frontiersin.org/articles/10.3389/fnetp.2022.867551/full#supplementary-material

REFERENCES

Blanco, P. J., Feijóo, R. A., and Urquiza, S. A. (2007). A Unified Variational Approach for Coupling 3D-1D Models and its Blood Flow Applications. *Comput. Methods Appl. Mech. Eng.* 196, 4391–4410. doi:10.1016/j.cma.2007.05.008

Bordones, A. D., Leroux, M., Kheyfets, V. O., Wu, Y. A., Chen, C. Y., and Finol, E. A. (2018). Computational Fluid Dynamics Modeling of the Human Pulmonary Arteries with Experimental Validation. *Ann. Biomed. Eng.* 46, 1309–1324. doi:10.1007/s10439-018-2047-1

Burrowes, K. S., Clark, A. R., Marcinkowski, A., Wilsher, M. L., Milne, D. G., and Tawhai, M. H. (2011a). Pulmonary Embolism: Predicting Disease Severity. *Phil. Trans. R. Soc. A.* 369, 4255–4277. doi:10.1098/rsta.2011.0129

Burrowes, K. S., Clark, A. R., and Tawhai, M. H. (2011b). Blood Flow Redistribution and Ventilation-Perfusion Mismatch during Embolic Pulmonary Arterial Occlusion. *Pulm. Circ.* 1, 365–376. doi:10.4103/2045-8932.87302

Burrowes, K. S., Hunter, P. J., and Tawhai, M. H. (2005). Anatomically Based Finite Element Models of the Human Pulmonary Arterial and Venous Trees Including Supernumerary Vessels. *J. Appl. Physiol.* 99, 731–738. doi:10.1152/japplphysiol.01033.2004

Capuano, F., Loke, Y.-H., and Balaras, E. (2019). Blood Flow Dynamics at the Pulmonary Artery Bifurcation. *Fluids* 4, 190. doi:10.3390/fluids4040190

Caretto, L., Gosman, A., Patankar, S., and Spalding, D. (1973). "Two Calculation Procedures for Steady, Three-Dimensional Flows with Recirculation," in Proceedings of the third international conference on numerical methods in fluid mechanics (Berlin, Germany: Springer), 60–68.

Cho, Y. I., and Kensey, K. R. (1991). Effects of the Non-newtonian Viscosity of Blood on Flows in a Diseased Arterial Vessel. Part 1: Steady Flows. *Biorheology* 28, 241–262. doi:10.3233/bir-1991-283-415

Clark, A. R., Burrowes, K. S., and Tawhai, M. H. (2010). Contribution of Serial and Parallel Microperfusion to Spatial Variability in Pulmonary Inter- and Intra-acinar Blood Flow. *J. Appl. Physiol.* 108, 1116–1126. doi:10.1152/japplphysiol.01177.2009

Clark, A. R., Burrowes, K. S., and Tawhai, M. H. (2011a). The Impact of Micro-embolism Size on Haemodynamic Changes in the Pulmonary Micro-circulation. *Respir. Physiol. Neurobiol.* 175, 365–374. doi:10.1016/j.resp.2010.12.018

Clark, A. R., Kumar, H., and Burrowes, K. (2017). Capturing Complexity in Pulmonary System Modelling. *Proc. Inst. Mech. Eng. H* 231, 355–368. doi:10.1177/0954411916683221

Clark, A. R., Milne, D., Wilsher, M., Burrowes, K. S., Bajaj, M., and Tawhai, M. H. (2014). Lack of Functional Information Explains the Poor Performance of 'clot Load Scores' at Predicting Outcome in Acute Pulmonary Embolism. *Respir. Physiol. Neurobiol.* 190, 1–13. doi:10.1016/j.resp.2013.09.005

Clark, A. R., Tawhai, M. H., Hoffman, E. A., and Burrowes, K. S. (2011b). The Interdependent Contributions of Gravitational and Structural Features to Perfusion Distribution in a Multiscale Model of the Pulmonary Circulation. *J. Appl. Physiol.* 110, 943–955. doi:10.1152/japplphysiol.00775.2010

Clark, A. R., and Tawhai, M. H. (2018). Temporal and Spatial Heterogeneity in Pulmonary Perfusion: a Mathematical Model to Predict Interactions between Macro- and Micro-vessels in Health and Disease. *Anziam J.* 59, 562–580. doi:10.1017/s1446181118000111

Colebank, M. J., Qureshi, M. U., Rajagopal, S., Krasuski, R. A., and Olufsen, M. S. (2021). A Multiscale Model of Vascular Function in Chronic Thromboembolic Pulmonary Hypertension. *Am. J. Physiology-Heart Circulatory Physiol.* doi:10.1152/ajpheart.00086.2021

[Dataset] Patakar, H. (1980). *Numerical Heat Transfer and Fluid Flow (Hemisphere Series on Computational Methods in Mechanics and thermal Science)*.

Ebrahimi, B. S., Tawhai, M. H., Kumar, H., Burrowes, K. S., Hoffman, E. A., Wilsher, M. L., et al. (2021). A Computational Model of Contributors to Pulmonary Hypertensive Disease: Impacts of Whole Lung and Focal Disease Distributions. *Pulm. Circ.* 11, 20458940211056527. doi:10.1177/20458940211056527

Ebrahimi, B. S., Tawhai, M. H., Kumar, H., and Clark, A. R. (2019). Wave Reflection in an Anatomical Model of the Pulmonary Circulation in Local and Global Hypertensive Disease. *Annu. Int. Conf. IEEE Eng. Med. Biol. Soc.* 2019, 4973–4976. doi:10.1109/EMBC.2019.8857948

Edwards, P. D., Bull, R. K., and Coulden, R. (1998). Ct Measurement of Main Pulmonary Artery Diameter. *Bjr* 71, 1018–1020. doi:10.1259/bjr.71.850.10211060

Fernandez, J. W., Mithraratne, P., Thrupp, S. F., Tawhai, M. H., and Hunter, P. J. (2004). Anatomically Based Geometric Modelling of the Musculo-Skeletal System and Other Organs. *Biomech. Model. mechanobiology* 2, 139–155. doi:10.1007/s10237-003-0036-1

Ferziger, J. H., Perić, M., and Street, R. L. (2002). *Computational Methods for Fluid Dynamics, Vol. 3*. Berlin, Germany: Springer.

Formaggia, L., Gerbeau, J. F., Nobile, F., and Quarteroni, A. (2002). Numerical Treatment of Defective Boundary Conditions for the Navier-Stokes Equations. *SIAM J. Numer. Anal.* 40, 376–401. doi:10.1137/s003614290038296x

Formaggia, L., Gerbeau, J. F., Nobile, F., and Quarteroni, A. (2001). On the Coupling of 3D and 1D Navier-Stokes Equations for Flow Problems in Compliant Vessels. *Comput. Methods Appl. Mech. Eng.* 191, 561–582. doi:10.1016/s0045-7825(01)00302-4

Formaggia, L., Nobile, F., Quarteroni, A., and Veneziani, A. (1999). Multiscale Modelling of the Circulatory System: a Preliminary Analysis. *Comput. Vis. Sci* 2, 75–83. doi:10.1007/s007910050030

Fung, Y. C. (1984). Microcirculation. *Biodynamics* 1984, 224–289. doi:10.1007/978-1-4757-3884-1_5

Fung, Y. C., and Sobin, S. S. (1972). Elasticity of the Pulmonary Alveolar Sheet. *Circ. Res.* 30, 451–469. doi:10.1161/01.res.30.4.451

Fung, Y. C., and Sobin, S. S. (1969). Theory of Sheet Flow in Lung Alveoli. *J. Appl. Physiol.* 26, 472–488. doi:10.1152/jappl.1969.26.4.472

Gao, F., Ueda, H., Gang, L., and Okada, H. (2013). Fluid Structure Interaction Simulation in Three-Layered Aortic Aneurysm Model under Pulsatile Flow: Comparison of Wrapping and Stenting. *J. Biomech.* 46, 1335–1342. doi:10.1016/j.jbiomech.2013.02.002

Gattinoni, L., Tognoni, G., Pesenti, A., Taccone, P., Mascheroni, D., Labarta, V., et al. (2001). Effect of Prone Positioning on the Survival of Patients with Acute Respiratory Failure. *N. Engl. J. Med.* 345, 568–573. doi:10.1056/nejmoa010043

Gehr, P., Bachofen, M., and Weibel, E. R. (1978). The normal Human Lung: Ultrastructure and Morphometric Estimation of Diffusion Capacity. *Respiration Physiol.* 32, 121–140. doi:10.1016/0034-5687(78)90104-4

Haefeli-Bleuer, B., and Weibel, E. R. (1988). Morphometry of the Human Pulmonary Acinus. *Anat. Rec.* 220, 401–414. doi:10.1002/ar.1092200410

Hlastala, M. P., and Glenny, R. W. (1999). Vascular Structure Determines Pulmonary Blood Flow Distribution. *Physiology* 14, 182–186. doi:10.1152/physiologyonline.1999.14.5.182

Hoffman, E. A., Clough, A. V., Christensen, G. E., Lin, C.-l., McLennan, G., Reinhardt, J. M., et al. (2004). The Comprehensive Imaging-Based Analysis of the Lung. *Acad. Radiol.* 11, 1370–1380. doi:10.1016/j.acra.2004.09.005

Hopkins, S. R., Henderson, A. C., Levin, D. L., Yamada, K., Arai, T., Buxton, R. B., et al. (2007). Vertical Gradients in Regional Lung Density and Perfusion in the Supine Human Lung: the Slinky Effect. *J. Appl. Physiol.* 103, 240–248. doi:10.1152/japplphysiol.01289.2006

Horsfield, K., and Gordon, W. I. (1981). Morphometry of Pulmonary Veins in Man. *Lung* 159, 211–218. doi:10.1007/bf02713917

Horsfield, K. (1978). Morphometry of the Small Pulmonary Arteries in Man. *Circ. Res.* 42, 593–597. doi:10.1161/01.res.42.5.593

Hu, L., Ouyang, R., Sun, A., Wang, Q., Guo, C., Peng, Y., et al. (2020). Pulmonary Artery Hemodynamic Assessment of Blood Flow Characteristics in Repaired Tetralogy of Fallot Patients versus Healthy Child Volunteers. *Quant Imaging Med. Surg.* 10, 921–933. doi:10.21037/qims.2020.03.23

Huang, W., Yen, R. T., McLaurine, M., and Bledsoe, G. (1996). Morphometry of the Human Pulmonary Vasculature. *J. Appl. Physiol.* 81, 2123–2133. doi:10.1152/jappl.1996.81.5.2123

Issa, R. I. (1986). Solution of the Implicitly Discretised Fluid Flow Equations by Operator-Splitting. *J. Comput. Phys.* 62, 40–65. doi:10.1016/0021-9991(86)90099-9

Jasak, H. (1996). *Error Analysis and Estimation for the Finite Volume Method with Applications to Fluid Flows*.

Kang, W., Clark, A. R., and Tawhai, M. H. (2018). Gravity Outweighs the Contribution of Structure to Passive Ventilation-Perfusion Matching in the Supine Adult Human Lung. *J. Appl. Physiol.* 124, 23–33. doi:10.1152/japplphysiol.00791.2016

Kheyfets, V. O., O'Dell, W., Smith, T., Reilly, J. J., and Finol, E. A. (2013). Considerations for Numerical Modeling of the Pulmonary Circulation-Aa Review with a Focus on Pulmonary Hypertension. *J. Biomech. Eng.* 135, 61011–61015. doi:10.1115/1.4024141

Kheyfets, V. O., Rios, L., Smith, T., Schroeder, T., Mueller, J., Murali, S., et al. (2015). Patient-specific Computational Modeling of Blood Flow in the Pulmonary Arterial Circulation. *Comput. Methods Programs Biomed.* 120, 88–101. doi:10.1016/j.cmpb.2015.04.005

Kong, F., Kheyfets, V., Finol, E., and Cai, X. C. (2018). An Efficient Parallel Simulation of Unsteady Blood Flows in Patient-specific Pulmonary Artery. *Int. J. Numer. Method Biomed. Eng.* 34, e2952. doi:10.1002/cnm.2952

Krenz, G. S., and Dawson, C. A. (2003). Flow and Pressure Distributions in Vascular Networks Consisting of Distensible Vessels. *Am. J. Physiology-Heart Circulatory Physiol.* 284, H2192–H2203. doi:10.1152/ajpheart.00762.2002

Lau, E. M., Bailey, D. L., Bailey, E. A., Torzillo, P. J., Roach, P. J., Schembri, G. P., et al. (2014). Pulmonary Hypertension Leads to a Loss of Gravity Dependent Redistribution of Regional Lung Perfusion: a Spect/ct Study. *Heart* 100, 47–53. doi:10.1136/heartjnl-2013-304254

Osanlouy, M., Clark, A. R., Kumar, H., King, C., Wilsher, M. L., Milne, D. G., et al. (2020). Lung and Fissure Shape Is Associated with Age in Healthy Never-Smoking Adults Aged 20-90 Years. *Sci. Rep.* 10, 16135. doi:10.1038/s41598-020-73117-w

Oshima, M., Torii, R., Kobayashi, T., Taniguchi, N., and Takagi, K. (2001). Finite Element Simulation of Blood Flow in the Cerebral Artery. *Comput. Methods Appl. Mech. Eng.* 191, 661–671. doi:10.1016/s0045-7825(01)00307-3

Passalacqua, A., and Fox, R. O. (2011). Implementation of an Iterative Solution Procedure for Multi-Fluid Gas-Particle Flow Models on Unstructured Grids. *Powder Technol.* 213, 174–187. doi:10.1016/j.powtec.2011.07.030

Passerini, T., Luca, M. D., Formaggia, L., Quarteroni, A., and Veneziani, A. (2009). A 3d/1d Geometrical Multiscale Model of Cerebral Vasculature. *J. Eng. Math.* 64, 319–330. doi:10.1007/s10665-009-9281-3

Pedley, T. J., Schroter, R. C., and Sudlow, M. F. (1970). Energy Losses and Pressure Drop in Models of Human Airways. *Respiration Physiol.* 9, 371–386. doi:10.1016/0034-5687(70)90093-9

Perktold, K., and Rappitsch, G. (1995). Computer Simulation of Local Blood Flow and Vessel Mechanics in a Compliant Carotid Artery Bifurcation Model. *J. Biomech.* 28, 845–856. doi:10.1016/0021-9290(95)95273-8

Perktold, K., Resch, M., and Peter, R. O. (1991). Three-dimensional Numerical Analysis of Pulsatile Flow and wall Shear Stress in the Carotid Artery Bifurcation. *J. Biomech.* 24, 409–420. doi:10.1016/0021-9290(91)90029-m

Pillalamarri, N. R., Piskin, S., Patnaik, S. S., Murali, S., and Finol, E. A. (2021). Patient-specific Computational Analysis of Hemodynamics in Adult Pulmonary Hypertension. *Ann. Biomed. Eng.* 49, 3465–3480. doi:10.1007/s10439-021-02884-y

Pries, A. R., Secomb, T. W., and Gaehtgens, P. (1996). Biophysical Aspects of Blood Flow in the Microvasculature. *Cardiovasc. Res.* 32, 654–667. doi:10.1016/s0008-6363(96)00065-x

Qureshi, M. U., Vaughan, G. D. A., Sainsbury, C., Johnson, M., Peskin, C. S., Olufsen, M. S., et al. (2014). Numerical Simulation of Blood Flow and Pressure Drop in the Pulmonary Arterial and Venous Circulation. *Biomech. Model. Mechanobiol* 13, 1137–1154. doi:10.1007/s10237-014-0563-y

Read, J. (1969a). Redistribution of Stratified Pulmonary Blood Flow during Exercise. *J. Appl. Physiol.* 27, 374–377. doi:10.1152/jappl.1969.27.3.374

Read, J. (1969b). Stratified Pulmonary Blood Flow: Some Consequences in Emphysema and Pulmonary Embolism. *Bmj* 2, 44–46. doi:10.1136/bmj.2.5648.44

Schäfer, M., Barker, A. J., Kheyfets, V., Stenmark, K. R., Crapo, J., Yeager, M. E., et al. (2017). Helicity and Vorticity of Pulmonary Arterial Flow in Patients with Pulmonary Hypertension: Quantitative Analysis of Flow Formations. *J. Am. Heart Assoc.* 6, e007010. doi:10.1161/JAHA.117.007010

Schäfer, M., Ivy, D. D., Abman, S. H., Stenmark, K., Browne, L. P., Barker, A. J., et al. (2019). Differences in Pulmonary Arterial Flow Hemodynamics between Children and Adults with Pulmonary Arterial Hypertension as Assessed by 4d-Flow Cmr Studies. *Am. J. Physiology-Heart Circulatory Physiol.* 316, H1091–H1104. doi:10.1152/ajpheart.00802.2018

Sobin, S., Fung, Y., Tremer, H., and Lindal, R. (1979). "Distensibility of Human Pulmonary Capillary Blood-Vessels in the Interalveolar Septa," in *Microvascular Research* (San Diego, CA: Academic press inc jnl-comp subscriptions 525 B ST, STE 1900), Vol. 17, S87.

Su, Z., Hunter, K. S., and Shandas, R. (2012). Impact of Pulmonary Vascular Stiffness and Vasodilator Treatment in Pediatric Pulmonary Hypertension: 21 Patient-specific Fluid-Structure Interaction Studies. *Comput. Methods Programs Biomed.* 108, 617–628. doi:10.1016/j.cmpb.2011.09.002

Swan, A. J., Clark, A. R., and Tawhai, M. H. (2012). A Computational Model of the Topographic Distribution of Ventilation in Healthy Human Lungs. *J. Theor. Biol.* 300, 222–231. doi:10.1016/j.jtbi.2012.01.042

Tang, B. T., Fonte, T. A., Chan, F. P., Tsao, P. S., Feinstein, J. A., and Taylor, C. A. (2011). Three-dimensional Hemodynamics in the Human Pulmonary Arteries under Resting and Exercise Conditions. *Ann. Biomed. Eng.* 39, 347–358. doi:10.1007/s10439-010-0124-1

Tang, B. T., Pickard, S. S., Chan, F. P., Tsao, P. S., Taylor, C. A., and Feinstein, J. A. (2012). Wall Shear Stress Is Decreased in the Pulmonary Arteries of Patients with Pulmonary Arterial Hypertension: An Image-Based, Computational Fluid Dynamics Study. *Pulm. Circ.* 2, 470–476. doi:10.4103/2045-8932.105035

Tawhai, M. H., Hunter, P., Tschirren, J., Reinhardt, J., McLennan, G., and Hoffman, E. A. (2004). Ct-based Geometry Analysis and Finite Element Models of the Human and Ovine Bronchial Tree. *J. Appl. Physiol.* 97, 2310–2321. doi:10.1152/japplphysiol.00520.2004

Tawhai, M. H., Nash, M. P., Lin, C.-L., and Hoffman, E. A. (2009). Supine and Prone Differences in Regional Lung Density and Pleural Pressure Gradients in the Human Lung with Constant Shape. *J. Appl. Physiol.* 107, 912–920. doi:10.1152/japplphysiol.00324.2009

Urquiza, S. A., Blanco, P. J., Vénere, M. J., and Feijóo, R. A. (2006). Multidimensional Modelling for the Carotid Artery Blood Flow. *Comput. Methods Appl. Mech. Eng.* 195, 4002–4017. doi:10.1016/j.cma.2005.07.014

Vignon-Clementel, I. E., Alberto Figueroa, C., Jansen, K. E., and Taylor, C. A. (2006). Outflow Boundary Conditions for Three-Dimensional Finite Element Modeling of Blood Flow and Pressure in Arteries. *Comput. Methods Appl. Mech. Eng.* 195, 3776–3796. doi:10.1016/j.cma.2005.04.014

Wang, Z., and Chesler, N. C. (2011). Pulmonary Vascular wall Stiffness: an Important Contributor to the Increased Right Ventricular Afterload with Pulmonary Hypertension. *Pulm. Circ.* 1, 212–223. doi:10.4103/2045-8932.83453

West, J. B. (1999). Distribution of Pulmonary Blood Flow. *Am. J. Respir. Crit. Care Med.* 160, 1802–1803. doi:10.1164/ajrccm.160.6.hh1-99

West, J. B., Dollery, C. T., and Naimark, A. (1964). Distribution of Blood Flow in Isolated Lung; Relation to Vascular and Alveolar Pressures. *J. Appl. Physiol.* 19, 713–724. doi:10.1152/jappl.1964.19.4.713

Wieslander, B., Ramos, J. G., Ax, M., Petersson, J., and Ugander, M. (2019). Supine, Prone, Right and Left Gravitational Effects on Human Pulmonary Circulation. *J. Cardiovasc. Magn. Reson.* 21, 69–15. doi:10.1186/s12968-019-0577-9

Yamada, Y., Yamada, M., Yokoyama, Y., Tanabe, A., Matsuoka, S., Niijima, Y., et al. (2020). Differences in Lung and Lobe Volumes between Supine and Standing Positions Scanned with Conventional and Newly Developed 320-Detector-Row Upright Ct: Intra-individual Comparison. *Respiration* 99, 598–605. doi:10.1159/000507265

Yen, R. T., Fung, Y. C., and Bingham, N. (1980). Elasticity of Small Pulmonary Arteries in the Cat. *J. Biomech. Eng.* 102, 170–177. doi:10.1115/1.3138218

Zhou, Q., Gao, J., Huang, W., and Yen, R. (2002). Vascular Impedance Analysis in Human Pulmonary Circulation. *Biomed. Sci. Instrum* 42, 433–434. doi:10.1115/imece2002-33525

Conflict of Interest: EH is a founder and shareholder of VIDA Diagnostics, a company commercializing lung image analysis software developed, in part, at the University of Iowa.

The remaining authors declare that the research was conducted in the absence of any commercial or financial relationships that could be construed as a potential conflict of interest.

Publisher's Note: All claims expressed in this article are solely those of the authors and do not necessarily represent those of their affiliated organizations, or those of the publisher, the editors and the reviewers. Any product that may be evaluated in this article, or claim that may be made by its manufacturer, is not guaranteed or endorsed by the publisher.

frontiers | Frontiers in Network Physiology

ORIGINAL RESEARCH
published: 25 April 2022
doi: 10.3389/fnetp.2022.868470

Why Hearing Aids Fail and How to Solve This

Ruedi Stoop *

Institute of Neuroinformatics, University and ETH of Zürich, Zurich, Switzerland

Hearing is one of the human's foremost sensors; being able to hear again after suffering from a hearing loss is a great achievement, under all circumstances. However, in the long run, users of present-day hearing aids and cochlear implants are generally only halfway satisfied with what the commercial side offers. We demonstrate here that this is due to the failure of a full integration of these devices into the human physiological circuitry. Important parts of the hearing network that remain unestablished are the efferent connections to the cochlea, which strongly affects the faculty of listening. The latter provides the base for coping with the so-called cocktail party problem, or for a full enjoyment of multi-instrumental musical plays. While nature clearly points at how this could be remedied, to achieve this technologically will require the use of advanced high-precision electrodes and high-precision surgery, as we outline here. Corresponding efforts must be pushed forward by coordinated efforts from the side of science, as the commercial players in the field of hearing aids cannot be expected to have a substantial interest in advancements into this direction.

OPEN ACCESS

Edited by:
Plamen Ch. Ivanov,
Boston University, United States

Reviewed by:
Sebastiano Stramaglia,
University of Bari Aldo Moro, Italy
Giorgio Mantica,
University of Insubria, Italy

***Correspondence:**
Ruedi Stoop
ruedi@ini.phys.ethz.ch

Specialty section:
This article was submitted to Systems Interactions and Organ Networks, a section of the journal Frontiers in Network Physiology

Received: *02 February 2022*
Accepted: *14 March 2022*
Published: *25 April 2022*

Citation:
Stoop R (2022) Why Hearing Aids Fail and How to Solve This. Front. Netw. Physiol. 2:868470. doi: 10.3389/fnetp.2022.868470

Keywords: hearing network physiology, hearing aids, listening process, source separation, cochlear embedding, hair cells innervation

INTRODUCTION

Comparing vision with hearing demonstrates that humans depend as much on auditory as on visual inputs. The compensation of corresponding sensory deficits is, at least in milder cases, much simpler and more successful in the visual domain (glasses and lenses) than in audition.

To improve hearing, in extension of the hollow hand, humans used early on animal horns and hallow bones, cf. **Figure 1**. Later on, these solutions were succeeded by more efficient ear trumpets, made of metal. All of these remedies worked via the bundling of the arriving sound waves at the level of the outer ear. As is shown by the limited influence of the outer ear on the hearing threshold, see **Figure 2**, this strategy is able to contribute to speech and sound intelligibility only to a limited extent.

Whereas weakness in visual focusing can be compensated by optical glasses, a convincing idea of how to cope with corresponding problems in the auditory field seems to be still missing. Present outer-ear artificial hearing aids, as well as inner-ear cochlear implants, have not yet made any serious attempt to restore the active processes that are naturally involved in biological hearing. Digital hearing aids use computer chip technology to convert sound waves into digital signals, which opens the road to complex input signal processing. As most hearing aid users value speech intelligibility as their top priority, speech enhancers, directional microphones, and noise and feedback cancellation come standard with top-of-the-line hearing aids, helping their users to hear speech even in loud and noisy environments. Among the biggest achievements presented, they process auditory signals according to input volume: Soft speech is made audible, while loud speech is kept comfortable. These implemented capabilities are mostly helpful if an intrinsically useful signal (e.g., speech) is to be

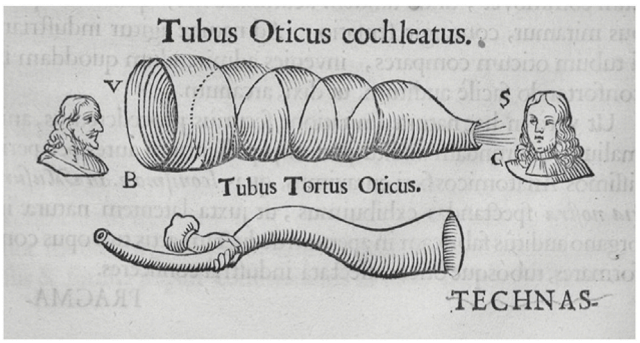

FIGURE 1 | Horns used as hearing devices. From (Kircher, 1673).

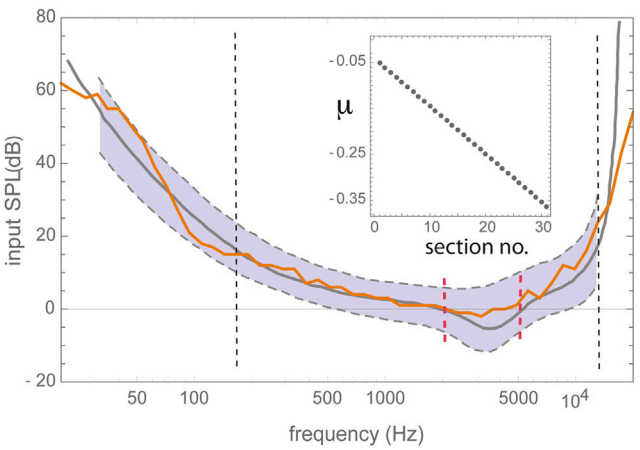

FIGURE 2 | Human hearing threshold. Black dashed vertical lines delimit the proper frequency range of the Hopf cochlea model composed of 30 discretized sections of excitabilities ("Hopf parameters") μ, centered around decaying center frequencies CF (cf. text references for the model); red vertical lines delimit the area of outer ear influence. Gray curves: data from Zwicker's publication Zwicker and Heinz, 1955, extrapolations thereof dashed. Gray shading: observed human variability. Adapted from (Kanders et al., 2017).

separated from an intrinsically un-useful disturber (e.g., noise). As soon as we deal with several signals of potential similar importance (e.g., two speakers), the task becomes a difficult one. Regarding a separation of individual voices from a mixture of voices (the so-called cocktail problem), as well as regarding the perception of music, the results remain to be rather limited, if compared to the human faculty.

EMOCS AT THE HEART OF ARTIFICIAL HEARING AIDS PROBLEMS

The heart of the problem that prohibits hearing aids from making more substantial progress comes from two sides. The most advanced hearing aids boast that, in contrast to competitors, they start to distort by their processing input only above 113 dB SPL "Combining this with a music program that allows as little interaction as possible from the more advanced features in the hearing aid, this higher maximum input level allows musicians to enjoy music even in one of these sophisticated hearing aids" (University of Colorado at, 2017; Croghan et al., 2014). This hints at that digital filter and amplification approaches applied to the input signal are too complicated, and inefficient. For digital implementations of the correctly understood nature of the inner ear (the cochlea), neither this (see **Figures 2, 3**), nor the reproduction of all salient features of human "psychoacoustic" hearing, are difficult tasks (cf. Kern, 2003; Kern and Stoop, 2003; Stoop and Kern, 2004a; Stoop and Kern, 2004b; Martignoli and Stoop, 2010; Gomez and Stoop, 2014; Kanders et al., 2017).

As such a sensor can easily be combined with present-day cochlear implant stimulation electrodes, the real challenge to be solved is the cocktail-party problem. In current hearing aid technology, directional microphones are still the top-notch solution for this problem, although in the meantime methods that use the properties of the sources have been demonstrated to work extremely well (but come with some computational demand). In one of these approaches (Kern and Stoop, 2011),

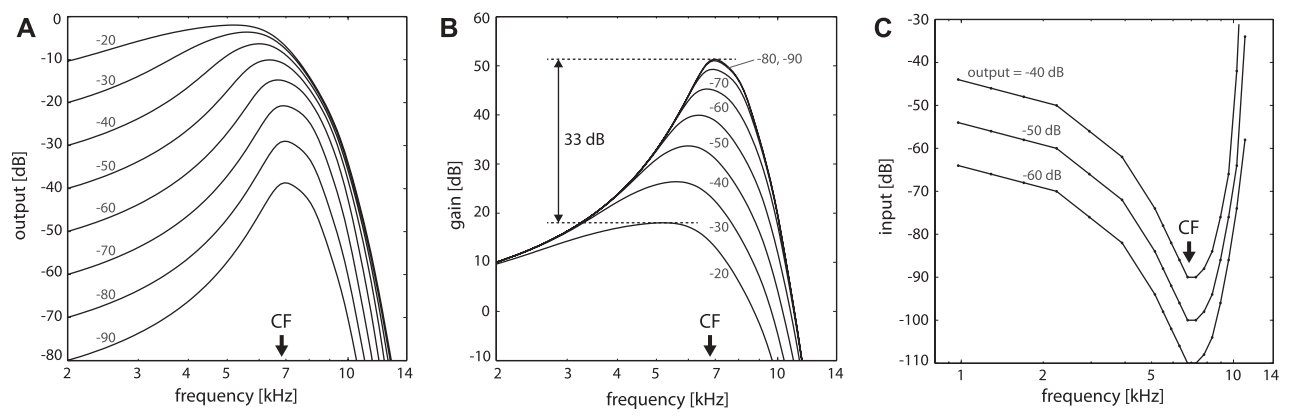

FIGURE 3 | Close-to-biology small signal amplifier implementation, including subcritical tuning and influence of cochlear fluid (endolymph). Hopf cochlea covering 14.08–0.44 kHz with 20 sections; output at Section 5 (CF = 6.79 kHz), stimulation by pure tones. Numbers denote input levels in dB; CF: section's central frequency. **(A)** Response in dB, **(B)** gain in dB; a difference of 33 dB in peak gain for two input levels differing by 70 dB corresponds to observations in chinchilla (between 20 and 90 dB SPL curves, 32.5 + dB (Ruggero et al., 1997)). **(C)** Tuning curves for fixed output levels. Numbers denote input levels in dB; CF: section's central frequency.

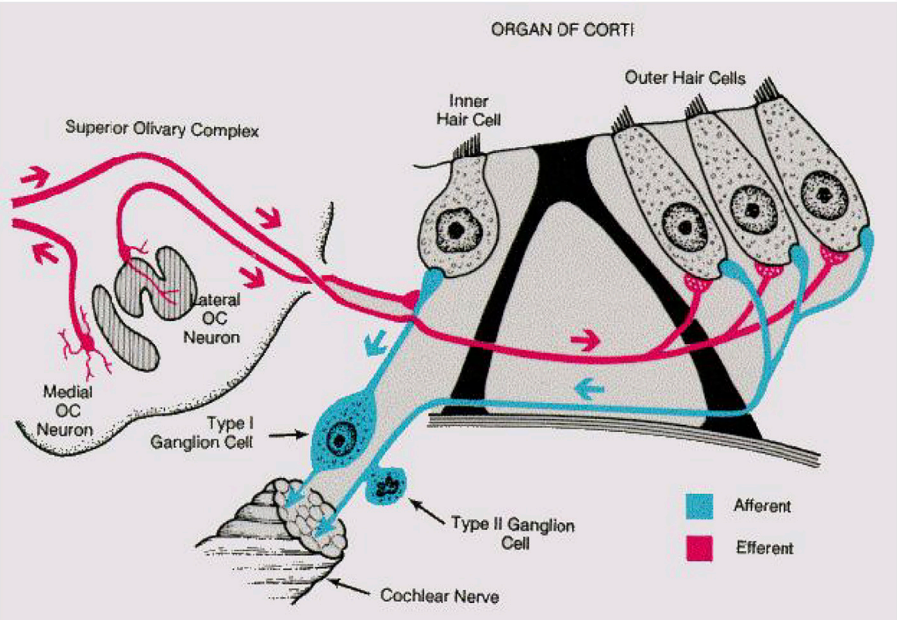

FIGURE 4 | Mammalian listening circuit. Adapted from (Spoendlin, 1966b).

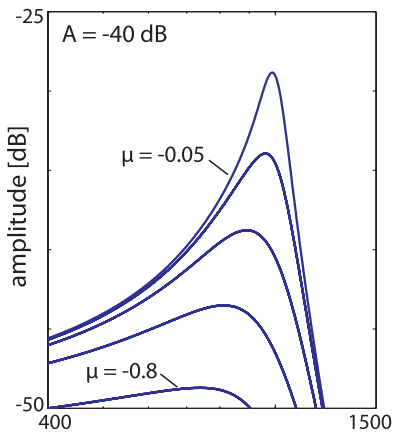

FIGURE 5 | Single Hopf amplifier response (Kern, 2003; Kern and Stoop, 2003), describing the behaviour of outer hair cells with a preferred frequency CF embedded into the basilar membrane. Frequency selectivity regarding different distances $\mu \in \{-0.05, -0.1, -0.2, -0.4, -0.8\}$ from bifurcation point (showing slightly more asymmetry if compared to **Figure 3**).

a speaker's main sound properties are extracted using wavelet-like filters and adapted to changing speech by the "matching pursuit approach". The work showed that deterministic signal features can be exploited for signal separation of several voices under quite general conditions, which reaches far beyond the noise-speech issue handled by current-day hearing aids (Author Anonyms, 2022).

The core of this approach was borrowed from how mammalian (and to a large extent more general: animal) hearing is embedded into feedback loops telling the hearing sensor what to listen to. The lack of an appropriate embedding of the hearing aids into the natural sensory network physiology is the main obstacle against arriving at better hearing aids. The cochlea, the mammalian hearing sensor, hosts in the case of humans at birth, on the order of 3,500 inner hair cells and 12,000 outer hair cells. Outer hair cells amplify the shallow fluid surface waves into which the hearing sensor has converted arial sounds after their arrival at the cochlea (Kern, 2003; Kern and Stoop, 2003). Unfortunately, ageing and inflammatory processes strongly affect—almost exclusively—the outer hair cells in an irreversible manner; the inner hair cells that pick up the amplified wave signals and relay them onwards to the cortex, remain generally unaffected. Biological studies have established that hearing is additionally embedded into several neural loops. In the past, this has been described to great physiological details in the works of Spoendlin (Spoendlin, 1966a; Spoendlin, 1966b), see **Figure 4**. Most of the current-day's drawings of the cochlear innervation details are based, often without mentioning, on that work.

From these and ensuing physiological studies on, the purpose of the eminent innervation of the organ of Corti by means of efferent, almost exclusively inhibitory, connections has remained an open problem. The general belief was that they could play a role in the coding of the sound towards neural signals, cf. (Spoendlin, 1966b). The main argument for the particular innervation by efferent cochlear neurons appears to have been that (quotes from Ref. (Spoendlin, 1966b)) "a great number of even small inputs could generate and action potential at the initial segment," "the role of the efferent fibres for the coding of the acoustic message at the level of the organ of Corti is not yet entirely understood. The only directly demonstrated action is an inhibitory effect on the afferent nerve impulses. This inhibition is,

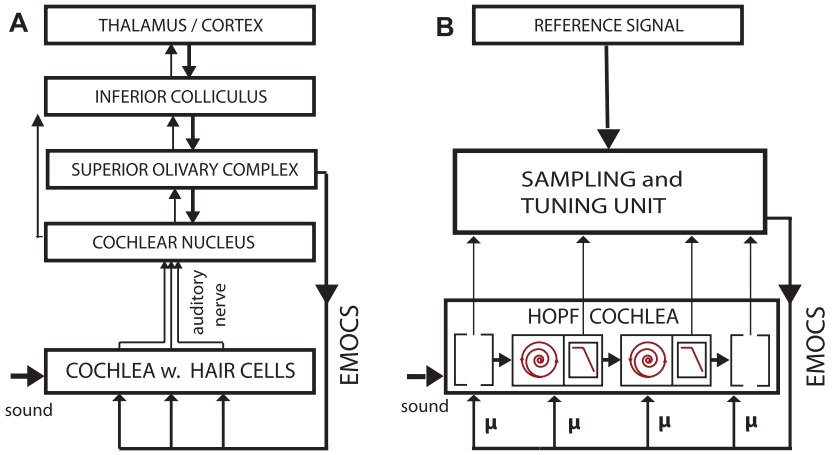

FIGURE 6 | (A) Biological vs. **(B)** artificial implementation of the hearing—listening circuit. Listening is a dedicated activity that requests and represents a particular computational effort, involving "EMOCS" (efferent medial olivocochlear stimulations), adapted from (Kern and Stoop, 2011).

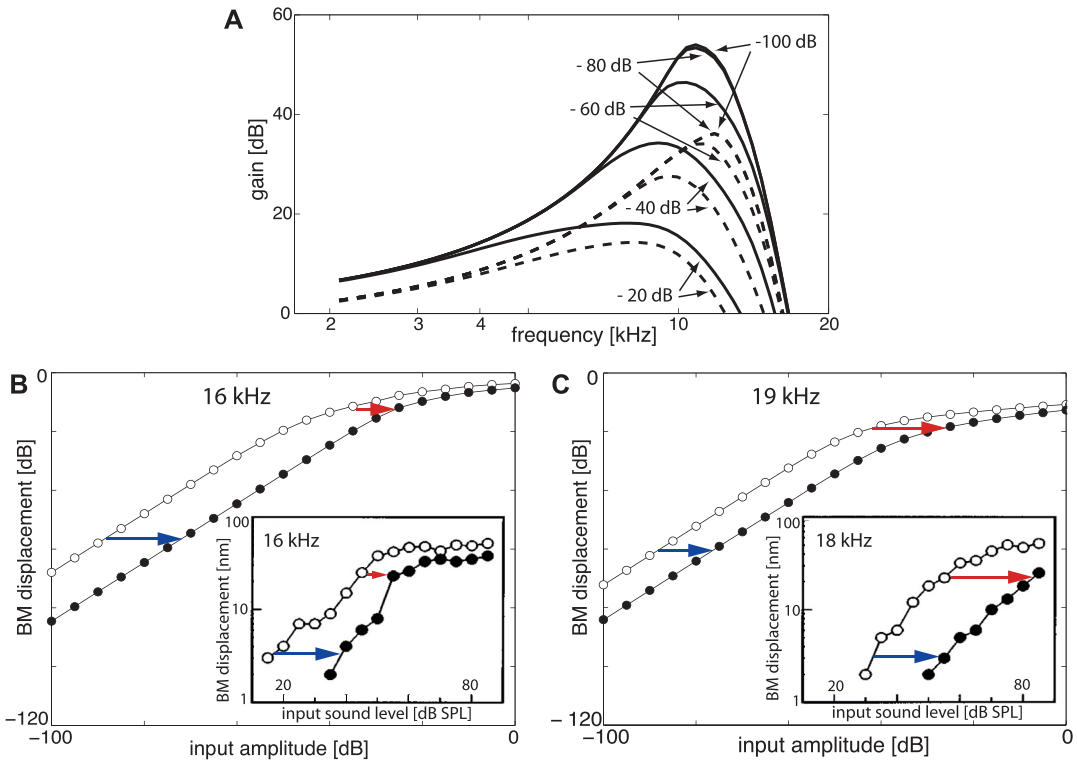

FIGURE 7 | EMOCS effects: **(A)** Gain isointensity curves at Section 5 (f_{ch} = 1.42 kHz) without (solid lines) and with (dashed lines) EMOC input. From flat tuning (μ = −0.1 for all sections, EMOC stimulation is implemented by shifting to μ_5 = −1.0 (− 80 and − 100 dB lines collapse). **(B)** Upon 16 and **(C)** 19 kHz pure tone EMOCS, implemented by a shift from a flat tuned cochlea from μ_2 = −0.05 to μ_2 = −0.5, BM levels at Section 2 (f_{ch} = 16.99 kHz) shift from open circles to full circles. Insets: Corresponding animal experiments (Russell and Murugasu, 1997).

however, not very strong and it is hard to believe that such ab extensive efferent innervation system in the cochlear receptor would have only such a limited function. It is more likely that the efferent fibres have a much more complex function than this relatively restricted inhibition which can be measured. They might influence the afferent impulses in a more qualitative than quantitative fashion," "Many different phenomena of the auditory physiology might depend on the efferent innervation of

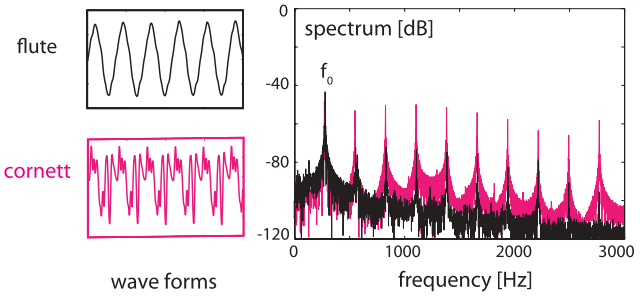

FIGURE 8 | Sounds of a cornett and a flute (left) at the same fundamental frequency f_0, superimposed (right), static case.

the cochlea. However, only a few have been directly demonstrated hitherto as for the adaptation phenomenon," "As long as these coding mechanisms can not be simulated, an artificial cochlea will only provide a very rudimentary function". After Spoendlin, this view persisted, in essence, until today.

HOW EMOCS WORK

In our view, these loops, however, foster the biological need of mammals to identify a large spectrum of pre-defined relevant signals as follows. Mathematically, the properties of the outer hair-cells can be represented by dynamical systems that are close to a Hopf bifurcation and act as small-signal amplifiers

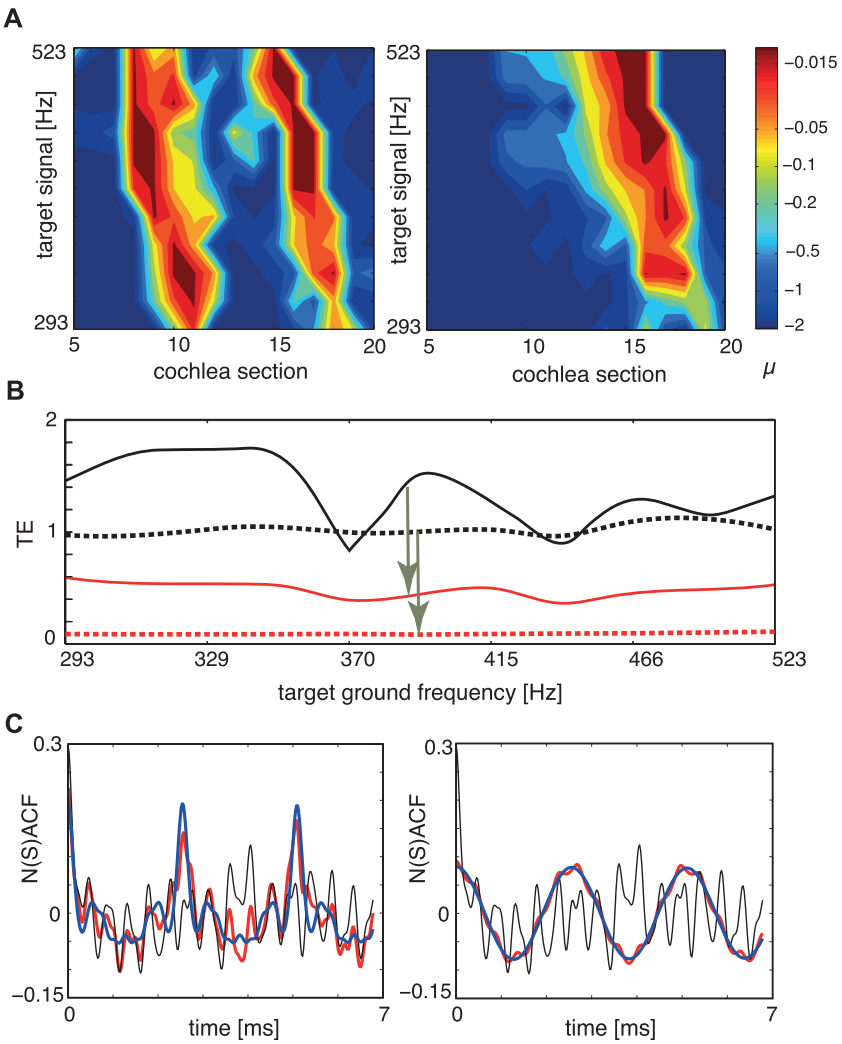

FIGURE 9 | Sound separation, dynamic case, where the target instrument changes the height of the generated tone: **(A)** Tuning patterns, dynamical case. Colors indicate the Hopf parameter values of the sections. Left: Cornett vs. flute (disturber). Right: Flute vs. cornett (disturber). **(B)** TE for the two target signals of **(A)**. Flat tuning: black; μ-tuning: red. Full: cornett target, dashed: flute target. Arrows indicate improvements by EMOCS. **(C)** NSACF, NACF for the two target signals of **(A,B)** at a chosen target ground frequency. Flat tuning: black, μ-tuning: red, target signal: blue. Targets at 392 Hz, disturbers at 2,216 Hz. After Ref. (Gomez et al., 2014).

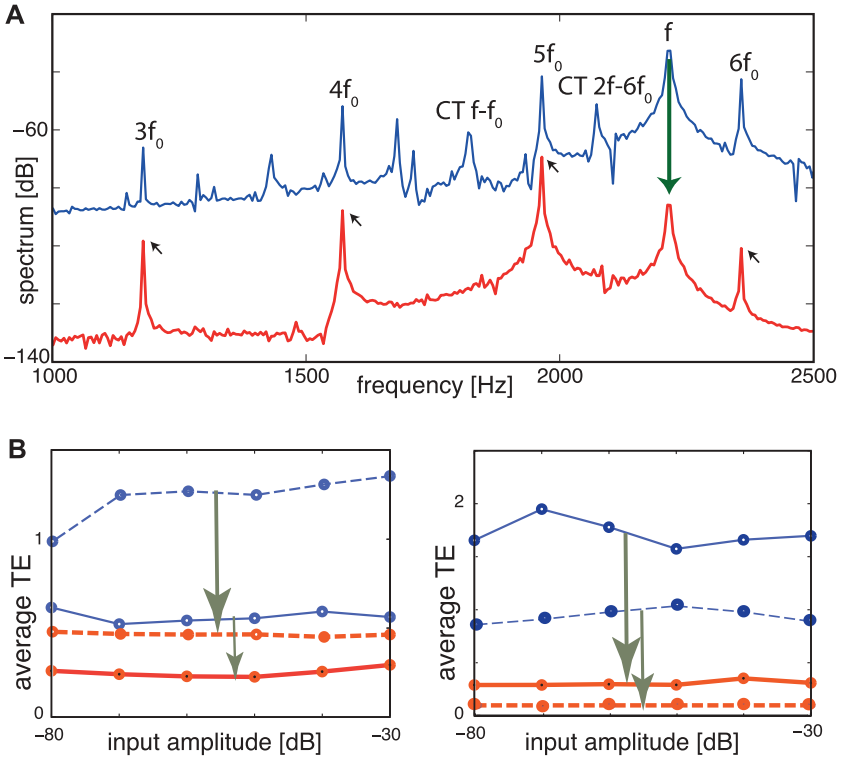

FIGURE 10 | TE improvement by μ-tuning, static case. **(A)** Frequency spectrum at Section 8 (*CF* = 1964 Hz). Blue: Flat tuning (−80 dB, target cornett f_0 = 392 Hz, disturber flute f = 2,216 Hz). Cross-combination tones (CT, two explicitly labeled) between the flute's fundamental f and higher harmonics of the cornett are clearly visible. Red: Optimized tuning. f (flute) and cross-combination frequencies are suppressed, leaving a harmonic series of the target (small arrows). **(B)** Averaged TE over 13 different fundamental target frequencies (steps of 1 semitone) demonstrates input amplitude independence. Blue lines: flat tuning. Red lines: optimized μ-tuning. Left panel: (full lines) target sound cornett (277–554 Hz), disturbing sound flute (at 277 Hz); (dashed lines) same target but flute at 2,216 Hz. Right panel: same experiment with target and disturber interchanged. TE improvements: arrows in **(B)**. From (Gomez et al., 2014).

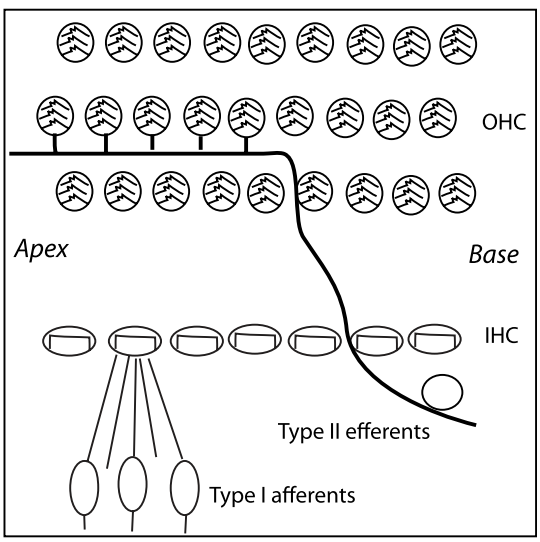

FIGURE 11 | Cochlear hair-cells innervation.

(Derighetti et al., 1985; Wiesenfeld and McNamara, 1985; Wiesenfeld and McNamara, 1986; Camalet et al., 2000; Eguíluz et al., 2000; Duke and Jülicher, 2003; Kern, 2003; Kern and Stoop, 2003; Magnasco, 2003). Systems close to a Hopf bifurcation not only depend on the input strength and frequency of the stimulating signal, but also on how close the system actually is to the Hopf bifurcation (whereas in the concurrent approach of Refs. (Eguíluz et al., 2000; Magnasco, 2003), this point was left open, in Refs. (Camalet et al., 2000; Duke and Jülicher, 2003), systems were required to be poised exactly at the bifurcation point). The distance to the bifurcation point is the main element that rules the amplifier's specificity, see **Figure 5**. Moreover, this feature provides the access point for the embedding of the sensor into the physiological network.

There is strong biological evidence that EMOCS (efferent medial olivocochlear stimulations) regulate the Hopf elements' distances to the bifurcation point, see **Figure 6**, most likely in a stronger manner than originally anticipated by Spoendlin. Activated EMOCS drive the system away from the bifurcation point, exerting in this way an inhibitory effect on the targeted Hopf amplifiers, see **Figure 7**. Changed individual amplification entrains striking effects at the level of the whole sensory organ. A recent work (Stoop and Gomez, 2016) focused on the excitation network from the nonlinear interaction of excited amplifiers generating combination tones. It was shown that under absence of EMOCS, signals of two complex tones of random amplitude and frequency, generated "activation networks" with

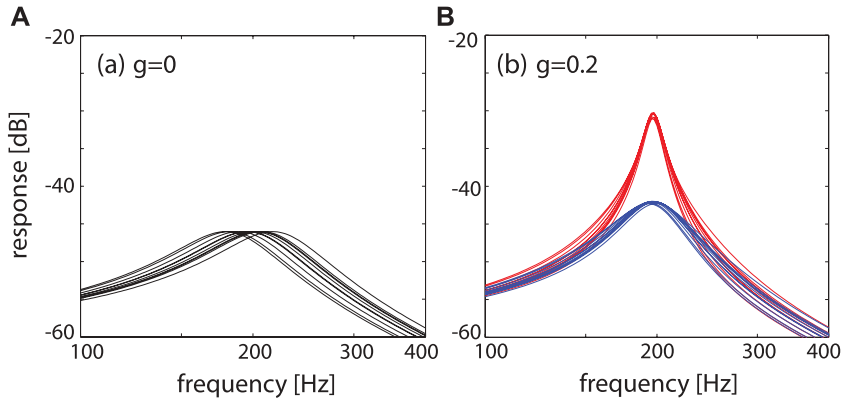

FIGURE 12 | Effects of signal coupling. Response of $N = 10$ systems, characteristic frequencies distributed around 200 Hz, to a test signal of amplitude – 60 dB. **(A)** Uncoupled, $\mu = -0.2$, **(B)** signal-coupled (blue: $\mu = -0.3$, red: $\mu = -0.2$), exhibiting a coherent and sharply tuned response around $f_c \approx 200$ Hz. From (Gomez et al., 2016).

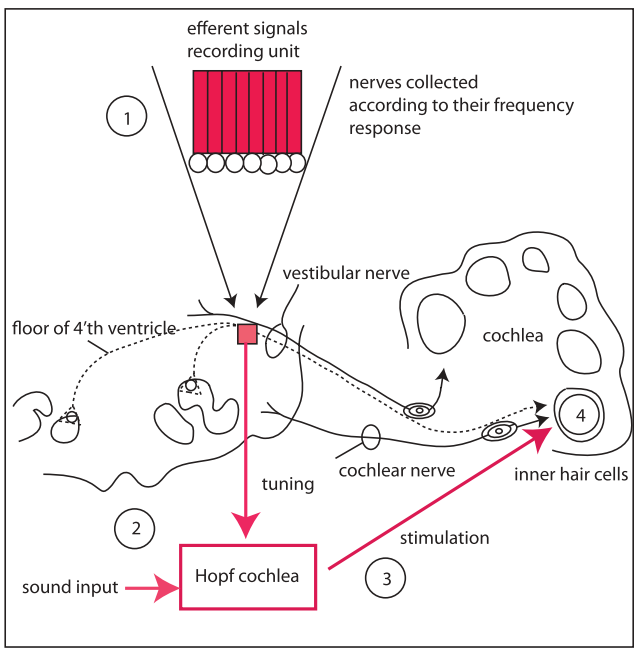

FIGURE 13 | Proposed solution of the listening problem: Using a recording array for the efferent signals to the cochlea (1), the Hopf cochlea (2) is tuned away from the "flat" (i.e., normally distributed μ's) according to the will of the listener. The tuned amplified signal is then sent to the stimulation electrodes (3) of inner hair cells (4). In the recording unit (1), the efferent nerves are grouped according to their frequency response and subject to the micro-surgical limitations.

the size s of links being distributed according the typical critical branching network paradigm (exponent $a = 3/2$, at – 60 dB input, the typical strength of human speech). Stronger input (– 50 dB) yields distributions that are typical for supercritical states, whereas upon EMOC activation, the distributions change into a subcritical shape. This reveals that at the most relevant working condition, the system's information-receiving predisposition is at criticality, whereas listening (implemented by means of EMOCS) is characterized by subcritical states (Lorimer et al., 2015).

LISTENING TO SOUNDS

In the following we demonstrate how EMOCS represent the faculty of listening at the biological level. For this, we reinterpret earlier results (Gomez et al., 2014) on sound separation from mixtures of sounds, see **Figure 8**.

To achieve separation, the listening process fosters a previously identified subset of amplifiers, disposing amplifiers that are not associated with the desired signal. This process is implemented in biology with the help of information from the brain, mediated by means of EMOCS: Nerves leading from the brain to the cochlea via medial olivocochlear stimulation suppress the efficacy of the targeted cochlea sections by, technically speaking, pushing corresponding Hopf amplifiers further away from their point of bifurcation, cf. **Figure 4**. The correctness of this translation from biology to the model has, we re-iterate, been fully corroborated by the available data from the biological effects by EMOCS in **Figure 7**.

In **Figure 9** we report the result of our biomorphic implementation of the listening process, where in subpanel a) we show how the tuning of the amplifiers changes, as the target object, the musical organ, increases its fundamental frequency in time. To assess how close we arrive to the target, we use our tuning error measure TE that has the expression $TE(x, y) = \frac{\|\text{norm.}(\sum_i ACF(f_i(x+y))) - NACF(x)\|_2}{\|\text{norm.}(\sum_i ACF(f_i(x+y))) - NACF(y)\|_2}$, where f_i denotes the output at section i of the cochlea and the summations extend over the N sections. NACF is the full normalized summary autocorrelation function accounting for all sound characteristics such as e.g., timbre); to measure how strongly a mixture of two input sounds x, y, is biased towards component x, we use the Euclidean distance between the full mixture's NACF ("NSACF")and the target signal x's NACF, divided by the Euclidean distance between the full

mixture's NACF ("NSACF") and the undesired signal y's NACF. TE values are between 0 and ∞, where $TE = 0$ indicates a perfect focus, and a larger TE is a less successful target focus. If one source dominates the mixture, then even before tuning, TE values below unity may emerge. The results displayed in panel b) demonstrate the implemented processes' efficacy also for time-varying target signals. For fixed target ground signals, panel c) demonstrates how close we get in terms of NACF (red) to the target signals (blue). More information can be extracted by scrutinizing the static case at the level of the signals' spectra, evaluated at variable signal strengths, which exhibits how EMOCS succeed in suppressing in particular the combination tones among the two signals, see **Figure 10A**). Also upon a variation of the input amplitudes of the two signals, the tuning errors remain small (see **Figure 10B**).

A second principle that comes to the aid of the EMOCS is the particular efferent innervation within the cochlea, see **Figure 11**. The particular arrangement of the innervation of out hair cells expresses a feedforward signal-coupling scheme that has been analyzed in Ref. (Gomez et al., 2016), with the result that such an arrangement fosters a collective signal-sharping, as is demonstrated in **Figure 12**. Such a signal sharpening may explain the surprising frequency discrimination (Spoendlin, 1966b) of the mammalian hearing sensor. To exhibit this, we consider two frequency-rescaled unforced Hopf systems that interact via their output signals (i.e., perform a "signal-coupling"), which yields $\frac{d}{dt}z_1 = \omega_1(\mu + i)z_1 - |z_1|^2 z_1 + \frac{g_{21}}{2}z_2$, $\frac{d}{dt}z_2 = \omega_2(\mu + i)z_2 - |z_2|^2 z_2 + \frac{g_{12}}{2}z_1$, where ω_1, ω_2 are the characteristic frequencies of the systems and g_{ij} captures the coupling from system i to system j; the factor of 1/2 facilitates the generalisation to the N systems used for **Figure 12**, where we can see that signal-coupling leads to a sharpening of the response. In our biomorphic model, the corresponding signal sharpening is comprised in the degree of compartimalization of the cochlea combined with appropriately chosen tuning parameters μ.

A Program for Solving the Listening Problem

For the implementation of the full physiological hearing circuitry, we propose to use a recording array for the efferent signals to the cochlea, that will serve to tune the Hopf cochlea away from the "normally" distributed μ's (that decay slowly along the cochlea, see (Gomez and Stoop, 2014; Kanders et al., 2017)), reflecting in this way the will of the listener to focus on the remaining signal part. In the recording unit, the efferent nerves are grouped according to the intrinsic biological resolution modulo the available micro-surgical possibilities. The grouped signal then modifies the Hopf cochlear amplification such that the input signal to the cochlea is selectively amplified in the described manner, whereupon it is sent towards the stimulation electrodes of the inner hair cells, see **Figure 13**. With such a setting—that we hope to be feasible in the near future—hearing could become fully restored, reconciling the limitations of present-day hearing aids.

Conclusion

Our work opens a perspective towards the development of more adequate cochlear implant hearing aids, responding to the listener's desire for the selection of particular sounds. This is of importance for the cocktail party problem as well as for listening to many-instrumental music. With the recognition of the physiological network that hearing is embedded in, and with the proper re-embedding of the biomorphic Hopf cochlea (Stoop et al., 2008) into this physiological network, we can reach far beyond of what is presently achievable by present-day hearing sensor technology. The task to achieving this in the near future should, however, preferentially not be delegated the hearing-aid industry, as the latter cannot be too much interested in the corresponding shift from digital engineering to high-precision micro-surgery, required for the embedding of the sensor into the physiological network of hearing.

DATA AVAILABILITY STATEMENT

The original contributions presented in the study are included in the article, further inquiries can be directed to the corresponding author.

AUTHOR CONTRIBUTIONS

The author confirms being the sole contributor of this work and has approved it for publication.

REFERENCES

Author AnonymsStoop, R., and Gomez, F. (2022). *Even the Perception of Harmonic vs. Non-harmonic Sounds Can Be Derived from the Physics of the Hopf Cochlea*. (manuscript in preparation 2022).

Camalet, S., Duke, T., Jülicher, F., and Prost, J. (2000). Auditory Sensitivity provided by Self-Tuned Critical Oscillations of Hair Cells. *Proc. Natl. Acad. Sci. U.S.A.* 97, 3183–3188. doi:10.1073/pnas.97.7.3183

Croghan, N. B., Arehart, K. H., and Kates, J. M. (2014). Music Preferences with Hearing Aids: Effects of Signal Properties, Compression Settings, and Listener Characteristics. *Ear Hear* 35, e170–84. doi:10.1097/AUD.0000000000000056

Derighetti, B., Ravani, M., Stoop, R., Meier, P. F., Brun, E., and Badii, R. (1985). Period-doubling Lasers as Small-Signal Detectors. *Phys. Rev. Lett.* 55, 1746–1748. doi:10.1103/physrevlett.55.1746

Duke, T., and Jülicher, F. (2003). Active Traveling Wave in the Cochlea. *Phys. Rev. Lett.* 90, 158101–158104. doi:10.1103/physrevlett.90.158101

Eguíluz, V. M., Ospeck, M., Choe, Y., Hudspeth, A. J., and Magnasco, M. O. (2000). Essential Nonlinearities in Hearing. *Phys. Rev. Lett.* 84, 5232–5235. doi:10.1103/physrevlett.84.5232

Fastl, H., and Zwicker, E. (2007). *Psychoacoustics - Facts and Models*. 3rd edition. Berlin): Springer-Verlag.

Gomez, F., Lorimer, T., and Stoop, R. (2016). Signal-coupled Subthreshold Hopf-type Systems Show a Sharpened Collective Response. *Phys. Rev. Lett.* 116, 108101. doi:10.1103/physrevlett.116.108101

Gomez, F., Saase, V., Buchheim, N., and Stoop, R. (2014). How the Ear Tunes in to Sounds: A Physics Approach. *Phys. Rev. Appl.* 1, 014003. doi:10.1103/physrevapplied.1.014003

Gomez, F., and Stoop, R. (2014). Mammalian Pitch Sensation Shaped by the Cochlear Fluid. *Nat. Phys* 10, 530–536. doi:10.1038/nphys2975

Kanders, K., Lorimer, T., Gomez, F., and Stoop, R. (2017). Frequency Sensitivity in Mammalian Hearing from a Fundamental Nonlinear Physics Model of the Inner Ear. *Sci. Rep.* 7, 9931–9938. doi:10.1038/s41598-017-09854-2

Kern, A. (2003). *A Nonlinear Biomorphic Hopf-Amplifier Model of the Cochlea*. PhD Thesis ETH No. 14915 (Zürich, Switzerland: ETH Zurich).

Kern, A., and Stoop, R. (2003). Essential Role of Couplings between Hearing Nonlinearities. *Phys. Rev. Lett.* 91, 128101. doi:10.1103/physrevlett.91.128101

Kern, A., and Stoop, R. (2011). Principles and Typical Computational Limitations of Sparse Speaker Separation Based on Deterministic Speech Features. *Neural Comput.* 23, 2358–2389. doi:10.1162/neco_a_00165

Kircher, A. (1673). *Phonurgia nova Sive Conjugium Mechanico-Physicum Artis & Naturae Paranympha Phonosophia Concinnatum (R. Dreherr, Kempten)*.

Lorimer, T., Gomez, F., and Stoop, R. (2015). Two Universal Physical Principles Shape the Power-Law Statistics of Real-World Networks. *Sci. Rep.* 5, 12353. –8. doi:10.1038/srep12353

Magnasco, M. O. (2003). A Wave Traveling over a Hopf Instability Shapes the Cochlear Tuning Curve. *Phys. Rev. Lett.* 90, 058101058104. doi:10.1103/PhysRevLett.90.058101

Martignoli, S., and Stoop, R. (2010). Local Cochlear Correlations of Perceived Pitch. *Phys. Rev. Lett.* 105, 048101. doi:10.1103/PhysRevLett.105.048101

Ruggero, M. A., Rich, N. C., Recio, A., Narayan, S. S., and Robles, L. (1997). Basilar-membrane Responses to Tones at the Base of the chinchilla Cochlea. *The J. Acoust. Soc. America* 101, 2151–2163. doi:10.1121/1.418265

Russell, I. J., and Murugasu, E. (1997). Medial Efferent Inhibition Suppresses Basilar Membrane Responses to Near Characteristic Frequency Tones of Moderate to High Intensities. *J. Acoust. Soc. America* 102, 1734–1738. doi:10.1121/1.420083

Spoendlin, H. (1966). "The Innervation of the Organ of Corti," in *Symposium on Electron Microscopy* (London: Inst. of Laryngology and Otology), 717–738.

Spoendlin, H. (1966). The Organization of the Cochlear Receptor. *Fortschr Hals Nasen Ohrenheilkd* 13, 1-227.

Stoop, R., and Gomez, F. (2016). Auditory Power-Law Activation Avalanches Exhibit a Fundamental Computational Ground State. *Phys. Rev. Lett.* 117, 038102. doi:10.1103/PhysRevLett.117.038102

Stoop, R., and Kern, A. (2004). Two-tone Suppression and Combination Tone Generation as Computations Performed by the Hopf Cochlea. *Phys. Rev. Lett.* 93, 268103. doi:10.1103/PhysRevLett.93.268103

Stoop, R., and Kern, A. (2004). Essential Auditory Contrast-Sharpening Is Preneuronal. *Proc. Natl. Acad. Sci. U.S.A.* 101, 9179–9181. doi:10.1073/pnas.0308446101

Stoop, R., Kern, A., and Vyver, V. D. J. P. (2008). *Sound Analyzer Based on a Biomorphic Design*. US Patent US20080197833A1 (Zürich, Switzerland: Universitaet Zuerich).

University of Colorado at Boulder (2017). When Hearing Aid Users Listen to Music, Less Is More. *ScienceDaily* 27. www.sciencedaily.com/releases/2014/10/141027145056.

Wiesenfeld, K., and McNamara, B. (1985). Period-doubling Systems as Small-Signal Amplifiers. *Phys. Rev. Lett.* 55, 13–16. doi:10.1103/physrevlett.55.13

Wiesenfeld, K., and McNamara, B. (1986). Small-signal Amplification in Bifurcating Dynamical Systems. *Phys. Rev. A.* 33, 629–642. doi:10.1103/physreva.33.629

Zwicker, E., and Heinz, W. (1955). Zur Häufigkeitsverteilung der menschlichen Hörschwelle. *Acustica* 5, 75–80.

Conflict of Interest: The author declares that the research was conducted in the absence of any commercial or financial relationships that could be construed as a potential conflict of interest.

frontiers | Frontiers in Network Physiology

TYPE Original Research
PUBLISHED 04 October 2022
DOI 10.3389/fnetp.2022.877474

OPEN ACCESS

EDITED BY
Alireza Mani,
University College London,
United Kingdom

REVIEWED BY
Milan Paluš,
Czech Academy of Sciences, Czechia
Rossella Rizzo,
University of Palermo, Italy

*CORRESPONDENCE
Małgorzata Andrzejewska,
malgorzata.andrzejewska.dokt@pw.edu.pl

SPECIALTY SECTION
This article was submitted to Systems Interactions and Organ Networks, a section of the journal Frontiers in Network Physiology

RECEIVED 16 February 2022
ACCEPTED 24 August 2022
PUBLISHED 04 October 2022

CITATION
Andrzejewska M, Żebrowski JJ, Rams K, Ozimek M and Baranowski R (2022), Assessment of time irreversibility in a time series using visibility graphs. *Front. Netw. Physiol.* 2:877474. doi: 10.3389/fnetp.2022.877474

Assessment of time irreversibility in a time series using visibility graphs

Małgorzata Andrzejewska[1]*, Jan J. Żebrowski[1], Karolina Rams[1], Mateusz Ozimek[1] and Rafał Baranowski[2]

[1]Cardiovascular Physics Group, Physics of Complex Systems Division, Faculty of Physics, Warsaw University of Technology, Warszawa, Poland, [2]Institute of Cardiology, Warszawa, Poland

In this paper, we studied the time-domain irreversibility of time series, which is a fundamental property of systems in a nonequilibrium state. We analyzed a subgroup of the databases provided by University of Rochester, namely from the THEW Project. Our data consists of LQTS (Long QT Syndrome) patients and healthy persons. LQTS may be associated with an increased risk of sudden cardiac death (SCD), which is still a big clinical problem. ECG-based artificial intelligence methods can identify sudden cardiac death with a high accuracy. It follows that heart rate variability contains information about the possibility of SCD, which may be extracted, provided that appropriate methods are developed for this purpose. Our aim was to assess the complexity of both groups using visibility graph (VG) methods. Multivariate analysis of connection patterns of graphs built from time series was performed using multiplex visibility graph methods. For univariate time series, time irreversibility of the ECG interval QT of patients with LQTS was lower than for the healthy. However, we did not observe statistically significant difference in the comparison of RR intervals time series of the two groups studied. The connection patterns retrieved from multiplex VGs have more similarity with each other in the case of LQTS patients. This observation may be used to develop better methods for SCD risk stratification.

KEYWORDS

irreversibility, visibility graphs, heart rate variability, repolarization, kld

1 Introduction

Physiological systems, such as the human body, for example, are considered complex (Seely and Macklem, 2012). Such systems use energy to build increasingly complex and ordered structures. This ability of self-organization is related to the directivity of energy flow and the irreversibility of the processes taking place (Costa et al., 2005). Healthy organisms are believed to work under conditions that are far from equilibrium. Such states are characterized by the production of entropy. This results from the fact that organisms form an ordered structure during development, therefore, for the second law of thermodynamics to be preserved, this process must be balanced by the production of entropy (Seely and Macklem, 2012). There is also a hypothesis that the assessment of this

production can be used to diagnose the state of dynamic equilibrium of the organism (Seely and Macklem, 2012).

In physiology, the condition in which the stable conditions of the internal environment of the body are maintained is called homeostasis. To survive, the organism requires the maintenance of an appropriate concentration of many quantities, such as nutrients, oxygen concentration and various ions. In addition, the maintaining of appropriate temperature and blood pressure levels is required (Chladekova et al., 2012). There are gradients of these quantities in the body, which are related to metabolism and have a significant impact on the rate of production of entropy of the system. In turn, it is known from statistical physics that this rate is related to the irreversibility of the studied processes (Seely and Macklem, 2012).

In the case of healthy and young organisms are characterized by a greater complexity, related to the greater adaptability of such organisms (Seely and Macklem, 2012). The decrease in the possibility of self-organization, and, therefore, the decrease in irreversibility over time, can be associated with aging of the organism or may be due to diseases (Costa et al., 2005). Many studies show that such a decrease may be associated with a decreased heart rate variability (Seely and Macklem, 2012). In statistical terms, a signal can be considered irreversible when its statistical properties change after reversing the passage of time.

Different studies, e.g. (Jose and Taylor, 1969), have showed that pharmacological blockade of cardiac autonomic control reduces heart rate variability and increases its basal beating rate in humans. This is due to autonomic control by both sympathetic and parasympathetic nervous system and dominant inhibition of cardiac pacemaker by the vagus nerve in healthy humans. This natural rate of an unperturbed sinus node is called intrinsic heart rate (IHR) and it declines with age (Jose and Taylor, 1969; Opthof, 2000). Assessing IHR may provide an insight into the pathological mechanisms and help with antiarrhythmic therapies (Marcus et al., 1990). The difference between IHR and mean HR defines an operational range for neural and hormonal regulation. As this difference diminishes in time, it is observed that heart rate variability measures will also decline with age (Jandackova et al., 2016).

Regarding the Long QT syndrome (LQTS), an inherited proarrhythmic cardiac abnormality, the clinical target of our research is not to simply diagnose the disease. There are simple ECG-based methods to distinguish patient from healthy individuals (Schwartz et al., 2012). We rather refer to the fact that the patients with LQTS are more susceptible to develop fatal cardiac arrhythmias (Mathias et al., 2013). It follows that LQTS is a risk factor for sudden cardiac arrest (SCA) (Goldenberg et al., 2011). The clinical goal of this study is to assess irreversibility in a group that has an arrhythmic substrate (Vijayakumar et al., 2014). This substrate is present in all LQTS patients, but its severity is unknown. Risk stratification in this group will be a difficult task which requires a prospective study.

On the other hand (Suboh et al., 2019), have shown that the use of artificial intelligence (AI) algorithms can predict sudden cardiac arrest from ECGs with up to 92% efficiency. This means that the even a short ECG strip, and most notably the normal sinus rhythm variability contains information about the possibility of SCA. AI is usually non-conclusive, and it is difficult to relate the results of its performance to the measured parameters. Explainable artificial intelligence is evolving (Samek et al., 2019), but the information it provides is formulated in the feature space of the model, e.g., the convolutional network, and not in the concept space of traditional ECG or HRV analysis. However, the exceptionally high success rate of the AI methods convinces that there is reason to study individuals at increased risk of sudden cardiac arrest and compare them with healthy individuals. The key feature of the normal cardiac rhythm, which is believed to carry important clinical information is its complexity. The concept of complexity is complicated and can be explained using different methods, e.g., fractal analysis, entropy, or irreversibility (Fiskum et al., 2018). When studying heart rate variability, the question of which concept space will be the best to describe the patient's clinical condition recurs. Measures of irreversibility applied here can be used to differentiate groups, and they become interesting candidates to better assess the risk of SCA and improve patient management, to increase life expectations and reduce mortality.

In this paper, we analyze only a part of the physiological network of the human, namely, we assess time irreversibility of time series taken from ECG recordings. The purpose of this paper is to analyze irreversibility in a group of patients with the LQTS (Long QT syndrome) and compare them to a group of healthy persons to identify dynamical correlates of the arrhythmogenic substrate. However, comparing time irreversibility descriptors presented below with standard statistics shows that both approaches provide similar results in distinguishing between groups (Figure 6 below). The mean and standard deviation of QT intervals are greater in the LQTS group. These indicators are simplified, however, and the use of irreversibility over time provides a way to distinguish between differences in the dynamics caused by reversible and irreversible processes (Lacasa et al., 2012). The presence of time irreversibility indicates the existence of nonlinear processes such as dissipative chaos (Li et al., 2021). Ilya Prigogine discovered the existence of dissipative structures (Prigogine, 1978), which are spontaneously self-organizing complex system states that arise far from equilibrium. Living organisms, including humans, can be looked at as dissipative structures far from a thermodynamic equilibrium (Li et al., 2021). They are characterized by a high degree of complexity, which can be estimated using non-linear properties of human heartbeat (Seely and Macklem, 2012). To compare the results for time asymmetric patterns with irreversibility measures using KLD, we calculated the Porta and Guzik indices.

LQTS is a genetically determined dysfunction of ion channels or the proteins that regulate them. This disease leads to serious symptoms, including fainting or loss of consciousness. It can also cause sudden cardiac arrest (SCA). A prolonged QT interval can be acquired or congenital. The clinical course of the disease varies depending on which gene has been mutated. The most common types of LQTS are LQTS 1, 2 and 3. In the case of LQTS type 1, which is most of the cases we study in this paper, the mutation disrupts the slow potassium current (Seebohm et al., 2008). Symptoms of the disease most often occur during exercise, in contrast to, for example, LQTS2, where they are induced during increased catecholamine release in early morning (Wilde et al., 1999).

Complex networks are increasingly used in various fields of science. Currently, graphs are used in many practical problems, including in computer networks, where the representation of the network in the form of a graph facilitates the routing of data packets on the Internet (Oehlers and Fabian, 2021), in medicine to study the spread of viruses (Keeling and Eames, 2005; Alarcón-Ramos et al., 2018), or research on the dynamics of social networks, e.g., the spread of rumors (Agliari et al., 2017). Historically, Kullback-Leibler divergence (KLD) was proposed for measuring time asymmetry in the beginning of the 1950s and during the next decade its relation to entropy production was shown (Gaspard, 2004; Parrondo et al., 2009). In our study, we used visibility graphs (VG) methods (Lacasa et al., 2008) to assess the time irreversibility of selected time series. VG allow to map time series to the form of graphs. This makes it possible to study the information contained in such records with the use of complex network research tools. In this way, graph theory can be used to study nonlinear signals (Lacasa et al., 2008).

This paper is constructed as follows: in Section 2, we introduce time irreversibility methods both for one dimensional time series and multivariate time series. In Section 3, we describe the data, which were used for our analysis, and introduce our methodology for preparing data extracted from ECG recordings from the THEW database (University of Rochester Medical Center, 2022; University of Rochester Medical Center Healthy Individuals, 2022). In Section 4, we present our results for nighttime recordings of healthy people and of patients with LQTS. In Section 5, we conclude.

2 Methods

2.1 Visibility graphs

Graphs were also looked at from the medical point of view (Mason and Verwoerd, 2007). The authors of the publication (Lacasa et al., 2012) showed that the increase in entropy per unit time can be described by determining the Kullback-Leibler divergence (KLD), usually denoted KLD ($p \,||\, q$) for a given random variable x and probability distributions $p(x)$ and $q(x)$. However, this measure gives only the lower bounds of entropy production (Lacasa et al., 2012). For two probability distributions p and q, describing the process in accordance with and contrary to the passage of time, KLD it is given by the relationship (Lin, 1991):

$$KLD(p\|q) = \sum_x p(x) log \frac{p(x)}{q(x)}. \tag{1}$$

Such a graph is created by connecting the vertices that meet a specific visibility criterion. Figure 1 shows an example of a time series in the form of a bar graph. When analyzing human heart rhythm records, each bar corresponds to a single value of the RR interval (measured as the time between two successive R-waves in the ECG trace). Each such interval is also the vertex of the graph, into which the time series is transformed (Iacovacci and Lacasa, 2016).

Two vertices are connected to each other when the heights of the corresponding bars meet the following visibility criterion (Lacasa and Flanagan, 2015). For the time series $S = \{x(t)\}_{t=1}^{T}$ for each element $x_i(t)$ being the vertex of such a graph, two vertices i and j are connected by an edge, if each different $x_k(t)$ satisfies condition:

$$x_k < x_i + \frac{k-i}{j-i}\left[x_j - x_i\right], \text{for each } i < k < j. \tag{2}$$

2.2 Horizontal visibility graphs

Another type of graph is the horizontal visibility graph. It differs from the basic version in that, in this case, two vertices are connected to each other only if they can be joined together in a bar graph of the time series by a horizontal line without intersecting the vertices between them (Lacasa et al., 2012). An example is shown in Figure 2.

In general, for the time series $S = \{x(t)\}_{t=1}^{T}$ the following condition of horizontal visibility can be written (Lacasa and Flanagan, 2015):

Two vertices $x_i(t)$ of the graph are connected with each other if and only if the following relation is satisfied:

$$x_i, x_j > x_n, \text{ for every } i < n < j. \tag{3}$$

2.3 Directed horizontal visibility graphs

This is a graph that is an extension of the horizontal visibility graph. The direction of the flow of time is taken into consideration. The temporal arrow is considered by using

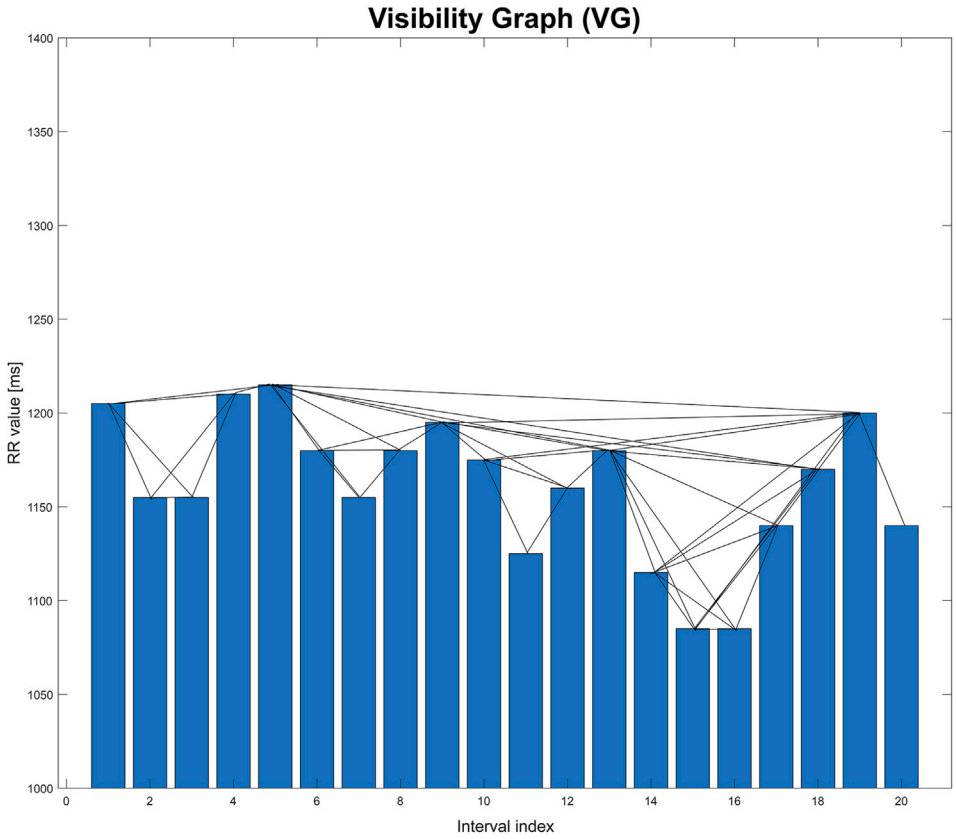

FIGURE 1
Graphical illustration of visibility graph (VG). This graph is based on an extract from one of the records studied in the paper.

directed graphs. For each vertex, you can specify the edges that enter it from the vertices that precede it, and the edges that connect it to the next vertices that follow it in time. The direction of connections is consistent with the passage of time (Lacasa and Flanagan, 2015).

The degree of the vertex $k(t)$ consists of the following sum:

$$k(t) = k_{in}(t) + k_{out}(t). \tag{4}$$

$k_{in}(t)$ is the number of edges entering a given vertex, associated with vertices in the past. On the other hand, $k_{out}(t)$ is defined as the number of edges emerging from a given vertex. This is related to the connections of a given vertex with the "future" elements of the time series (Lacasa and Flanagan, 2015). An example of such a graph is shown in Figure 3.

The analysis of the dHVG allows the use of information on the degree distributions of the incoming and outgoing vertices. Based on the difference in these distributions, the degree of irreversibility of the time series tested can be estimated. This difference can be interpreted as the distance (in the sense of distributions) between the probability distributions of the input vertices $P_{in}(k)$ and that of the output $P_{out}(k)$. Generally, $P(k)$ is the fraction of all nodes in the network that have degree k and it describes the probability that a randomly selected node will have degree k (Lacasa and Flanagan, 2015).

One of the measures that allows to describe the difference between the distributions $P_{in}(k)$ and $P_{out}(k)$ is the Kullback-Leibler divergence:

$$KLD[P_{out}(k)\|P_{in}(k)] = \sum_k P_{out}(k) \cdot \ln \frac{P_{out}(k)}{P_{in}(k)}, \tag{5}$$

where:

k - vertex degree and $k = k_{in} + k_{out}$

$P_{in}(k)$- degree distribution of input vertices

$P_{out}(k)$ - degree distribution of exit vertices.

In statistical physics, the measure KLD can be used to measure the time irreversibility of non-equilibrium processes and to estimate the entropy production during such processes (Lacasa et al., 2012). It was shown in (Lacasa et al., 2012) that this measure enables to distinguish discrete time series obtained from reversible and irreversible time series.

The signal is invertible when:

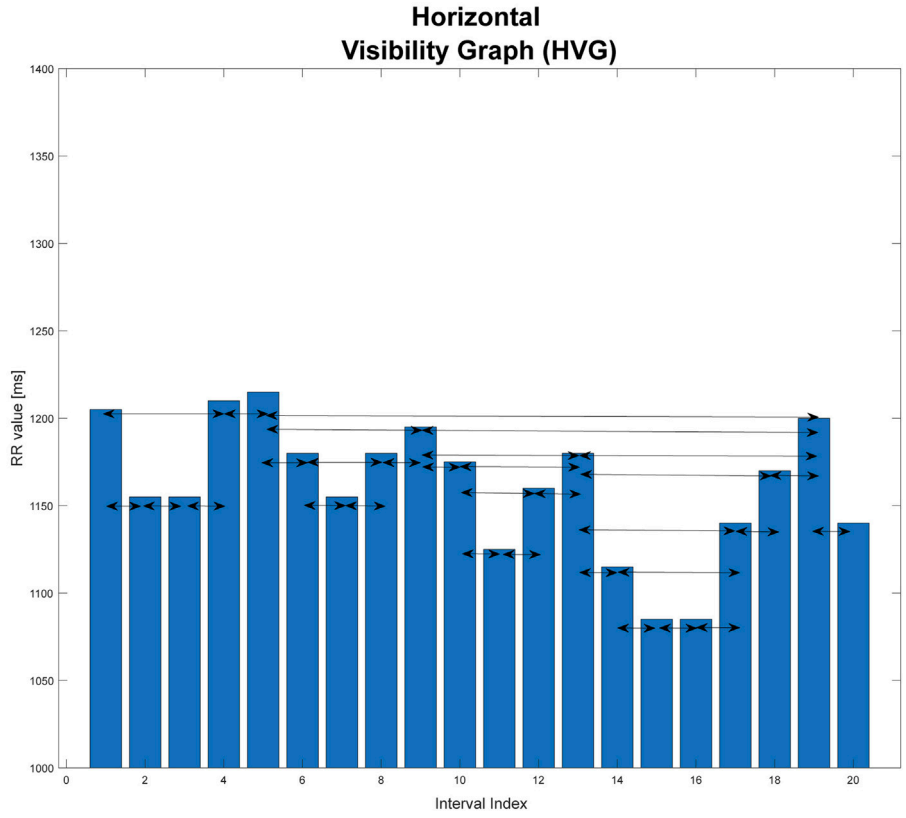

FIGURE 2
Graphical illustration of horizontal visibility graph (HVG). This graph is based on an extract from one of the records studied in the paper.

$$\lim_{n \longrightarrow \infty} KLD[P_{out}(k) \| P_{in}(k)] = 0. \tag{6}$$

where n is number of vertices in the graph. In this case, the probability distributions $P_{in}(k)$ and $P_{out}(k)$ are equal.

For stationary signals, KLD is the lower limit of the non-equilibrium entropy production during the time evolution of the process.

The Jensen-Shannon Divergence (JSD) is a measure of divergence based on KLD. Its main advantage is that, in contrast to the Kullback-Leibler divergence, it always has a finite value, which allows to avoid infinity obtained when calculating KLD (Nielsen, 2020).

JSD can be determined as the mean KLD divergence of the distributions $P_{in}(k)$, $P_{out}(k)$ and their mixed distribution $M = \frac{P_{in}(k)+P_{out}(k)}{2}$ (Nielsen, 2020):

$$JSD[P_{out}(k) \| P_{in}(k)] = \frac{1}{2}(KLD[P_{out}(k) \| M] + KLD[P_{in}(k) \| M]. \tag{7}$$

After the substitution, the final formula is:

$$JSD[P_{out}(k) \| P_{in}(k)] = = \frac{1}{2}\left[\sum_k P_{out}(k) \cdot \ln \frac{P_{out}(k)}{\frac{1}{2} \cdot [P_{out}(k) + P_{in}(k)]} + \sum_k P_{in}(k) \cdot \ln \frac{P_{in}(k)}{\frac{1}{2} \cdot [P_{out}(k) + P_{in}(k)]}\right]. \tag{8}$$

2.4 Multivariate methods

Now, we consider an M-dimensional real valued time series. Using such data, an M-layer Multiplex network is constructed (Lacasa et al., 2015). In our case, we have a set of α data ($\alpha = 3$ for the intervals RR, QT and DI of the ECG trace). Each of them is a series of real data from index 1 to the length of signal N. For each of them, we construct the HVG in accordance with the single-layer algorithm (Lacasa et al., 2012; Lacasa et al., 2015; Lacasa et al., 2017). The Multiplex Visibility graph is created in such a way that it is described by a matrix $\mathcal{A} = \{A^{[1]}, A^{[2]}, A^{[3]}\}$, the

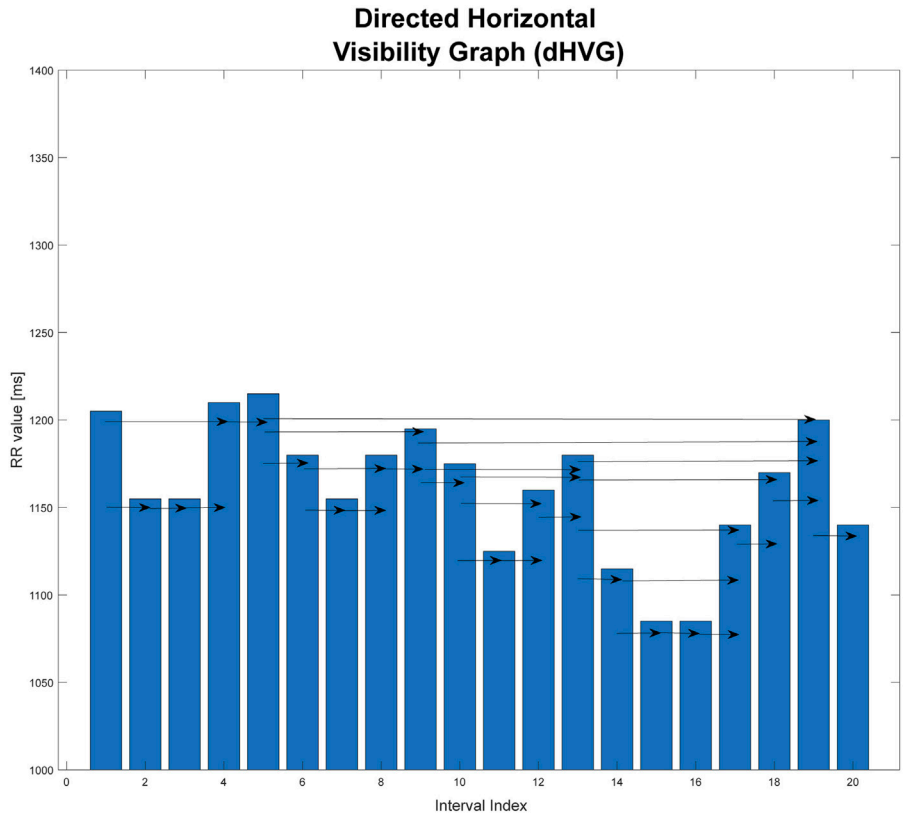

FIGURE 3
Graphical illustration of directed horizontal visibility graph (dHVG). This graph is based on an extract from one of the records studied in the paper.

elements of which are the adjacency matrices of the VG of each of the examined data sets (in our case, the intervals RR, QT and DI).

Average edge overlap $< o >$ is defined as follows (Lacasa et al., 2015):

$$< o > = \frac{1}{K}\sum_{i,j} o_{ij}, o_{ij} = \frac{1}{M}\sum_{\alpha} a_{ij}^{[\alpha]}. \quad (9)$$

where K is the total number of edges and o_{ij} is the overlap of the edges between the vertices i and j situated in different layers. It is defined as follows: we sum for each pair ij the appropriate terms in the adjacency matrix (equal to 1 if these vertices are connected to each other in each layer, 0 otherwise). This is then normalized by the number of layers. $o_{ij} = 0$, when the nodes i and j are not connected to each other in any layer, and 1 when they are in all of them. Next, we sum these values over i, j and average over the number of i, j pairs. Thus, the more similar the connection patterns in the layers are, the larger $< o >$ we obtain. $< o >$ equals 1, when all the layers are identical (Lacasa et al., 2015; Lacasa et al., 2017).

We compute the adjacency matrices for directed graphs according to the passage of time and after inverting the sequence of the records. Then, we will obtain matrices which in KLD are used to determine $P_{in}(k)$—the degree distribution of input vertices and $P_{out}(k)$—the degree distribution of output vertices. Having these two data sets, for each of them we calculate the average edge overlap and then calculate the absolute value from the difference of these values. Directed average edge overlap:

$$davo = abs(< o_{in} > - < o_{out} >). \quad (10)$$

We also used interlayer mutual information (IMI) (Lacasa et al., 2015) as another measure of quantification of the presence of interlayer correlations. For two layers α and β, IMI between the degree distributions k_α and k_β is defined as:

$$I_{\alpha,\beta} = \sum_{k_\alpha}\sum_{k_\beta} P(k_\alpha, k_\beta) log \frac{P(k_\alpha, k_\beta)}{P(k_\alpha)P(k_\beta)} \quad (11)$$

During the calculation of IMI, after the division of the signal into non-overlapping windows of 600 interval length, we used the EMD method (Stallone et al., 2020) to remove the trend from the data. To do so, we separated the last four IMFs and their sum we

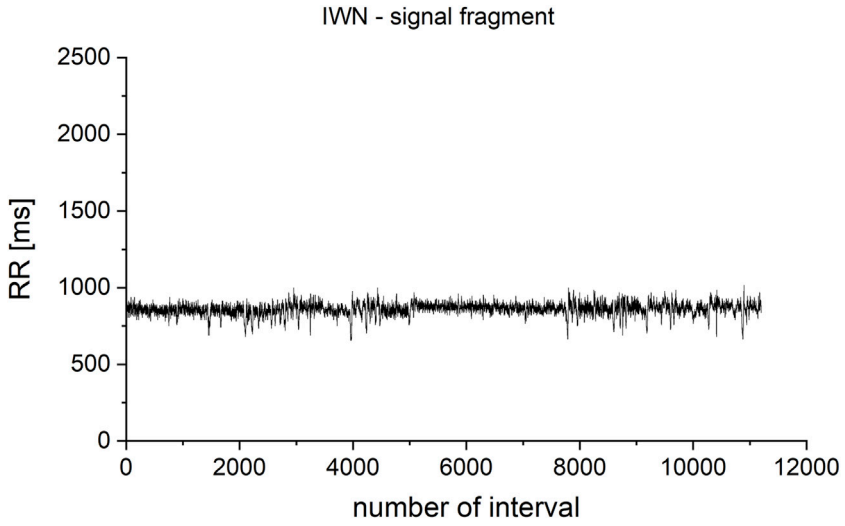

FIGURE 4
Fragment selected from the IWN patient's heart rhythm record. The total analyzed record length was from N = 100 to N = 11,200 iterations. Successive fragments of increasing length were selected, starting at the beginning of the time series.

subtracted from the signal. This was required for proper calculations of mutual information (Hoyer et al., 2005).

2.5 Asymmetry indices

Porta's Index (P%) (Porta et al., 2008) compares the number of negative increments between consecutive members of the time series with the number of all non-zero increments. It is defined by the formula:

$$P\% = \frac{N(\Delta RR^{-})}{N(\Delta RR \neq 0)} * 100\%. \quad (12)$$

This index can range from 0 to 100%. The irreversibility over time is implied by P% values significantly different from 50%. Moreover, P% values greater than 50% indicate that the number of negative increments ΔRR^{-} in the signal $RR_i - RR_{i+1}$ is greater than the number of positive increments ΔRR^{+}.

To make the values of this index more readable, below we subtract 50 from all values obtained for the different cases studied. In this way, the zero of this index indicates a completely reversible time series. We treat the next index (described below) in the same way.

Guzik's index (G%) (Piskorski and Guzik, 2007; Porta et al., 2008) is determined as the ratio of the sum of the squares of the positive differences $RR_i - RR_{i+1} > 0$ to the sum of all differences $RR_i - RR_{i+1}$ in the signal squared. This index can also be defined as the ratio of the sum of squared of positive differences $RR_i - RR_{i+1} > 0$ from diagonal in the Poincaré plot (this is a scatter plot describing the dependence $RR_{i+1} = f(RR_i)$ (Piskorski and Guzik, 2007)) signal to the distance of all ΔRR from the diagonals. It is given by the formula:

$$G\% = \frac{\sum_{i=1}^{N(\Delta RR^{+})} \Delta RR^{+^2}(i)}{\sum_{i=1}^{N(\Delta RR)} \Delta RR^{2}(i)} * 100\%. \quad (13)$$

G% can take values from 0 to 100%. The signal irreversibility over time is implied, as in the case of the Porta's index, by G% values significantly different from 50%. For clarity, we subtract 50 form the value obtained for each case studied. This is the same procedure that we used for Porta's index.

3 Data and methodology

Two databases from the THEW Project (University of Rochester Medical Center, 2022; University of Rochester Medical Center Healthy Individuals, 2022) were used to provide the RR, QT, and the DI intervals (diastolic interval - the time between the end of the T segment and the beginning of the next QRS complex). We used the following THEW databases: E-HOL-03-0202-003 (202 ECGs of healthy individuals) and E-HOL-03-0480-013 (480 ECGs of the Long QT Syndrome patients forming 4 subgroups by genotype).

In this paper, we analyze a subgroup for each of these databases: It consists of 61 (38 women) LQTS patients and 114 (59 women) healthy persons. The range of age is limited to 18–60 years.

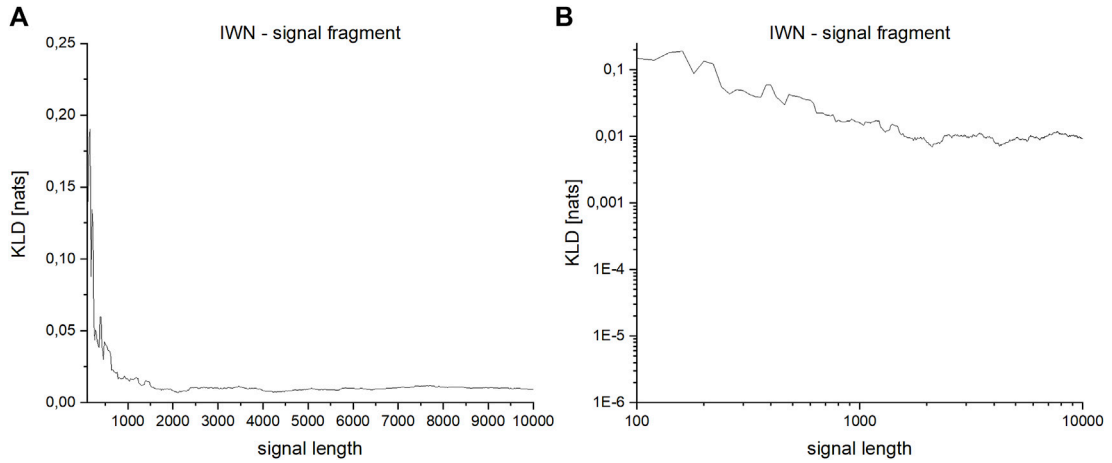

FIGURE 5
(A,B)—Dependence of KLD on the length of the series for a fragment of the signal derived from the heart rhythm of a healthy person: **(A)**—linear scale, **(B)**—logarithmic scale.

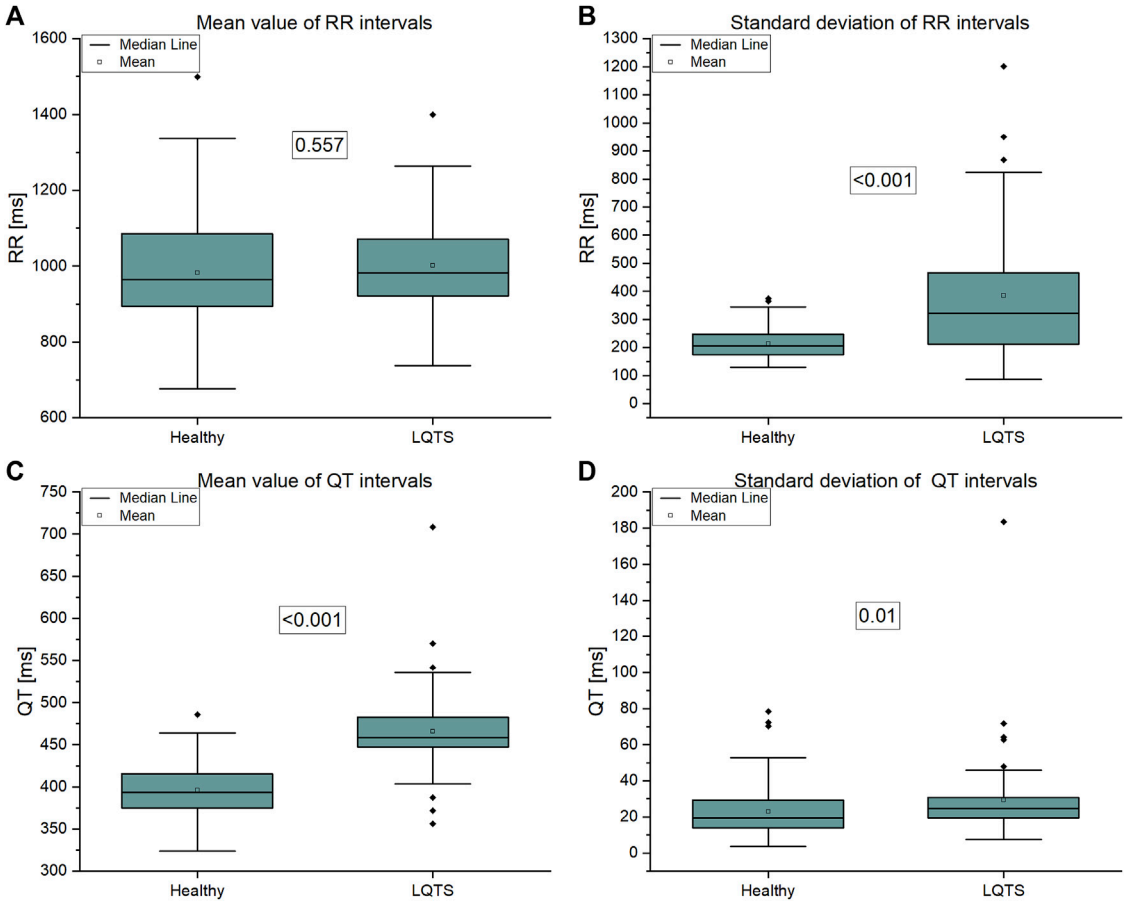

FIGURE 6
(A) Mean value of RR intervals time series, **(B)** Standard deviation of RR intervals time series, **(C)** Mean value of QT intervals time series, **(D)** Standard deviation of QT intervals time series.

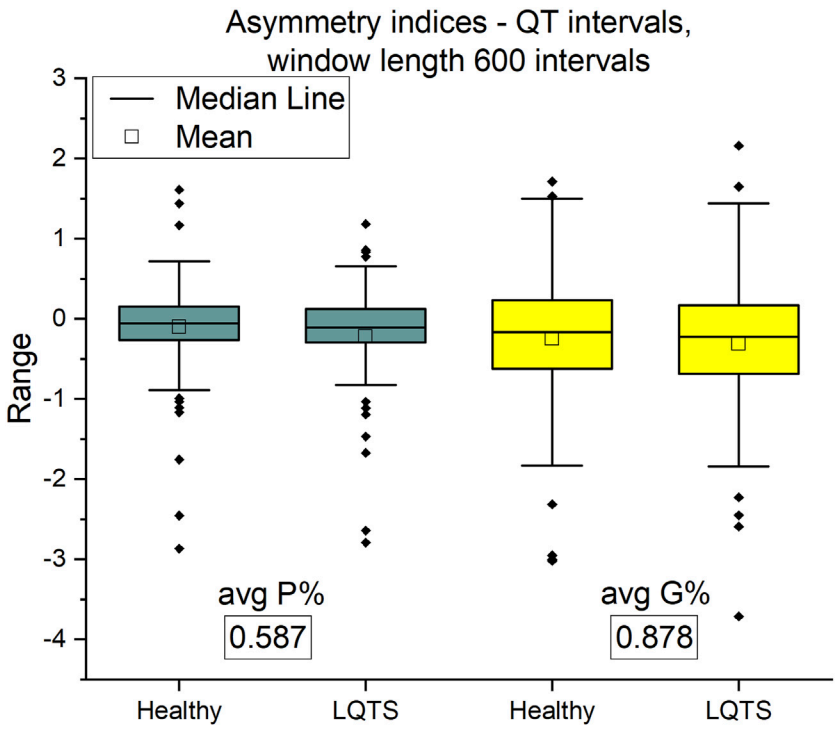

FIGURE 7
Porta *P%* and Guzik G% indices for QT intervals. Window length equals 600 intervals. *p*-values for each comparison are presented in boxes below the name of the given irreversibility parameter.

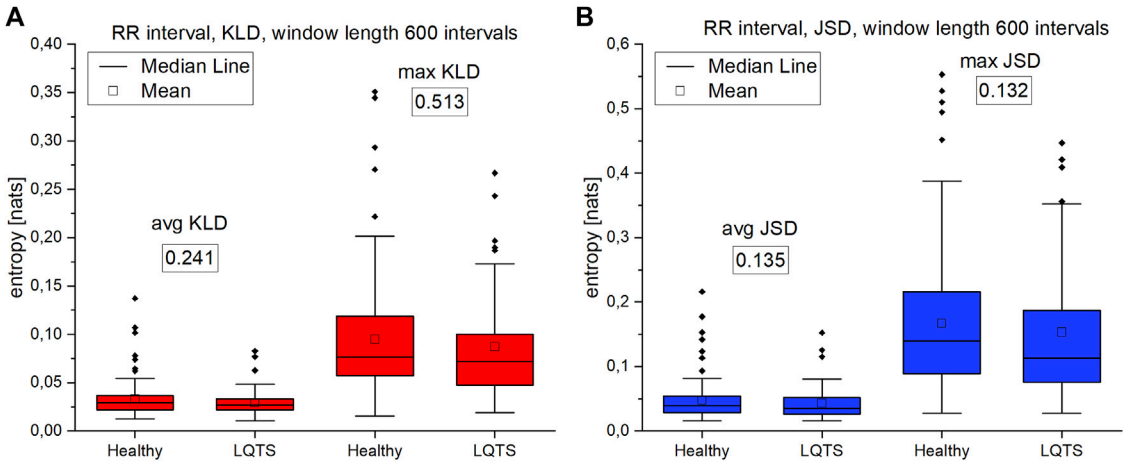

FIGURE 8
(A)—Kullback-Leibler divergence (KLD) for RR intervals. **(B)** Jensen-Shannon divergence (JSD) for RR intervals. Window length equals 600 intervals. *p*-values for each comparison are presented in boxes below the name of the given irreversibility parameter.

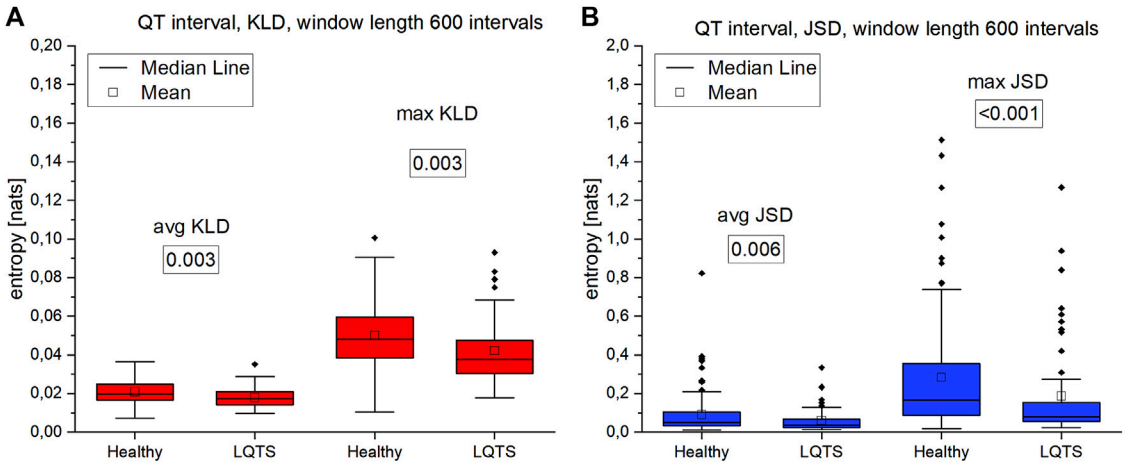

FIGURE 9
(A)—Kullback-Leibler divergence (KLD) for QT intervals. **(B)** Jensen-Shannon divergence (JSD) for QT intervals. Window length equals 600 intervals. *p*-values for each comparison are presented in boxes below the name of the given irreversibility parameter.

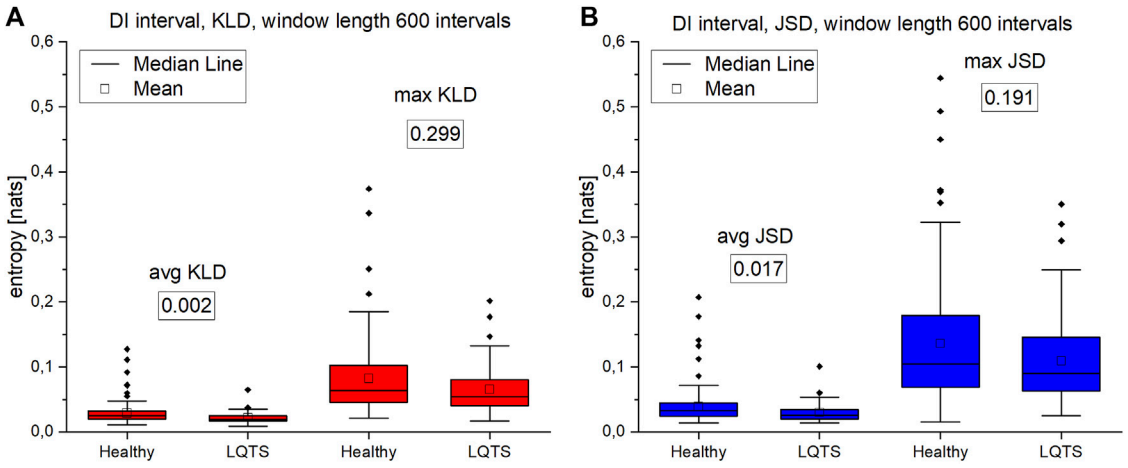

FIGURE 10
(A)—Kullback-Leibler divergence (KLD) values for DI intervals. **(B)** Jensen-Shannon divergence (JSD) values for DI intervals. Window length equals 600 intervals. Values presented in boxes on charts are corresponding *p*-values. *p*-values for each comparison are presented in boxes below the name of the given irreversibility parameter.

To calculate the RR and QT intervals, firstly, the R waves in the ECG signals had to be obtained. To achieve that, proper annotation files derived from the THEW database were placed onto the signals and then filtered to delete those R waves that had not been annotated as either normal or arrhythmic. This method, however, resulted in the R waves being misplaced by an irregular offset, rendering them incorrect. To compensate for these offsets a hybrid algorithm was developed. The algorithm used the R waves detection toolset available in the Neurokit2 package for Python 3, which allowed for correct detection of the R waves. However, the results of this operation would have had to be manually selected for each separate file, as this method gave no information if the peak was normal, arrhythmic or of other kind. In addition, it was oversensitive towards labelling other types of waves as R waves when the signal was of especially bad quality. The hybrid algorithm combined the two methods, i.e., using the annotation files and the Neurokit2 toolset, and compared the results of both, deleting the offsets from the first method. Based on the obtained R waves, the wave detection toolset available in the

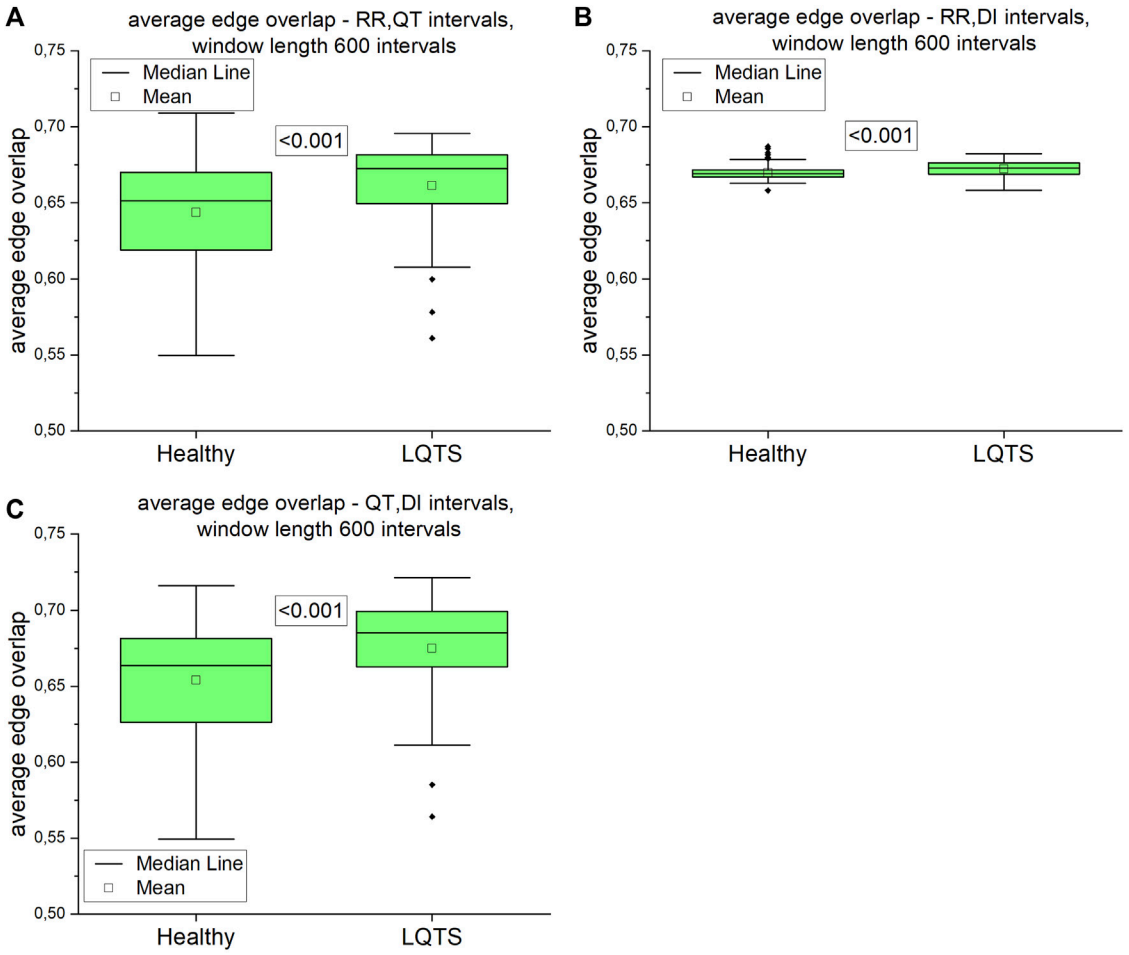

FIGURE 11
Average edge overlap calculated for pairs of time series: **(A)** RR and QT intervals time series, **(B)** RR and DI intervals time series, **(C)** QT and DI intervals time series. Using the Kolgomorov-Smirow test, we obtained the *p*-values presented in the boxes. The window length equals 600 intervals.

Neurokit2 package was used to find other waves, among which there were the Q waves and T waves offsets. To obtain the RR and QT intervals, the difference between R(i) and R(i+1) as well as the differences between Q(i) and T_offset(i) were calculated.

KLD values and multivariate methods were determined using Matlab R2021b, while statistical tests and graphs were done using OriginPro 2021b.

All signals were divided into non-overlapping windows of length 600 intervals. The numbers next to the pairs of boxplots on Figures 6–11 are the corresponding *p*-values (Kolgomorov-Smirnov test). This non-parametric test was chosen because the data distributions do not meet the criterion of fitting a normal distribution (Shapiro-Wilk normality test).

KLD was calculated only for the nighttime recordings of the heart rhythm. Because of the different time for every patient for going to sleep, for each case the period of observation was selected using the average RR value over time (Gierałtowski et al., 2012; Żebrowski et al., 2015). These records were also analyzed with the use of windows (the tested signal was divided into adjacent, non-overlapping windows). Windows with the lengths of 400, 600, 900, 1,200 and 2000 intervals were used. A window with the length of 600 RR intervals was finally used for the analysis, this value was considered optimal. The selection of such a window width was made after analyzing the results for other window widths. For the 600 interval window length, we obtained the best results in comparing the study groups. The window with a width of 400 intervals is too short for the method to give perfect identification of irreversibility (Zanin and Papo, 2021), while the results for windows of 900, 1,200 and 1800 intervals showed a dispersion of the results which was too large. The result is the average obtained from all windows of a given length into which the time series was divided into.

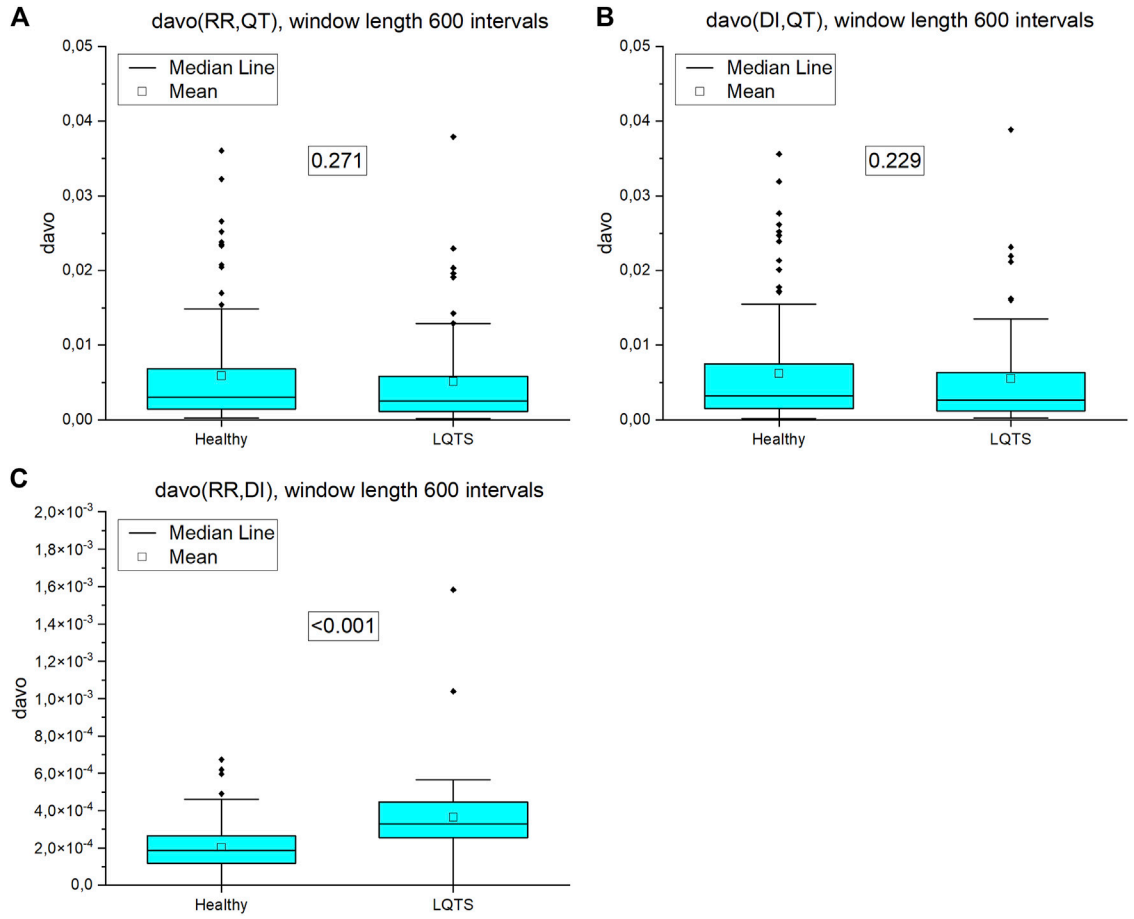

FIGURE 12
Directed average edge overlap (davo) calculated for pairs of nighttime series (window length 600 intervals): **(A)** RR and QT intervals time series, **(B)** DI and QT intervals time series, **(C)** RR and DI intervals time series. *p*-values for each comparison are presented in the boxes.

The dependence of the results of irreversibility measures on the length of the analyzed time series was also checked. For this purpose, a fragment of a record of the heart rhythm of a healthy male from the database of the Institute of Cardiology (patient IWN, Figure 4) was checked. The total record length analyzed in the study was from $N = 100$ to $N = 11{,}200$ intervals. Successive fragments of increasing length were selected, starting at the beginning of the time series.

For windows of the length 600 intervals, KLD still do not fully stabilize, but it is the optimum between the correctness of the method (low dependence on the length of the tested time series), the quality of the obtained results (statistical significance measured in the Kolgomorov-Smirnov test using the *p*-value value), and the time required to carry out the calculations (Figure 5A). To represent the dynamics more clearly for shorter signals, for which there is a large difference between the analyzed values, the results are also presented in a logarithmic scale (Figure 5B).

4 Results

4.1 Assessing time irreversibility of nighttime recordings using VG

The analysis on signal level using simple statistics shows that statistically significant differences between groups are present in QT mean (which follows from the definition of LQTS) and in both standard deviations, which are greater in LQTS group (Figure 6).

Asymmetry indices are based on differences between adjacent values of time series intervals. On the contrary, KLD estimates time irreversibility using number of points that each value of time series could reach without crossing with other points (Li et al., 2021). The asymmetry indices show no difference between groups (Figure 7). Therefore, we are interested in more complicated descriptors of dynamics of time series.

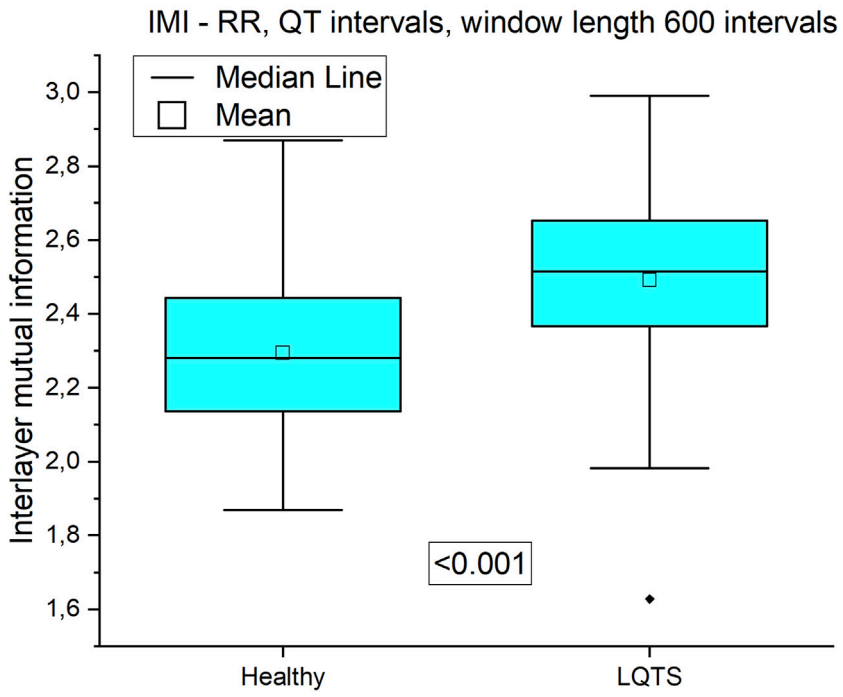

FIGURE 13
Interlayer mutual information of RR and QT time series.

In the case of VG, we compare the average and maximum values obtained from the calculations in non-overlapping windows of the selected intervals. Because in many cases the minimum values were close to zero, they were omitted from the results.

The comparison of the results for RR intervals for the healthy subjects with the patients with LQTS indicates that there are no statistically significant differences (Figures 8A,B), which would indicate no influence of the studied disease on the irreversibility of the heart rhythm. On the other hand, differences manifest themselves in the case of QT intervals (Figures 9A,B). Healthy persons are characterized by statistically significant greater irreversibility with respect to time of the QT intervals than that of the patients with LQTS.

However, there are also significant differences between the KLD and JSD for the RR and QT intervals. In the former case, they are lower. For healthy persons, the median for average KLD for the RR intervals is 0.01984 nats and median for average JSD is 0.05071 nats, while for QT it is respectively 0.01725 nats and 0.03468 nats.

The analysis of max values of KLD and JSD using the DI intervals (Figures 10A, B) follows the results obtained for the RR time series, which is consistent with the results in (Ozimek et al., 2021). There is no difference in the irreversibility between analyzed groups. However, in the case of average KLD and average JSD here we observe higher values for the healthy indicating a larger irreversibility for the healthy.

For night recordings, statistically significant differences with the use of VG were obtained only in the case of mean and maximum values of KLD and JSD for the time series of QT intervals. However, there are no differences in the irreversibility in time between the healthy and the LQTS patients for heart rate variability. In the statistically significant cases presented above, healthy persons are characterized by a larger value of irreversibility with respect to time.

4.2 Assessing time irreversibility of nighttime recordings using multivariate time series

Our next step was to analyze multivariate time series. First, we calculated the average edge overlap between two of the three analyzed intervals. The results are presented on Figure 11.

The difference between average edge overlaps for the healthy and LQTS patients is present in all pairs of time series. The edge overlaps for LQTS patients are larger, which indicates that the graphs from these time series are more similar in all the group.

Directed average edge overlap, *davo* (Eq. 14) equals zero for reversible signals, the greater the value of *davo*, the more

irreversible the signal, as the degree of layer similarity will vary depending on the direction of the passage of time. In the case of significant statistical differences, the davo obtained is, on the average, larger for LQTS patients (Figure 12), however we noticed this behavior only for the pair RR and DI intervals, where davo is much lower than for RR, QT and QT, DI intervals. The differences between groups observed in the case of average edge overlap are significantly reduced when davo is calculated, which indicates the level of irreversibility of the selected time series pairs.

For our data, only in the case of the comparison interlayer mutual information of the RR and QT intervals, we obtained statistically significant results (Figure 13). Interlayer mutual information was larger for the LQTS group.

5 Discussion and conclusion

It should be noted, that for the several measures presented above, we were able to obtain a statistical significance. This proves that the arrhythmogenic substrate manifests itself in irreversibility measures, which is the research hypothesis of this paper. This result encourages us to design a prospective study, in which the irreversibility measures will be correlated with the clinical findings in the follow-up period, to directly assess cardiac mortality. Irreversibility measures have proved themselves to be good candidates for such a study.

In this paper, we used signals divided into non-overlapping windows of length of 600 intervals. Such short cardiovascular series are processed to assess the short-term regulation of heart rate variability (Cohen and Taylor, 2002; Porta et al., 2009)

Summarizing the results of using VG for univariate time series, we obtained a statistically significant difference between the healthy and LQTS patients in the time irreversibility of QT intervals. The time irreversibility of QT intervals is larger for the healthy. This difference is larger for the maximum values of both KLD (Figure 9A) and JSD (Figure 9B). Moreover, using the Jensen-Shannon divergence gives a better group differentiation in this case. However, no significant difference between the groups was obtained for the heart rhythm. The choice of divergence is also important: changing from KLD to JSD results in a better differentiation of the groups (i.e., a lower p-value) for RR and QT intervals.

For multivariate time series, when the average edge overlap was analyzed, the connection patterns between RR and QT intervals were more like each other for the LQTS patients than for the healthy. However, when we introduce time irreversibility, namely in the form of directed average edge overlap, the results change. In this case, we did not obtain a statistically significant difference for pairs of the RR and QT and as well as the DI and QT intervals. Interlayer mutual information shows that the degree distributions between HVG obtained for the RR and QT intervals are more correlated for the LQTS patients. The presence of nonstationarities can affect the results for interlayer mutual information (Hoyer et al., 2005). Before analysis, trend-like nonstationarities were removed from the signals using EMD (Hoyer et al., 2005).

Jiang et al. (2013) found that the degree distribution of VG of RR intervals changes during meditation, which corresponds to an adjustment of the autonomous neural system. Here, we compare the difference in the degree distribution according to the direction and opposite to the direction of the time arrow. This difference used to calculate KLD does not change in LQTS subjects for the heart rate, whereas a difference between the groups occurs for QT intervals. On the contrary, multivariate methods show that the similarity of these dynamics in pairs of values is greater for individuals with LQTS, while after considering the opposite direction in time, i.e., estimating the irreversibility of such similarity, it turns out that the only difference is for the pair RR, DI where the direction of similarity is also preserved, i.e., it is greater for individuals with LQTS.

A direct comparison of the results obtained for different time series intervals can be difficult, because two systems, which have similar 1/f scaling may have different level of complexity (Ivanov et al., 2009). Ivanov et al. showed that comparing healthy people with a group with cardiopulmonary instability expresses different power-law scaling behavior (Ivanov et al., 1996). However, Mathias et al. performed a population study (Mathias et al., 2013), where 1,206 patients with LQTS were studied. The results shows that the estimated higher QTc (QT corrected for heart rate) intervals variation can be associated with a higher risk of cardiac events. This phenomenon depends on which gene was mutated and it is greatest for persons with LQTS1. In the case of QT, we observe lower values of KLD, i.e., a smaller level of irreversibility for patients with LQTS.

The measures presented in this paper do not allow a risk stratification in the LQTS group, due to insufficient patient information. However, knowing which of these parameters has the highest statistical power concerning distinguishing the groups, it is possible to define them as candidates for the identification of a clinical parameter to support the work of physicians, especially in the evaluation of SCD.

Data availability statement

Publicly available datasets were analyzed in this study. This data can be found here: The data analyzed in this study is subject to the following licenses/restrictions: Both data sets belong to the THEW Project (http://thew-project.org/databases.htm) available upon registration. Requests to access these datasets should be directed to http://thew-project.org/databases.htm.

Ethics statement

Ethical review and approval was not required for the study on human participants in accordance with the local legislation and institutional requirements. The patients/participants provided their written informed consent to participate in this study.

Author contributions

All the calculations and figures, as well as the basic structure of the paper were done by MA. The data and consultation on the use of data in the research were provided by KR and MO. General supervising and basic structure of manuscript were prepared by JZ. RB was medical science supervisor.

Funding

Research was funded by (POB Biotechnology and Biomedical Engineering) of Warsaw University of Technology within the Excellence Initiative: Research University (IDUB) program 1820/16/Z01/POB4/2021.

Acknowledgments

We are grateful to all members, especially Teodor Buchner and Monika Petelczyc, of our Cardiovascular Physics Group for fruitful discussions.

Conflict of interest

The authors declare that the research was conducted in the absence of any commercial or financial relationships that could be construed as a potential conflict of interest.

Publisher's note

All claims expressed in this article are solely those of the authors and do not necessarily represent those of their affiliated organizations, or those of the publisher, the editors and the reviewers. Any product that may be evaluated in this article, or claim that may be made by its manufacturer, is not guaranteed or endorsed by the publisher.

References

Agliari, E., Pachon, A., Rodriguez, P. M., and Tavani, F. (2017). Phase transition for the Maki-Thompson rumour model on a small-world network. *J. Stat. Phys.* 169, 846–875. doi:10.1007/s10955-017-1892-x

Alarcón-Ramos, L. A., Bernal Jaquez, R., and Schaum, A. (2018). Output-feedback control of virus spreading in complex networks with quarantine. *Front. Appl. Math. Stat.* 4, 34. doi:10.3389/fams.2018.00034

Chladekova, L., Czippelova, B., Turianikova, Z., Tonhajzerova, I., Calkovska, A., Baumert, M., et al. (2012). Multiscale time irreversibility of heart rate and blood pressure variability during orthostasis. *Physiol. Meas.* 33, 1747–1756. doi:10.1088/0967-3334/33/10/1747

Cohen, M. A., and Taylor, J. A. (2002). Short-term cardiovascular oscillations in man: Measuring and modelling the physiologies. *J. Physiol.* 542, 669–683. doi:10.1113/jphysiol.2002.017483

Costa, M., Goldberger, A. L., and Peng, C. K. (2005). Broken asymmetry of the human heartbeat: Loss of time irreversibility in aging and disease. *Phys. Rev. Lett.* 95, 198102–198105. doi:10.1103/PhysRevLett.95.198102

Fiskum, C., Andersen, T. G., Bornas, X., Aslaksen, P. M., Flaten, M. A., and Jacobsen, K. (2018). Non-linear heart rate variability as a discriminator of internalizing psychopathology and negative affect in children with internalizing problems and healthy controls. *Front. Physiol.* 9, 561. doi:10.3389/fphys.2018.00561

Gaspard, P. (2004). Time-reversed dynamical entropy and irreversibility in markovian random processes. *J. Stat. Phys.* 117, 599–615. doi:10.1007/s10955-004-3455-1

Gierałtowski, J., Zebrowski, J. J., and Baranowski, R. (2012). Multiscale multifractal analysis of heart rate variability recordings with a large number of occurrences of arrhythmia. *Phys. Rev. E Stat. Nonlin. Soft Matter Phys.* 85, 021915–021916. doi:10.1103/PhysRevE.85.021915

Goldenberg, I., Horr, S., Moss, A. J., Lopes, C. M., Barsheshet, A., McNitt, S., et al. (2011). Risk for life-threatening cardiac events in patients with genotype-confirmed long-QT syndrome and normal-range corrected QT intervals. *J. Am. Coll. Cardiol.* 57, 51–59. doi:10.1016/j.jacc.2010.07.038

Hoyer, D., Pompe, B., Chon, K. H., Hardraht, H., Wicher, C., and Zwiener, U. (2005). Mutual information function assesses autonomic information flow of heart rate dynamics at different time scales. *IEEE Trans. Biomed. Eng.* 52, 584–592. doi:10.1109/TBME.2005.844023

Iacovacci, J., and Lacasa, L. (2016). Sequential motif profile of natural visibility graphs. *Phys. Rev. E* 94, 052309. doi:10.1103/PhysRevE.94.052309

Ivanov, P. C., Ma, Q. D. Y., Bartsch, R. P., Hausdorff, J. M., Nunes Amaral, L. A., Schulte-Frohlinde, V., et al. (2009). Levels of complexity in scale-invariant neural signals. *Phys. Rev. E Stat. Nonlin. Soft Matter Phys.* 79, 041920. doi:10.1103/PhysRevE.79.041920

Ivanov, P., Rosenblum, M., Peng, C. K., Mietus, J., Havlin, S., Eugene Stanley, H., et al. (1996). Scaling behaviour of heartbeat intervals obtained by wavelet-based time-series analysis. *Nature* 383, 323–327. doi:10.1038/383323a0

Jandackova, V. K., Scholes, S., Britton, A., and Steptoe, A. (2016). Are changes in heart rate variability in middle-aged and older people normative or caused by pathological conditions? Findings from a large population-based longitudinal cohort study. *J. Am. Heart Assoc.* 5, e002365. doi:10.1161/JAHA.115.002365

Jiang, S., Bian, C., Ning, X., and Ma, Q. D. Y. (2013). Visibility graph analysis on heartbeat dynamics of meditation training. *Appl. Phys. Lett.* 102, 253702. doi:10.1063/1.4812645

Jose, A. D., and Taylor, R. R. (1969). Autonomic blockade by propranolol and atropine to study intrinsic myocardial function in man. *J. Clin. Invest.* 48, 2019–2031. doi:10.1172/JCI106167

Keeling, M. J., and Eames, K. T. D. (2005). Networks and epidemic models. *J. R. Soc. Interface* 2, 295–307. doi:10.1098/rsif.2005.0051

Lacasa, L., and Flanagan, R. (2015). Time reversibility from visibility graphs of nonstationary processes. *Phys. Rev. E Stat. Nonlin. Soft Matter Phys.* 92, 022817. doi:10.1103/PhysRevE.92.022817

Lacasa, L., Luque, B., Ballesteros, F., Luque, J., and Nuno, J. C. (2008). From time series to complex networks: The visibility graph. *Proc. Natl. Acad. Sci.* 105 (13), 4972. doi:10.1073/pnas.0709247105

Lacasa, L., Mariño, I. P., Miguez, J., Nicosia, V., and Gómez-Gardeñes, J. (2017). Identifying the hidden multiplex architecture of complex systems. 1-8. Available at: http://arxiv.org/abs/1705.04661 (Accessed October 01, 2017).

Lacasa, L., Nicosia, V., and Latora, V. (2015). Network structure of multivariate time series. *Sci. Rep.* 5, 15508–15509. doi:10.1038/srep15508

Lacasa, L., Nuñez, A., Roldán, E., Parrondo, J. M. R., and Luque, B. (2012). Time series irreversibility: A visibility graph approach. *Eur. Phys. J. B* 85, 217. doi:10.1140/epjb/e2012-20809-8

Li, Y., Li, J., Liu, J., Xue, Y., Cao, Z., and Liu, C. (2021). Variations of time irreversibility of heart rate variability under normobaric hypoxic exposure. *Front. Physiol.* 12, 607356. doi:10.3389/fphys.2021.607356

Lin, J. (1991). Divergence measures based on the shannon entropy. *IEEE Trans. Inf. Theory* 37, 145–151. doi:10.1109/18.61115

Marcus, B., Gillette, P. C., and Garson, A. (1990). Intrinsic heart rate in children and young adults: An index of sinus node function isolated from autonomic control. *Am. Heart J.* 119 (4), 911–916. doi:10.1016/s0002-8703(05)80331-x

Mason, O., and Verwoerd, M. (2007). Graph theory and networks in biology. *IET Syst. Biol.* 1, 89–119. doi:10.1049/iet-syb:20060038

Mathias, A., Moss, A. J., Lopes, C. M., Barsheshet, A., McNitt, S., Zareba, W., et al. (2013). Prognostic implications of mutation-specific QTc standard deviation in congenital long QT syndrome. *Heart* 10, 720–725. doi:10.1016/j.hrthm.2013.01.032

Nielsen, F. (2020). On a generalization of the jensen-shannon divergence and the jensen-shannon centroid. *Entropy* 22, E221. doi:10.3390/e22020221

Oehlers, M., and Fabian, B. (2021). Graph metrics for network robustness—A survey. *Mathematics* 9, 895. doi:10.3390/math9080895

Opthof, T. (2000). The normal range and determinants of the intrinsic heart rate in man. *Cardiovasc. Res.* 45, 177–184. doi:10.1016/S0008-6363(99)00322-3

Ozimek, M., Żebrowski, J. J., and Baranowski, R. (2021). Information flow between heart rhythm, repolarization, and the diastolic interval series for healthy individuals and LQTS1 patients. *Front. Physiol.* 12, 611731–611739. doi:10.3389/fphys.2021.611731

Parrondo, J. M. R., van den Broeck, C., and Kawai, R. (2009). Entropy production and the arrow of time. *New J. Phys.* 11, 073008. doi:10.1088/1367-2630/11/7/073008

Piskorski, J., and Guzik, P. (2007). Geometry of the Poincaré plot of RR intervals and its asymmetry in healthy adults. *Physiol. Meas.* 28, 287–300. doi:10.1088/0967-3334/28/3/005

Porta, A., Casali, K. R., Casali, A. G., Gnecchi-Ruscone, T., Tobaldini, E., Montano, N., et al. (2008). Temporal asymmetries of short-term heart period variability are linked to autonomic regulation. *Am. J. Physiol. Regul. Integr. Comp. Physiol.* 295, 550–R557. doi:10.1152/ajpregu.00129.2008

Porta, A., D'addio, G., Bassani, T., Maestri, R., and Pinna, G. D. (2009). Assessment of cardiovascular regulation through irreversibility analysis of heart period variability: A 24 hours holter study in healthy and chronic heart failure populations. *Philos. Trans. A Math. Phys. Eng. Sci.* 367, 1359–1375. doi:10.1098/rsta.2008.0265

Prigogine, I. (1978). Time, structure, and fluctuations. *Science* 201, 777–785. doi:10.1126/science.201.4358.777

W. Samek, G. Montavon, A. Vedaldi, L. K. Hansen, and K.-R. Müller (Editors) (2019). *Explainable AI: Interpreting, explaining and visualizing deep learning* (Cham: Springer International Publishing). doi:10.1007/978-3-030-28954-6

Schwartz, P. J., Crotti, L., and Insolia, R. (2012). Long-QT syndrome from genetics to management. *Circ. Arrhythm. Electrophysiol.* 563, 868–877. doi:10.1161/circep.111.962019

Seebohm, G., Strutz-Seebohm, N., Ureche, O. N., Henrion, U., Baltaev, R., MacK, A. F., et al. (2008). Long QT syndrome-associated mutations in KCNQ1 and KCNE1 subunits disrupt normal endosomal recycling of IKs channels. *Circ. Res.* 103, 1451–1457. doi:10.1161/CIRCRESAHA.108.177360

Seely, A. J. E., and Macklem, P. (2012). Fractal variability: An emergent property of complex dissipative systems. *Chaos* 22, 013108. doi:10.1063/1.3675622

Stallone, A., Cicone, A., and Materassi, M. (2020). New insights and best practices for the successful use of Empirical Mode Decomposition, Iterative Filtering and derived algorithms. *Sci. Rep.* 10, 15161. doi:10.1038/s41598-020-72193-2

Suboh, M. Z., Jaafar, R., Nayan, N. A., and Harun, N. H. (2019). ECG-based detection and prediction models of sudden cardiac death: Current performances and new perspectives on signal processing techniques. *Int. J. Onl. Eng.* 15, 110–126. doi:10.3991/ijoe.v15i15.11688

University of Rochester Medical Center (2022). Congential long QT syndrome. Available at: http://thew-project.org/Database/E-HOL-03-0480-013.html (Accesses December 01, 2018).

University of Rochester Medical Center Healthy Individuals (2022). Healthy individuals - telemetric and holter ECG warehouse. Available at: http://thew-project.org/Database/E-HOL-03-0202-003.html (Accesses December 01, 2018).

Vijayakumar, R., Silva, J. N. A., Desouza, K. A., Abraham, R. L., Strom, M., Sacher, F., et al. (2014). Electrophysiologic substrate in congenital long QT syndrome: Noninvasive mapping with electrocardiographic imaging (ECGI). *Circulation* 130, 1936–1943. doi:10.1161/CIRCULATIONAHA.114.011359

Wilde, A. A. M., Jongbloed, R. J. E., Doevendans, P. A., Düren, D. R., Hauer, R. N. W., van Langen, I. M., et al. (1999). Auditory stimuli as a trigger for arrhythmic events differentiate HERG- related (LQTS2) patients from KVLQT1-related patients (LQTS1). *J. Am. Coll. Cardiol.* 33, 327–332. doi:10.1016/S0735-1097(98)00578-6

Zanin, M., and Papo, D. (2021). Algorithmic approaches for assessing irreversibility in time series: Review and comparison. *Entropy* 23, 1474. doi:10.3390/e23111474

Żebrowski, J. J., Kowalik, I., Orłowska-Baranowska, E., Andrzejewska, M., Baranowski, R., and Gierałtowski, J. (2015). On the risk of aortic valve replacement surgery assessed by heart rate variability parameters. *Physiol. Meas.* 36, 163–175. doi:10.1088/0967-3334/36/1/163

frontiers | Frontiers in Network Physiology

TYPE Original Research
PUBLISHED 07 October 2022
DOI 10.3389/fnetp.2022.943239

OPEN ACCESS

EDITED BY
Plamen Ch. Ivanov,
Boston University, United States

REVIEWED BY
Alessio Perinelli,
University of Trento, Italy
Fumikazu Miwakeichi,
Institute of Statistical Mathematics (ISM), Japan

*CORRESPONDENCE
Toshihiro Tanizawa,
toshihiro_tanizawa@mail.toyota.co.jp

SPECIALTY SECTION
This article was submitted to Systems Interactions and Organ Networks, a section of the journal Frontiers in Network Physiology

RECEIVED 13 May 2022
ACCEPTED 08 September 2022
PUBLISHED 07 October 2022

CITATION
Tanizawa T and Nakamura T (2022), Detecting the relationships among multivariate time series using reduced auto-regressive modeling.
Front. Netw. Physiol. 2:943239.
doi: 10.3389/fnetp.2022.943239

Detecting the relationships among multivariate time series using reduced auto-regressive modeling

Toshihiro Tanizawa[1]* and Tomomichi Nakamura[2]

[1]Data Analysis Group, InfoTech, Connected Advanced Development Division, Toyota Motor Corporation, Tokyo, Japan, [2]Graduate School of Information Science, University of Hyogo, Kobe, Japan

An information theoretic reduction of auto-regressive modeling called the Reduced Auto-Regressive (RAR) modeling is applied to several multivariate time series as a method to detect the relationships among the components in the time series. The results are compared with the results of the transfer entropy, one of the common techniques for detecting causal relationships. These common techniques are pairwise by definition and could be inappropriate in detecting the relationships in highly complicated dynamical systems. When the relationships between the dynamics of the components are linear and the time scales in the fluctuations of each component are in the same order of magnitude, the results of the RAR model and the transfer entropy are consistent. When the time series contain components that have large differences in the amplitude and the time scales of fluctuation, however, the transfer entropy fails to detect the correct relationships between the components, while the results of the RAR modeling are still correct. For a highly complicated dynamics such as human brain activity observed by electroencephalography measurements, the results of the transfer entropy are drastically different from those of the RAR modeling.

KEYWORDS

multivariate time series, statistical modeling, transfer entropy, model selection, auto-regressive models

1 Introduction

To understand the dynamical properties of any complicated systems including those in physiology, we have to analyze a set of signals generated by the system under consideration, varying in time and interrelated with each other, which is referred to as multivariate time series. Though it is surely important to understand the time dependence of each component of the time series separately, it is also crucial to detect the directed relationships among the components, in which the structure and functionality of the system are partially embodied. In many cases including those in physiology, however, the system is so complicated that we have no theoretical argument to identify the relationships from the first principle and we have to detect them only from observed data.

There are several common techniques for such detection. Among them, the Granger causality is probably the most classical and well-known [Granger (1969)]. This technique tries to detect causal relationship between two components from the improvement of prediction errors of the one of the two components by including the signals of the other component. Other techniques, such as the Directed Transfer Function [Kamiński and Blinowska (1991); Kamiński et al. (2001)] or Partial Directed Coherence [Baccalá and Sameshima (2001)] are based on the Vector Auto-Regressive (VAR) model with the coefficients transformed into the frequency domain to investigate the spectral properties. Schreiber (2000) has introduced another measure to detect the relationships called transfer entropy by an extension of the concept of mutual information.

An important feature of these techniques is that they are pairwise measures. In other words, these measures are calculated by taking all pairwise combinations out of a set of the components contained in the time series. It is not obvious, however, whether the relationships among components more than three can always be broken into pairwise relationships. For instance, let us consider the case in which two pairs of components, (A, B) and (A, C), are directly related within each pair. Despite that there is no direct relationship between B and C, the pairwise measure would detect a non-zero value of indirect relationship *via* A and we need an appropriately chosen threshold to determine the acceptance of this relationship. Though there are several procedures such as the surrogate data method (Theiler et al. 1992) in choice of the threshold value, it would be preferable if we have a method that enables us to extract the direct relationships from an entire set of components without pairwise break-up and threshold.

When the number of components are large (~ 100), it is clear that using pairwise measures is impractical. Relating to this point, Papana et al. (2021) have recently published a comparative study of various causality measures in the time domain aiming at detecting direct causality in multivariate time series. The main focus of the authors is the detectability of the causality measures of direct relationships among multivariate time series of components as many as 100. The authors thus compare causality measures with various dimension reduction techniques, such as subset regression (Breiman 1995; Yang and Wu 2016), model reduction (Brüggemann 2003; Shojaie and Michailidis 2010; Siggiridou and Kugiumtzis 2016), and non-uniform embedding (Vlachos and Kugiumtzis 2010; Faes et al. 2011; Kugiumtzis 2013).

In this article, we investigate multivariate time series of a moderate number of components up to 10 and show that pairwise measures such as transfer entropy might fail in detecting relationships among components even for time series of this relatively small number of components. As a technique that enables us to extract relationships from an entire set of components without pairwise break-up and threshold, we take the Reduced Auto-Regressive (RAR) modeling firstly proposed by Judd and Mees (1995) and compare the results to those of the transfer entropy proposed by Schreiber (2000), which is one of the commonest pairwise measures in the time domain.

This article is organized as follows. In Section 2, we describe the RAR modeling technique and the transfer entropy after setting the mathematical notations. In Section 3, we apply the RAR modeling technique to two artificial systems, both of which are three-component time series defined by linear equations. The results are compared to the values of transfer entropy and it is shown that the transfer entropy cannot detect correct relationships when the time series contains different time scales in fluctuation, even when the signals are generated by linear equations. In Section 4, we apply the RAR modeling technique to a set of electroencephalography (EEG) data composed of 10 channels and compare the results with those of the transfer entropy. Discussion and Summary are in Section 5.

2 Theoretical backgrounds

2.1 Multivariate time series

We consider a set of multivariate time series, $X = \{\mathbf{x}(t)\}_{t=0}^{N-1} = \{\mathbf{x}(0), \mathbf{x}(1), \ldots, \mathbf{x}(N-1)\}$, where $\mathbf{x}(t) = (x_0(t), x_1(t), \ldots, x_{M-1}(t))^T$ is a column vector composed from M signals generated from a system under consideration at discrete time t with equal intervals. The superscript T stands for taking the transpose. Throughout this article, we consider multivariate time series observed at an equal time interval and the source that generates the i-th signal is referred to as the i-th component in this article. In time series, the signals at the present time are related to the signals of at some previous time called "lag". In this article, we are also interested in the relationships among the components. For example, if the present signal of component i is determined by previous values of other components, say, 1, 3, 6, at lag 2, 1, 5, respectively, we expect that there might be a mathematical expression

$$x_i(t) = f(x_1(t-2), x_3(t-1), x_6(t-5)), \tag{1}$$

where f is a function that determines the relationship, which might be potentially non-linear. It should be emphasized that, in this article, the term "relationship" is used only in this meaning and we do not discriminate whether the relationship is "causal" or "correlational".

2.2 Reduced auto-regressive model

The time series modeling for multivariate time series, $\{\mathbf{x}(t)\}_{t=0}^{N-1}$, attempts to represent the present state of the time series $\mathbf{x}(t)$ by functions of the past states, $\{\mathbf{x}(t-1), \mathbf{x}(t-2), \ldots\}$,

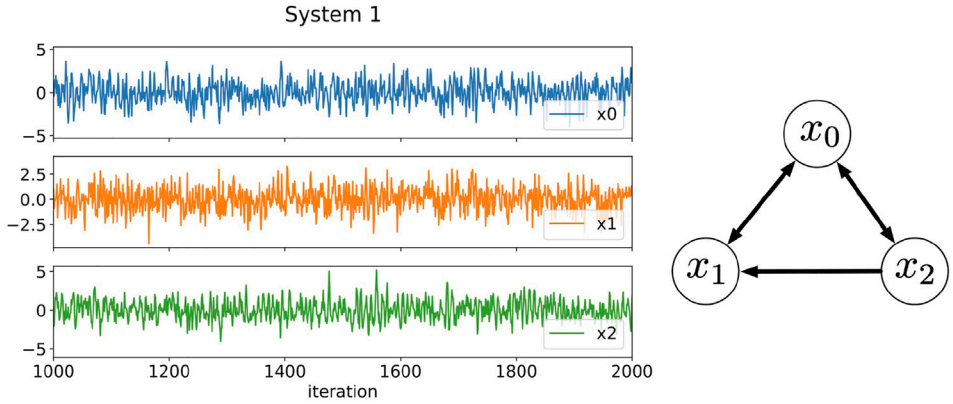

FIGURE 1
Three-component time series data generated by Eqs. 16–18 and the relationships among the components. The plotted data are a part of results from 1,000 to 2000 iterations. In System 1, the time scales of the fluctuations of each component are in the same order of magnitude.

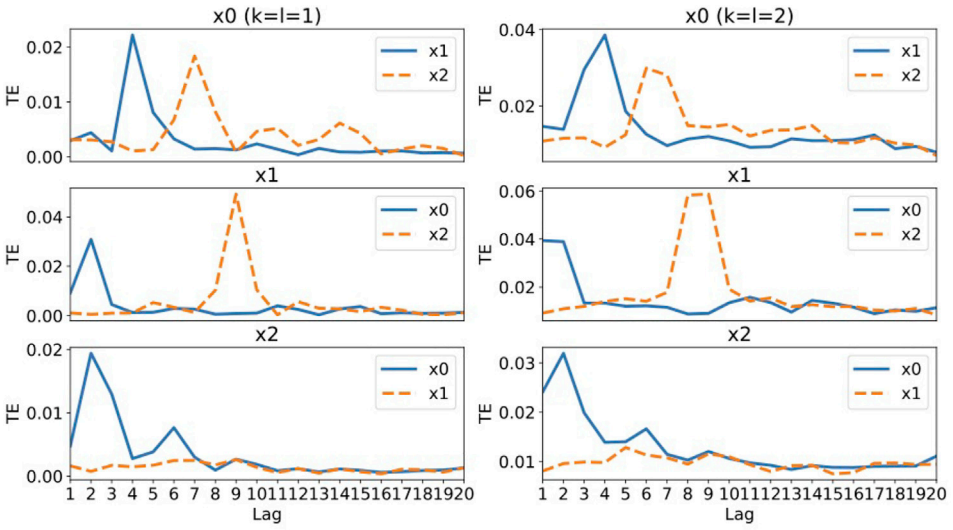

FIGURE 2
The values of transfer entropy of each component from other components for time delay (lag) up to 20. We plot the values for $k = l = 1$ in the left column and the values for $k = l = 2$ in the right column for comparison. A large value of transfer entropy indicates that a large amount of information gain exists at the lag from the corresponding components.

$$x_i(t) = f_i(\mathbf{x}(t-1), \mathbf{x}(t-2), \ldots, \mathbf{x}(t-L)) \quad (i = 0, 1, \ldots, M-1), \tag{2}$$

for each i-th component, where we denote the maximum time delay (lag) as L. When the underlying dynamics of the system generating the multivariate time series is unknown, choosing an appropriate function form, f_i, for each component and an appropriate value of the maximum lag, L, in practice are no trivial tasks and necessarily become heuristic. In this article, we limit ourselves to the function form in Eq. 2 to be linear with respect to their arguments. This limitation might be considered as a drawback, since quite a few time series data generated by real-world systems are potentially non-linear. Tanizawa et al. (2018) have shown, however, that, even for the case in which the time series data are non-linearly distorted, the linear modeling technique can identify the built-in periodicities correctly. We thus believe that linear modeling has a rather wide range of applicability if the non-linearity is not so strong as to induce the

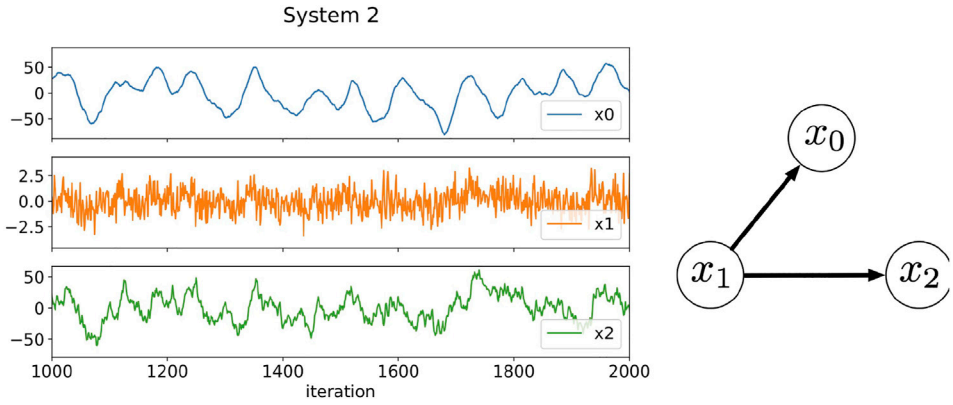

FIGURE 3
Three-component time series data generated by Eqs. 22–24 and the relationships among the components. The plotted data are a part of results from 1,000 to 2000 iterations. In this artificial system, the time scales in the fluctuations of each component are different: Component x_0 fluctuates slowly, component x_1 fluctuates rapidly, and component x_2 fluctuates intermediately.

dynamics to be chaotic and if the relationships and periodicities built in the time series are sufficiently retained. In linear modeling, the value of the i-th component at time t is represented as

$$x_i(t) = a_{i,0} + \sum_{j,k} a_{i,j,k}\, x_j\left(t - l_{i,j,k}\right) + \varepsilon_i(t) \quad (i = 0, 1, \ldots, M-1), \tag{3}$$

where $a_{i,0}$ is the constant term in the modeling of the i-th component, which is allowed to vanish and $\varepsilon_i(t)$ is a dynamic noise, which is an independently and identically distributed Gaussian random variable with mean zero and finite variance at t. Apart from the constant term, the value of the i-th component at present time is represented by a linear combination of the values of other components, $x_j(t - l_{i,j,k})$, at previous time with lag $l_{i,j,k}$ and parameter $a_{i,j,k}$. The subscripts of the lags and the parameters, $\{i, j, k\}$, indicate that they appear in the modeling of the i-th components with the term of the j-th component at the k-th lag. If we take all the terms $x_j(t - l)$ $(j = 0, 1, \ldots, M-1; l = 1, 2, \ldots, L)$ up to the maximum lag L, this model is identical to the Vector Auto-Regressive (VAR) model.

Here we take another model, which is an information theoretic reduction of linear models and referred to as the Reduced Auto-Regressive (RAR) model [Judd and Mees (1995; 1998)]. The RAR model extracts a subset of terms that are most relevant for describing the behaviors of the multivariate time series selected by a suitably chosen information criterion.

To be concrete, let us assume that we have a set of observed values of four-component multivariate time series, $\{x_i(0), x_i(1), \ldots, x_i(N-1)\}$ $(i = 0, 1, 2, 3)$, to be fitted in the linear form Eq. 3,

$$\hat{x}_i(t) = a_{i,0} + \sum_{j=0}^{3} \sum_{k} a_{i,j,k}\, x_j\left(t - l_{i,j,k}\right) \quad (i = 0, 1, 2, 3). \tag{4}$$

Here, we represent the value of the model for the i-th component at time t as $\hat{x}_i(t)$, while the observed value as $x_i(t)$. The terms $x_j(t - l_{i,j,k})$ included in the model are selected from a "pool of terms", which is called a "dictionary". For example, if we take the maximum lag as $L = 25$, the dictionary for the model of the i-th component contains 101 terms, which are

$$\begin{aligned}&\{1, x_0(t-1), \ldots, x_0(t-25), x_1(t-1), \ldots, x_1(t-25),\\ &x_2(t-1), \ldots, x_2(t-25), x_3(t-1), \ldots, x_3(t-25)\}\end{aligned} \tag{5}$$

with element 1 for the constant term. From this dictionary, we extract the optimal subset of terms and determine the values of parameters, a_{i0}, $a_{i,j,k}$ corresponding to the extracted terms by minimizing a suitably chosen information criterion.

Information criteria have a general form,

$$\begin{aligned}&(\text{Number of data}) \times \log(\text{Mean square prediction error})\\ &+ (\text{Penalty for the number of terms}).\end{aligned} \tag{6}$$

The mean square prediction error is the average of the squared norm of the prediction error vector, $\mathbf{e} = (x_i(0) - \hat{x}_i(0), x_i(1) - \hat{x}_i(1), \ldots, x_i(N-1) - \hat{x}_i(N-1))^T$, which represents the difference between the observed values and the values calculated from the model, Eq. 4. Since the observed values inevitably contain dynamical and observational noise, minimizing only the mean square prediction error leads to over-fitting and deteriorate the ability of the model in prediction. Information criteria compensate this deficiency with the penalty for the number of terms, which favors a small number of terms in the model. Among several

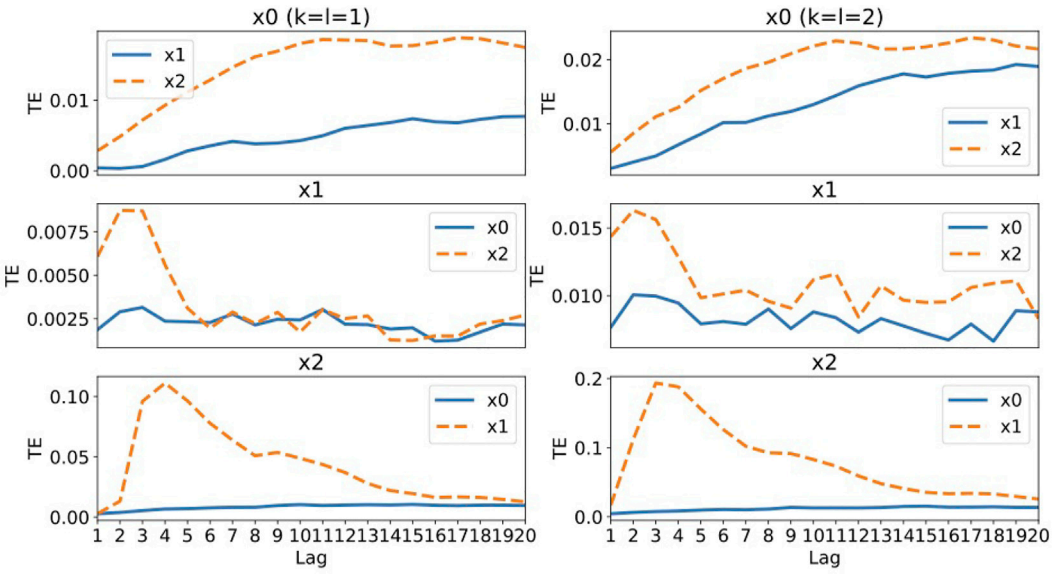

FIGURE 4
The values of transfer entropy of each component from other components for various values of time delay (lag) up to 20. We plot the values for $k = l = 1$ in the left column and the values for $k = l = 2$ in the right column for comparison. A large value of transfer entropy indicates that a large amount of information gain exists at the lag from the corresponding components.

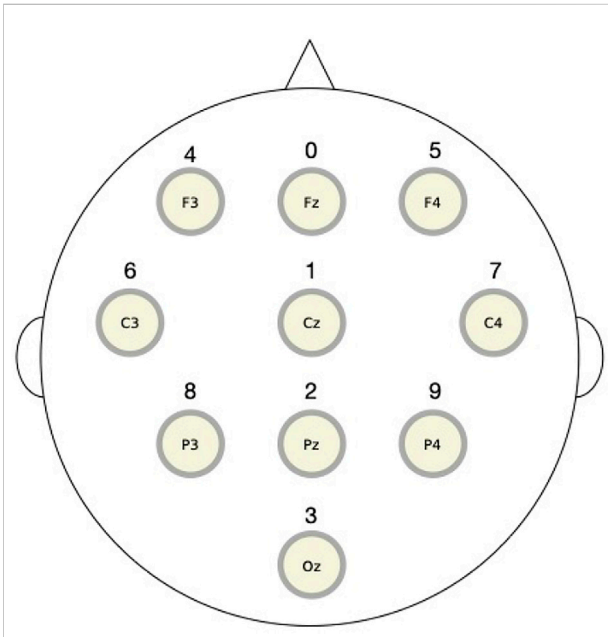

FIGURE 5
The placement of 10 electrodes in International 10–20 System for electroencephalography measurements. The top (bottom) is the front (back) direction of the head. The digits over the circles representing electrodes are the component numbers used in the RAR modeling.

information criteria proposed in the literature, we take the Description Length (DL) suitably modified by Judd and Mees (1995) as the information criterion in this article. This DL has proven to be effective even in modeling nonlinear dynamics and has fewer approximations than other information criteria (Judd and Mees (1998); Small and Judd (1999)). Assuming that the dynamic noise, $\varepsilon_i(t)$, in Eq. 2 is Gaussian, and the parameters, $a_{i,0}$ and $a_{i,j,l}$, are chosen to minimize the sum of squares of the prediction errors, $\mathbf{e}^T \cdot \mathbf{e}$, Judd and Mees have shown that the description length is bounded by

$$\mathrm{DL}(K) = \left(\frac{N}{2} - 1\right)\ln\frac{\mathbf{e}^T\mathbf{e}}{N} + (K-1)\left(\frac{1}{2} + \ln\gamma\right) - \sum_{i=1}^{K}\ln\delta_i, \quad (7)$$

where N is the length of the time series to be fitted, K is the number of the parameters that take non-zero values (or the model size), and the variables δ_i $(i = 1, 2, \ldots, k)$ can be interpreted as the relative precision to which the parameters are specified. For the details of the variables δ_i, see Judd and Mees (1995) and Judd and Mees (1998). The number γ is a constant and typically fixed to be $\gamma = 32$ for choosing a small model size K.

To extract the optimal subset to minimize $\mathrm{DL}(K)$ from the dictionary of terms, we have to resort a practical selection algorithm, since the exhaustive search is an NP-hard problem when the dictionary contains over a dozen of terms. In this article, we adopt an algorithm proposed by Nakamura et al.

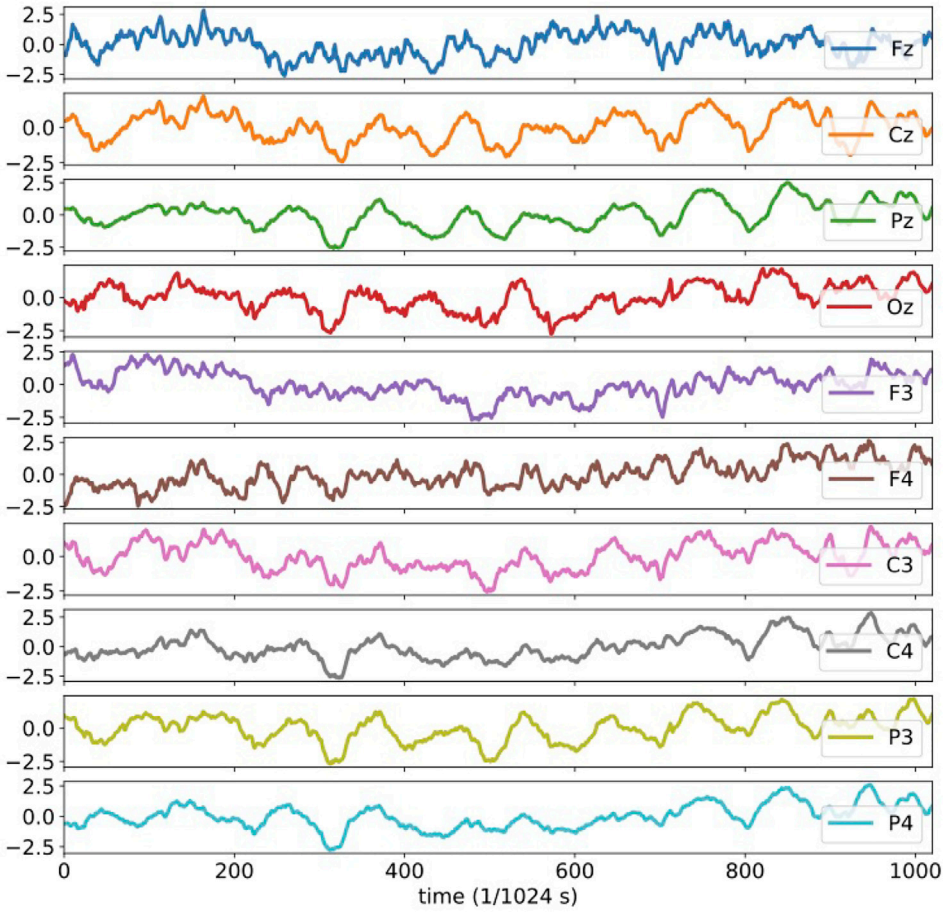

FIGURE 6
The plots of the 10 channel electroencephalography signals analyzed in the present section. All plotted data are normalized and dimensionless.

(2004). Instead of the exhaustive search, this algorithm begins from identifying the model of the shortest size, $K = 1$, then we look for the term to be added to obtain a smaller value of DL. The model size thus become larger one-by-one until DL ceases to decrease, which is called the bottom-up method. To avoid to be trapped in a local minimum, we proceed a little further to increase the model size, K, and then go back to decrease the model size one-by-one until DL ceases to decrease, which is called the top-down method. We repeat these bottom-up and top-down methods until the optimal models in two methods coincide with each other. Nakamura et al. (2004) have proven that this algorithm is able to obtain better models in most cases than other algorithms with reasonable computation time.

A typical result of RAR modeling takes the form

$$\hat{x}_0(t) = 1.34 + 0.39x_0(t-1) - 0.20x_0(t-3) + 0.31x_1(t-4) + 0.20x_3(t-7), \tag{8}$$

which includes only the terms, $x_0(t-1)$, $x_0(t-3)$, $x_1(t-4)$, and $x_3(t-7)$, in the dictionary. The RAR model thus includes only terms of relevant components and lags, which is the most important difference between the RAR model and the VAR model. Due to this difference, we are able to identify the directed relationships among components in multivariate time series. For instance, Eq. 8 implies that component x_0 is affected by x_1 and x_3 apart from x_0 itself. It should also be emphasized that there are strong information theoretic arguments to support that the RAR model can detect any periodicities built into given time series [Small and Judd (1999)].

2.3 Transfer entropy

Transfer entropy is an information theoretic measure for quantifying the information flow between two univariate time series, which we denote here as $\{\ldots, x(0), x(1), \ldots, x(N-1), \ldots\}$and

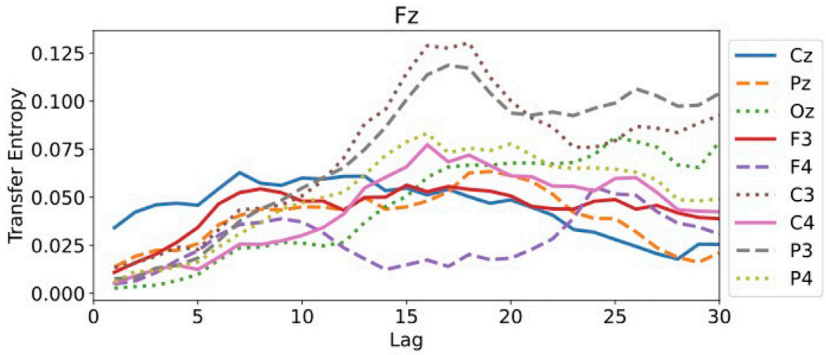

FIGURE 7
The values of transfer entropy of component Fz from other components with respect to the lags up to 30. All values are in the same order of magnitude and do not show distinct peaks.

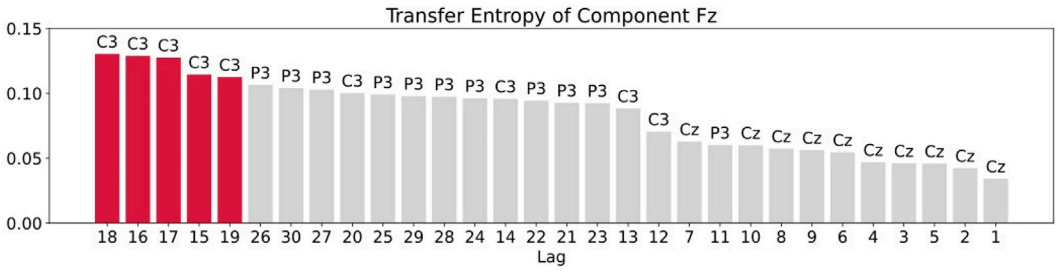

FIGURE 8
Plot of the components and the maximum values of transfer entropy of component Fz for each lag up to 30 sorted in the descending order of the values of transfer entropy. The red bars are the top five values of transfer entropy. For component Fz, all top five values come from component C3.

$\{\ldots, \tilde{x}(0), \tilde{x}(1), \ldots, \tilde{x}(N-1), \ldots\}$. They are not necessarily related to each other. Let us assume that the values $x(t)$ and $\tilde{x}(t)$ at each time t are independent draws from two discrete stochastic variables, $X = (x_0, \ldots, x_i, \ldots, x_{I-1})$ and $\tilde{X} = (\tilde{x}_0, \ldots, \tilde{x}_j, \ldots, \tilde{x}_{J-1})$, respectively, as the simplest example. It is well known in information theory that the average number of bits needed to optimally encode independent draws from X is given by the Shannon entropy $H_X = -\sum_{i=0}^{I-1} P(x_i)\log_2 P(x_i)$, where $P(x_i)$ is the probability for $X = x_i$. The extra information gain of the state of $X = x_i$ by obtaining the state of $\tilde{X}$ is measured by the entropy decrease

$$\Delta H_{X\leftarrow\tilde{X}}(x_i) = -P(x_i)\log_2 P(x_i) - \sum_{j=0}^{J-1} P\left(\tilde{x}_j\right) P\left(x_i|\tilde{x}_j\right) \left(-\log_2 P\left(x_i|\tilde{x}_j\right)\right) \quad (9)$$

$$= \sum_{j=0}^{J-1} P\left(x_i, \tilde{x}_j\right) \log_2 \frac{P\left(x_i|\tilde{x}_j\right)}{P(x_i)}, \quad (10)$$

where $P(x_i, \tilde{x}_j)$ is the joint probability for $(X, \tilde{X}) = (x_i, \tilde{x}_j)$ and $P(x_i|\tilde{x}_j) = P(x_i, \tilde{x}_j)/P(\tilde{x}_j)$ is the conditional probability for $X = x_i$ under the condition of $\tilde{X} = \tilde{x}_j$. Finally the total information gain of X by the knowledge of $\tilde{X}$ is obtained by the summation over x_i, which is

$$\Delta H_{X\leftarrow\tilde{X}} = \sum_{i=0}^{I-1} \Delta H_{X\leftarrow\tilde{X}}(x_i) = \sum_{i=0}^{I-1}\sum_{j=0}^{J-1} P\left(x_i, \tilde{x}_j\right) \log_2 \frac{P\left(x_i|\tilde{x}_j\right)}{P(x_i)}. \quad (11)$$

Noticing that

$$\frac{P\left(x_i|\tilde{x}_j\right)}{P(x_i)} = \frac{P\left(x_i, \tilde{x}_j\right)}{P(x_i)P\left(\tilde{x}_j\right)}, \quad (12)$$

we see that the information gain in this simplest case is symmetric with respect to X and $\tilde{X}$ and measures the mutual correlation between X and $\tilde{X}$.

Schreiber (2000) extended this concept to the directional information flow between two time series. As time series data have correlation in time direction, the joint probability of signals between different times, $P(x(t), x(t'))$ cannot be separated as the product, $P(x(t)) \cdot P(x(t'))$. By taking this feature into consideration, Schreiber defined the transfer entropy from $\tilde{X}$

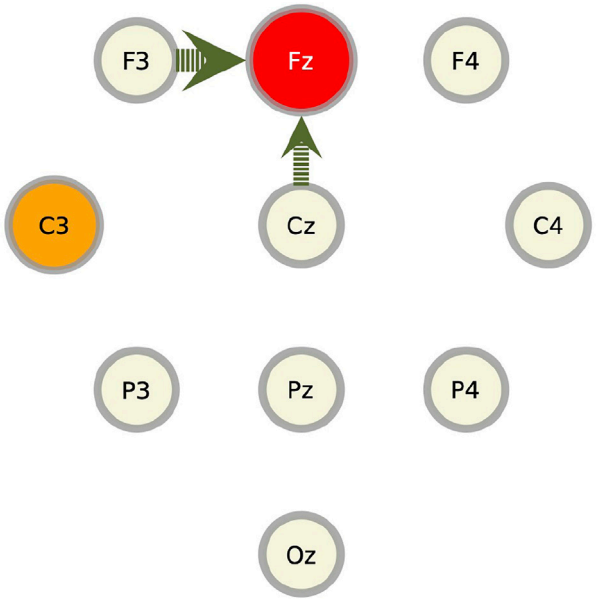

FIGURE 9
Pictorial summary of the results of the RAR model and the transfer entropy for component Fz. The target component Fz is represented by the red circle. The circles from which the arrows emanate, which are Cz and F3, represent the components contained in the RAR model with the width of the arrows being proportional to the number of appearance of the component in the RAR model. For the case of component Fz, component Cz appears two times and component F3 appears three times. The orange circles represent the components that give the top 5 values of transfer entropy for each lag, which is only C3.

to X as the information gain of the time series X by obtaining the values of $\tilde{X}$, which is

$$T_{X\leftarrow\tilde{X}}(L,k,l)=\sum_{t=0}^{N-1}P\left(x(t+L),x_t^{(k)},\tilde{x}_t^{(l)}\right)\log_2\frac{P\left(x(t+L)|x_t^{(k)},\tilde{x}_t^{(l)}\right)}{P\left(x(t+L)|x_t^{(k)}\right)}, \tag{13}$$

where

$$x_t^{(k)}=\{x(t-k+1),x(t-k+2),\ldots,x(t)\}, \tag{14}$$

$$\tilde{x}_t^{(l)}=\{\tilde{x}(t-l+1),\tilde{x}(t-l+2),\ldots,\tilde{x}(t)\}. \tag{15}$$

Here we slightly extend the definition by Schreiber to include the time difference L that can be a positive integer larger than one to measure the effect of time delay in information flow.

The transfer entropy is non-negative and becomes zero when X and $\tilde{X}$ are statistically independent. For the values of k and l, the value $k=l=1$ is commonly used. In this article, we compare two cases for $k=l=1$ and $k=l=2$ in Section 3. It should be noted that the transfer entropy between two time series is asymmetric in X and $\tilde{X}$, which enables us to determine the directional relationship between these two time series. Another important point to be mentioned is that the transfer entropy is a pairwise quantity by definition. To investigate the directional relationships among multivariate time series whose components are more than three, we should calculate and compare the values of transfer entropy of all pairs in the components of the time series.

3 Experiments on artificial linear systems

In this section, we apply the RAR modeling technique to two artificial systems, both of which are represented by linear combinations of the terms of three components with various distinctive lags to investigate the directional relationship among the components and compare the results to the ones obtained from the calculated values of transfer entropy. The difference between these two time series is the time scales of fluctuations of each component. While the time scales of fluctuations of all components in the first system (System 1) are similar, the time scales in the second system (System 2) differ from each other.

3.1 System 1: A case with fluctuations in similar time scales

The time series of System 1 are generated by the following linear equations:

$$x_0(t)=0.4x_0(t-1)-0.2x_0(t-3)+0.3x_1(t-4)+0.2x_2(t-7)+\varepsilon_0(t), \tag{16}$$

$$x_1(t)=0.2x_0(t-2)+0.3x_2(t-9)+\varepsilon_1(t), \tag{17}$$

$$x_2(t)=0.2x_0(t-2)+0.5x_2(t-1)-0.3x_2(t-3)+\varepsilon_2(t), \tag{18}$$

where $\varepsilon_i(t)$ $(i=0,1,2)$ are the dynamic noise that are drawn from independently and identically distributed (IID) Gaussian random variables with mean zero and standard deviation 1.0. This system generates non-divergent signals. The time scales in the fluctuations of each component are in the same order of magnitude, as it can be seen in Figure 1. It should also be noted that component x_1 are generated by other components, x_0 and x_2 and not related to the previous values of x_1 itself. In Figure 1, the relationships among the components are also depicted.

We generate 10000 data points for each component of System 1 after sufficient number of iterations to erase initial value dependence to build the RAR model. In the modeling, we set the maximum time delay $L=25$. The dictionary contains therefore 76 terms, which are 25 terms for the three components plus one constant term. Having in mind that we build RAR models from electroencephalography data with 1,025 observations in Section 4, we divide these 10,000 data points into 10 intervals each of which contains 1,000 data points

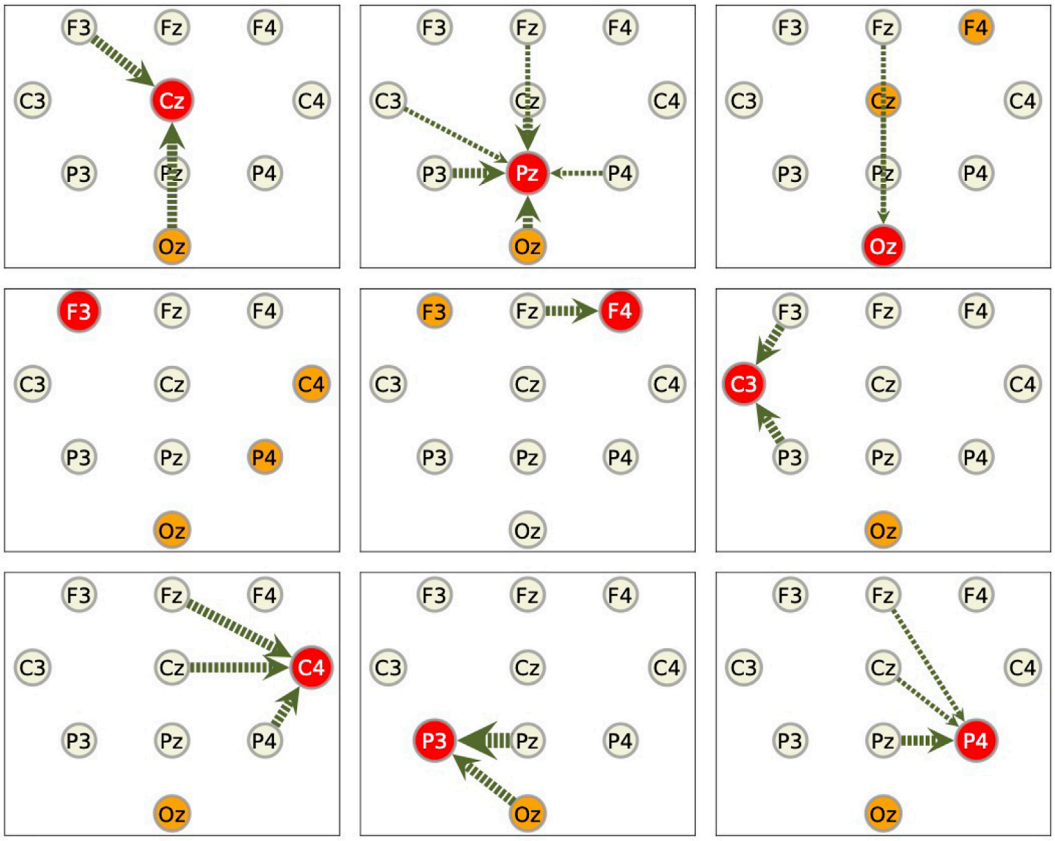

FIGURE 10
Summarized results for other components. Red circles represent the target components against which the RAR models are built. The arrows are the directed relationships indicated by the corresponding RAR models. The orange circles are the components that gives large values of transfer entropy to the target nodes. See the caption of Figure 9 for the details. Since the RAR model of component F3 contains only terms of F3 itself, there are no arrows in the picture for F3.

and compare the results of RAR modeling corresponding to each divided interval. The results are summarized as

$$\hat{x}_0(t) = 0.41\,(2)x_0(t-1) - 0.21\,(2)x_0(t-3) + 0.31\,(4)x_1(t-4) + 0.20\,(3)x_2(t-7), \tag{19}$$

$$\hat{x}_1(t) = 0.20\,(3)x_0(t-2) - 0.31\,(2)x_2(t-9), \tag{20}$$

$$\hat{x}_2(t) = 0.20\,(2)x_0(t-2) + 0.49\,(2)x_2(t-1) - 0.28\,(3)x_2(t-3). \tag{21}$$

The notation for the values of the parameters such as 0.41(2) represents that the mean value of the parameter of $x_0(t-1)$ over the models for 10 intervals is 0.41 with the standard deviation of 0.02. Notice that all terms included in the definitions, Eqs. 16–18, are recovered with correct values of parameters within appropriate statistical errors and contain no other unnecessary terms.

Figure 2 shows the values of transfer entropy calculated from the same data as used in the RAR modeling summarized in Eqs. 19–21, though all 10,000 data points for each component are used in this calculation. To see the effect of the values of k and l in the definition of transfer entropy, Eq. 13, we calculate the values for $k = l = 1$, which are most commonly used, and $k = l = 2$ for comparison.

Let us examine the results of for $k = l = 1$ (the left column of Figure 2). For component x_0, the large values of transfer entropy come from component x_1 at lag 4 and component x_3 at lag 7. Compared to the generator of x_0 defined by Eq. 16, these peaks are consistent with the terms $x_1(t-4)$ and $x_3(t-7)$ in the generator of x_0. For component x_1, peaks appear at lag 2 for component x_0 and at lag 9 for component x_2, which are also consistent with the terms $x_0(t-2)$ and $x_2(t-9)$ in the generator of x_1, Eq. 17. For component x_2, the large value of transfer entropy at lag 2 for component x_0 is consistent with the term $x_0(t-2)$ in Eq. 18, though there is another small peak at lag 6 for component x_0, which does not have any corresponding term in Eq. 18. The values for component x_1 are almost zero, which is reasonable, since component x_2 is independent of x_1. For the results of $k = l = 2$ (the right column of Figure 2), the behaviors are almost the same as those of $k = l = 1$ except that there appear

two consecutive peaks, since the correlation of $x(t+L)$ with $x(t)$, $x(t-1)$, $\hat{x}(t)$, and $\hat{x}(t-1)$ are taken into account for $k=l=2$. As it is also seen later in the results of another artificial system, Figure 4, taking $k=l=1$ would be sufficient for the purpose of identifying the directional relationships among components in time series. For the case of System 1, in which the time scales of the fluctuations of each components are in the same order of magnitude, transfer entropy is able to detect the correct relationships among components in multivariate time series as well as the RAR modeling does.

3.2 System 2: A case with fluctuations with different time scales

The time series of System 2 are generated by the following linear equations:

$$x_0(t) = 1.29x_0(t-1) - 0.3x_0(t-4) + 0.25x_1(t-3) + \varepsilon_0(t), \tag{22}$$

$$x_1(t) = 0.3x_1(t-1) + 0.2x_1(t-6) + \varepsilon_1(t), \tag{23}$$

$$x_2(t) = 5.0x_1(t-3) + 0.9x_2(t-1) + \varepsilon_2(t), \tag{24}$$

where $\varepsilon_i(t)$ $(i=0,1,2)$ are the dynamic noise drawn from IID Gaussian random variables with mean zero and standard deviation 1.0 as in System 1. Figure 3 plots the signals generated by these equations and the relationships among the components. The most prominent feature of this system is the differences in the time scale of fluctuation of each component. Component x_0 fluctuates slowly over about 50 iterations, component x_1 fluctuates rapidly in almost every iteration, and component x_2 fluctuates intermediately in time scale between those of x_0 and x_1. It should also be noticed that component x_1, which has the smallest amplitude and is independent of other components, affects components x_0 and x_2. In this regard, System 2 has more complicated characteristics than System 1, even though the dynamics is represented by linear equations.

As in the case of System 1, we generate 10,000 data points for each component of System 2 to build the RAR model, then we divide these 10,000 data points into 10 intervals each of which contains 1,000 data points and compare the corresponding results of RAR modeling. We set the maximum lag as $L=25$ and use the same dictionary containing 76 terms as used for System 1. The results are summarized as

$$\hat{x}_0(t) = 1.286(7)x_0(t-1) - 0.296(8)x_0(t-4) + 0.25(2)x_1(t-3), \tag{25}$$

$$\hat{x}_1(t) = 0.30(3)x_1(t-1) + 0.19(2)x_1(t-6), \tag{26}$$

$$\hat{x}_2(t) = 5.01(3)x_1(t-3) + 0.900(1)x_2(t-1). \tag{27}$$

As in the case of System 1, all terms and parameters are correctly recovered within reasonable statistical errors for System 2 in spite of the differences in the amplitude and the time scale of fluctuation for each components.

Figure 4 shows the values of transfer entropy calculated using all 10,000 data points of the same data as used in the RAR modeling summarized in Eqs. 25–27. As in the case of Systems 1, we calculate the values of transfer entropy for both $k=l=1$ and $k=l=2$ for comparison. First of all, the values of the transfer entropy of component x_0 shows no distinctive peaks, which is remarkably different from those of components x_1 and x_2. Moreover, the values from component x_2 are always larger than those of component x_1, though the generator of x_0 defined by Eq. 22 is independent of component x_2. This deceptive result might be caused by the fact that the amplitudes of components x_0 and x_2 are in the same order. For x_1, the values are very small around 0.0075 and the large values come from x_2 at lags 2 and 3, though there are no such terms in the generator of x_1, Eq. 23. The small values might be related to the fact that component x_1 is independent of other components, though for decisive conclusion for the independence we need to estimate the effect of dynamical and/or observational noise using a method like surrogate generation based approach. For component x_2, the large values of transfer entropy come from x_1 at lags 3 and 4 that might corresponds to the term $x_1(t-3)$ in Eq. 24, though the values of transfer entropy show a long tail after the peak, which might be incompatible with Eq. 24. For the results of $k=l=2$ (the right column of Figure 2), the behaviors are almost the same as those of $k=l=1$. Even if the dynamics is represented by linear equations and the signals contain a small amount of Gaussian noise, the transfer entropy begins to fail in capturing the correct relationships among components for System 2 containing different time scales in fluctuation of each component.

4 Results on electroencephalography data

In this section, we apply the RAR modeling to electroencephalography (EEG) data and compare the results to the values of transfer entropy. The EEG signals used here were recorded from a healthy human adult during resting state with eyes closed in an electrically shielded room and have been analyzed by other methods in Rapp et al. (2005). The data were simultaneously obtained from 10 channels of the unipolar 10–20 Jasper registration scheme and digitized at 1,024 Hz using a twelve-bit digitizer. In Figure 5, we show the placement of 10 electrodes in International 10–20 System. Artifact corrupted records were removed from the analyses. The EEG impedances were less than 5 kΩ. The data were amplified by gain equal to 18,000, and amplifier frequency cut-off settings of 0.03 Hz and 200 Hz were used.

The 10 channel electroencephalography signals analyzed here are plotted in Figure 6. It should be noted that the plotted data are all normalized and dimensionless. The activities of human brain are, undoubtedly, highly complicated and non-

linear by nature. We should therefore be careful whether there might be suitable interval and duration of time for the dynamics to be approximated in linear forms. Tanizawa et al. (2018) have shown that the RAR modeling is able to detect correct relationships among components even for dynamical systems represented by non-linear differential equations such as the Rössler system. Since there is no explicit description of the results of RAR modeling of the EEG data in Tanizawa et al. (2018), we rebuild the RAR models for these 10 EEG time series, expecting the models contain correct information about the relationships among the components. We use 1,025 data points (1 s) for each component (channel) to build multivariate RAR models. We set the maximum lag as $L = 25$ and the dictionary contains therefore 251 terms, which are 25 terms for the 10 components with one constant term. We show the result for the component Fz explicitly, which is

$$\begin{aligned}\hat{x}_{\mathrm{Fz}}(t) = {} & 0.96x_{\mathrm{Fz}}(t-1) + 0.46x_{\mathrm{Cz}}(t-1) - 0.43x_{\mathrm{Cz}}(t-2) \\ & - 0.091x_{\mathrm{F3}}(t-5) + 0.17x_{\mathrm{F3}}(t-13) \\ & - 0.095x_{\mathrm{F3}}(t-20). \end{aligned} \tag{28}$$

From this model, component Fz is influenced by component Cz at lag 1 and 2 and component F3 at lag 5, 13, and 20. In Figures 11, 12 of Appendix, we show the behaviors of simulated signals generated from the RAR models and their power spectral densities.

For the transfer entropy, we use the same data points as those used in RAR model building and calculate the information gain from the correlation in the signals between all pairs of component Fz and each of other channels up to the maximum lag 30. According to the analysis described in Section 3, we set $k = l = 1$ in calculating transfer entropy. The results of the calculation is plotted in Figure 7. From this plot, we see that all values of transfer entropy are in the same order of magnitude and show no distinct peaks that suggest important components and lags. We also plot in Figure 8 the components and the maximum values of transfer entropy of component Fz for each lag up to 30 sorted in the descending order of the values of transfer entropy. According to the calculations of transfer entropy for component Fz, the information gain from component C3 is the largest. The component C3, however, does not appear in the RAR model of component Fz in Eq. 28. The values of transfer entropy for other components show similar behaviors.

We summarize these results for component Fz in Figure 9. In this figure, the target component against which the RAR model and the transfer entropy are calculated (in this case, Fz), is represented by a red slightly large circle. The circles from which the arrows emanate (in this case, Cz and F3), represent the components contained in the RAR model with the width of the arrows being proportional to the number of appearance of the component in the RAR model. In this case, component Cz appears two times and component F3 appears three times. The orange circles represent the components that give the top 5 values of transfer entropy for each lag. In this case, all top 5 values only come from component C3 (See Figure 8). From this figure, we also see the spatial information of the components included in the RAR model and the components that gives large values of transfer entropy.

As for the other nine components, we show only the summarized results in Figure 10. Generally speaking, the components that give large values of transfer entropy are not related to the components included in the RAR models. It is also to be noticed that the component Oz, which is placed at the back of the head, appears frequently as the component of large transfer entropy values, though it is not likely the outcome of direct influence of this component on the target components.

5 Discussion and summary

For two artificial linear systems described in Section 3, the results of the transfer entropy are consistent with those of the RAR modeling, if the values and the time scales in fluctuation of the signals are in the same order of magnitude (System 1). In this case the dynamics of the components are well separated and pairwise methods such as the transfer entropy work well. If the time series contain components whose values and time scale of fluctuation are significantly different from each other (System 2), however, the transfer entropy begins to fail in detecting correct relationships among components, while the RAR modeling is still able to give the correct relationships.

For the application to EEG data in Section 4, the relationships indicated by the results of transfer entropy are drastically different from those indicated by the RAR modeling. Though, within our knowledge, there are no decisive research work in the literature in this regard, we think it is partially because of the insufficiency of pairwise measures for detecting relationships among components that potentially contain various time scales in dynamics for those seen in brain activity. In contrast, it is known that the RAR modeling can detect correct relationships even when the underlying system is non-linear (Tanizawa et al. (2018)). We understand that it would be a controversial issue whether EEG data can be representable by linear models or not. Even in a case in which that the dynamics is represented by a linear system, however, transfer entropy might fail in detecting the correct relationships among the components in multivariate time series, if they contain several time scales in different orders of magnitude. Though we do not claim that the relationships detected by the RAR modeling technique are always correct, detecting the relationships among components in multivariate time series by RAR modeling could be a promising technique with a wide range of applicability.

In summary, we have applied the RAR modeling technique to several multivariate time series as a method to detect the relationships among the components in the time series and compared the results with those of a pairwise measure, transfer entropy in this article. When the relationships between the dynamics of the components are linear and the

time scales in the fluctuation of each component are in the same order of magnitude, the results of the RAR model and the transfer entropy are consistent. When the time series contain components that have large differences in the amplitude and the time scales of fluctuation, however, the transfer entropy fails to capture the correct relationships between the components, while the results of the RAR modeling are still correct. For a highly complicated dynamics such as human brain activity observed by electroencephalography measurements, the results of the transfer entropy are drastically different from those of the RAR modeling.

Data availability statement

The original contributions presented in the study are included in the article/Supplementary Material; further inquiries can be directed to the corresponding author.

Author contributions

TT conceived the idea of numerical calculations presented in this article and carried out the computation. TT and TN verified and discussed the results. TT took the lead in writing the manuscript with the critical feedback from TN.

Acknowledgments

TT and TN would like to acknowledge Paul E. Rapp of Uniformed Services University for providing us with the EEG data used in Rapp et al. (2005). The authors would also like to acknowledge referees for valuable suggestions.

Conflict of interest

TT is employed by Toyota Motor Corporation.

The remaining author declares that the research was conducted in the absence of any commercial or financial relationships that could be construed as a potential conflict of interest.

Publisher's note

All claims expressed in this article are solely those of the authors and do not necessarily represent those of their affiliated organizations, or those of the publisher, the editors and the reviewers. Any product that may be evaluated in this article, or claim that may be made by its manufacturer, is not guaranteed or endorsed by the publisher.

References

Baccalá, L. A., and Sameshima, K. (2001). Partial directed coherence: A new concept in neural structure determination. *Biol. Cybern.* 84, 463–474. doi:10.1007/PL00007990

Breiman, L. (1995). Better subset regression using the nonnegative garrote. *Technometrics* 37 373–384.

Brüggemann, I. (2003). Measuring monetary policy in germany: A structural vector error correlation approach. *German Economic Review* 4 307–339.

Faes, L., Nollo, G., and Porta, A. (2011). Information-based detection of nonlinear granger causality in multivariate processes via a nonuniform embedding technique. *Physical Review E* 83 051112.

Granger, C. W. J. (1969). Investigating causal relations by econometric models and cross-spectral methods. *Econometrica* 37, 424–438. doi:10.2307/1912791

Judd, K., and Mees, A. (1998). Embedding as a modeling problem. *Phys. D. Nonlinear Phenom.* 120, 273–286. doi:10.1016/s0167-2789(98)00089-x

Judd, K., and Mees, A. (1995). On selecting models for nonlinear time series. *Phys. D. Nonlinear Phenom.* 82, 426–444. doi:10.1016/0167-2789(95)00050-e

Kamiński, M., Ding, M., Truccolo, W. A., and Bressler, S. L. (2001). Evaluating causal relations in neural systems: Granger causality, directed transfer function and statistical assessment of significance. *Biol. Cybern.* 85, 145–157. doi:10.1007/s004220000235

Kamiński, M. J., and Blinowska, K. J. (1991). A new method of the description of the information flow in the brain structures. *Biol. Cybern.* 65, 203–210. doi:10.1007/BF00198091

Kugiumtzis, D. (2013). Direct-coupling information measure from nonuniform embedding. *Physical Review E* 87 062918.

Nakamura, T., Kilminster, D., Judd, K., and Mees, A. (2004). A comperative study of model selection methods for nonlinear time series. *Int. J. Bifurc. Chaos* 14, 1129–1146. doi:10.1142/s0218127404009752

Papana, A., Siggiridou, E., and Kugiumtzis, D. (2021). Detecting direct causality in multivariate time series: A comparative study. *Communications in Nonlinear Science and Numerical Simulation* 99 105797.

Rapp, P. E., Cellucci, C. J., Watanabe, T. A. A., and Albano, A. M. (2005). Quantitative characterization of the complexity of multichannel human eegs. *Int. J. Bifurc. Chaos* 15, 1737–1744. doi:10.1142/s0218127405012764

Schreiber, T. (2000). Measuring information transfer. *Phys. Rev. Lett.* 85, 461–464. doi:10.1103/PhysRevLett.85.461

Shojaie, A., and Michailidis, G. (2010). Discovering graphical granger causality using the truncating lasso penalty. *Bioinformatics* 26 i517–i523.

Siggiridou, E., and Kugiumtzis, D. (2016). Granger causality in multivariate time series using a time-ordered restricted vector autoregressive model. *IEEE Transactions Signal Processing* 65 1759–1773.

Small, M., and Judd, K. (1999). Detecting periodicity in experimental data using linear modeling techniques. *Phys. Rev. E* 59, 1379–1385. doi:10.1103/physreve.59.1379

Tanizawa, T., Nakamura, T., Taya, F., and Small, M. (2018). Constructing directed networks from multivariate time series using linear modelling technique. *Phys. A Stat. Mech. its Appl.* 512, 437–455. doi:10.1016/j.physa.2018.08.137

Theiler, J., Eubank, S., Longtin, A., Galdrikian, B., and Farmer, J. D. (1992). Testing for nonlinearity in time series: the method of surrogate data. *Physica D: Nonlinear Phenomena* 58 77–94.

Yang, Y., and Wu, L. (2016). Nonnegative adaptive lasso for ultra-high dimensional regression models and a two-stage method applied in financial modeling. *Journal of Statistical Planning and Inference* 174 52–67.

Vlachos, I., and Kugiumtzis, D. (2010). Nonuniform state-space reconstruction and coupling detection. *Physical Review E* 82 016207.

Appendix

In this Appendix, we show the behaviors of simulated EEG signals generated by the RAR models and their power spectral densities in the frequency domain. Here the RAR models are constructed from the first 769 observations of each EEG channels to compare the simulated signals to the last 256 observations.

Figure 11 are the plots of simulated signals generated by the RAR models with the last 281 observed EEG signals for comparison. The RAR signals are generated with 25 observed signals prior to the last 256 signals as initial values and contain Gaussian random numbers with mean 0 and standard deviations determined from the fitting errors of each channels in RAR modeling as dynamic noise. Though the observed signals and the simulated ones are not identical because of the dynamic noise, the behaviors seem to be quite similar.

Figure 12 are the plots of the power spectral densities of simulated signals from the RAR models. Plotted values are the averages of the power spectral densities over 100 independent runs of simulation. Significant contributions come from frequencies up to about 20 Hz that correspond to the region of α waves.

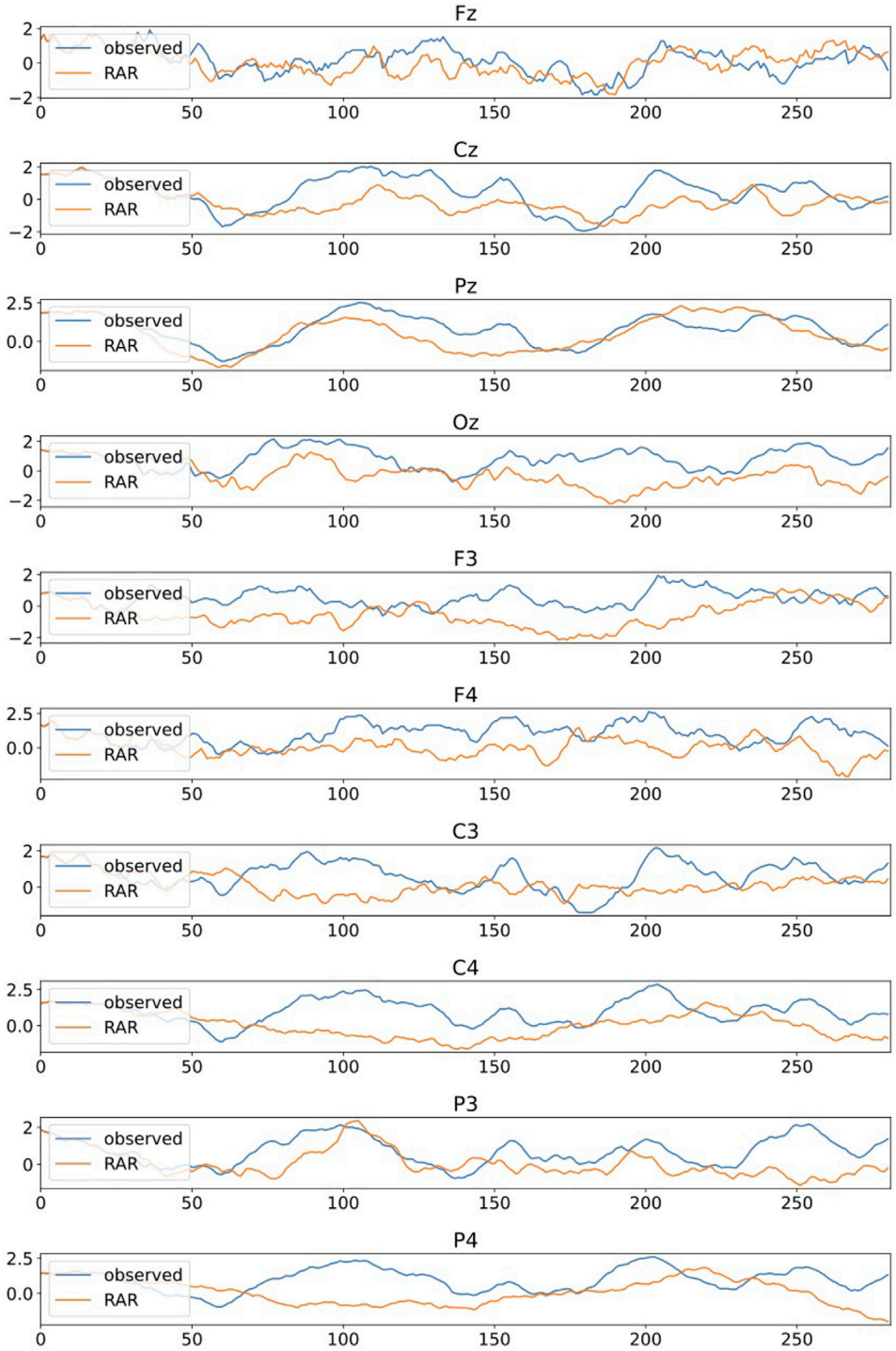

FIGURE 11
Comparative plots of the observed EEG signals and the signals generated by the RAR models, which are constructed from the first 769 observations of each channel. The observed EEG signals are the last 281 (= 25 + 256) signals of each channel and the RAR signals are generated by the corresponding RAR models with 25 observed signals prior to the last 256 signals as initial values. Simulated signals also contain Gaussian random numbers with mean 0 and standard deviations determined from the fitting errors of each channels in RAR modeling as dynamic noise.

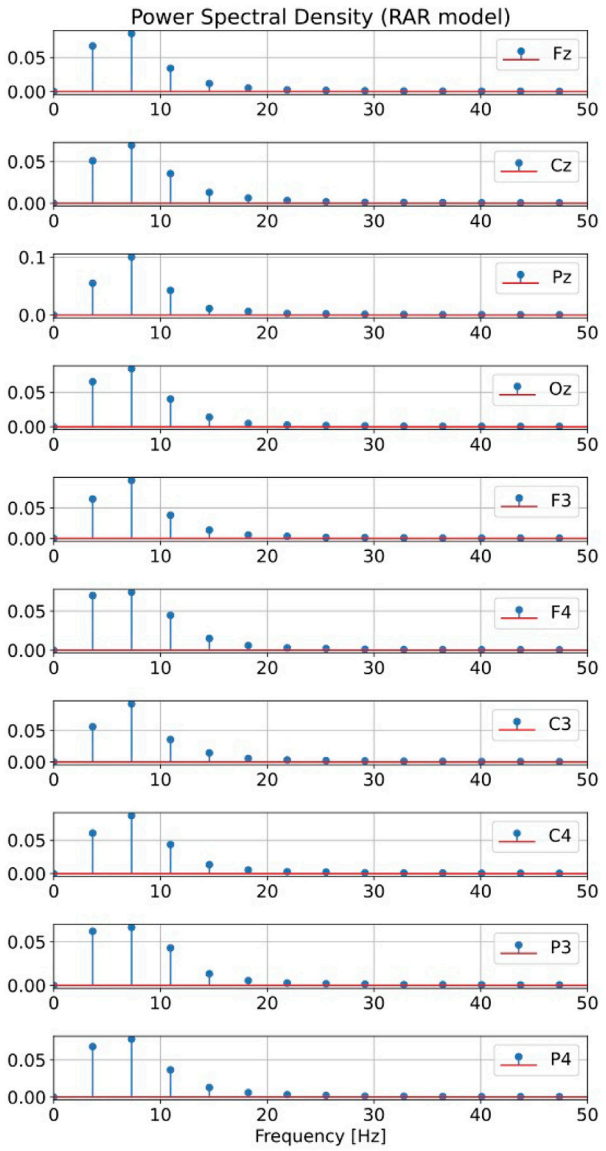

FIGURE 12
Plots of the power spectral densities of simulated signals from the RAR models. Plotted values are the averages of the power spectral densities over 100 independent runs of simulation. Significant contributions come from frequencies up to about 20 Hz.

frontiers | Frontiers in Network Physiology

TYPE Original Research
PUBLISHED 13 October 2022
DOI 10.3389/fnetp.2022.890906

OPEN ACCESS

EDITED BY
Plamen Ch. Ivanov,
Boston University, United States

REVIEWED BY
Ruben Yvan Maarten Fossion,
Universidad Nacional Autónoma de México, Mexico
Marianna La Rocca,
Università degli Studi di Bari "A. Moro", Italy

*CORRESPONDENCE
Julieta Ramos-Loyo,
julieta.ramos@academicos.udg.mx

SPECIALTY SECTION
This article was submitted to Generalized Nets and Fuzzy Sets, a section of the journal Frontiers in Network Physiology

RECEIVED 07 March 2022
ACCEPTED 15 September 2022
PUBLISHED 13 October 2022

CITATION
Ramos-Loyo J, Olguín-Rodríguez PV, Espinosa-Denenea SE, Llamas-Alonso LA, Rivera-Tello S and Müller MF (2022), EEG functional brain connectivity strengthens with age during attentional processing to faces in children.
Front. Netw. Physiol. 2:890906.
doi: 10.3389/fnetp.2022.890906

EEG functional brain connectivity strengthens with age during attentional processing to faces in children

Julieta Ramos-Loyo[1]*, Paola V. Olguín-Rodríguez[2,3], Sara E. Espinosa-Denenea[1], Luis A. Llamas-Alonso[4], Sergio Rivera-Tello[1] and Markus F. Müller[3,5,6]

[1]Instituto de Neurociencias, Universidad de Guadalajara, Guadalajara, Jalisco, México, [2]Instituto de Ciencias Nucleares, Universidad Nacional Autónoma de México, Ciudad de México, México, [3]Centro de Ciencias de La Complejidad, Universidad Nacional Autónoma de México, Ciudad de México, México, [4]Universidad Autónoma de Baja California, Ensenada, México, [5]Centro de Investigación en Ciencias, Universidad Autónoma del Estado de Morelos, Cuernavaca, Morelos, México, [6]Centro Internacional de Ciencias A. C., Cuernavaca, Morelos, México

Studying functional connectivity may generate clues to the maturational changes that occur in children, expressed by the dynamical organization of the functional network assessed by electroencephalographic recordings (EEG). In the present study, we compared the EEG functional connectivity pattern estimated by linear cross-correlations of the electrical brain activity of three groups of children (6, 8, and 10 years of age) while performing *odd-ball* tasks containing facial stimuli that are chosen considering their importance in socioemotional contexts in everyday life. On the first task, the children were asked to identify the sex of faces, on the second, the instruction was to identify the happy expressions of the faces. We estimated the stable correlation pattern (SCP) by the average cross-correlation matrix obtained separately for the resting state and the task conditions and quantified the similarity of these average matrices comparing the different conditions. The accuracy improved with higher age. Although the topology of the SCPs showed high similarity across all ages, the two older groups showed a higher correlation between regions associated with the attentional and face processing networks compared to the youngest group. Only in the youngest group, the similarity metric decreased during the sex condition. In general, correlation values strengthened with age and during task performance compared to rest. Our findings indicate that there is a spatially extended stable brain network organization in children like that reported in adults. Lower similarity scores between several regions in the youngest children might indicate a lesser ability to cope with tasks. The brain regions associated with the attention and face networks presented higher synchronization across regions with increasing age, modulated by task demands.

KEYWORDS

functional connectivity, neural networks, EEG, children, age, attention, face processing

Introduction

The brain is a hyperconnected structure, enclosing anatomically and functionally organized networks. Its intrinsic connectivity patterns can be reconfigured dynamically and adaptively as a consequence of environmental demands (Cohen & D'Esposito, 2016) and may suffer maturational changes at the functional (Smit et al., 2012; Qin et al., 2015) and structural level (Hagmann et al., 2010; Fan et al., 2011).

A close relationship between structural and functional connectivity has been proposed, although there is no perfect match because function reflects complex multisynaptic interactions in structural networks (Park & Friston, 2013; Suárez et al., 2020). Suárez et al. (2020) remark that functional connectivity at rest is thought to reflect the spontaneous neural activity of a finely orchestrated spatio-temporal pattern, which should be reproducible like those observed during tasks performance which patterns are highly organized, reproducible, and comparable with tasks-driven activation patterns. Most of the studies addressing the structural and functional brain connectivity relationships have been conducted using functional magnetic resonance (fMRI) (Park & Friston, 2013; Suárez et al., 2020). Nevertheless, some related work has also been performed using brain electrical activity (EEG) (Chu et al., 2015). Moreover, Arzate-Mena et al. (2022) encountered a straight relationship between the EEG stable correlation pattern (SCP) and the fMRI resting-state network that reflects different time expressions of the same brain activity.

EEG has proven useful to study functional connectivity, as its fine temporal resolution allows the assessment of fast dynamic processes. Different approaches have emerged to extract brain dynamics information from EEG (Pereda et al., 2005; Ansari-Asl et al., 2006; Boccaletti et al., 2006; Bullmore & Sporns, 2009; Bakhshayesh et al., 2019). However, even when highly nonlinear systems are under consideration, linear measures may perform equally well or even better than nonlinear techniques (Mormann et al., 2005; Ansari-Asl et al., 2006; Bakhshayesh et al., 2019), which seems particularly true for the analysis of EEG-signals (Mormann et al., 2005; Müller et al., 2011; Bakhshayesh et al., 2019). Therefore, in the present study, we focus on linear cross-correlations to estimate functional networks.

Regarding linear cross-correlation between selected electrodes located in different scalp regions, Corsi-Cabrera et al. (1997, 2007) observed high within-subject stability in repeated measures across weeks and months in healthy women. In the studies of Müller et al. (2014) and Olguín-Rodríguez et al. (2018), a well-pronounced average cross-correlation pattern was found that spans over the whole scalp. This pattern seems to be independent from the physiological state of a subject like different sleep stages, or awake with open or closed eyes, and remains stable even during a peri-ictal transition of a focal onset seizure. Moreover, this correlation structure seems to have a universal character, since it shows notably high similarity also between subjects. Undoubtedly, finding stationary patterns in otherwise highly nonstationary multivariate data is an important topic, as it can give us insight into the main mechanisms controlling the dynamics of a complex system such as the human brain.

The present study was motivated by the hypothesis articulated by Olguín-Rodríguez et al. (2018) that the SCP reflects the necessarily correlated ongoing brain activity whose one of its principal functions consists in maintaining the brain in an optimal dynamical mode for information processing such that deviations or fluctuations around this stable scaffold are expressions of the actual physiological brain state.

However, the brain develops during the lifespan, and particularly during childhood and adolescence, it suffers crucial structural changes. Thus, the question remains whether a distinct stationary pattern of relationships encompassing the entire scalp is also found in children as in adult subjects, and second, whether the SCP based on functional relationships also undergoes changes such as those in the structural reorganization of brain networks. Furthermore, it might be interesting to prove whether also in children cognitive brain states could be better described and characterized by deviations from the SCP.

Some hints in favor of this hypothesis can be found in the literature. Generally, changes in frequency bands amplitude have been described in children while they are at rest and during the performance of cognitive tasks (i.e. Benninger et al., 1984; Marshall et al., 2002; Clarke et al., 2001; Perone et al., 2018). Concerning EEG functional connectivity maturation, some studies have been conducted in the resting state. In an early report, Marosi et al. (1992) found an increase in EEG coherence with higher age. In another study (Thatcher et al., 2008), authors observed maturational changes in intra-hemispheric coherence in children and adolescents aged 6 months to 16 years. That study reported large changes in EEG coherence and phase in children aged 6 months to 4 years, followed by a significant linear trend towards higher coherence in short inter-electrode distances, and longer phase delays in long inter-electrode distances. Along this line, Fair et al. (2009) observed that functional brain development proceeds from a local to a distributed communication organization. It is worth noting that disruptions in EEG functional connectivity have been described in different disorders such as attentional deficit-hyperactivity disorders (Barry et al., 2002; Murias et al., 2007), autism spectrum disorder (Kikuchi et al., 2013), and intellectual disability (Gasser et al., 1987).

However, only sparse data exist that addressed EEG functional connectivity during cognitive processing in typically-developing children. Machinskaya and Kurganskiĭ (2012) compared coherent activity between children (7-8 years old) and adults during a working memory task. While they reported for the adult group, an increase of the coherence in

the alpha band between frontoparietal regions, predominantly in the right hemisphere, in children they detect significant coherence values in the inferior-temporal and parietal cortical regions coherence in the theta band. These results are interpreted in terms of a relative immaturity of the mechanisms of executive control of working memory in children. In adults, variations in functional connectivity during the processing of diverse tasks include global and specific network changes associated with information processing (i.e. Daume et al., 2017; Hearne et al., 2017; Maurits et al., 2006; Vatansever et al., 2017).

In the present study, we were interested in exploring the developmental changes during attentional processes using high salient emotional stimuli such as facial expressions, due to their relevance in social interaction and adaptation (Dekowska et al., 2008). As Driver and Frackowiak (2001) state, selective attention allows people to process some stimuli more thoroughly than others, which is partly under voluntary control, and partly determined by stimulus salience. Like other cognitive abilities, facial and emotional recognition improves with age in school-age children. For example, Damaskinou and Watling (2018) presented evidence that 10-year-olds overperform 6-year-olds on emotional recognition tasks.

One of the most widely used paradigms for studying brain electrical responses originated during facial emotional recognition is the odd-ball task. Fichtenholtz et al. (2007) propose that the odd-ball task may be useful to study the interaction of the attention and emotion processing. In this paradigm, the participant is asked to respond to a specific low-probability target stimulus which is presented within a stream of high-probability non-target stimuli.

Some EEG and MEG studies employing several analysis approaches have achieved to find functional connectivity among the face-sensitive brain areas of the ventral visual pathway that includes primary occipital regions, the inferior-temporal cortex, and especially the fusiform face area (Yang et al., 2015; Maffei & Sessa, 2021; Yin et al., 2021). However, little is known about developmental changes in functional connectivity during cognitive activity, particularly during face processing. Cohen Kadosh et al. (2011) examined the fMRI connectivity of the core face network and observed that it develops during childhood. However, children did not show the modulation in the functional network connections by task demands found in adults.

A recent fMRI study (Harrewijn et al., 2021) was conducted to test the similarity in functional connectivity between rest and while performing a dot-probe task with neutral, happy, and angry faces in 13 years-old children. Results revealed that functional connectivity during rest and a dot-probe task was positively correlated and that the similarity levels were related to threat bias. In another study in adults, Yin et al. (2021) found that during face processing, the EEG brain network was more efficient for information transfer and exchange compared with non-face processing.

To our knowledge, the presence of a SCP in EEG activity has not been studied in children so far, neither at rest nor during task performance. Studying EEG functional connectivity in typically-developing children may shed light on the normal maturational changes in the brain dynamics organization while performing a cognitive task with salient stimuli (faces) across ages and it may provide a basis for the understanding of functional abnormalities in special populations. Finally, the estimation of variations from the stationary correlation patterns may provide differentiation of dynamical transient changes during different cognitive states in children like those observed in adult subjects (Olguín-Rodríguez et al., 2018). Therefore, the aims of the present study were threefold:

1) To identify a possible SCP in children similar to that found in adults;
2) To evaluate the global variations *via* similarity estimates between SCP and the correlation pattern of each condition during an odd-ball task with facial stimuli.
3) To identify the effects of age *via* possible changes of the coupling between brain regions, during the performance of two tasks that requires attention and face processing.

We hypothesized that a correlation pattern like that found in adults would exist in children. The similarity metric will show lower values during cognitive activity than during resting state, indicating higher transient dynamical features. In addition, we predicted that cross-correlations would increase with age and will be modulated by task demands.

Methods

Participants

The sample consisted of 64 right-handed children, distributed into three age groups, each with a range of 11 months (G1: 10 boys and seven girls, mean age = 6.30, SD = 0.44; G2: 13 boys and nine girls, mean age = 8.31, SD = 0.37 and; G3: 15 boys and 10 girls, mean age = 10.2, SD = 0.45). The children group were homogeneous with respect to their age and school grade and normal IQ scores. None had any history of neurological disorders. The parents provided their written informed consent for their children´s participation in this study. The project was approved by the Ethics Committee of the Institute of Neurosciences following the Declaration of Helsinki.

EEG recording

EEG was continuously recorded during the experimental conditions: at rest with eyes opened and during task

performance in the leads F3, F4, Fz, C3, C4, Cz, T3, T4, T5, T6, P3, P4, Pz, O1, and O2 according to the 10/20 International System with linked earlobes as a reference with a sampling rate of 500 Hz. To this end, we used a Medicid five acquisition device. Electrode impedances were assured to be less than 5 kOhms. To control artifacts caused by ocular movements an electrooculogram was recorded simultaneously *via* two electrodes located at the extreme upper corner of the right eye and the lower outer edge of the left eye, respectively. During acquisition, the signal was bandpass filtered between 0.01 and 50 Hz.

Experimental design

An oddball paradigm was used for the presentation of two tasks. In one of them, the children had to recognize the facial expressions of happiness; and in another one, they had to identify the sex of the models. For each task, a total of 200 stimuli were randomly presented, of which 70% were non-target frequent stimuli and the remaining 30% were the target infrequent ones. Each trial started with a fixation point (a white cross) in the center of the screen with a variable duration between 800 and 1,300 ms, followed by either a frequent or a target stimulus presented for 700 ms.

Participants were asked to respond to the target stimuli by pressing a key. For the happiness condition, the target stimuli were faces with a happiness expression, while the non-target stimuli consisted of men´s and women´s faces with a neutral expression. For the sex recognition task, the target stimuli were female faces and the non-target male ones.

Procedure

Once the presence of the inclusion criteria for each participant were determined, we asked the child to sit 60 cm away in front of the computer screen and perform the task, avoiding eye and head movements while the faces were shown. We counterbalanced the presentation of the two tasks among participants and allowed a 5-min rest period between them. Before starting each task, participants underwent a training block of 10 trials to assure that they have completely understood the instructions.

EEG analysis

After visual inspection, data preprocessing was conducted applying Independent Components Analysis (ICA) to remove eye movements (Delorme & Makeig, 2004). On the average we used 25 artifacts free EEG segments that corresponded exclusively to correct responses to the targets which were considered for further analysis. Anterior-temporal electrodes (T3 and T4) were excluded because signals were contaminated with artifacts in some children and these regions are not directly involved in face identification or attentional processes. The computer codes for the numerical analysis were elaborated using MATLAB.

Continuous EEG signals were first segmented into windows of T = 1 s length. In the case of the tasks, this window began in synchrony with the stimulus presentation. We then, filtered the signals by a fourth-order Butterworth filter (1-25 Hz). We calculated for each segment the Pearson's correlation coefficients, *viz.* zero-lag cross-correlations,

$$C_{ij} = \frac{1}{T}\sum_{k=1}^{T} X_i(t_k) X_j(t_k)$$

between each pair of electrodes, adapting the procedure followed in previous studies (Arzate-Mena et al., 2022; Müller et al., 2014; Olguín-Rodríguez et al., 2018). Here C_{ij} denotes the cross-correlation matrix of two time series $X_i(t_k)\, X_j(t_k)$, T denotes the number of samples of the data segment ($i,j = 1, \ldots, N$ and $k = 1, \ldots T$) and N the number of electrodes. In this formula, the data $X_i(t_k)\, X_j(t_k)$ are normalized to zero mean and unit variance, such that the correlation coefficient takes values between ± 1. The resulting matrix is real-symmetric and all diagonal elements are equal to one. Then we estimated the individual stable correlation pattern (SCP) by averaging all the correlation matrices of all conditions (resting state and tasks) for each participant.

To obtain the similarity metric, we calculated the correlation values (Pearson´s analysis) between the SCP and the correlation matrix of each EEG segment based on the procedure used by Olguín-Rodríguez et al. (2018) and Arzate-Mena et al. (2022). Thereby, we ordered the triangle of each matrix in a vector and normalized its elements to zero mean unit variance to ensure that Pearson coefficients take values between one and minus one. Then we estimated the Pearson coefficients between these vectors. Note, lower similarity indicates larger topological changes of the functional network with respect to the average. These changes, viz deviations from the SCP might be characteristic for the condition under consideration.

Statistical analysis

For testing behavioral differences in the number of correct responses and reaction times between conditions as a function of age, we applied mixed ANOVAs (age x conditions). The SCP correlation coefficients were compared among age groups through a Welch´s *t*-test. In addition, we applied a mixed ANOVA (age x conditions) to evaluate similarity metric differences. Greenhouse corrections were applied when necessary and Bonferroni corrections for multiple testing of

TABLE 1 Percentage of correct responses and the reaction times in each age group (6, 8 and 10 years old).

	Correct responses		Reaction times	
	Sex Mean (SD)	Happiness Mean (SD)	Sex Mean (SD)	Happiness Mean (SD)
6	50.68 (17.52)	76.27 (12.11)	766.98 (73.46)	723.27 (79.24)
8	70.15 (19.75)	80.83 (15.91)	681.76 (95.04)	659.31 (58.75)
10	76.27 (12.20)	90.67 (7.33)	647.42 (55.78)	619.17 (56.50)

pairwise comparisons. A p-value less than 0.05 was considered for significant differences.

To observe an overall effect of age and conditions, we calculated the average difference (task–rest) of the correlation matrices for sex and happiness, and their empirical cumulative distribution functions using the elements below the main diagonal. Then, a two-sample Kolmogorov-Smirnov (K-S) test was applied to determine the probability that two samples derived for the different age-groups (6 vs. 8, 8 vs. 10, and 6 vs. 10 years) stem from the same probability distribution. We illustrate our results of considerable changes of the average cross-correlation matrices like a network upon the scalp, where "considerable" means that the changes surpass a threshold of one standard deviation above or below the SCP-value.

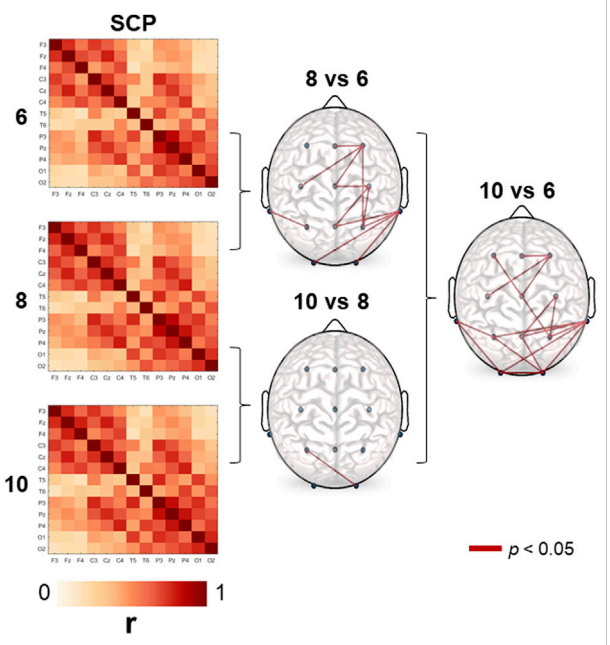

FIGURE 1
Stable correlation pattern (SCP) for each age group. Connection lines indicate the age-significant differences (6, 8, and 10-year-old) in cross-correlation values on a 5% significance level according to the t-test. Correlation estimates turn out to be systematically higher in the older group in all comparisons.

Results

Behavioral results

At the behavioral level, the percentage of correct responses increased and the reaction times decreased with higher age (Table 1). However, differences were apparent between the two tasks, with the sex-based one showing greater difficulty. A significant interaction of age X conditions ($F_{(2,61)}$= 5.43, p = 0.01,η^2 = 0.15) revealed that the accuracy rate was lowest in the youngest group in relation to the other two groups on the sex task ($p < 0.01$), and in relation to the 10-years-olds on the happiness task. The sex task showed lower accuracy than the happiness one in all groups ($p < 0.01$).

Reaction times to the target stimuli showed significant differences for both age ($F_{(2,61)}$= 17.69, p = 0.001,η^2 = 0.36) and conditions ($F_{(1,61)}$= 11.72, p = 0.01,η^2 = 0.16). Reaction times were shorter in the older groups than in the group of 6-years-old ($p < 0.001$), and shorter for the happiness than the sex condition ($p < 0.001$).

Stable correlation pattern

As it can be observed in Figure 1, the structure of the average correlation matrices is very similar across the age groups. However, some differences are observable among the age groups. Systematically, we observed that correlations increase with age. In the graph on the right-hand side of Figure 1 we show the correlation coefficients of between those electrode pairs that resulted significant on a 5%-level according to the t-test. The differences were basically seen in a longitudinal arranged network that includes frontal, central, and parietal regions, and another posterior network that includes posterior-temporal, parietal, and occipital regions.

Note, the SCP obtained in the present study is qualitatively different from those presented in Müller

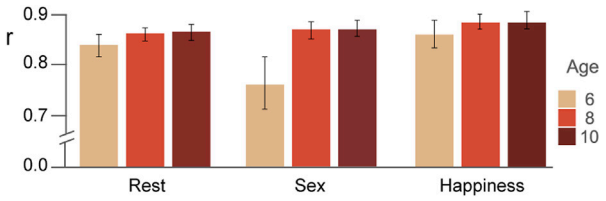

FIGURE 2
Similarity estimated *via* Pearson correlations (mean and standard errors) between the stable pattern and the average correlation matrix of each condition and for each age group are displayed.

et al. (2014) and Olguín-Rodríguez et al. (2018). This striking difference is due to the different reference schemes used. While in those studies the median reference has been chosen, in the present work we used here linked earlobes. As outlined in Rios-Herrera et al. (2019), the earlobe reference may induce redundant information to all data channels, which provokes elevated correlations between all electrode pairs. However, the fact that we obtained also a pronounced stationary correlation pattern using this reference scheme, substantiates the argumentation expressed in those studies (Müller et al., 2014; Olguín-Rodríguez et al., 2018).

Similarity between the stable pattern and the correlation matrices averaged separately for each condition

In Figure 2, the Pearson coefficients for the comparison of the SCP and the correlation matrix averaged separately for each condition are displayed for each age group. The ANOVA revealed significant differences for the factors of age ($F_{(2,61)} = 10{,}41$, $p = 0.01$,$\eta^2 = 0.25$), conditions ($F_{(4,122)} = 38.87$, $p = 0.01$,$\eta^2 = 0.38$) and for interaction between them ($F_{(4,122)} = 8.77$, $p = 0.01$,$\eta^2 = 0.22$). We observed lower similarity metric values in the youngest children compared to the eight- and 10-year-old groups in the sex condition ($p < 0.01$).

Rest-to-task cumulative distributions

Figure 3A illustrates rest-to-task subtraction in correlation values for the sex and happiness conditions according to the thresholds obtained by the cumulative distributions functions including the three age groups. Regions that showed an increment (red), as well as those which showed a decrement (blue) during performance of each task in relation to the resting state, are presented. As it can be observed, in the 6-year-olds group, an increase in synchronization between some electrode pairs occurred but there was also a decrease between several pairs

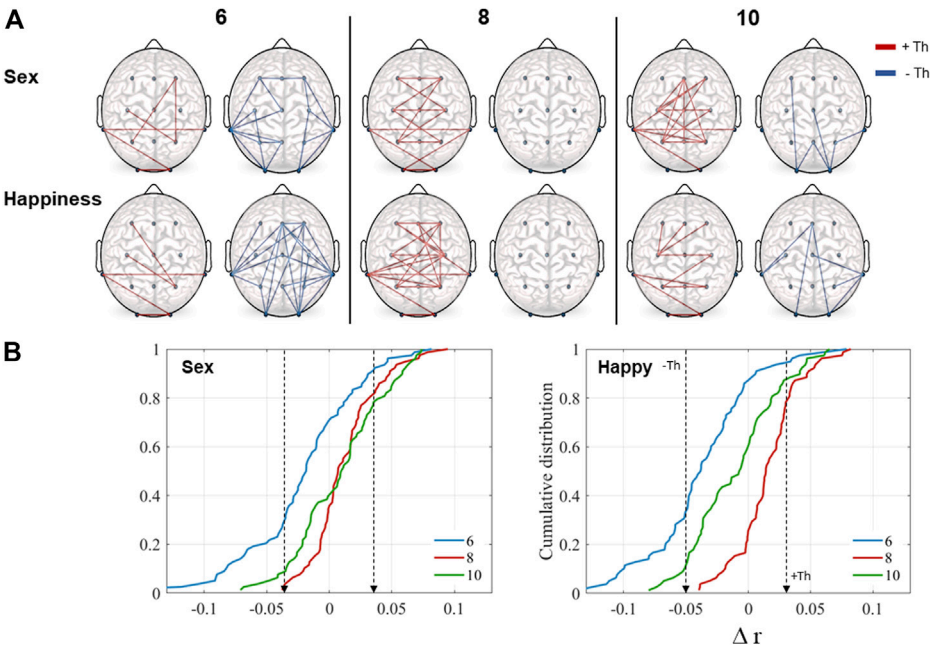

FIGURE 3
(A) Representation of task-to-rest subtraction in correlation values (Δr). Edges are traced when Δr surpassed the positive and negative thresholds. Red lines indicate an increase in correlation values and the negative ones a decrease. For sex condition: $+Th = 0.04$ and $-Th = -0.04$. For happiness: $+Th = 0.03$ and $-Th = -0.05$. **(B)** Age differences in cumulative distribution curves of task-to-rest subtraction for each task. Dotted arrows indicate the thresholds used for tracing the graphs.

in both conditions. In the 8-year-olds group, there was only an increase in correlation, on one hand, between pairs of those regions related to the attentional network (frontal, central, and parietal), and on the other, those related to the face core network (posterior-temporal, parietal and occipital). Finally, in the oldest group, there was also an increase between some of the same regions, mainly in the sex condition, adding frontal-parietal connections. As well, there was a decrease between some long-distance connections including occipital regions.

The K-S test revealed significant differences among the age groups in the cumulative distributions. In general, all distributions were statistically different (Figure 3B). Differences were found to be significant for the sex condition (6 vs. 8, $D(78) = 0.48$, $p = 0.001$; 8 vs. 10, $D(78) = 0.21$, $p = 0.04$; 6 vs. 10, $D(78) = 0.32$, $p = 0.001$) and in the happiness condition (6 vs. 8, $D(78) = 0.7$, $p = 0.001$; 8 vs. 10, $D(78) = 0.41$, $p = 0.001$; 6 vs. 10, $D(78) = 0.33$, $p = 0.001$). On both tasks, the 6-years-old children had negative values, indicating lower correlation values during the tasks compared to the resting condition. In contrast, results for the groups of eight- and 10-years-old displayed positive values, indicating increased correlation.

Discussion

We first verified the existence of a stable stationary correlation pattern (SCP) in children aged 6-10 years. Functional connectivity increased with age mainly in a longitudinal network that included frontal, central, and parietal regions, but also in a posterior network comprised of posterior-temporal, parietal, and occipital regions. The similarity coupling of the SCP with each condition pattern showed age-dependent changes as a function of task demand. Overall, the youngest children showed a lower correlation value while executing the sex task.

Children displayed a similar SCP to that observed previously in healthy adults in different physiological states -wakefulness and sleep stages-as well as with epilepsy using the same analytical approach. In addition, pronounced correlations between distant electrode pairs has been found using the median EEG-reference, but then with negative sign (Arzate-Mena et al., 2022; Müeller et al., 2014; Olguín-Rodríguez et al., 2018). The finding of an SCP indicates that children´s brains exhibit a stable functional organization pattern from an early age, while also highlighting the importance of spontaneous brain activity in the resting state where, though not related to a known synchronized event, diverse cognitive activity is occurring. Since similarities between structural and functional connectivity have been described (Suárez et al., 2020), and the structural pattern is established early in development (Fan et al., 2011), one could expect a stable functional pattern to emerge in early childhood. Based on their study of brain connectivity in five- and 7-year-olds in the resting-state, Boersma et al. (2011) posited that a shift from random to more organized small-world functional networks characterize normal brain maturation.

Although the SCP was quite similar among the three groups, age-dependent differences appeared. Overall, correlation values from the SCP increased with age between electrode pairs corresponding primarily to regions related to the attentional network (frontal, central and parietal), and those related to the face network (posterior-temporal, parietal and occipital). The differences between the six- and 8-year-olds were clearly lateralized in the right hemisphere. Similar differences were observed between the six- and 10-year-olds but with a more local increase in the attentional network, and between regions related to the face network. The structure of these age pattern changes shows a relation to tasks type (odd-ball) and stimuli (faces) used. On a working memory task, Baum et al. (2019) described an increase of the structural-functional coupling, primarily in the rostrolateral prefrontal cortex across development (8-23 years), that showed higher inter-individual variability during task performance than at rest. Shirer et al. (2011) observed shifting patterns of fMRI connectivity associated with distinct cognitive states in adults.

Our results partially concur with other studies which found that EEG coherence within hemisphere regions increases as a function of age (Marosi et al., 1992; Barry et al., 2004; Thatcher et al., 2008). The increase in functional connectivity may be partially due to the increase of anatomical connections in the corpus callosum and other fibers and its myelination, which have been associated with the maturation of various cognitive functions (Hagmann et al., 2010; Tanaka-Arakawa et al., 2015). In this regard, the maturation of the corpus callosum and other cortical connections may form anatomical substrates that facilitate information transfer during task performance in older children. Fair et al. (2008) found that a similar default network to the one in adults is only sparsely connected in children aged seven to nine, and that there is a continuous increase in correlation strength over age between long-range connections of the network.

The similarity coupling analysis revealed global changes in the stability of the SCP and the changes that emerged from specific ongoing activity during execution of the odd-ball tasks. The youngest children showed a marked decrease in the similarity metric in the sex condition that did not happen in the other two groups. It is noteworthy that the sex task proved to be more difficult than the happiness one, with the difficulty residing in the perceptual features of the faces presented, since all the clues that facilitate identifying sex -hair and make-up- were removed, leaving only the face contour. Apparently, the youngest children had not completely developed the abilities required to process specific identifying features of faces. In contrast, happiness expressions are the ones recognized best and more quickly and precisely from childhood through adulthood (Juth et al., 2005; Mancini et al., 2013; Chronaki et al., 2015; Brechet,

2017) and may be processed using a more holistic strategy. Another point to consider is that happiness is the emotion that most attracts people´s attention (Becker et al., 2011), so it could help improve performance on odd-ball tasks. Hearne et al. (2017) described that although the increment in task complexity did not change the established modular architecture, it did affect selective patterns of connectivity among frontoparietal, subcortical, cingulo-opercular, and default-mode networks. Larger increases in network efficiency within the newly established task modules were associated with higher reasoning accuracy. Our results partially agree with those obtained by Harrewijn et al. (2021) with fMRI, as they determined that functional connectivity patterns during rest and while executing a dot-probe task -with neutral, happy, and angry faces-were positively correlated, and that the similarity levels in 13 years-old children were primarily related to threat bias.

Some fMRI studies, conducted in adults, mention the relationship between the resting-state and active cognitive patterns. Smith et al. (2009) demonstrated that the functional networks utilized by a brain in action are continuously and dynamically active even when subjects are at rest. In their work, Cole et al. (2014) identified a whole-brain network architecture across different tasks that was quite similar to the resting-state network architecture, suggesting an intrinsic, standard architecture of functional brain organization. However, the task-general network architecture was able to distinguish task states from the resting condition. Based on the foregoing, we propose that the similarity metric is a global brain connectivity index that is appropriate for estimating age-related and dynamic changes according to task demand.

Differences across ages related to task demands were also visible in the cumulative distributions. The 6-years-old children had negative values on both tasks, indicating lower correlation values during the tasks compared to the resting state. The two older groups, in contrast, showed mainly positive values, indicating enlarged correlation. As it can be seen in the rest-to-task subtractions, network changes indicate that an increase in synchronization between some electrode pairs occurred in the 6-year-old-group, accompanied by a decrease between several pairs in both conditions. The correlation decrements displayed a different pattern between tasks, though. The 8-year-old group only showed an increase in correlation, on the one hand, between pairs of regions related to the attentional network (frontal, central, and parietal), and on the other, those related to the face core network (posterior-temporal, parietal and occipital). Finally, the oldest group showed an increase between some of the same regions, mainly in the sex condition, but added frontal-parietal connections. There was a decrease between some long-distance connections, including occipital regions. Miskovic et al. (2015) observed that the oldest age group in their work (11-years-old) exhibited the densest patterns of EEG functional connectivity across distant cortical regions, specifically in the alpha band. Those findings are broadly consistent with one of the more replicable fMRI results involving a trend toward increased integration among distant neural networks (Betzel et al., 2014; Fair et al., 2008; 2009; Supekar et al., 2009). In an fMRI study, Brázdil et al. (2007) found a bidirectional information flow between frontal and parietal regions, mainly in the right hemisphere, involved in attentional processing during an odd-ball task. Those regions are also some of the principal structures considered in the generation of P3b, which has been implicated in the closure of the cognitive event encoding cycle (Halgren, et al., 1998).

With respect to the core face network, Cohen Kadosh et al. (2011) examined the fMRI connectivity during identity and happiness task, observing that although the overall structure of the final mature network was present in 7 years-old children, it develops across childhood. The children in that study, however, did not show the modulation in the functional network connections by task demands that was seen in adults. The authors suggested that the emergence of the face network is due to continuous specialization and fine-tuning within the regions of this network.

While most previous research has analyzed resting-state EEG functional connectivity, we observed changes during task performance that required the involvement of various processes and the activation of underlying neural networks. Briefly, our results support the notion that EEG functional connectivity accounts for age-related developmental changes in cognitive abilities related to processes of attention and face identification.

Our study does, however, presents some limitations, first, the small sample size. Second, we used only the 10/20 System montage, including a few electrodes associated to the main regions involved in odd-ball task performance. Further studies could address changes in all frequency bands, since some studies have found major changes in functional connectivity in the theta and alpha bands during task performance. Moreover, the study of sex differences in functional connectivity across ages would be desirable, since there is evidence of different EEG patterns in both sexes in adults, and during the resting stage in children.

Conclusion

Findings from this study suggest that a base EEG functional network pattern exists from early childhood, which reorganizes across child development. Moreover, functional connectivity is modulated to dynamically adapt to the demands of information processing. The similarity metric may represent an index of global brain connectivity that could be useful in estimating age- and task-related changes. Rest-to-task correlation variations could indicate that the older children in our study generated more

efficient coupling of the areas related to the attentional- and face networks, which may underlie the improvement performance they achieved. The study of EEG functional connectivity, therefore, seems to offer a promising approach to discerning maturational changes during the development of diverse cognitive processes and to our understanding of functional disorders in clinical populations.

Data availability statement

The raw data supporting the conclusion of this article will be made available by the authors upon reasonable request.

Ethics statement

The studies involving human participants were reviewed and approved by Ethical Comitee of the Institute of Neurosciences, University of Guadalajara. Written informed consent to participate in this study was provided by the participants' legal guardian.

Author contributions

JR-L: Conceptualization, Methodology, Validation, Supervision, Funding acquisition, Project administration, Writing–original draft, Writing—review and editing. PO-R: Methodology, Data Curation, Software, Visualization, Conceptualization, Methodology, Writing—original draft, Writing—review and editing. SE-D. Data acquisition, Data Curation, Conceptualization, Methodology, writing—editing. LL-A: Conceptualization, Writing—review and editing. SR-T: Data Curation, Software, Visualization, Methodology, Writing—review and editing. MM: Conceptualization, Methodology, Writing–review and editing.

Funding

The research has received funding from CONACYT (A1-S-46286 and CF-263377).

Acknowledgments

We thank Yermein Benitez for technical assistant and Paul Kersey for editing the manuscript.

Conflict of interest

The authors declare that the research was conducted in the absence of any commercial or financial relationships that could be construed as a potential conflict of interest.

Publisher's note

References

Ansari-Asl, K., Senhadji, L., Bellanger, J. J., and Wendling, F. (2006). Quantitative evaluation of linear and nonlinear methods characterizing interdependencies between brain signals. *Phys. Rev. E Stat. Nonlin. Soft Matter Phys.* 74 (3), 031916. doi:10.1103/PhysRevE.74.031916

Arzate-Mena, J. D., Abela, E., Olguín-Rodríguez, P. V., Ríos-Herrera, W., Alcauter, S., Schindler, K., et al. (2022). Stationary EEG pattern relates to large-scale resting state networks–An EEG-fMRI study connecting brain networks across time-scales. *NeuroImage* 246, 118763. doi:10.1016/j.neuroimage.2021.118763

Bakhshayesh, H., Fitzgibbon, S. P., Janani, A. S., Grummett, T. S., and Pope, K. J. (2019). Detecting connectivity in EEG: A comparative study of data-driven effective connectivity measures. *Comp. Bio. Med.* 105, 1–16. doi:10.1016/j.compbiomed.2019.103329

Barry, R. J., Clarke, A. R., McCarthy, R., and Selikowitz, M. (2002). EEG coherence in attention-deficit/hyperactivity disorder: A comparative study of two DSM-IV types. *Clin. Neurophysiol.* 113 (4), 579–585. doi:10.1016/S1388-2457(02)00036-6

Barry, R. J., Clarke, A. R., McCarthy, R., Selikowitz, M., Johnstone, S. J., and Rushby, J. A. (2004). Age and gender effects in EEG coherence: I. Developmental trends in normal children. *Clin. Neurophysiol.* 115 (10), 2252–2258. doi:10.1016/j.clinph.2004.05.004

Baum, G. L., Cui, Z., Roalf, D. R., Ciric, R., Betzel, R. F., Larsen, B., et al. (2019). Development of structure–function coupling in human brain networks during youth. *Proc. Natl. Acad. Sci. U. S. A.* 117 (1), 771–778. doi:10.1073/pnas.1912034117

Becker, R., Reinacher, M., Freyer, F., Villringer, A., and Ritter, P. (2011). How ongoing neuronal oscillations account for evoked fMRI variability. *J. Neurosci.* 31, 11016–11027. doi:10.1523/JNEUROSCI.0210-11.2011

Benninger, C., Matthis, P., and Scheffner, D. (1984). EEG development of healthy boys and girls. Results of a longitudinal study. *Electroencephalogr. Clin. Neurophysiol.* 57 (1), 1–12. doi:10.1016/0013-4694(84)90002-6

Betzel, R. F., Byrge, L., He, Y., Goñi, J., Zuo, X. N., and Sporns, O. (2014). Changes in structural and functional connectivity among resting-state networks across the human lifespan. *Neuroimage* 102, 345–357. doi:10.1016/j.neuroimage.2014.07.067

Boccaletti, S., Latora, V., Moreno, Y., Chavez, M., and Hwang, D. U. (2006). Complex networks: Structure and dynamics. *Phys. Rep.* 424 (4-5), 175–308. doi:10.1016/j.physrep.2005.10.009

Boersma, M., Smit, D. J. A., de Bie, H. M. A., Van Baal, G. C. M., Boomsma, D. I., de Geus, E. J. C., et al. (2011). Network analysis of resting state EEG in the developing young brain: Structure comes with maturation. *Hum. Brain Mapp.* 32, 413–425. doi:10.1002/hbm.21030

Brázdil, M., Mikl, M., Mareček, R., Krupa, P., and Rektor, I. (2007). Effective connectivity in target stimulus processing: A dynamic causal modeling study of visual oddball task. *Neuroimage* 35 (2), 827–835. doi:10.1016/j.neuroimage.2006.12.020

Brechet, C. (2017). Children's recognition of emotional facial expressions through photographs and drawings. *J. Genet. Psychol.* 178 (2), 139–146. doi:10.1080/00221325.2017.1286630

Bullmore, E., and Sporns, O. (2009). Complex brain networks: Graph theoretical analysis of structural and functional systems. *Nat. Rev. Neurosci.* 10, 186–198. doi:10.1038/nrn2575

Chronaki, G., Hadwin, J. A., Garner, M., Maurage, P., and Sonuga-Barke, E. J. (2015). The development of emotion recognition from facial expressions and non-linguistic vocalizations during childhood. *Br. J. Dev. Psychol.* 33 (2), 218–236. doi:10.1111/bjdp.12075

Chu, C. J., Tanaka, N., Diaz, J., Edlow, B. L., Wu, O., Hämäläinen, M., et al. (2015). EEG functional connectivity is partially predicted by underlying white matter connectivity. *Neuroimage* 108, 23–33. doi:10.1016/j.neuroimage.2014.12.033

Clarke, A. R., Barry, R. J., McCarthy, R., and Selikowitz, M. (2001). Age and sex effects in the EEG: Development of the normal child. *Clin. Neurophysiol.* 112 (5), 806–814. doi:10.1016/S1388-2457(01)00488-6

Cohen, J. R., and D'Esposito, M. (2016). The segregation and integration of distinct brain networks and their relationship to cognition. *J. Neurosci.* 36 (48), 12083–12094. doi:10.1523/JNEUROSCI.2965-15.2016

Cohen Kadosh, K., Cohen Kadosh, R., Dick, F., and Johnson, M. H. (2011). Developmental changes in effective connectivity in the emerging core face network. *Cereb. Cortex* 21 (6), 1389–1394. doi:10.1093/cercor/bhq215

Cole, M. W., Bassett, D. S., Power, J. D., Braver, T. S., and Petersen, S. E. (2014). Intrinsic and task-evoked network architectures of the human brain. *Neuron* 83 (1), 238–251. doi:10.1016/j.neuron.2014.05.014

Corsi-Cabrera, M., Galindo-Vilchis, L., Del-Río-Portilla, Y., Arce, C., and Ramos-Loyo, J. (2007). Within-subject reliability and inter-session stability of EEG power and coherent activity in women evaluated monthly over nine months. *Clin. Neurophysiol.* 118 (1), 9–21. doi:10.1016/j.clinph.2006.08.013

Corsi-Cabrera, M., Solis-Ortiz, S., and Guevara, M. A. (1997). Stability of EEG inter-and intrahemispheric correlation in women. *Electroencephalogr. Clin. Neurophysiol.* 102 (3), 248–255. doi:10.1016/S0013-4694(96)95179-6

Damaskinou, N., and Watling, D. (2018). Neurophysiological evidence (ERPs) for hemispheric processing of facial expressions of emotions: Evidence from whole face and chimeric face stimuli. *Laterality* 23 (3), 318–343. doi:10.1080/1357650X.2017.1361963

Daume, J., Gruber, T., Engel, A. K., and Friese, U. (2017). Phase-amplitude coupling and long-range phase synchronization reveal frontotemporal interactions during visual working memory. *J. Neurosci.* 37 (2), 313–322. doi:10.1523/JNEUROSCI.2130-16.2016

Dekowska, M., Kuniecki, M., and Jaśkowski, P. (2008). Facing facts: Neuronal mechanisms of face perception. *Acta Neurobiol. Exp.* 68 (2), 229–252.

Delorme, A., and Makeig, S. (2004). Eeglab: An open source toolbox for analysis of single-trial EEG dynamics including independent component analysis. *J. Neurosci. Methods* 134 (1), 9–21. doi:10.1016/j.jneumeth.2003.10.009

Driver, J., and Frackowiak, R. S. (2001). Neurobiological measures of human selective attention. *Neuropsychologia* 39 (12), 1257–1262. doi:10.1016/S0028-3932(01)00115-4

Fair, D. A., Cohen, A. L., Dosenbach, N. U., Church, J. A., Miezin, F. M., Barch, D. M., et al. (2008). The maturing architecture of the brain's default network. *Proc. Natl. Acad. Sci. U. S. A.* 105, 4028–4032. doi:10.1073/pnas.0800376105

Fair, D. A., Cohen, A. L., Power, J. D., Dosenbach, N. U., Church, J. A., Miezin, F. M., et al. (2009). Functional brain networks develop from a "local to distributed" organization. *PLoS Comput. Biol.* 5 (5), e1000381. doi:10.1371/journal.pcbi.1000381

Fan, Y., Shi, F., Smith, J. K., Lin, W., Gilmore, J. H., and Shen, D. (2011). Brain anatomical networks in early human brain development. *Neuroimage* 54 (3), 1862–1871. doi:10.1016/j.neuroimage.2010.07.025

Fichtenholtz, H. M., Hopfinger, J. B., Graham, R., Detwiler, J. M., and LaBar, K. S. (2007). Happy and fearful emotion in cues and targets modulate event-related potential indices of gaze-directed attentional orienting. *Soc. Cogn. Affect. Neurosci.* 2 (4), 323–333. doi:10.1093/scan/nsm026

Gasser, T., Jennen-Steinmetz, C., and Verleger, R. (1987). EEG coherence at rest and during a visual task in two groups of children. *Electroencephalogr. Clin. Neurophysiol.* 67 (2), 151–158. doi:10.1016/0013-4694(87)90038-1

Hagmann, P., Sporns, O., Madan, N., Cammoun, L., Pienaar, R., Wedeen, V. J., et al. (2010). White matter maturation reshapes structural connectivity in the late developing human brain. *Proc. Natl. Acad. Sci. U. S. A.* 10744, 19067–19072. doi:10.1073/pnas.1009073107

Halgren, E., Marinkovic, K., and Chauvel, P. (1998). Generators of the late cognitive potentials in auditory and visual oddball tasks. *Electroencephalogr. Clin. Neurophysiol.* 106 (2), 156–164. doi:10.1016/S0013-4694(97)00119-3

Harrewijn, A., Kitt, E. R., Abend, R., Matsumoto, C., Odriozola, P., Winkler, A. M., et al. (2021). Comparing neural correlates of conditioned inhibition between children with and without anxiety disorders - a preliminary study. *Behav. Brain Res.* 5, 399. doi:10.1016/j.bbr.2020.112994

Hearne, L. J., Cocchi, L., Zalesky, A., and Mattingley, J. B. (2017). Reconfiguration of brain network architectures between resting-state and complexity-dependent cognitive reasoning. *J. Neurosci.* 37 (35), 8399–8411. doi:10.1523/JNEUROSCI.0485-17.2017

Juth, P., Lundqvist, D., Karlsson, A., and Öhman, A. (2005). Looking for foes and friends: Perceptual and emotional factors when finding a face in the crowd. *Emotion* 5 (4), 379–395. doi:10.1037/1528-3542.5.4.379

Kikuchi, M., Shitamichi, K., Yoshimura, Y., Ueno, S., Hiraishi, H., Hirosawa, T., et al. (2013). Altered brain connectivity in 3-to 7-year-old children with autism spectrum disorder. *Neuroimage. Clin.* 2, 394–401. doi:10.1016/j.nicl.2013.03.003

Machinskaya, R. I., and Kurgansky, A. V. (2012). A comparative electrophysiological study of regulatory components of working memory in adults and seven-to eight-year-old children: An analysis of coherence of EEG rhythms. *Hum. Physiol.* 38 (1), 1–13. doi:10.1134/S0362119712010136

Maffei, A., and Sessa, P. (2021). Event-related network changes unfold the dynamics of cortical integration during face processing. *Psychophysiology* 58, 5e13786. doi:10.1111/psyp.13786

Mancini, G., Agnoli, S., Baldaro, B., Ricci Bitti, P. E., and Surcinelli, P. (2013). Facial expressions of emotions: Recognition accuracy and affective reactions during late childhood. *J. Psychol.* 147 (6), 599–617. doi:10.1080/00223980.2012.727891

Marosi, E., Harmony, T., Sánchez, L., Becker, J., Bernal, J., Reyes, A., et al. (1992). Maturation of the coherence of EEG activity in normal and learning-disabled children. *Electroencephalogr. Clin. Neurophysiol.* 83 (6), 350–357. doi:10.1016/0013-4694(92)90070-X

Marshall, P. J., Bar-Haim, Y., and Fox, N. A. (2002). Development of the EEG from 5 months to 4 years of age. *Clin. Neurophysiol.* 113 (8), 1199–1208. doi:10.1016/S1388-2457(02)00163-3

Maurits, N. M., Scheeringa, R., van der Hoeven, J. H., and de Jong, R. (2006). EEG coherence obtained from an auditory oddball task increases with age. *J. Clin. Neurophysiol.* 23 (5), 395–403. doi:10.1097/01.wnp.0000219410.97922.4e

Miskovic, V., Ma, X., Chou, C. A., Fan, M., Owens, M., Sayama, H., et al. (2015). Developmental changes in spontaneous electrocortical activity and network organization from early to late childhood. *Neuroimage* 118, 237–247. doi:10.1016/j.neuroimage.2015.06.013

Mormann, F., Fell, J., Axmacher, N., Weber, B., Lehnertz, K., Elger, C. E., et al. (2005). Phase/amplitude reset and theta–gamma interaction in the human medial temporal lobe during a continuous word recognition memory task. *Hippocampus* 15 (7), 890–900. doi:10.1002/hipo.20117

Müller, M. F., Baier, G., Jiménez, Y. L., García, A. O. M., Rummel, C., and Schindler, K. (2011). Evolution of genuine cross-correlation strength of focal onset seizures., Evolution of genuine cross-correlation strength of focal onset seizures. *J. Clin. Neurophysiol.* 28 (5), 450–462. doi:10.1097/WNP.0b013e318231c894

Müller, M. F., Rummel, C., Goodfellow, M., and Schindler, K. (2014). Standing waves as an explanation for generic stationary correlation patterns in noninvasive EEG of focal onset seizures. *Brain Connect.* 4 (2), 131–144. doi:10.1089/brain.2013.0192

Murias, M., Webb, S. J., Greenson, J., and Dawson, G. (2007). Resting state cortical connectivity reflected in EEG coherence in individuals with autism. *Biol. Psychiatry* 62 (3), 270–273. doi:10.1016/j.biopsych.2006.11.012

Olguín-Rodríguez, P. V., Arzate-Mena, J. D., Corsi-Cabrera, M., Gast, H., Marín-García, A., Mathis, J., et al. (2018). Characteristic fluctuations around stable attractor dynamics extracted from highly nonstationary electroencephalographic recordings. *Brain Connect.* 8 (8), 457–474. doi:10.1089/brain.2018.0609

Park, H. J., and Friston, K. (2013). Structural and functional brain networks: From connections to cognition. *Science* 342 (6158), 1238411. doi:10.1126/science.1238411

Pereda, E., Quiroga, R. Q., and Bhattacharya, J. (2005). Nonlinear multivariate analysis of neurophysiological signals. *Prog. Neurobiol.* 77 (1-2), 1–37. doi:10.1016/j.pneurobio.2005.10.003

Perone, S., Palanisamy, J., and Carlson, S. M. (2018). Age-related change in brain rhythms from early to middle childhood: Links to executive function. *Dev. Sci.* 21, 6e12691. doi:10.1111/desc.12691

Qin, J., Chen, S. G., Hu, D., Zeng, L. L., Fan, Y. M., Chen, X. P., et al. (2015). Predicting individual brain maturity using dynamic functional connectivity. *Front. Hum. Neurosci.* 16, 9 418. doi:10.3389/fnhum.2015.00418

Ríos-Herrera, W. A., Olguín-Rodríguez, P. V., Arzate-Mena, J. D., Corsi-Cabrera, M., Escalona, J., Marín-García, A., et al. (2019). The influence of EEG references on the analysis of spatio-temporal interrelation patterns. *Front. Neurosci.* 941. doi:10.3389/fnins.2019.00941

Shirer, W. R., Ryali, S., Rykhlevskaia, E., Menon, V., and Greicius, M. D. (2011). Decoding subject-driven cognitive states with whole-brain connectivity patterns. *Cereb. Cortex* 22 (1), 158–165. doi:10.1093/cercor/bhr099

Smit, D. J., Boersma, M., Schnack, H. G., Micheloyannis, S., Boomsma, D. I., Hulshoff Pol, H. E., et al. (2012). The brain matures with stronger functional connectivity and decreased randomness of its network. *PLoS One* 7 (5), e36896. doi:10.1371/journal.pone.0036896

Smith, S. M., Fox, P. T., Miller, K. L., Glahn, D. C., Fox, P. M., Mackay, C. E., et al. (2009). Correspondence of the brain's functional architecture during activation and rest. *Proc. Natl. Acad. Sci. U. S. A.* 106, 13040–13045. doi:10.1073/pnas.0905267106

Suárez, L. E., Markello, R. D., Betzel, R. F., and Misic, B. (2020). Linking structure and function in macroscale brain networks. *Trends Cogn. Sci.* 24 (4), 302–315. doi:10.1016/j.tics.2020.01.008

Supekar, K., Musen, M., and Menon, V. (2009). Development of large-scale functional brain networks in children. *PLoS Biol.* 7 (7), e1000157. doi:10.1371/journal.pbio.1000157

Tanaka-Arakawa, M. M., Matsui, M., Tanaka, C., Uematsu, A., Uda, S., Miura, K., et al. (2015). Developmental changes in the corpus callosum from infancy to early adulthood: A structural magnetic resonance imaging study. *PLoS One* 10, e0118760. doi:10.1371/journal.pone.0118760

Thatcher, R. W., North, D. M., and Biver, C. J. (2008). Development of cortical connections as measured by EEG coherence and phase delays. *Hum. Brain Mapp.* 29 (12), 1400–1415. doi:10.1002/hbm.20474

Vatansever, D., Bzdok, D., Wang, H. T., Mollo, G., Sormaz, M., Murphy, C., et al. (2017). Varieties of semantic cognition revealed through simultaneous decomposition of intrinsic brain connectivity and behaviour. *Neuroimage* 158, 1–11. doi:10.1016/j.neuroimage.2017.06.067

Yang, Y., Qiu, Y., and Schouten, A. C. (2015). Dynamic functional brain connectivity for face perception. *Front. Hum. Neurosci.* 9, 662. doi:10.3389/fnhum.2015.00662

Yin, Y., Zheng, X., Hu, B., Zhang, Y., and Cui, X. (2021). EEG emotion recognition using fusion model of graph convolutional neural networks and LSTM. *Appl. Soft Comput.* 100, 106954. doi:10.1016/j.asoc.2020.106954

Frontiers in
Network Physiology

Explores how diverse physiological systems and organs interact

The first journal to focus on the mechanisms through which systems and organs interact and integrate to generate a variety of physiologic states.

Discover the latest Research Topics

See more →

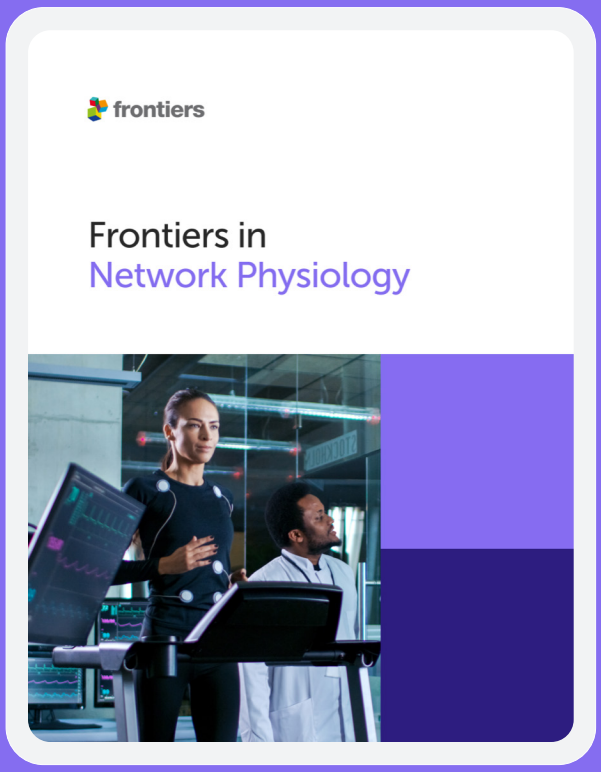

Frontiers

Avenue du Tribunal-Fédéral 34
1005 Lausanne, Switzerland
frontiersin.org

Contact us

+41 (0)21 510 17 00
frontiersin.org/about/contact